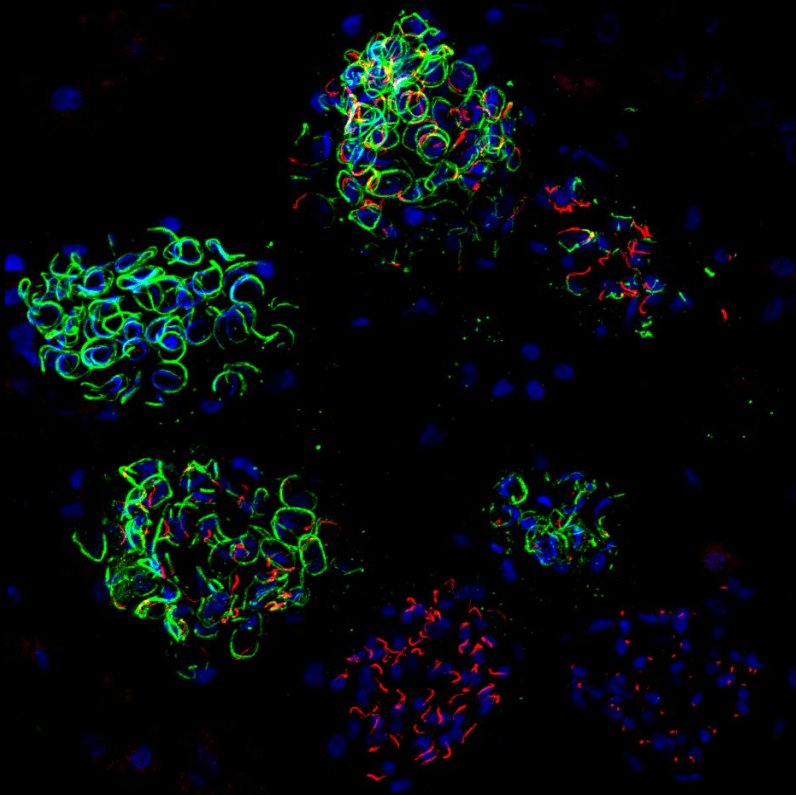


De novo centriole biogenesis during
spermatogenesis in the model bryophyte
Physcomitrium patens

Sónia Alexandra Gomes Pereira



Dissertation presented to obtain the Ph.D degree in Integrative
Biology and Biomedicine

Instituto de Tecnologia Química e Biológica António Xavier | Universidade Nova de Lisboa

Oeiras,
June, 2021



UNIVERSIDADE
NOVA
DE LISBOA

De novo centriole biogenesis during
spermatogenesis in the model bryophyte
Physcomitrium patens

Sónia Alexandra Gomes Pereira

Dissertation presented to obtain the Ph.D degree in Integrative
Biology and Biomedicine

Instituto de Tecnologia Química e Biológica António Xavier | Universidade Nova de Lisboa

Research work coordinated by:



Oeiras, June, 2021



Declaration

I hereby declare that this dissertation, and the data herein contained, are the result of my own work conducted between August 2016 to March 2021 in the laboratories of Doctor Jörg Dieter Becker and Doctor Mónica Bettencourt-Dias, at the Instituto Gulbenkian de Ciência in Oeiras, Portugal.

Financial support for this work was granted by a Doctoral Fellowship awarded to Sónia Gomes Pereira by Fundação para a Ciência e Tecnologia (FCT): PD/BD/114350/2016; the EVOREPRO ERA-CAPS project: ERA-CAPS-0001-2014; and an ERC grant: ERC-2015-CoG-683258-Birth&Death. Acquisition of the electron tomography data presented in Chapter 3 was partially supported by a Cristian Boulin fellowship (EMBL) awarded to Sónia Gomes Pereira.

I also declare that all contributions have been acknowledged in the appropriate “Author contributions” or “Acknowledgments” sections.

From the work developed during this period, resulted the following publications:

Gomes Pereira, S., Sousa, A.L., Nabais, C., Paixão, T., Holmes, A.J., Schorb, M., Goshima, G., Tranfield, E.M., Becker, J.D., and Bettencourt-Dias, M. The 3D architecture and molecular foundations of *de novo* centriole assembly via bicentrioles (*BioRxiv preprint, in revision*);

Gomes Pereira, S., Dias Louro, M.A., and Bettencourt-Dias, M. (2021). Biophysical and quantitative principles of centrosome biogenesis and structure. *Annual Reviews of Cell and Developmental Biology (in press)*;

Nabais, C., **Gomes Pereira, S.**, and Bettencourt-Dias, M. (2018). Noncanonical Biogenesis of Centrioles and Basal Bodies. *Cold Spring Harbor Symposia on Quantitative Biology Volume 82:123-135*.

Acknowledgements / Agradecimientos

“Science is a way of thinking much more than it is a body of knowledge.” — *Carl Sagan*

It is incredible to look back and realize 5 years have gone by, and that the person who now writes these words is not the same one who once wrote that “Origin and Fate of Plant Centrioles” Ph.D project. Over these years I grew so much (both professionally and personally). I will be forever grateful for the many people who made that possible (some of which I will likely forget to mention here!).

First, I thank my supervisors Mónica Bettencourt-Dias and Jörg D. Becker, for taking the leap of faith with me! For accepting this project and my ideas; for all the resources and opportunities over the years; for always allowing me to openly share my unpublished work and ideas; and most importantly, for always giving me the independence to fail (or to succeed) on my own!

To my collaborators: Ana Vinagre (who always went above and beyond for this project), Catarina Nabais, Tiago Paixão, Alexander J. Holmes, Martin Schorb, Gohta Goshima, and Erin M. Tranfield - thank you for your availability and incredible help, and for all the exciting discussions (sometimes in the middle of the night).

I am deeply grateful to all the scientists who paved the way for this work to be possible, and to those who kindly took the time to talk to me, making me a better scientist and person! Although it is impossible to name all, I would like to highlight Philippe Bastin (for I will always cherish our long conversations, that always encouraged me to keep going), Gohta Goshima (for always being available to share his views, irregardless of the times of day, and for his incredible generosity), Paul Guichard (and his scepticism in my cartwheel data, pushing me to find other ways and work harder), Elif Nur Firat-Karalar (for kindly telling me

that this was not my Ph.D project, but my lifelong one! We will see, who knows?!), and Tony Hyman (for always taking the time to talk about my work, but also about other aspects of my Ph.D life).

I am grateful to the Jury members (Prof. Tim Stearns, Prof. Magdalena Bezanilla, Dr. Ben Engel and Dra. Susana Lopes), who promptly accepted the invitation to evaluate my Ph.D Thesis, in what I expect will be a very interesting and exciting discussion!

I would like to acknowledge my thesis committee members: Élio Sucena, José Pereira-Leal, and Raquel Oliveira; for always making me work harder, and fight for what I believed.

Finally, to all my past and present lab colleagues, for their help and support throughout the years. Particularly, Leonor Boavida and Paulo Duarte, for their endless wisdom in the realms of cloning; and Paulo Navarro, for always providing me with his very unique and fresh perspective.

On the personal side, there are many, many, many people that I am forever grateful to have in my life. Some were with me for the whole ride, some arrived later... Yet, hopefully all will stay!

To Miguel Bento, the person who was there through all of it. Who made the good moments always better, and the bad ones tolerable. I am grateful to have shared this journey with you, for all your support (meals included); and specially, for all the moments of silence, when just existing is enough. I hope we have plenty of those still ahead of us!

À minha família, especialmente à minha mãe (Maria de) Fátima, avó Alda, avô Hermínio, e à minha irmã Sofia, por me terem ensinado a lutar por mim e pelos meus princípios, por acreditarem em mim, e por estarem sempre presentes nos piores momentos!

To all the cats in the family, Liz (who started this journey with me, but sadly could not finish it), Hera and Xist (who torment my nights and my

Christmas tree, but brighten my days), and the rest of the pack (Preta, Jonas, Kiko, Simba and Ary), for their enormous (although not intentional) emotional support, crazy moments and their picture-perfect poses.

To my incredible friends, none of which could walk this path for me or carry my cross, but that were always there with signs, nets and first-aid kits (chocolate and tea included), ready to get me back up on my feet whenever I fell. Particularly, Ana Vinagre for her incredible (neverending!) energy, Joana Rodrigues (for the best hugs in the world!), Catarina Nabais (for never letting me feel alone), and Sara Ramos (for always making me laugh, even on the worst of days)...

Thank you Doctor Donna Peach, for creating the most supportive research community in the world - the PhDForum! Who didn't necessarily make me more productive, but who made every isolation day special and fun. I have never met - and I doubt that I ever will - such an incredible group of loving, generous, and caring humans (and pets). Your continuous support and influence makes me a better person! Looking forward to celebrating many more successes with you all!

To my “vintage” and current *Hwarang* family, thank you for always reminding me of our principles: Courtesy, Integrity, Perseverance, Self-Control and Indomitable Spirit; all of which were incredibly precious in this journey. But also for, even not knowing or understanding anything about science, always asking and listening...

I am deeply grateful to so many others (e.g. Andreia Mindouro, João Costa, Susana Ladeiro, João Sobral), and I could write a thesis about it but... I won't! One of those was enough! Sorry to all who I didn't personally name here. Thank you all for these incredible 5 years!

“I think I'm quite ready for another adventure” — *Bilbo Baggins*

“It’s a dangerous business, Frodo, going out of your door,’ he used to say. ‘You step into the Road, and if you don’t keep your feet, there is no telling where you might be swept off to.’” — *Frodo Baggins*

J.R.R. Tolkien, Three Is Company, The Fellowship of the Ring

Summary

Centrioles play dual roles within Eukaryotic cells, being a key component of the main microtubule-organizing center of animal cells - the centrosome, and serving as basal bodies for cilia/flagella assembly. Due to their critical functions, centriole biogenesis is tightly regulated in time, space and number.

In many eukaryotes, one centriole (daughter) assembles in close proximity to a pre-existing one (its mother), once per cell cycle. Such mechanism for centriole assembly is known as centriole duplication, and is thought to represent the ancestral pathway for centriole biogenesis. However, centrioles also assemble *de novo* in many cell types, tissues and species, with particular pathways and structures being employed to achieve such a goal. For example, in land plants with motile sperm cells, centrioles assemble *de novo via* two almost-exclusive structures: bicentrioles (e.g. bryophytes), or blepharoplasts (e.g. *Ginkgo biloba*). Nevertheless, and contrasting with centriole duplication, the mechanisms regulating *de novo* centriole biogenesis remain largely unknown. This is partially due to the lack of amenable model organisms and tools to tackle such processes. Still, this unexplored diversity is critical to understanding centrioles' assembly, evolution and functions.

During my Ph.D, I aimed at understanding *de novo* centriole assembly in the model bryophyte *Physcomitrium patens* (*P. patens*). I started by developing the required protocols for high-resolution imaging of *P. patens* sexual reproduction (Chapter 2). Such tools can easily be adapted for other processes and species, providing valuable resources to a broader community.

Then, combining transmission electron microscopy and tomography, I characterized the bicentriole-mediated *de novo* centriole biogenesis in *P. patens* with unprecedented detail (Chapter 3). These bicentrioles are composed of two similar centrioles with opposite polarities, connected by

a seemingly continuous cartwheel. Several microtubules emanate from these bicentrioles, suggesting they might assemble from, or act as, microtubule organizing centers. Additionally, I also revealed that the two sister centrioles mature asymmetrically, containing naked cartwheel regions and microtubule triplets of distinct lengths. Moreover, the length of the microtubule triplets was also found to vary within the same centriole. However, the surprising structural asymmetries identified do not appear to constrain ciliary beating, with both cilia being able to beat asynchronously, as well as synchronously.

In this work, I also set out to add the first molecular data to this unique pathway for centriole biogenesis, by investigating the localization and functions of known centriolar components conserved throughout the vast majority of ciliated eukaryotes (Chapter 4). This confirmed the structural asymmetries between both sister centrioles, further revealing the assembly of two bicentrioles in the sperm mother cell that localize at the mitotic spindle poles. Functional characterization of such components reinforced the idea of a common molecular pathway for centriole biogenesis, relying on SAS6 cartwheel's rings stabilized by Cep135/Bld10, which enables cartwheel-microtubule attachment. Finally, POC1 and SAS4 are likely to be involved in the assembly of the centriolar wall, although only POC1 appears to play a critical role in this process, in contrast to what is known for several animal species where CPAP/SAS4 is key for centriole assembly.

Finally (Chapter 5), I discuss how this work provides new insights into *de novo* centriole assembly and maturation, reinforcing the idea that these processes are less constrained than previously thought, with the same molecular components leading to diverse structural features. My work also highlights the relevance of exploring fundamental processes in distinct species, particularly as more tools become available.

Sumário

Os centríolos desempenham um duplo papel dentro das células eucarióticas, sendo um dos principais componentes do dominante centro organizador de microtúbulos das células animais - o centrossoma, e servindo como corpos basais para a biogénese de cílios/flagelos. Devido às suas funções essenciais, a biogénese de centríolos é bastante regulada no tempo, espaço e em número.

Em muitos organismos eucariotas, um centríolo (filho) “nasce” próximo a um pré-existente (sua mãe), uma vez por ciclo celular. Esse mecanismo de montagem do centríolo é conhecido como duplicação de centríolos, e é considerado como a via ancestral para a sua biogénese. No entanto, os centríolos também aparecem *de novo* em vários tipos de células, tecidos e espécies, a partir de mecanismos e estruturas específicas. Por exemplo, em plantas com espermatozoides móveis, os centríolos surgem *de novo* a partir de duas estruturas quase exclusivas: bicentríolos (por exemplo, nos briófitos) ou blefaroplastos (por exemplo, em *Ginkgo biloba*). No entanto, e contrastando com a duplicação de centríolos, os mecanismos que regulam a biogénese de centríolos *de novo* permanecem maioritariamente desconhecidos. Isto deve-se em parte à falta de organismos-modelo, e de ferramentas adequadas para estudar tais processos. Ainda assim, esta diversidade inexplorada é crítica para a compreensão da biogénese, evolução e função dos centríolos.

Durante o meu doutoramento, tive como objetivo compreender o aparecimento *de novo* dos centríolos no briófito *Physcomitrium patens* (*P. patens*). Comecei por desenvolver os protocolos necessários para a imagiologia da reprodução sexual de *P. patens* com a resolução necessária (Capítulo 2). Estas ferramentas podem agora ser facilmente adaptadas para outros processos e espécies, representando recursos valiosos para uma comunidade mais ampla.

Posteriormente, combinando microscopia eletrônica de transmissão e tomografia eletrônica, caracterizei com notável detalhe, a biogénese de centríolos mediada por bicentríolos em *P. patens* (Capítulo 3). Mostrando que tais bicentríolos são compostos por dois centríolos semelhantes com polaridades opostas conectados por um *cartwheel* aparentemente contínuo. Vários microtúbulos emanam destes bicentríolos, sugerindo que tais podem surgir de, ou actuar, como centros organizadores de microtúbulos. Além disso, este trabalho também revelou que os dois centríolos da mesma célula são modificados assimetricamente, contendo regiões de *cartwheel* sem microtúbulos e com tripletos de comprimentos distintos. Além disso, o comprimento dos tripletos também parece variar dentro do mesmo centríolo. No entanto, as surpreendentes assimetrias estruturais identificadas não parecem restringir o batimento dos cílios, sendo ambos capazes de bater tanto de forma assíncrona quanto síncrona.

Com este trabalho, também me propus adicionar os primeiros dados moleculares a esta via única para a biogénese de centríolos, investigando a localização e funções de componentes centriolares conhecidos, e conservados na grande maioria dos eucariotas ciliados (Capítulo 4). Esta estratégia permitiu-me confirmar as assimetrias estruturais entre os dois centríolos, revelando ainda o aparecimento de dois bicentríolos na célula-mãe do esperma, que se localizam nos pólos do fuso mitótico. A caracterização funcional de tais componentes reforçou a ideia de uma via comum para a biogénese de centríolos, dependendo de anéis de SAS6 para formar o *cartwheel*. Tais anéis são estabilizados por Cep135/Bld10, que também torna possível ligação dos microtúbulos ao *cartwheel*. Finalmente, POC1 e SAS4 parecem estar envolvidos na montagem da parede centriolar, embora apenas PpPOC1 pareça desempenhar um papel crítico neste processo, em contraste

com o que é conhecido em várias espécies animais onde CPAP/SAS4 é essencial para a biogénese de centríolos.

Finalmente (Capítulo 5), discuto como este trabalho fornece novos dados sobre a biogénese e maturação de centríolos *de novo*, reforçando a ideia de que esses processos são mais flexíveis do que se pensava, com diferentes características estruturais formadas a partir dos mesmos componentes moleculares. O meu trabalho também destaca a importância de investigar processos fundamentais em espécies diversas, especialmente à medida que mais ferramentas vão ficando disponíveis.

List of Abbreviations

2D: Two-dimensional, *xy*

3D: Tri-dimensional, *xyz*

aa: Amino acids

AeD: Amorphous electron density

AFS: Automated freeze substitution

AKAP: A-kinase anchoring protein

ANAPC4: Anaphase-promoting complex subunit 4

ANOVA: Analysis of variance

ANRKD: Ankyrin repeat domain-containing protein

BF: Brightfield

BIC: Bayesian information criterion

BLAST: Basic local alignment search tool

Bld10: Bald 10 (also known as Cep135)

bp: Base pairs

BSA: Bovine serum albumin

C. elegans: *Caenorhabditis elegans*

C. reinhardtii: *Chlamydomonas reinhardtii*

C2CD3: C2 domain-containing protein 3

CAMSAP: Calmodulin-regulated spectrin-associated protein

Cas9: CRISPR associated protein 9

CCDC: Coiled-coil domain-containing protein

CDK5RAP2: Cyclin dependent kinase 5 regulatory subunit associated protein 2 (also known as Cep215)

Cep: Centrosomal protein

CID: Cartwheel inner density

CLASP: Cytoplasmic linker-associated protein

CLEM: Correlative light and electron microscopy

Cnn: Centrosomin

CP: Centrosomal protein

CPAP: Centrosomal P4.1-associated protein (also known as SAS4)
CRISPR: Clustered regularly interspaced short palindromic repeats
D. melanogaster: *Drosophila melanogaster*
DA: Distal appendage
DAI: Days after induction (of sexual reproduction)
DAPI: 4',6-diamidino-2-phenylindole
DDSA: Dodecenyl succinic anhydride specially distilled
Deup1: Deuterosome assembly protein 1
DMP-30: Tris-(dimethylaminomethyl) phenol
DNA: Deoxyribonucleic acid
E. coli: *Escherichia coli*
EB: End binding protein
Eg5: Kinesin-like protein KIF11 (also known as Kinesin-5)
EGTA: Ethylene glycol tetraacetic acid
EHD: EH (Eps15 homology) domain-containing
EM: Electron microscopy
ER: Endoplasmic reticulum
ET: Electron tomography
FBF: Fas-binding factor
FDA: Fluorescein diacetate
FPS: Frames per second
FRAP: Fluorescence recovery after photobleaching
FS: Freeze substitution
G418: Geneticin
GDP: Guanosine diphosphate
GFP: Green fluorescent protein
gRNA: Guide ribonucleic acid
GTP: Guanosine triphosphate
H. sapiens: *Homo sapiens*
HAUS: augmin-like complex

HPF: High pressure freezing

HR: Homologous recombination

IFT: Intraflagellar transport

K. O.: Knock-out

kb: Kilo base pairs

LA: Locomotory apparatus

LECA: Last eukaryotic common ancestor

LS: Lamellar strip

M. polymorpha: *Marchantia polymorpha*

MAP: Microtubule-associated protein

MIP: Microtubule inner protein

MLS: Multilayered structure

MT: Microtubule

MTOC: Microtubule organizing center

NA: Numerical aperture

ND: Not determined

NEDD1: Neural precursor cell expressed, developmentally down-regulated 1 (also known as GCP-WD)

NMA: Methyl-5-norbornene-2,3-dicarboxylic anhydride

NP-40: Nonidet P-40

OCT: Optimal cutting temperature compound

ODF2: Outer dense fibers 2

ON: Overnight (12 to 16hours)

P. patens: *Physcomitrium patens*

PACSIN: Protein kinase C and casein kinase substrate in neurons

PB: Phosphate buffer

PBS: Phosphate buffered saline

PCM: Pericentriolar material

PCNT: Pericentrin

PCR: Polymerase chain reaction

PEG: Polyethylene glycol

PF: Protofilament

PIk: Polo-like kinase

POC: Proteome of the centriole

PPB: Preprophase band

PpBld10: *Physcomitrium patens*' Bld10 gene (Pp3c9_9030v3.1)

PpBld10: *Physcomitrium patens*' Bld10 protein

PpPoc1: *Physcomitrium patens*' POC1 longest coding sequence (Pp3c16_11590V3.1)

PpPOC1: *Physcomitrium patens*' POC1 protein

PpSas4: *Physcomitrium patens*' sas4 gene (Pp3c14_14590V3.1)

PpSAS4: *Physcomitrium patens*' SAS4 protein

PpSas6: *Physcomitrium patens*' sas6 gene (Pp3c23_8210v3.1)

PpSAS6: *Physcomitrium patens*' SAS6 protein

RNAi: Interference ribonucleic acid

ROI: Region of interest

rpm: Rotations per minute

RT: Room temperature

SAS: Spindle assembly abnormal protein

Sas6_CC: Sas6/XLF/XRCC4 coiled-coil

SAS6_N: SAS N-terminal domain

SCLT: Sodium channel and clathrin linker

SDA: Subdistal appendage

SIM: Structured illumination microscopy

SNAP: Soluble NSF (N-ethylmaleimide-sensitive factor) attachment protein

SPD: Spindle defective

SPICE: Spindle and centriole-associated protein

STIL: SCL/TAL1 (stem cell leukemia/T-cell acute lymphoblastic leukemia 1)-interrupting locus protein

TCHP: Trichoplein keratin filament-binding protein

Tcp10_C: T-complex protein 10 C-terminus

TEM: Transmission electron microscopy

TZ: Transition zone

vs.: *versus*

WD40: Beta-transducin domain

WT: Wild-type

γ -TuRC: γ -Tubulin ring complex

Δ bld10: Deletion of PpBld10 coding sequence (Pp3c9_9030v3.1)

Δ poc1: Deletion of PpPOC1 longest coding sequence

(Pp3c16_11590V3.1)

Δ sas4: Deletion of PpSAS4 coding sequence (Pp3c14_14590V3.1)

Δ sas6: Deletion of PpSAS6 coding sequence (Pp3c23_8210v3.1)

Table of Contents

Declaration	i
Acknowledgements / Agradecimentos	ii
Summary	vi
Sumário	viii
List of Abbreviations	xi
Table of Contents	xvi
Chapter 1. General introduction	1
1.1 The microtubule cytoskeleton	2
1.1.1 Microtubules in plant cells	5
1.1.2 Microtubules in animal cells	9
1.1.2.1 Centrosome, centrioles and cilia	10
1.2 Centriole structure and dynamics	12
1.2.1 Centriole structure	12
1.2.1.1 Cartwheel assembly and elongation	17
1.2.1.2 Centriolar wall assembly and elongation	17
1.2.2 Centriole biogenesis	18
1.2.2.1 Centriole duplication	19
1.1.2.2 <i>De novo</i> centriole biogenesis	20
1.2.3 Centriole maturation	23
1.2.3.1 Regulation of centriole's length	23
1.2.3.2 Centriole/basal body docking and ciliogenesis	24
1.2.4 Centrioles in development	26
1.2.4.1 Centriole remodeling during spermatogenesis	27
1.2.5 Centriole evolution and structural diversity	30
1.3 Evolution of plant sexual reproduction	37
1.3.1 Plant evolution	37
1.3.2 Plant sexual reproduction	43
1.3.2.1 Architecture of motile sperm cells	46
1.4 Centrioles in land plants	49

1.4.1 The blepharoplast-mediated pathway	50
1.4.2 The bicentriole-mediated pathway	52
1.4.3 <i>Physcomitrium patens</i> as a model organism to study <i>de novo</i> centriole biogenesis	54
1.5 Framework for the thesis	57
1.6 References	60
Chapter 2. Advanced imaging methods for the study of <i>P. patens</i> spermatogenesis	91
2.1 Abstract	92
2.3 Introduction	92
2.4 Plant maintenance and growth	95
2.5 Transmission electron microscopy of developing sperm cells in <i>P.</i> <i>patens</i>	96
2.5.1 Chemical fixation protocol	97
2.5.1.1 Material and equipment	97
2.5.1.2 Reagents and solutions	98
2.5.1.3 Protocol	99
2.5.2 High pressure freezing followed by freeze substitution (HPF+FS)	106
2.5.2.1 Material and equipment	106
2.5.2.2 Reagents and solutions	107
2.5.2.3 Protocol	108
2.6 Light microscopy approaches for <i>P. patens</i> sperm cells	111
2.6.1 Immunofluorescence of tissue cryosections	111
2.6.1.1 Material and equipment	111
2.6.1.2 Reagents and solutions	112
2.6.1.3 Protocol	113
2.6.2 Immunofluorescence of individualized cells	121
2.6.2.1 Material and equipment	121
2.6.2.2 Reagents and solutions	122

2.6.2.3 Protocol	122
2.6.3 Live imaging of discharged sperm cells	128
2.6.3.1 Material, reagents and equipment	128
2.6.3.2 Solutions	128
2.6.3.3 Protocol	129
2.7 Results and discussion	133
2.7.1 <i>P. patens</i> asynchronous spermatogenesis enables the analysis of several developmental stages within the same sample	133
2.7.2 Spermatogenesis milestones revealed by light and electron microscopy	136
2.7.3 The mature spermatids of <i>P. patens</i>	143
2.7.4 Distinct protocols provide different, and yet complementary, insights	146
2.8 Conclusion	149
2.9 Author contributions and acknowledgements	150
2.9.1 Author contributions	150
2.9.2 Acknowledgements	150
2.10 References	151
Chapter 3. The 3D architecture of <i>P. patens</i> centrioles: bicentriole-mediated assembly and asymmetrical maturation	156
3.1 Abstract	157
3.2 Introduction	158
3.3 Methods	160
3.3.1 <i>P. patens</i> strains and growth conditions	160
3.3.2 Transmission electron microscopy	161
3.3.2.1 Chemically fixed samples	161
3.3.2.2 High pressure frozen-freeze substituted samples	162
3.3.2.3 Electron tomography and segmentation	164
3.3.3 Fast timelapse imaging of sperm cell motility, tracking and analysis	164

3.4 Results	165
3.4.1 The bicentriole-mediated pathway for <i>de novo</i> centriole biogenesis	165
3.4.2 3D ultrastructural analysis of centriole assembly reveals asymmetrical centriole maturation	171
3.4.2.1 Centrioles assemble as a bicentriole which contains two centrioles of opposite polarities and nucleates microtubules ...	171
3.4.2.2 The two similar centrioles separate and associate with the multilayered structure	174
3.4.2.3 Sister centrioles mature asymmetrically	176
3.4.3 <i>P. patens</i> cilia display two distinct behaviours: synchronous and asynchronous beating	179
3.5 Discussion	182
3.6 Author contributions and acknowledgements	187
3.6.1 Author contributions	187
3.6.2 Acknowledgements	187
3.7 References	188
Chapter 4. An evolutionary conserved module for centriole assembly and diversification	193
4.1 Abstract	194
4.2 Introduction	195
4.3 Methods	198
4.3.1 Ortholog identification, similarity and expression analysis ...	198
4.3.2 <i>P. patens</i> transgenic strain generation	199
4.3.2.1 Vector construction and preparation	199
4.3.2.2 Transformation	200
4.3.2.3 Selection and genotyping	200
4.3.3 <i>P. patens</i> strains and growth conditions	201
4.3.4 Immunofluorescence, 3D-SIM imaging and signal length analysis	202

4.3.4.1 Immunofluorescence and 3D-SIM	202
4.3.4.2 Signals length quantification and distribution	203
4.3.5 Transmission electron microscopy of chemically fixed samples	204
4.3.6 Correlative light and electron microscopy (CLEM)	204
4.3.7 Sperm cell motility assessment	206
4.3.8 Fertility rate analysis and statistics	206
4.4 Results	207
4.4.1 Conserved core centriole proteins are preferentially expressed during <i>P. patens</i> gametogenesis	207
4.4.2 Localization of SAS6 and POC1 reveal differences between sister centrioles	210
4.4.2.1 SAS6 and POC1 localization report the bicentriole-mediated pathway for centriole biogenesis	211
4.4.2.2 Two distinct SAS6 and POC1 length populations	215
4.4.2.3 PpSAS6 localizes to both cartwheels as well as to the MLS	217
4.4.3 Core centriolar proteins appear to have conserved their functions throughout evolution	220
4.4.3.1 Despite localizing to the MLS, PpSAS6 is only required for cartwheel assembly	223
4.4.3.2 PpBld10 is required for cartwheel elongation	225
4.4.3.3 PpPOC1 is involved in centriole wall assembly	228
4.4.3.4 CPAP/SAS4 is not essential for proper centriole assembly in <i>P. patens</i>	230
4.4.3.5 Proper centriole and cilia structures are essential for sperm motility and fertility	233
4.5 Discussion	236

4.5.1 Transcriptional regulation of <i>de novo</i> centriole biogenesis in <i>P. patens</i>	237
4.5.2 New findings on the bicentriole-mediated <i>de novo</i> centriole assembly, revealed by co-localization of SAS6 and POC1	239
4.5.3 A conserved cartwheel assembly module	240
4.5.4 Conservation and particularities of <i>P. patens</i> centriolar walls	241
4.6 Author contributions and acknowledgements	245
4.6.1 Author contributions	245
4.6.2 Acknowledgements	246
4.7 References	246
4.8 Supplementary information	255
Chapter 5. General discussion	270
5.1 Temporal, spatial and numerical regulation of centriole biogenesis	272
5.2 Centriole length and asymmetries	276
5.3 Centriole remodeling, cilia beating, and fate of the locomotory apparatus	280
5.4 Evolution and diversification of centriole assembly	284
5.4 References	288

Chapter 1.

General introduction

1.1 The microtubule cytoskeleton

The cytoskeleton of eukaryotic cells is an intracellular network of actin, microtubules and intermediate filaments. It provides cells with the structural organization required to regulate their morphology, physiology and mechanical properties (Chakraborty et al., 2020). Particularly, microtubules (MTs) play critical roles in cell motility and division, wherein they assemble the bipolar mitotic spindle (Wittmann et al., 2001; Garcin and Straube, 2019).

MTs are assembled from α - β - tubulin heterodimers arranged linearly in a head-to-tail arrangement to form protofilaments (PFs), with an end terminated by β -tubulin - the plus-end; and another with α -tubulin exposed - the minus-end (Figure 1.1). These PFs associate laterally assembling hollow cylindrical filaments with approximately 25nm of diameter and whose length can reach several micrometers - the microtubules (Akhmanova and Steinmetz, 2015; Chakraborty et al., 2020). While *in vitro*, MTs contain a variable number of PFs (ranging from 11 to 18), *in vivo* most MTs are composed of 13 PFs (Tilney et al., 1973; Wade et al., 1990; Chakraborty et al., 2020). Microtubules display dynamic instability, alternating between phases of assembling and disassembling, by addition or loss of tubulin heterodimers (Mitchison and Kirschner, 1984; Desai and Mitchison, 1997). Microtubule polymerization occurs mostly from the plus-end, and is accompanied by hydrolysis of the β -tubulin-bound GTP to GDP. However, such hydrolysis leads to conformational changes that destabilize the microtubule lattice and promote MT depolymerization (Weisenberg et al., 1976; Hyman et al., 1995; Alushin et al., 2014). Therefore, the 'GTP-cap'-model was proposed to explain how MT growth can endure such destabilization. In this model, the MT plus-end is enriched in GTP-bound tubulin enabling persistent MT growth (Figure 1.1), while the loss of such cap results in

abrupt MT shrinkage, also called catastrophe. Such catastrophes can be followed by periods of MT regrowth, or rescue (Mitchison and Kirschner, 1984; Desai and Mitchison, 1997). Such dynamic instability of the microtubules is critical to enable the fast MT network rearrangements required for several cellular processes, such as chromosome search-and-capture during mitosis (Blackwell et al., 2017).

In addition to their critical structural role in the microtubule, α - and β -tubulin molecules contain disordered C-terminal tails that can be target of several post-translational modifications (Figure 1.1), such as glutamylation, glycylation, and acetylation. Moreover, acetylation might also take place on the luminal side of the tubule. Together, these modifications define a “tubulin code”, tailoring the MT properties and functions (Janke and Magiera, 2020). Another way by which cells regulate MT properties, functions and MT-based processes is by interactions between MTs and microtubule associated proteins (MAPs, Figure 1.1). MAPs help regulate MT polymerization, depolymerization and bundling dynamics (e.g. γ -tubulin, katanin and tau), bind MT ends (e.g. EB1), and serve as motor proteins, generating forces for MT-based movement and intracellular trafficking (Bodakuntla et al., 2019). Microtubule-based intracellular transport is mostly driven by two types of microtubule motors: kinesins - mostly responsible for plus-end directed transport; and dyneins - moving towards the minus-end (Burute and Kapitein, 2019). Interestingly, plants lack cytoplasmic dynein motors. Hence, the minus-end directed transport in plant cells is dependent on a plant-specific kinesin family (Kinesin-14), which displays minus-end directed movement (Ali and Yang, 2020).

In order to efficiently build and regulate a functional MT network, cells must control microtubule organization and nucleation. MT nucleation occurs mostly from specialized locations in the cell called microtubule organizing centers (MTOCs), and frequently relies on γ -tubulin ring

complexes (γ -TuRCs). These complexes serve as seeds for α/β - tubulin heterodimers to initiate MT growth and cap MT minus-ends, preventing their depolymerization (Figure 1.1)(Pickett-Heaps, 1974; Zheng et al., 1995; Farache et al., 2018). Distinct organelles and locations may serve as MTOCs in different cell types and species. This is regulated by interactions between γ -TuRCs and specific adaptors, restricting microtubule nucleation and organization (Sulimenko et al., 2017). Finally, MTs may themselves serve as platforms for nucleation of other MTs, a process called MT branching, involving the MAP HAUS/augmin which enables γ -TuRC association with pre-existing MTs (Figure 1.1)(Goshima et al., 2008; Petry et al., 2013).

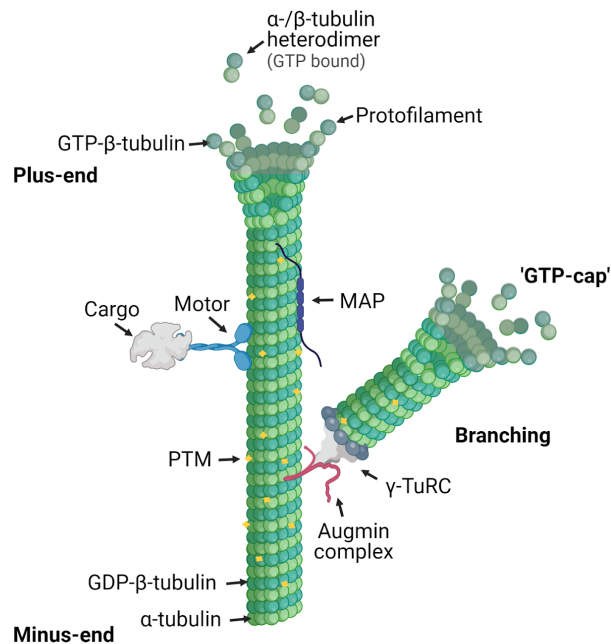


Figure 1.1: Microtubule structure and dynamics. Microtubules are constituted by protofilaments of α -tubulin (light green) and β -tubulin (dark green) heterodimers. The minus-end terminates in α -tubulin, while the plus-end has exposed β -tubulin, and is where polymerization occurs. The 'GTP-cap' (shaded regions) is the region containing GTP-bound

β -tubulin which, upon polymerization, is hydrolyzed to GDP- β -tubulin. Microtubules are decorated by several microtubule associated proteins (MAPs), some of which can bind the microtubule lattice (MAP in purple) or serve as molecular motors (Motor in blue), transporting cargoes (in grey) along the microtubule. Moreover, the C-terminal tails of α - and β -tubulin are targets of post-translational modifications (PTM, yellow starts), which together with MAPs regulate the dynamics and functions of microtubules. Microtubule growth usually starts from a γ -tubulin ring complex (γ -TuRC, in grey), and microtubules themselves may serve as platforms for microtubule nucleation, leading to microtubule branching. In this case, molecules such as the augmin complex (in red) guide γ -TuRC to the pre-existing microtubule surface and enable microtubule polymerization. Figure created with BioRender.com.

1.1.1 Microtubules in plant cells

Microtubule nucleation in plant cells is known to occur from organelles such as the plasma membrane, nuclear envelope and plastids (Brown and Lemmon, 2007). However, as plant cells lack discrete MTOCs, MT-dependent MT nucleation is of particular importance, being the main process for MT nucleation during assembly of several plant specific MT arrays (Figure 1.2)(Lee and Liu, 2019). In fact, while in animal cells γ -tubulin is particularly localized at MTOCs, in plants it decorates the MT arrays along their lengths, being critical for MT branching (Liu et al., 1993; Murata et al., 2005). Both NEDD1/GCP-WD and augmin participate in γ -tubulin/ γ -TuRCs recruitment to the existing MTs, allowing for MT branching to occur (Liu et al., 2014; Walia et al., 2014). Yet, in order to adjust and respond to environmental changes, plant MT networks also need to be dynamic. Such dynamicity is partially guaranteed by the action of MT severing enzymes such as katanin, being required to sustain proper cell elongation (Burk et al., 2001;

Nakamura et al., 2010; Lindeboom et al., 2013). MT severing generates new MT minus-ends, which are vulnerable to catastrophe. MAPs such as tortifolia1, spiral2 and γ -TuRC cap these minus-ends, stabilizing the microtubules (Buschmann et al., 2004; Fan et al., 2018; Nakamura et al., 2018; Yagi et al., 2018).

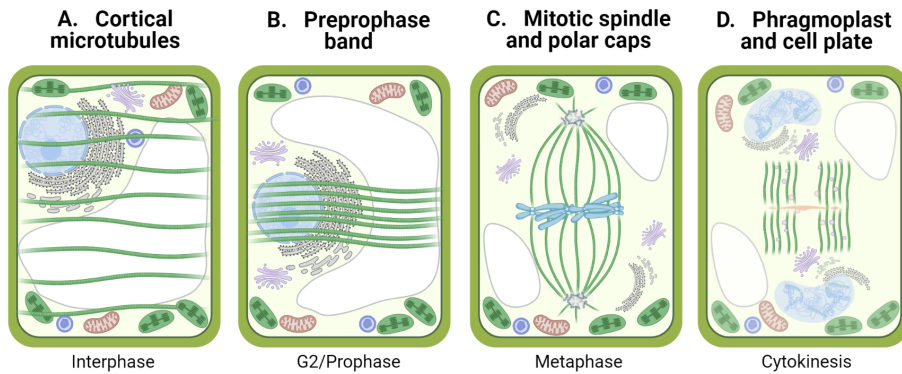


Figure 1.2: Microtubule arrays in plant cells. **A.** Cortical microtubule array. In non-dividing plant cells, microtubules are arranged in a parallel manner, being mostly nucleated/docked to the plasma membrane; **B.** Preprophase band (PPB). In preparation for mitosis (in G2/prophase), microtubules get enriched and assemble into a band of parallel microtubules - the preprophase band, defining the cell division plan; **C.** Mitotic spindle and polar caps. In plants, the mitotic spindle is acentrosomal and instead, microtubules are organized from γ -TuRC enriched regions named polar caps. Some plant species lack polar caps, but have functionally similar structures to ensure spindle bipolarity at metaphase; **D.** Phragmoplast and cell plate deposition. Separation of daughter cells during cytokinesis is achieved through fusion of Golgi derived vesicles that lead to cell plate deposition. The unidirectional transport of such vesicles, as well as the location of the cell plate, are determined by the phragmoplast - an array of antiparallel microtubules with their plus-ends facing the midline, and oriented perpendicularly to

the division plane. The phragmoplast, as well as the cell plate, expand centrifugally from the mid-region to the cell's periphery. Figure created with BioRender.com.

In addition to MT-dependent MT nucleation, new MTs are also nucleated from the plasma membrane in a γ -TuRC-dependent manner (Nakamura et al., 2010). Indeed, this process is thought to be important to establish the cortical MT array in non-dividing plant cells. The cortical MT array is composed of several parallel microtubule filaments (Figure 1.2A) and plays important roles in cell expansion and plant morphogenesis, by regulating cellulose deposition (Shaw et al., 2003; Paredes et al., 2006; Lee and Liu, 2019). Cortical MTs display different arrangements in specialized cells, such as in the guard cells of the stomata and the water-conducting xylem cells, in order to enable the cell's physiological functions (Cyr and Palevitz, 1995).

Most plant cells are surrounded by a rigid polysaccharide wall, which constricts their shape. Therefore, in order for plant cells to organize into tissues with a defined architecture, the plane of cellular division must be tightly controlled. While in animal cells mitotic spindle orientation is defined in metaphase, plant cells establish their division plane before mitosis. In preparation for cell division (late G2) plant cells assemble a highly-aligned cortical microtubule ring structure called preprophase band (PPB) (Figure 1.2B), which determines the cell division plane (Pickett-Heaps and Northcote, 1966; Schaefer et al., 2017). Several intrinsic and extrinsic factors influence PPB location, namely protein localization, tissue wounding and mechanical stress (Lintilhac and Vesecky, 1981; Hush et al., 1990; Hamant et al., 2008; Facette et al., 2019). PPB band assembly involves changes in MT dynamics to allow for MT enrichment at the determined location with simultaneous loss of cortical MTs from the areas above and below the PPB (Mineyuki et al.,

1989; Dhonukshe and Gadella, 2003; Vos et al., 2004). Although γ -TuRC localizes at the PPB, the requirement for new MT nucleation at this location remains undetermined (Liu et al., 1993; Janski et al., 2012; Rasmussen et al., 2013).

Disassembly of the PPB occurs by progressive narrowing of the MT band, which completely disappears after the mitotic spindle is formed. However, the site previously occupied by the PPB is marked by specific proteins, defining the cortical division site where cell plate deposition will occur (Buschmann et al., 2006; Walker et al., 2007). Despite its clear role in guiding the cell division plane, the absolute requirement for the PPB is still questioned. As even though mutant plants lacking PPBs show MT organization defects, irregular cell expansion and aberrations in division plane alignment, they still undergo normal cell and tissue differentiation (Traas et al., 1995; Spinner et al., 2013; Yi and Goshima, 2018). Furthermore other plant cells, such as the endosperm in flowering plants and caulonema cells in *Physcomitrium patens* (*P. patens*), never form PPBs during their division cycles (Doonan et al., 1985; Brown and Lemmon, 2001; Yi and Goshima, 2018).

The plant mitotic spindle is assembled before nuclear envelope breakdown, with microtubules nucleated from the surface of the nucleus forming a bipolar prospindle array. Shortly before breakdown of the nuclear envelope, these uniformly distributed nucleus-derived MTs start to focus in γ -tubulin-enriched regions, named polar caps. By prometaphase, the nuclear envelope breaks down and the PPB MTs disappear, with the spindle MTs emanating from the polar caps (Figure 1.2C)(Liu et al., 1993; Lee and Liu, 2019). While polar caps are not ubiquitous in the plant kingdom, several functionally similar structures can be found. For example, in hornworts spindle bipolarity is marked by a plastid-associated axial MT system, and in the liverwort *Marchantia polymorpha* discrete and focused MTOC structures, named polar

organizers, are present at opposite sides of the nucleus during prophase and initiate the assembly of the mitotic spindle (Brown and Lemmon, 1988; Shimamura et al., 2004; Buschmann et al., 2016).

As mitosis concludes and chromatids are segregated, MTs emerge between the two daughter nuclei. These MTs assemble into the phragmoplast, an elongated bipolar bundle of antiparallel microtubules with their plus ends facing the midline. The phragmoplast is composed of two distinct MT populations: interdigitating cross-linked MTs (which cross the phragmoplast midline), and non-interdigitating ones (Figure 1.2D)(Zhang et al., 1990; Liu et al., 1993; Ho et al., 2011). Cytokinesis involves *de novo* deposition of cell membrane and wall material in the cortical division site, forming the cell plate which separates the two daughter cells. The relationship between the cortical division site, previously defined by the PPB, and the phragmoplast is still not clear (Lee and Liu, 2019; Müller, 2019). Cell plate deposition occurs centrifugally by unidirectional transport of Golgi-derived vesicles, ensured by the antiparallel and bipolar organization of the phragmoplast, which concomitantly expands (Otegui et al., 2001; Steinborn et al., 2002; Ueda et al., 2003). As the cell division cycle is completed, with full separation of the two daughter cells by the cell plate and simultaneously disintegration of the phragmoplast, MT nucleation occurs from the nuclear envelope and the cell cortex, establishing the cortical MT array (Hasezawa et al., 1991; Granger and Cyr, 2000; Kumagai et al., 2003).

1.1.2 Microtubules in animal cells

In most animal cells, the centrosome represents the dominant MTOC (Figure 1.3A), assembling a radial MT network, which regulates intracellular transport and spindle pole formation, establishes cellular polarity and participates in cellular migration. However other organelles, such as the Golgi apparatus and nuclear envelope, also have MTOC

capacity (Figure 1.3A), and upon certain conditions, may even replace the centrosome as the main organizer of the MT network (Sulimenko et al., 2017; Meiring et al., 2020). This process usually takes place during cell differentiation and involves changes in cell polarization and centrosome inactivation. Indeed, some centrosomal MT-anchoring factors are re-shuttled to new locations, such as the case of CDK5RAP2/Cep215 and AKAP450, which are also involved in MT nucleation from the Golgi and nuclear envelope (Rivero et al., 2009; Gimpel et al., 2017). Yet, specific factors are required to nucleate/anchor MTs in their new locations, such as CLASP and CAMSAP/patronin proteins (Noordstra et al., 2016; Toya et al., 2016; Wu et al., 2016; Sulimenko et al., 2017; Takeda et al., 2018). Despite several recent advances, the exact mechanisms regulating centrosome inactivation and non-centrosomal MTOC formation still remain elusive.

1.1.2.1 Centrosome, centrioles and cilia

This section is adapted from: Nabais C, Gomes Pereira S, Bettencourt-Dias M (2018). Noncanonical Biogenesis of Centrioles and Basal Bodies. *Cold Spring Harbor Symposia on Quantitative Biology Volume 82*:123-135.

Each centrosome is composed of two cylindrical centrioles (Figure 1.3B), often 9-fold symmetric, surrounded by a dynamic proteinaceous matrix, called pericentriolar material (PCM). The PCM is responsible for anchoring and nucleating microtubules (Figure 1.3A).

Centrioles (Figure 1.3B), then called basal bodies, can also anchor to the cell membrane and template the growth of motile and immotile cilia (Figure 1.3C). In animals, most cell-types form only one cilium (the primary cilium) but others can form hundreds (multiciliogenesis). These

organelles are required for both cell and flow motility, and sensing environmental cues.

Therefore, centrioles play dual roles within eukaryotic cells: as important constituents of the centrosome; and as critical entities enabling ciliogenesis (Figure 1.3).

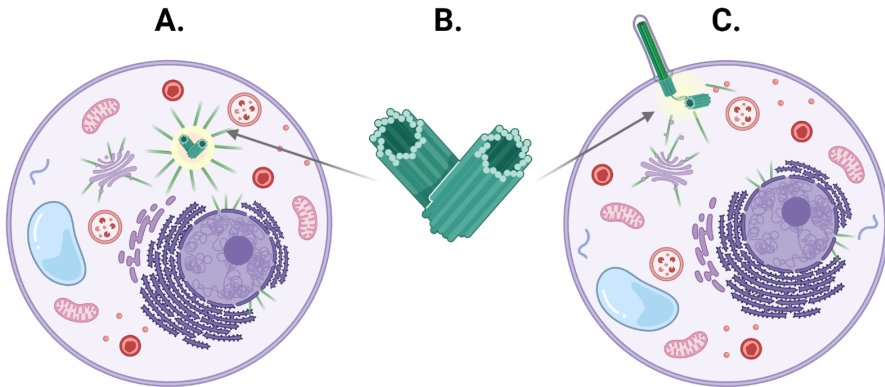


Figure 1.3: Centrioles in centrosomes and cilia. **A.** In most animal cells, the centrosome represents the main MTOC, assembling a radial microtubule network. The centrosome is composed of two centrioles (in dark green) and the pericentriolar matrix (in yellow), which anchors most of the microtubules. Other organelles, such as the Golgi apparatus and the nuclear envelope, also nucleate some microtubules; **B.** A pair of centrioles (in dark green), which are usually 9-fold symmetrical and composed of microtubule triplets. Centrioles perform dual functions within animal cells: as components of the centrosome, and serving as basal bodies during ciliogenesis; **C.** Upon certain conditions and in some cell types, one centriole may dock to the cellular membrane (in dark green) and template axonemal extension (in light green), assembling a cilium. Figure created with BioRender.com.

1.2 Centriole structure and dynamics

Sub-sections 1.2.1, 1.2.2, 1.2.3, and 1.2.4 were adapted from: Gomes Pereira S, Dias Louro MA, Bettencourt-Dias M. (2021). Biophysical and quantitative principles of centrosome biogenesis and structure. *Annual Reviews of Cell and Developmental Biology* (in press).

Sub-sections 1.2.2 and 1.2.5 were adapted from: Nabais C, Gomes Pereira S, Bettencourt-Dias M (2018). Noncanonical Biogenesis of Centrioles and Basal Bodies. *Cold Spring Harbor Symposia on Quantitative Biology Volume 82:123-135*.

1.2.1 Centriole structure

Centrioles are important to form centrosomes and cilia. While most known centrioles have characteristic microtubule triplet blades arranged in a 9-fold symmetry, their ultrastructure is incredibly complex (Figure 1.4)(LeGuennec et al., 2021), and somewhat variable across eukaryotes (Carvalho-Santos et al., 2011). Moreover, centrioles are polarized along their proximal-distal axis, resulting in distinct tilt angles between microtubule blades along their length (Anderson, 1972; Vorobjev and Chentsov, 1982; Li et al., 2012; Greenan et al., 2018). Centriole polarity is enforced by several structural components such as the cartwheel, a proximal centriolar scaffold; the pinhead, connecting the cartwheel to the microtubules; an inner scaffold, connecting all A-tubules; and an inter-triplet linker, called A-C linker which connects adjacent triplets. Furthermore, mammalian centrioles are decorated by other structures, such as the distal and subdistal appendages found on mother centrioles.

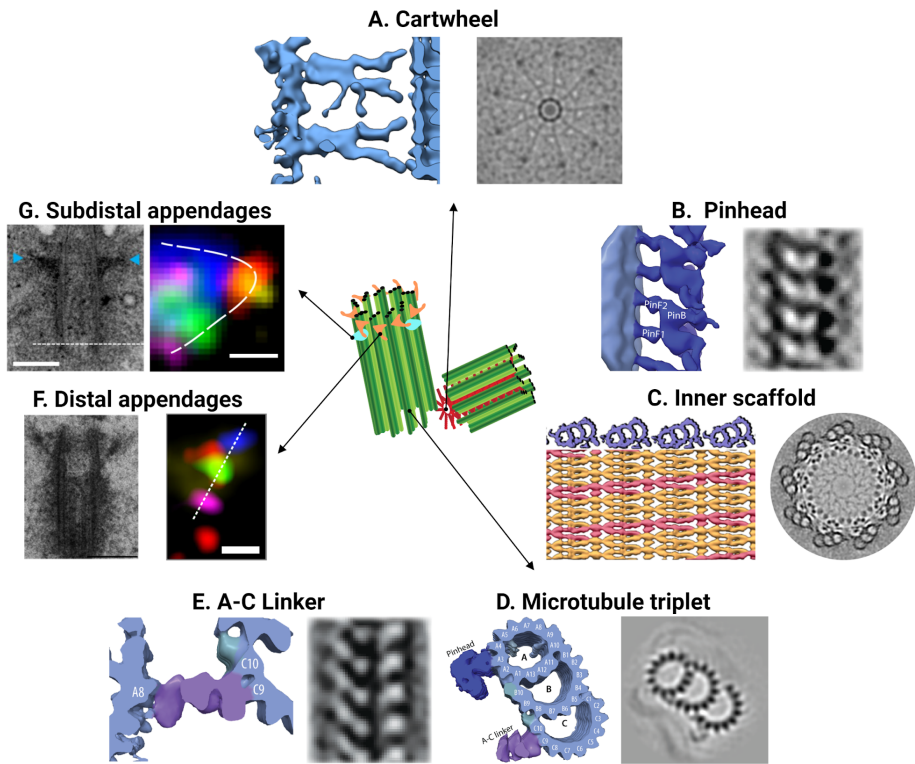


Figure 1.4: Overview of centriole structure. **A.** *Chlamydomonas* cartwheel longitudinal (left) and top (right) views (adapted from Klena et al., 2020); **B.** Pinhead model (left) and longitudinal view (right) of *Trichonympha* spp. (adapted from Nazarov et al., 2020); **C.** The inner scaffold seen from symmetrized images of *Chlamydomonas* centrioles (right) and part of its unrolled structure displaying its dense and helical arrangement (left) (adapted from Le Guennec et al., 2020); **D.** Transversal view (right) and model (left) of *Trichonympha* spp. microtubule triplet blades (adapted from Nazarov et al., 2020); **E.** *Trichonympha* spp. A-C linker transversal structural model (left) and longitudinal structure (right) (adapted from Nazarov et al., 2020); **F.** Human centrioles distal appendages seen by electron microscopy from the longitudinal centriole axis (left, reproduced from Bowler et al., 2019)

and their layered protein composition (right, adapted from Yang et al., 2018) with Cep83 in magenta, SCLT1 in green, FBF1 in blue, Cep163 in yellow and Cep89 in red; **G.** Longitudinal electron microscopy section of a human centriole with visible subdistal appendages (left), which are composed by ODF2 in magenta, Cep128 in green, Centriolin in blue, Ninein in yellow and Cep170 in red (right) (reproduced from Chong et al., 2020). Figure adapted from Gomes Pereira et al. (*in press*) and assembled in BioRender.com.

The cartwheel is the first detectable structure to be assembled and thought to act as a scaffold for centriole biogenesis, being important to determine its symmetry (Figure 1.4A)(Nakazawa et al., 2007; Hilbert et al., 2016). SAS6 is the major component of the cartwheel rings, being present in all species that have centrioles (Nakazawa et al., 2007; Carvalho-Santos et al., 2011). The first cartwheel structure determined, was found to consist of a stack of uniformly repeating SAS6 rings, with a hub and nine spokes (Guichard et al., 2012). Subsequently, it has been shown that the periodicity of ring stacking varies slightly between species, with the possibility of compacted double rings assembling by stacking of two single offset rings (Guichard et al., 2017; Klena et al., 2020; Nazarov et al., 2020). Similarly, spoke organization also differs between species, with spokes from consecutive rings merging in different conformations. As a result, the repeating structural unit of the cartwheel may differ between species and be composed of more than one single cartwheel ring (Klena et al., 2020). Such species-specific differences have been suggested to arise from molecular differences in protein conformation, as well as different mechanisms for assembly (Klena et al., 2020; Nazarov et al., 2020).

On the inside of the cartwheel hub, a cartwheel inner density (CID) was detected (Guichard et al., 2013). CIDs display 9-fold symmetry and

were observed in several species. Their periodicity appears to be double that of rings, suggesting that CIDs may be involved in connecting cartwheel rings and/or assembly of double rings (Klena et al., 2020; Nazarov et al., 2020). The molecular composition and functions for the conserved CIDs remain to be determined.

The tips of the cartwheel spokes bridge the cartwheel with the microtubule wall. This bridge is achieved through the pinhead, a structure composed of a pinbody and two pinfeet (Figure 1.4B). While the pinbody interacts with the cartwheel spokes, the pinfeet are vertically alternating structures that interact directly with the A-tubule. Furthermore, the pinfeet bends towards the proximal end, possibly imparting orientation of the microtubule triplets themselves (Guichard et al., 2013; Nazarov et al., 2020).

Several studies have reported the existence of a cylindrical sheet of material running along the centriole lumen, connecting all the A-tubules (Anderson, 1972; Vorobjev and Chentsov, 1982; Geimer and Melkonian, 2004). Indeed, along centriole length, the pinhead is replaced by an inner centriole scaffold (Figure 1.4C), involved in stabilizing the centriole barrel (Klena et al., 2020; Le Guennec et al., 2020; Steib et al., 2020). Recently, Le Guennec and colleagues (2020) described its ultrastructural organization (Figure 1.4C), revealing the evolutionary conservation of the inner scaffold, despite its species-specific differences.

The canonical centriolar barrel is composed of nine triplet microtubules. The A-tubule is the only complete microtubule, being slightly elliptical and containing 13 protofilaments (A1-13, numbered clockwise from the centriole luminal side). The B- and C-tubules only contain 10 protofilaments (B1-10 and C1-10, numbered clockwise from the centriole outer surface), sharing protofilaments with the A- and B-tubules, respectively (Figure 1.4D)(Linck and Stephens, 2007). Centriolar microtubules are the target of several tubulin post-translational

modifications (Janke and Magiera, 2020) and known to be decorated by several microtubule inner proteins (MIPs) and microtubule-associated proteins (MAPs). Although their exact functions remain unknown, the observation of several MIPs and MAPs periodically distributed along conserved protofilaments suggests they could stabilize the centriolar structure (Li et al., 2012; Greenan et al., 2018; Li et al., 2019).

An apparently flexible A-C linker connects protofilament A8 to protofilament C9 of adjacent microtubule blades (Figure 1.4E)(Guichard et al., 2013; Li et al., 2019). Its detailed structural organization and vertical periodicity varies between species, possibly resulting from molecular divergence. However, its attachment points appear to be conserved (Klena et al., 2020; Nazarov et al., 2020). Slight changes to the conformation of this linker might support, or be a consequence, of the intrinsic centriole polarity.

Centrioles within most cell types are never fully identical as the older, called “mother” centriole, has unique accessory structures called appendages, which practically disappear in preparation for mitosis (Vorobjev and Chentsov, 1982; Bowler et al., 2019). Appendages are classified based on their position on the centriole wall into distal and subdistal appendages. Distal appendages (DAs) are essential for ciliogenesis and are 9-fold electron dense trapezoidal-like projections that end in a small head (Figure 1.4F)(Tanos et al., 2013; Bowler et al., 2019). These projections are tilted in an opposite direction regarding the triplet microtubules, being associated with two of such blades (Anderson, 1972; Bowler et al., 2019). Subdistal appendages (SDAs) play roles in microtubule anchoring during interphase and localize immediately below DAs. SDAs emanate perpendicularly from the centriolar wall, being cone-shaped and variable in numbers (Figure 1.4G)(Vorobjev and Chentsov, 1982; Delgehyr et al., 2005).

1.2.1.1 Cartwheel assembly and elongation

The cartwheel is the first centriolar substructure to be assembled. *In vitro* cartwheel reconstitution has revealed that SAS6 self-organizing properties are critical for cartwheel assembly and ring stacking (Kitagawa et al., 2011; Guichard et al., 2017). It is now clear that SAS6 rings assemble by several routes, involving both the addition of homodimers as well as higher order oligomers (Nievergelt et al., 2018; Banterle et al.). Moreover, the assembly reaction is reversible, which might be critical for ensuring the 9-fold symmetry of the cartwheel (Banterle et al.).

Cartwheels protrude from the proximal end of centrioles (Klena et al., 2020). Indeed, cartwheel elongation is thought to occur mostly from this region, as this is where SAS6 is predominantly incorporated (Guichard et al., 2017; Aydogan et al., 2018). Moreover, SAS6 oligomers assemble in a somewhat helical configuration, being converted into rings by surface constraints, suggesting that SAS6 assembly and rings may have intrinsic chiral properties which could contribute to the polarity and chirality of centrioles themselves (Banterle et al.). Nevertheless, cartwheels composed of only SAS6 do not contain organized spokes. Indeed, proper cartwheel assembly requires both SAS6 and its binding partner Cep135/Bld10, which anchors the cartwheel spokes to the microtubule triplets (Guichard et al., 2017). Consequently, Cep135/Bld10 depletion disrupts the 9-fold symmetry of the cartwheel and hinders centriole biogenesis (Matsuura et al., 2004; Hiraki et al., 2007).

1.2.1.2 Centriolar wall assembly and elongation

During centriole biogenesis, each microtubule triplet blade assembles and elongates independently, with the A-tubule growing unilaterally from what appears to be a γ -tubulin ring complex (γ -TuRC) at its base. Then, B- and C-tubules branch and elongate bidirectionally from the surface of

the A- and B-tubules, respectively (Guichard et al., 2010; Li et al., 2019). After elongation, the γ -TuRC cap disappears from the A-tubule and both A- and B-tubules reach similar length. However, at the distal end of mammalian centrioles, only a partial C-tubule is seen, resulting in a doublet microtubule configuration (Greenan et al., 2018).

In contrast to the recently acquired knowledge regarding cartwheel assembly, the exact mechanisms by which cells control microtubule doublet and triplet assembly, particularly at the centrioles, remain unknown.

1.2.2 Centriole biogenesis

Due to their critical functions, it is essential that centriole biogenesis is tightly regulated. The mechanisms by which centrioles assemble within cells can be broadly divided into two categories: *de novo*, independently of pre-existing centrioles (Figure 1.5A); or canonically, *i.e.* near pre-existing structures, usually by cell cycle coupled duplication (Figure 1.5B). The mechanism used by each cell-type and organism seems highly dependent on the number of centrioles they have to begin with and how many will be generated. While in the canonical pathway, a single daughter is generated per mother per cycle, in most *de novo* pathways that number regulation is seemingly lost, allowing a variable number of centrioles to assemble.

Nevertheless, canonical and *de novo* pathways share many striking similarities, with the astonishing conservation of centriole ultrastructure being determined by a small number of conserved structural proteins, whose overexpression is sufficient to trigger centriole formation (Peel et al., 2007; Rodrigues-Martins et al., 2007; Carvalho-Santos et al., 2011), leading to the idea that self-assembling mechanisms might be at the foundation of centriole biogenesis. Yet, the intrinsic peculiarities of both *de novo* and canonical pathways, indicate that complex and

undiscovered mechanisms of centriole assembly and regulation may be at play. Therefore, understanding the common features between these pathways, as well as their molecular networks, will shed light on how centriole biogenesis is regulated in different cells and organisms.

1.2.2.1 Centriole duplication

In cycling cells, centrioles assemble in G1 to S transition, forming one daughter procentriole orthogonally to each pre-existing mother centriole (Figure 1.5B and 1.6B). A critical event in the initiation of centriole duplication is the recruitment of the Polo-like kinase 4 (Plk4) to the mother centriole (Bettencourt-Dias et al., 2005; Habedanck et al., 2005). Plk4 recruits and phosphorylates STIL, which in turn stabilizes Plk4 preventing its self-targeted degradation (Cunha-Ferreira et al., 2013; Ohta et al., 2018). Plk4 and STIL crosstalk will lead to SAS6 recruitment, triggering cartwheel self-assembly (Kratz et al., 2015; Arquint and Nigg, 2016; Ohta et al., 2018; Park et al., 2020).

After their assembly in S phase, procentrioles elongate and eventually undergo centriole-to-centrosome conversion in late G2, losing the cartwheel (in some mammalian species) and recruiting PCM (Fu et al., 2015). Centrosome maturation occurs as cells enter mitosis, involving PCM expansion and an increase in microtubule nucleation ability (Figure 1.5B). Although the exact molecular players underlying maturation differ between species, the overarching mechanism remains similar. Centrosome maturation relies on the activity of Plk1, an important cell cycle regulatory kinase (Polo in *Drosophila* and PLK-1 in *C. elegans*) (Lane and Nigg, 1996; Cabral et al., 2019). Plk1 activity triggers a positive feedback loop involving Cep192/Spd-2/SPD-2 in humans/flies/worms, that promotes PCM expansion around the mother centriole (Lee and Rhee, 2011; Woodruff et al., 2015; Alvarez-Rodrigo et al., 2019). In humans, the microtubule docking sites within the PCM, are

at least partially dependent on Plk1 phosphorylation of PCNT, Cep192 and CDK5RAP2/Cep125, as well as additional γ -tubulin recruitment factors, such as NEDD1/GDP-WD (Haren et al., 2009; Joukov et al., 2014). Similarly, Polo/PLK-1 activity on Cnn and SPD-5 promote proper γ -tubulin recruitment and microtubule aster formation in *D. melanogaster* (Conduit et al., 2014) and *C. elegans* (Woodruff et al., 2017).

To ensure mitotic spindle bipolarity, the two centrosomes need to separate and relocate to opposite poles of the cell. Centrosome separation requires disassembly of the linker that connects both centriolar pairs, a process known as centrosome disjunction (Agircan et al., 2014). Then, centrosomes migrate towards the spindle poles in a process involving several microtubule motors, such as the kinesin Eg5 and dyneins (Gaglio et al., 1996; Gönczy et al., 1999; Tanenbaum et al., 2008; Smith et al., 2011).

After mitosis, each daughter cell inherits exactly one pair of centrioles. Finally before the next G1, centrioles disengage, breaking the connection between centriole pairs and “licensing” them for the next duplication cycle (Figure 1.5B)(Agircan et al., 2014) .

1.1.2.2 De novo centriole biogenesis

Centrioles can assemble *de novo*, *i.e.* independently of pre-existing centrioles (Figure 1.5A), in several species. However, in most naturally occurring cases, the mechanisms remain poorly understood. The number of centrioles assembled *de novo* varies amongst species and tissues, with several pathways being employed to ensure assembly of the correct centriole number (Figure 1.6A). Centrioles may arise as single units (Figure 1.6C), as two centrioles coaxially oriented (bicentriole, Figure 1.6D), or in electron dense spheres called deuterosomes (in animals, Figure 1.6E) or blepharoplasts (in plants, Figure 1.6F)(Miki-Noumura, 1977; Riparbelli et al., 1998; Renzaglia and

Garbary, 2001). Intriguingly, such biogenesis pathways might not be mutually exclusive. During pharynx regeneration in planarians centrioles arise *de novo* asynchronously combining several different mechanisms/structures, with some being assembled as individual units, others as bicentrioles, and the remaining arising in small clusters (Li et al., 2020).

As in most animals, centrioles are lost during oogenesis and are delivered to the egg by the sperm upon fertilization. In insect eggs, when development is triggered without fertilization, single centrioles are formed *de novo* and nucleate tubulin monoasters (Miki-Noumura, 1977; Palazzo et al., 1992; Riparbelli et al., 1998; Riparbelli and Callaini, 2003). Parthenogenetic development is initiated when two asters are captured by the female pronuclei forming the first mitotic spindle (Riparbelli et al., 1998; Tram and Sullivan, 2000). Similarly, the centriole in mouse sperm is unable to nucleate microtubules after fertilization (Schatten et al., 1985; Gueth-Hallonet et al., 1993), so the first embryonic divisions are acentrosomal and centrioles are only detected by electron microscopy (EM) from 64-cell stage onwards (Gueth-Hallonet et al., 1993; Courtois et al., 2012).

Another example of single centriole biogenesis is the amoebae to flagellate transition in *Naegleria gruberi*, where it was thought that the two centrioles assembled *de novo* (Dingle and Fulton, 1966; Fulton and Dingle, 1971). Yet, by studying the localization of centrin and γ -tubulin during this transition, Fritz-Laylin and colleagues (2016) have shown that only the first centriole assembles *de novo* while the second one appears to duplicate from the first. There is no EM support for the underlying pathway and despite some molecular insights from recent studies (Suh et al., 2002; Kim et al., 2005; Fritz-Laylin et al., 2010; Lee et al., 2015; Fritz-Laylin and Fulton, 2016) the exact cascade is still unknown. Indeed, centriole duplication and *de novo* assembly appear to coexist, such as

observed in *Naegleria gruberi* (Fritz-Laylin et al., 2016) and *D. melanogaster* egg extracts overexpressing Plk4 (Figures 1.5A to B)(Nabais et al., 2021). Moreover in *Naegleria*, both centrioles form cilia, highlighting that centrioles formed *de novo* and canonically are equally capable of nucleating cilia.

Many multiciliated vertebrate tissues, e.g. the respiratory tract, the oviduct and the brain ependyma, are composed of multiciliated cells. These cells produce fluid flow and particle movement, through the coordinated beating of their motile cilia. During their differentiation, multiciliated cells assemble hundreds of basal bodies through the deuterosome-mediated pathway (Meunier and Azimzadeh, 2016). Electron microscopy studies described the formation of electron dense granules ('fibrogranular material') in the cytosol as the first morphological evidence of ciliogenesis (Sorokin, 1968; Dirksen, 1971; Vladar and Stearns, 2007). Progressively, these granules increase in size and condense into large spherical bodies - the deuterosomes - which show no discernible structure and are extremely electron dense, suggesting they consist of concentrated proteins (Figure 1.6E).

Recent studies have shown that, although deuterosomes might initially assemble in close proximity to the pre-existing centrioles within the cell (Al Jord et al., 2014), such are not required for deuterosome assembly (Mercey et al., 2019a; b; Zhao et al., 2019) (Figure 1.5C). Nevertheless, pre-existing centrioles can be used as platforms for centriole amplification (Mercey et al., 2019b; Ching and Stearns, 2020) (Figure 1.5C). Indeed, in the absence of both centrioles and deuterosomes, the correct centriole number assembles from a microtubule convergence area containing PCM proteins (Figure 1.5A)(Mercey et al., 2019a; b). Likewise, the progressive concentration of PCM and centriolar components is also observed before *de novo* centriole biogenesis in the mice early embryo (Courtois et al., 2012) and

in human cells after centriole removal (Figure 1.5A)(Khodjakov et al., 2002). Furthermore, PCM proteins were also suggested to play a role in promoting *de novo* centriole assembly in *D. melanogaster* (Nabais et al., 2021). Conceivably, microtubules could drive or facilitate the concentration of PCM and/or centriolar components above a critical threshold required to trigger *de novo* centriole biogenesis (Figure 1.5A).

1.2.3 Centriole maturation

1.2.3.1 Regulation of centriole's length

It is generally accepted that centriole length is relatively uniform within cell types, yet varying substantially between tissues and species. Although the exact mechanisms determining centriole size are not fully understood, several proteins are known to promote centriole elongation (Sharma et al., 2021). For instance, the direct interaction between the centrosomal protein CPAP/SAS4 and tubulin might regulate tubulin availability for microtubule elongation. Moreover, CPAP/SAS4 also caps the growing microtubule plus-ends *in vitro*, slowing elongation and increasing their stability (Sharma et al., 2016; Zheng et al., 2016). Interestingly, CPAP/SAS4 is regulated by Plk4 and STIL (Cizmecioglu et al., 2010; Tang et al., 2011; Moyer and Holland, 2019) and cooperates with SPICE and Cep120 (Comartin et al., 2013). Yet, how such interactions affect the spatiotemporal regulation of CPAP/SAS4 functions, and centriole elongation remains to be fully elucidated.

Other centriolar components, such as the distal cap protein CP110 and its binding partner Cep97, are known to negatively affect centriole length (Sharma et al., 2021). Cep97 recruits CP110, and together counteract CPAP/SAS4 activity, restricting centriole elongation (Spektor et al., 2007; Schmidt et al., 2009). Despite both being required for proper centriole length in flies (Franz et al., 2013; Dobbelaere et al., 2020), Cep97 also appears to have CP110-independent functions, interacting

with the microtubule acetylation machinery, and thereby promoting centriole stability (Dobbelaere et al., 2020). Nevertheless, it is still unclear if centriole length relies on active regulatory mechanisms, or if it results solely from a balance between positive and negative regulators. Another important aspect to consider is the fact that cell cycle perturbations seem to affect centriole length, with mitosis delays yielding longer centrioles (Kong et al., 2020). This suggests the existence of multiple control mechanisms along the cell cycle, analogous to centriole duplication, or the absence of length control altogether (Sullenberger et al., 2020).

1.2.3.2 Centriole/basal body docking and ciliogenesis

Cilia are composed of a modified centriole docked to the cellular membrane - the basal body; which, by elongation of its A- and B-tubules, templates the elongation of the microtubule extension - the axoneme. In between both of these structures there is a transition zone, a macromolecular complex that partitions the cilium from the cell body (Breslow and Holland, 2019; Kumar and Reiter, 2021).

Centriole docking to the cellular membrane is the first step of ciliogenesis. However, before a centriole is competent to dock, it needs to acquire appendages (Schmidt et al., 2012; Tanos et al., 2013). In human cells, before distal appendages (DAs) assemble, several daughter centriole proteins need to be removed. This is orchestrated by interactions between Talpid3 and C2CD3 (Wang et al., 2018). DAs start to assemble during G2, with the recruitment of C2CD3 and then CCDC41/Cep83 to the mother centriole's surface. Cep83 then recruits CCDC123/Cep89 and SCLT1. These constitute the inner DA components that remain associated with the mother centriole throughout the entire cell cycle. During late mitosis and early G1, the outer DA components Cep164, FBF1 and ANKRD26 are recruited, finalizing DA

assembly (Figure 1.4F)(Bowler et al., 2019). These outer components are temporarily lost again before the next mitosis. Currently, the relevance for such mitotic remodeling of DAs is unknown, however it was suggested that it could help balance the age of both centrioles and/or to ensure cilia reabsorption before cell division (Bowler et al., 2019).

As for distal appendages, subdistal appendage (SDA) assembly also occurs in a stepwise manner, with the inner components placed earlier in the hierarchy. SDA assembly starts with ODF2, whose organization is regulated by its interaction with Cep128 (Chong et al., 2020). ODF2 also interacts and recruits CCDC120, TCHP and might also be involved in recruitment of CCDC68. Together, these proteins recruit Cep170 and Ninein (Figure 1.4G), which are required for microtubule anchoring during interphase (Delgehr et al., 2005; Huang et al., 2017). However, SDAs appear to anchor only a subset of microtubules, whose functions remain unclear (Chong et al., 2020). Despite not being essential for ciliogenesis (Mazo et al., 2016), SDAs are involved in defining and coordinating ciliary beating (Kunimoto et al., 2012) and their loss affects Golgi-Cilia association and causes emergence of submerged cilia (Mazo et al., 2016).

The next step in ciliogenesis involves the formation of a ciliary vesicle through fusion of small pre-ciliary vesicles. Pre-ciliary vesicles are recruited *via* interactions between Cep164 and the vesicle transport machinery proteins Rabin8 and Rab8 (Schmidt et al., 2012). These small vesicles then fuse in a process mediated by membrane-shaping proteins, such as EHD1 and EHD3, their interactors PACSIN1, PACSIN2, and SNAP29 (Lu et al., 2015; Insinna et al., 2019). Afterwards, the distal centriole cap proteins CP110 and Cep97 are removed from the centriole, promoting its association with the membrane

and triggering microtubule elongation (Spektor et al., 2007; Goetz et al., 2012; Lu et al., 2015; Huang et al., 2018).

Finally, axoneme elongation is mediated by intraflagellar transport (IFT) proteins, such as IFT88 and IFT20, which are recruited to the ciliary base (Goetz et al., 2012; Tanos et al., 2013). Axoneme elongation can occur by two pathways: intracytoplasmic, in which the axoneme extends within the ciliary vesicle and then fuses to the plasma membrane, externalizing it (Sorokin, 1962); or plasma-associated, in which the axoneme extends outwards from a docked basal body (Sorokin, 1968).

1.2.4 Centrioles in development

Alterations to centriole length, general architecture and composition are common during development and have been associated with differential regulation of centrosomal components. In fact, regulation of SAS6 appears critical to define centriole length in different *D. melanogaster* tissues (Jana et al., 2018). Moreover, flies have centrioles with either doublet or triplet (sperm) microtubules, different lengths, orientations and/or PCM composition (Jana et al., 2018). Therefore, centriole structure appears tailored to tissue-specific functions.

Centriole number also varies amongst tissues, with some cells having multiple centrioles while others none, suggesting that different tissues might employ different mechanisms to control centriole number. For example, while in most multiciliated cells centriole number is amplified *via* the deuterosome-mediated pathway (see section 1.1.2.2), in the progenitor cells of mouse olfactory neurons, extra centrioles are assembled prior to multiciliation and cell division, in rosette-like structures (Figure 1.5C)(Ching and Stearns, 2020).

Centrosomes, and likely centrioles as well, are lost in several cell types including epithelial, muscle and egg cells (Werner et al., 2017).

While the detailed mechanisms for such process remain largely unknown, it was recently shown that during *D. melanogaster* oogenesis, the centrosome is dismantled inwardly: first Polo is delocalised from the centrosome, then PCM disappears, and finally centriolar components follow (Figure 1.5D)(Pimenta-Marques et al., 2016). Yet, centriole loss during mice oogenesis seems to occur despite PCM persistence (Simerly et al., 2018). Moreover, an intriguing mechanism is employed by starfish, wherein daughter centrioles are kept in the oocyte, whereas mother centrioles are extruded along with the polar bodies (Borrego-Pinto et al., 2016). These examples raise questions as to the mechanisms employed to regulate centriole loss in different species and particularly during sexual reproduction.

1.2.4.1 Centriole remodeling during spermatogenesis

From the first investigations of centriole biology, it has been proposed that centrioles are paternally inherited, being delivered to the acentriolar eggs by the sperm (Wilson, 1925). Several studies have supported this idea, showing the loss of centrioles/centrosomes during oogenesis in many animal species, and the delivery of centrioles by the sperm upon fertilization (Hertig and Adams, 1967; Schatten et al., 1985; Crozet et al., 2000; Manandhar et al., 2005; Avidor-Reiss et al., 2019). Exceptions to this rule are, as previously mentioned, the embryonic development in parthenogenetic insects and in mice (and other rodents), where centrioles arise *de novo* (see section 1.1.2.2). Indeed, during rodent spermatogenesis, centrioles are lost and therefore, can't serve as MTOCs for the first embryonic divisions (Schatten et al., 1985; Manandhar et al., 1998; Simerly et al., 2016).

The paternal centriolar inheritance relies on centrioles being kept during spermatogenesis. However, despite being present and inherited, sperm cell's centrioles are known to be remodeled during

spermatogenesis. The extent of such remodeling varies amongst species and includes attenuation of the microtubule nucleation activity, loss of PCM components, and centriole disintegration (Figure 1.5D)(Manandhar et al., 2005; Avidor-Reiss et al., 2019). Nevertheless, in most mammals and in *D. melanogaster*, spermatozoa contain two centrioles which are asymmetrically remodeled. While in mammalian sperm, the proximal centriole retains a barrel-like structure and the distal one is atypical (composed of splayed microtubules) (Fishman et al., 2018), in *D. melanogaster* sperm cells, it is the proximal centriole that shows an atypical structure (Blachon et al., 2009; Khire et al., 2016).

Such structural remodeling is also accompanied by molecular changes, which appear to be important for post-fertilization development. In *D. melanogaster* these include loss of some centriole components (e.g. CPAP/SAS4, SAS6 and Cep135/Bld10) as well as enrichment of others (e.g. POC1) (Blachon et al., 2009; Khire et al., 2015, 2016). Yet, despite their extensive remodeling, both centrioles appear to be able to recruit PCM and nucleate microtubules, serving as MTOCs for the first embryonic division (Blachon et al., 2014; Fishman et al., 2018). Nevertheless, the physiological requirement and the exact mechanisms regulating remodeling in each centriole and species remain unclear.

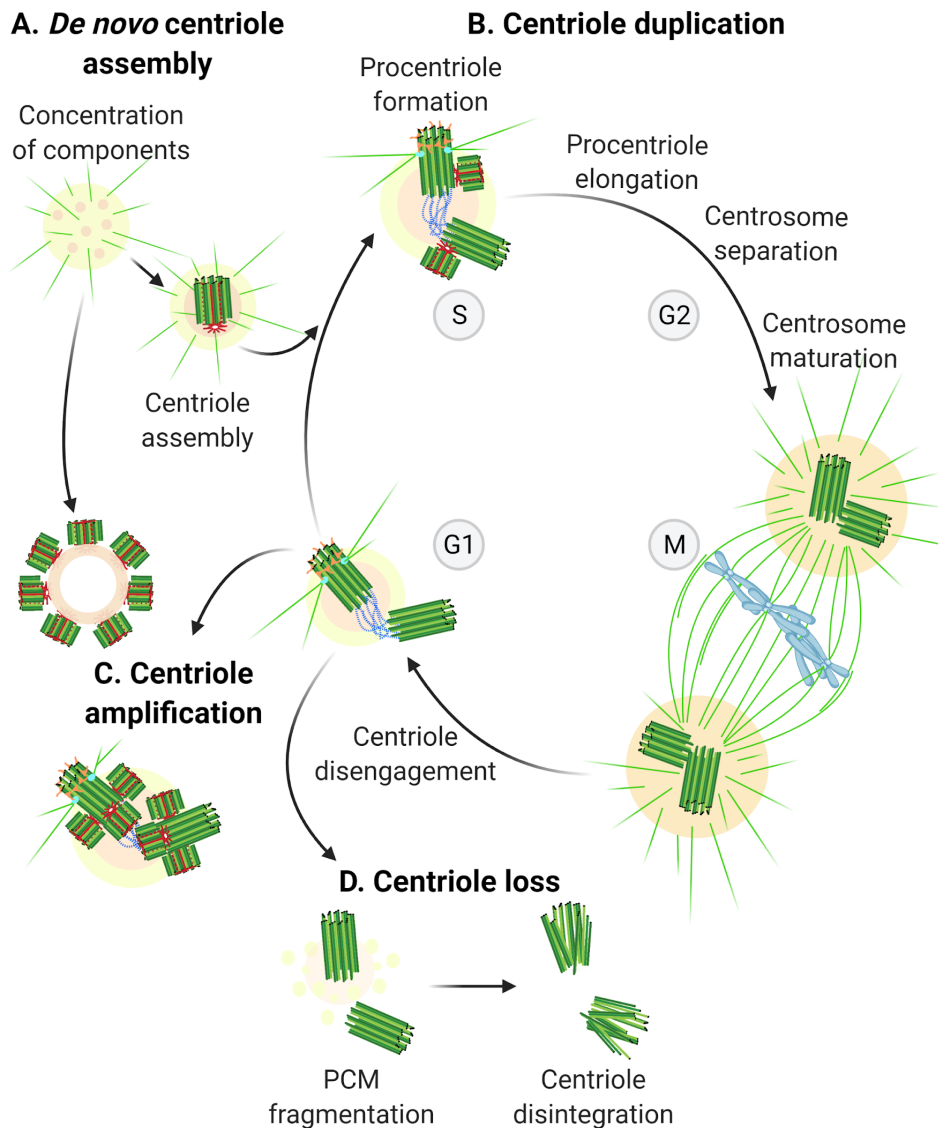


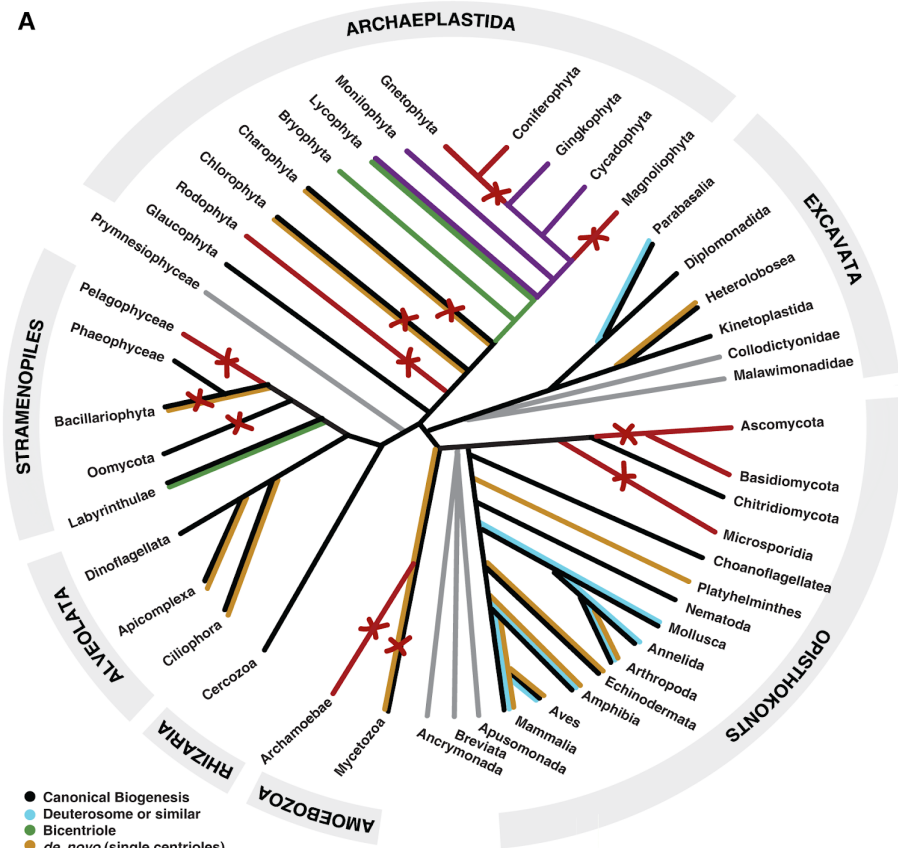
Figure 1.5: Centriolar dynamics within animal cells. **A.** In some cell types and developmental stages, centrioles are capable of assembling *de novo*, following the concentration of components and PCM-like proteins. In animals, centrioles assemble *de novo* as single centrioles or *via* deuterosomes; **B.** The centriole duplication cycle is coupled to the cell cycle. At the transition from G1-S, procentrioles assemble

transversally to the pre-existing centrioles. During S and G2 phases, procentrioles elongate, and centrosomes separate and mature (PCM expansion). Centrosomes anchor the spindle microtubules, serving as MTOCs during mitosis. Each daughter cell inherits one centrosome, containing two centrioles as it re-enters into G1; **C.** During differentiation, cells can increase their centriole numbers prior to multiciliation. This can occur through deuterosomes (*de novo*) or using pre-existing centrioles as platforms for centriole amplification (forming rosette-like structures); **D.** Other cell types lose/remodel their centrioles during differentiation. This process involves the loss of PCM components, followed by disassembly of the centriolar structure. Figure adapted from Gomes Pereira et al. (*in press*) and assembled in BioRender.com.

1.2.5 Centriole evolution and structural diversity

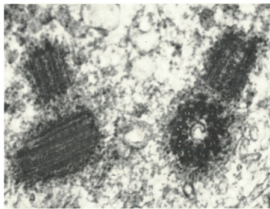
Centrioles (or basal bodies) are well conserved structures present across the eukaryotic tree of life and probably derived from a basal body-like organelle already present in the last eukaryotic ancestor (LECA). Indeed, centrioles are found in all 7 major eukaryotic lineages (Cavalier-Smith, 2002; Hodges et al., 2010). They have been lost within plant, fungi and amoebae lineages or reduced to some particular tissues or life cycle stages in other groups, acquiring new morphologies and modes of biogenesis (Figure 1.6A)(Renzaglia and Garbary, 2001; Woodland and Fry, 2008; Carvalho-Santos et al., 2011; Judelson et al., 2012; Yubuki and Leander, 2013).

A

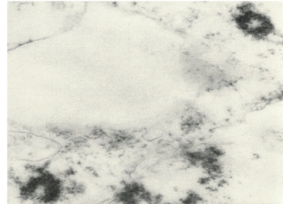


- Canonical Biogenesis
- Deuterosome or similar
- Bicentriole
- *de novo* (single centrioles)
- Blepharoplast
- ✳ CBBs lost in all/some species
- Unsensual taxonomy

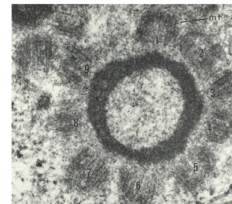
B. Duplication



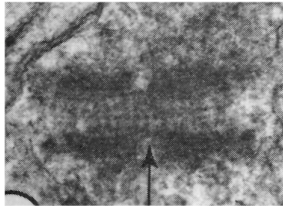
C. *De novo* (single units)



E. Deuterosome



D. Bicentriole



F. Blepharoplast

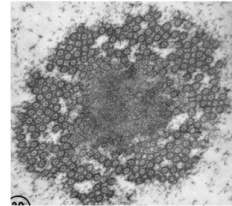


Figure 1.6: Centriole biogenesis across the eukaryotes. A. Consensus eukaryotic tree of life (selected groups; following Burki (2014) and Worden et al. (2015)). Centrioles/basal bodies were lost in multiple lineages (red lines and crosses: absent in all species within the groups; red crosses – lost in only some species within the lineage). The distinct centriole biogenesis pathways are represented in different colours: canonical biogenesis (black line) is the most prevalent pathway and probably, the ancestral one, deuterosome (blue line), the bicentriole (green line) and blepharoplast (purple line) are all evolutionary innovations, arising relatively recently in the eukaryotic history. Some pathways are more restricted to some groups, for example the canonical and deuterosome pathways are predominant in vertebrates, while most plants assemble centrioles through a bicentriole or a blepharoplast. There are some striking exceptions, like the presence of a deuterosome-like mechanism in the sperm of some invertebrates, and the massive centriole amplification observed within the Class Parabasalia (Excavata). In these cases, it was proposed that centriole biogenesis is driven by resident centrioles along a “ladder”-like configuration (Tamm and Tamm, 1980). There are also examples of convergent evolution among pathways, such as the presence of a bicentriole in Labyrinthulae (Stramenopila). **B.** Duplicating centrioles, wherein one daughter centriole assembles perpendicularly to each pre-existing one (adapted from Erlandson and De Harven (1971)); **C.** Centrioles assemble *de novo* as single entities in several naturally occurring scenarios, such as during parthenogenesis. This can be reproduced in artificially activated sea-urchin eggs (adapted from Miki-Noumura (1977)); **D.** Centrioles assembled in a bicentriole arrangement, *i. e.* coaxially oriented end-to-end and connected by a common cartwheel (arrow)(adapted from Moser and Kreitner (1970)); **E.** During multiciliogenesis in several animal species, centriole numbers are

amplified in unstructured electron dense granules, called deuterosomes (adapted from Dirksen (1971)); **F.** Multiciliated plant sperm cells assemble their centrioles within electron dense spheres of unstructured material, named blepharoplasts (adapted from Mizukami and Gall (1966)). Figure adapted from Nabais et al., 2018.

The ancestral centriole was most likely a basal body-like organelle composed of nine microtubule triplet blades arranged in a radially 9-fold symmetrical cylinder (Beisson and Wright, 2003), involved in the nucleation of motile cilia (Carvalho-Santos et al., 2011; Azimzadeh, 2014). Throughout evolution, the requirement for ciliary motility might have imposed a functional constraint on basal body architecture. Indeed, absence of cilia is correlated with centriole loss and the generation of MTOCs with very distinct morphology, like the spindle pole body of fungi and the nuclear-associated body of amoebae (Hodges et al., 2010; Azimzadeh, 2014). Moreover, a recent study by Gouw et al. (M. Gouw, *unpublished*) employed maximum parsimony landscapes to assess the probability of the cilium and the centriole-based centrosome being ancestral in specific eukaryotic lineages. This analysis favoured a convergent evolution hypothesis for the origin of centriole-based centrosomes, suggesting that centrioles were ancestral structures, independently co-opted as part of the centrosomes in different eukaryotic lineages. The acquisition of centrosomal functions might have occurred in a stepwise manner. First, by becoming part of the spindle poles, centrioles could ensure their equal segregation to daughter cells. This could favour PCM enrichment, and potentiate MTOC activity. Finally, the acquisition of cell cycle components would link centrosome biogenesis and segregation to cell cycle progression, allowing a much tighter regulation of its activity and copy-number in cells (Nigg and Holland, 2018).

Canonical duplication (Figure 1.6B) is the most prevalent pathway, and probably the ancestral one. It is present in every main branch of the eukaryotic tree (Figure 1.6A), though the mechanism is somewhat different in specific taxa. In some oomycetes such as *Saprolegnia ferax* and *Phytophthora infestans* (Stramenopiles) and in *Plasmodiophora spp.* (Rhizaria), daughter centrioles assemble in a 180 degree angle from their mother (coaxial orientation), rather than the usual 90 degrees, forming a bicentriole-like structure (Heath and Greenwood, 1970; Heath, 1974a; b; Garber and Aist, 1979). Therefore, the deuterosome, bicentriole and blepharoplast-mediated pathways might represent evolutionary innovations, arising relatively recently in evolution and in particular eukaryotic branches (Figure 1.6). In fact, a recent study argued that the deuterosomes are vertebrate-specific structures, arising just before tetrapode divergence. That is because the specific component of the deuterosome Deup1, is only found in the genomes of lobe-finned fish and tetrapods (Zhao et al., 2013). Throughout the eukaryotes, there are several examples of convergent evolution where unrelated groups appear to share similar strategies to assemble centrioles. For example, a bicentriole is formed *de novo* in the Stramenopila *Labyrinthula spp.* (Perkins, 1970), a similar mechanism to what is observed in the motile sperm of early land plants (Figure 1.6D)(Moser and Kreitner, 1970; Robbins, 1984; Renzaglia et al., 1999). Moreover, this suggests that the possibilities for making centrioles are somewhat limited, indicating some sort of constraints inherent to the process.

Constraints to centriole assembly might not be just morphological but also molecular and, in fact, all biogenesis pathways appear to share some core components. A specific set of centriolar proteins - SAS6, CPAP/SAS4, Cep135/Bld10, POC1, centrin – as well as α -, β - and γ -tubulin, is found in the genome of most eukaryotic species that

assemble centrioles, suggesting that this conserved module may function as part of an ancestral pathway for centriole assembly (Figure 1.7)(Carvalho-Santos et al., 2010; Hodges et al., 2010). Nonetheless, some of these proteins are not centriole-specific. Indeed, orthologs for centrin, α -, β - and γ -tubulin are found in species that do not assemble centrioles, suggesting other general MT/MTOC associated functions (Levy et al., 1996; Vaughn and Harper, 1998; Ito and Bettencourt-Dias, 2018). In support the idea of a conserved ancestral centriole biogenesis pathway, two of such conserved proteins - SAS6 and Cep135/Bld10 - appear to have an evolutionary conserved function in the early steps of centriole assembly, forming the cartwheel (Matsuura et al., 2004; Nakazawa et al., 2007; Hiraki et al., 2007; Guichard et al., 2017; Carvalho-Santos et al., 2011; and Banterle and Gönczy, 2017). Furthermore, Cep135/Bld10 has been shown to have tissue-specific functions (Carvalho-Santos et al., 2012), and protein divergence in SAS6 sequence was suggested to regulate the species-specific cartwheel organization observed (Klena et al., 2020; Nazarov et al., 2020). Still, functional studies and expression data are still scarce outside Opisthokonts, yet these are needed to validate the function of these (and other) components in each pathway, as well as the commonalities between all pathways.

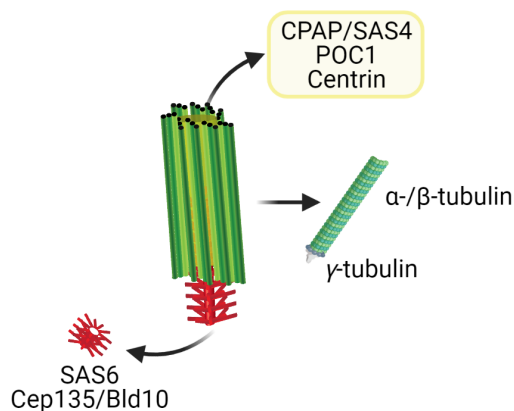


Figure 1.7: Ubiquitously conserved centriolar components. The proteins SAS6, Cep135/Bld10, CPAP/SAS4, POC1, Centrin, α -, β - and γ -tubulin are found in all species that assemble centrioles/basal bodies, despite distinct biogenesis pathways (Carvalho-Santos et al., 2010; Hodges et al., 2010). While some of these proteins play critical centriole-specific roles in cartwheel assembly (SAS6 and Cep135/Bld10) and in centriole elongation and stability (CPAP/SAS4 and POC1), others might play more general microtubule/MTOC roles, such as in microtubule assembly and nucleation (α -, β - and γ -tubulin). Interestingly, centrin proteins are conserved in species that lack centrioles/basal bodies, and might have ancestral MTOC related functions. Still they appear to have acquired centriole-specific functions (in duplication, separation, positioning/orientation and maintenance) throughout evolution (Levy et al., 1996; Koblenz et al., 2003; Vonderfecht et al., 2012; Zhang and He, 2012). Figure created with BioRender.com.

Despite the high conservation observed across eukaryotes, structural variations in centriole structure are observed both between species, as well as within the same organism. Such variations include microtubule walls with different conformations, lengths and symmetry (Jana, 2021). While most centrioles are composed of microtubule triplets, classical examples for microtubules with different wall conformations include the singlet or doublet microtubules in *C. elegans* embryos or ciliated sensory neurons (Pelletier et al., 2006; Nechipurenko et al., 2017), and the microtubule doublets or triplets found in most *D. melanogaster* tissues vs. its sperm, respectively (Callaini et al., 1997; Gottardo et al., 2015). Furthermore, while most centrioles retain their cartwheels, this structure is lost during mitosis in mammalian cells (Strnad et al., 2007) and *D. melanogaster* sperm (Blachon et al., 2009).

Centrioles also vary in length, with the canonical centrioles being around 450nm in height with a ~100nm long cartwheel (LeGuennec et al., 2021). Centrioles can be longer, reaching around 1.1 μ m in *Teranympha* (Nazarov et al., 2020), and 5 μ m in several *Trichonympha* species, accompanied by a ~4.5 μ m long cartwheel (Gibbons and Grimstone, 1960). As wall composition, length variations can also be detected within species. Strikingly, *D. melanogaster* is known to contain particular small centrioles (~100-250nm), however during spermatogenesis these elongate substantially, reaching over 1.3 μ m in length (Jana et al., 2018).

Finally, centrioles might also vary in symmetry. For instance, in *Lecudina tuzetae*, *Nymphon leptochelae* and in *Acerentomon microrhinus* spermatocytes centrioles display 6-, 12-, and 14-fold radial symmetry, respectively (van Deurs, 1973; Schrevel and Besse, 1975; Dallai et al., 2010). Interestingly, in the fungi *Sciara coprophila*, “giant centrioles” composed of variable number of centrioles (40-70+), containing either singlet or doublet microtubules, appear to be arranged in an oval conical-like configuration (Phillips, 1967). It would be interesting to understand how these variations are regulated/determined and if they rely on the same core components as canonical centrioles.

1.3 Evolution of plant sexual reproduction

1.3.1 Plant evolution

The Archaeplastida or Plantae supergroup is thought to have arisen from endosymbiosis of a cyanobacterium by a heterotrophic eukaryote. Today, it represents a diverse group of photosynthetic eukaryotes that can be found in both aquatic and terrestrial environments, including the

Glaucophyta, the Rhodophyta and the Viridiplantae lineages (McFadden, 2014; Dittami et al., 2017). At the root of the Archaeplastida, the glaucophytes (Figure 1.8) are unicellular algae found exclusively in freshwater habitats, being characterized by their uniquely underived blue-green plastid, called cyanelle (Kies and Kremer, 1986; Delwiche and Timme, 2011). The Rhodophyta, or red algae, are mostly found in marine environments, although they can also be found in freshwater and partially terrestrial ecosystems. Despite sharing some traits with land plants, such as multicellularity, apical growth and plasmodesmata, these organisms lack motile flagella and have evolved independently of land plants, forming a separate clade (Figure 1.8)(Delwiche and Timme, 2011; Terauchi et al., 2015; Moody, 2020).

The Viridiplantae includes all green algae (chlorophytes and charophytes) and the land plants (embryophytes), with charophytes and embryophytes constituting a monophyletic group named Streptophyta (Figure 1.8)(Leliaert et al., 2012; Rensing, 2018). Chlorophytes were the first organisms to acquire molecular mechanisms to cope with high levels of solar radiation, allowing their unicellular or colonial species (e.g. *Chlamydomonas* and *Volvox carteri*, respectively) to conquer shallow water environments (Dittami et al., 2017; Biswal and Panigrahi, 2021). Cilia/flagella similarities have long supported the notion that land plants have evolved from chlorophyte ancestors, however recent phylogenetic analysis based on molecular markers contradicted this view, supporting a divergence between the Chlorophyta and the Streptophyta (Figure 1.8)(McCourt, 1995; Kapraun, 2007; Hodges et al., 2012).

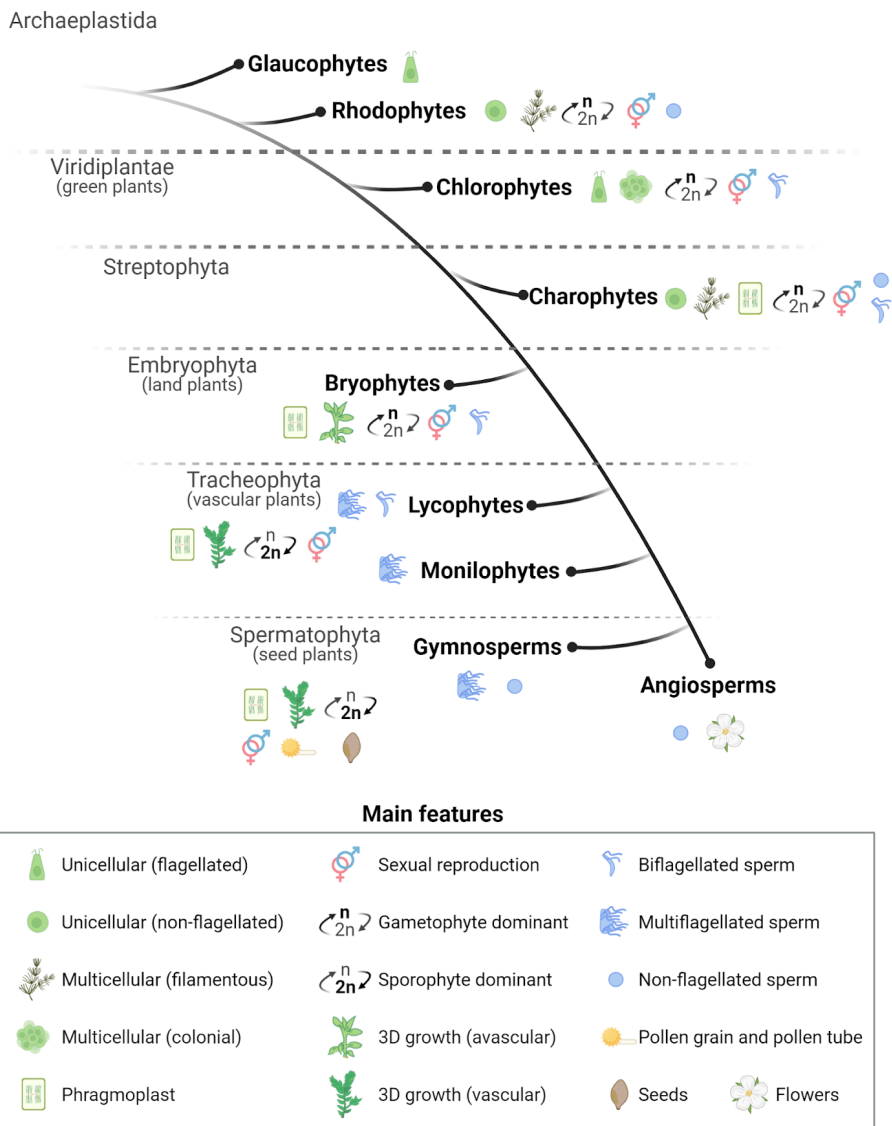


Figure 1.8: Plant evolution. The Plantae kingdom includes the glaucophytes, the rhodophytes (or red algae) and the Viridiplantae (or green plants) lineage. Glaucophytes are always unicellular and flagellated, while red algae might be unicellular or multicellular but are never flagellated. The Viridiplantae are further subdivided into the chlorophytes (which may be unicellular flagellated or multicellular

colonial) and the Streptophyta. Streptophyta include the unicellular or filamentous charophyte algae, in which only cytodifferentiated sperm cells of some species are flagellated, and where the phragmoplast first appeared; and the Embryophyta (or land plants). Embryophytes are divided into the avascular bryophytes (the first species to develop a 3D body plan) and tracheophytes (or vascular plants). The tracheophytes are vascular plants with a sporophyte-dominant (diploid) life cycle, and include the lycophytes, the monilophytes and the seed plants (or Spermatophyta). Lycophytes have biflagellated or multiflagellated sperm cells, while monilophytes always have multiflagellated sperm cells. Several non-highlighted features distinguish both groups (e.g. leaf architecture and positioning). Finally, seed plants are characterized by pollen-tube sperm-delivery and the existence of enclosed ovules which will support seed development. Gymnosperms have multiflagellated (cycads and *Ginkgo*) or immotile (non-flagellated; gnetales and conifers) sperm cells, while angiosperms only have non-flagellated sperm cells, being distinguished by the presence of flowers. Figure created with BioRender.com.

As streptophytes diverged, their morphologies and body plans became more complex, starting from simple unicellular to complex multicellular organisms, eventually capable of sustaining 3D growth (Moody, 2020). Charophytes are green algae that reside predominantly in freshwater environments. The phragmoplast is first detected in some lineages of this group, such as the case of the emerging model species *Chara braunii*, allowing for a better orientation of the cell division plane and the formation of 2D branched filaments (Figure 1.8)(Leliaert et al., 2012; Dittami et al., 2017; Nishiyama et al., 2018; Moody, 2020). Other important traits seem to have first appeared during Charophyta evolution, namely the appearance of hormone signaling pathways and

the transfer of plastid-encoded genes to the nuclear genome (Wang et al., 2015; de Vries et al., 2016). Charophytes are thought to be the closest living relatives of all land plants (embryophytes). While some charophytes are capable of sexual reproduction, their diploid stage is only composed by the zygote, which immediately undergoes meiosis. On the other hand, Embryophyta got their nomenclature for having a zygote capable of undergoing embryogenesis, progressing into an embryo that develops into a 3D body plan (Figure 1.8)(Rensing, 2018; Moody, 2020).

The terrestrial colonization by embryophytes represents a key event in the history of life on Earth, allowing photosynthesis to occur on its surface, which permanently changed it (Dittami et al., 2017; Rensing, 2018; Moody, 2020). This transition involved several evolutionary innovations and adaptations, including the development of a 3D body plan, cuticle, wall, cell and organ specialization (e.g. stomata, vascular tissues and sexual organs) for protection against several abiotic stress and the ever-changing environmental conditions (Kenrick and Crane, 1997; Kenrick, 2017; Rensing, 2018). Land plants are further subdivided based on the appearance of such innovations, with the main division being between vascular (Tracheophyta) and non-vascular plants (Bryophyta) (Figure 1.8). Despite the phylogenetic relationships amongst bryophyte lineages (mosses, liverworts and hornworts) still being debatable, it is widely accepted that they represent a monophyletic group, and the first species to colonize a terrestrial environment (Figure 1.8)(Mishler et al., 1994; Delwiche and Cooper, 2015; Szövényi et al., 2019). The key feature of all bryophytes, including the model species *Physcomitrium patens* (moss) and *Marchantia polymorpha* (liverwort), is their dominant haploid gametophyte life cycle, comprising a short diploid sporophyte stage which is nutritional dependent on the predominant haploid gametophyte (Kenrick, 2017; Rensing, 2018).

Vascular plants are characterized by the presence of vascular tissue specialized for water and nutrient transport, which allowed them to grow taller. This group includes lycophytes, monilophytes, gymnosperms and angiosperms. Lycophytes (such as *Selaginella moellendorffii*) are the closest group to the bryophytes, followed by monilophytes (horsetails and ferns), sisters to all seed plants (gymnosperms and angiosperms) (Figure 1.8)(Harrison and Morris, 2018; Szövényi et al., 2019). Vascular plants display a significant reduction of their gametophyte. Indeed, these have a sporophyte dominant life-cycle, which increased in complexity as they diverged (Kenrick and Crane, 1997; Rensing, 2018). For instance, the stem cell pool of the shoot apex varies in size between groups, from a single cell in lycophytes and some monilophytes, that periodically bifurcates, to several cells in horsetails and seed plants, where branching occurs sub-apically, leading to divergence in leaf primordia positioning (Harrison and Morris, 2018). Moreover while in ferns (such as *Marsilea vestita*), both gametophytes and sporophytes are free-living, in seed plants the gametophyte is significantly reduced to a few reproductive cells, from where a new sporophyte develops (Remy et al., 1993; Kenrick, 2017; Rensing, 2018).

Seeds were another key evolutionary innovation, developing from water-independent fertilization and allowing the new generation to resist long periods of time and harsh environmental conditions. The seed plants, or Spermatophyta, are subdivided into two major lineages: gymnosperms (or Acrogymnospermae) and angiosperms (or Angiospermae) (Figure 1.8)(Linkies et al., 2010). Several features differentiate these two groups, yet the most striking one is the presence of flowers in angiosperms, reason why these plants are also known as flowering plants. Indeed, in both gymnosperms (e.g. *Pinus pinea*) and angiosperms (e.g. *Arabidopsis thaliana*), seeds develop from fertilized ovules. However in angiosperms, ovules are enclosed inside ovaries and

may sustain the development of several seeds, generating fruits (Crane et al., 1995; Linkies et al., 2010).

1.3.2 Plant sexual reproduction

Sexual reproduction is widespread in eukaryotes, and thought to have been present in the LECA. It involves an alteration between the gametophytic (haploid) and sporophytic (diploid) generations. This takes place by fusion of haploid gametes into a diploid zygote (sporophytic generation), which eventually undergoes genetic recombination and ploidy reduction *via* meiosis, generating a new gametophyte. Sexual reproduction is thought to generate more/faster genetic diversity than asexual reproduction. Natural selection acts upon such genetic diversity, being particularly important in species' resilience to adapt and sustain environmental challenges. Still, sexual and asexual reproduction are not mutually exclusive, as some eukaryotic species can reproduce by both processes (Kondrashov, 1988; Goodenough and Heitman, 2014; Bai, 2015).

Sexual reproduction involves the differentiation of both male and female gametes. In animals, the germ cell lineage is established during early embryogenesis. However in plants, the germline is only established at maturity, with reproductive strategies varying amongst the distinct Plantae branches (Figure 1.8)(Berger and Twell, 2011). While direct evidence for sexual reproduction has not been found in glaucophytes or unicellular red algae, multicellular members of this group display sexual reproduction with dimorphic gametes, including non-flagellated sperm (Figure 1.8)(Searles, 1980; Umen and Coelho, 2019). In chlorophytes, reproduction might rely on the fusion of isogamous (morphological similar) or anisogamous (morphologically different) mating types (Figure 1.8). For instance, in the model chlorophyte *C. reinhardtii*, the zygote is formed by the fusion of two isogamous cells (one plus and one minus

mating type), while in *Volvox carteri*, gametogenesis yields a bigger female cell and a smaller male cell (anisogamous mating types)(Umen and Coelho, 2019). While chlorophytes can be flagellated throughout their life cycles, in Streptophyta, cilia/flagella are only assembled during sperm differentiation (Renzaglia and Garbary, 2001; Hodges et al., 2012). In fact, sexual reproduction has not been observed in early diverging charophytes, and others have lost the ability to assemble cilia, reproducing through means of non-flagellated sperm (Figure 1.8). Still, some late divergent lineages, such as the Charales and Coleochaetales, reproduce through means of motile biflagellated sperm cells (Figure 1.8), which differentiate in complex gametangia structures called globules (antheridia), and immotile oocytes, which differentiate in the nucules (archegonia)(Hackenberg and Twell, 2019; Umen and Coelho, 2019).

Motile sperm cells also differentiate in many land plants (Figure 1.8). In the haploid-dominant life cycle of bryophytes, environmental stimuli trigger sexual reproduction. Specialized sexual structures (gametangia) named antheridia and archegonia are formed, where biflagellated sperm and immotile egg cells, respectively, differentiate (Figure 1.8). Similarly to their algae ancestors, the bryophyte sperm is released into environmental water and swims to reach the egg cells, enclosed in the archegonia. After fertilization, the zygote develops *via* mitotic divisions, forming the diploid sporophyte capsule wherein meiosis occurs, producing haploid desiccation tolerant spores (During, 1979; Paolillo, 1981; Hackenberg and Twell, 2019).

Lycophytes and monilophytes are characterized by the appearance of heterospory, *i. e.* the production of spores with different sizes: smaller male microspores and bigger female megaspores. Micro and megaspores are the meiotic products, developing within the walls of the micro and megasporangia, respectively. These spores develop into the male and female gametophytes, respectively generating antheridia and

archegonia, wherein gametogenesis takes place (Bateman and DiMichele, 1994; Petersen and Burd, 2016; Hackenberg and Twell, 2019). As their ancestors, fertilization in these lineages also relies on water, with motile sperm cells being released into the environment. Yet, opposed to charophytes and bryophytes, the sperm cells of lycophytes may have two or more flagella, while in monilophytes these are always multiflagellated (Figure 1.8)(Renzaglia and Garbary, 2001). After being released, these sperm cells swim to reach the archegonia and fertilize the egg cell. The resulting embryo develops into a new sporophyte, which in turn will enclose spore mother cells that undergo meiosis, producing new sporangia. Heterospory is thought to have facilitated the synchronization of gametophytic development from the released spores, upon favorable environmental conditions (Bateman and DiMichele, 1994).

Over the course of evolution, the megagametophyte became permanently embedded in sporophytic tissues that support seed development. Consequently, in seed plants (gymnosperms and angiosperms) only the immature microgametophytes are released. This happens through means of desiccation tolerant pollen grains (Figure 1.8), allowing for fertilization to occur in a water-independent manner (Linkies et al., 2010; Magnani, 2018; Hackenberg and Twell, 2019). Gymnosperms display two distinct methods to complete spermatogenesis, with the sperm cells of cycads (Cycadophyta, e.g. *Zamia integrifolia*) and ginkgophytes (*Ginkgo biloba*) still relying on their cilia/flagella to swim through the viscous fluid, released by their haustorial pollen tubes, into the neck of the archegonium, achieving fertilization (Paolillo, 1981; Friedman, 1993; Renzaglia and Garbary, 2001). On the other hand, and similarly to angiosperms, Coniferophyta (conifers, e.g. *Pinus pinea*) and Gnetophyta (gnetales, e.g. *Gnetum gnemon*) sperm cells are no longer flagellated. In these species,

zooidogamy (swimming sperm) was lost and replaced by siphonogamy (pollen tube guided delivery of immotile sperm) (Figure 1.8)(Friedman, 1993; Renzaglia and Garbary, 2001; Hackenberg and Twell, 2019). Despite their lack of cilia/flagella, the sperm cells of flowering plants also display a particular microtubule bundle organization around their nuclei, possibly to maintain their shape (Palevitz and Tiezzi, 1992; Southworth and Cresti, 1997). Another key feature of flowering plant reproduction is the existence of a double fertilization event, where both the egg cell and a central cell are fertilized by individual sperm cells, giving rise to the embryo and endosperm (nurture tissue), respectively (Crane et al., 1995; Baroux et al., 2002; Linkies et al., 2010; Adhikari et al., 2020).

1.3.2.1 Architecture of motile sperm cells

Motile flagellated sperm cells are produced by all non-seed land plants (bryophytes, lycophytes and monilophytes) as well as some seed plants (cycads and ginkgophytes). These are specialized cells that need to swim in order to reach and fertilize the enclosed, non-motile egg cell. Therefore, it is of no surprise that such cells display unique and highly organized cellular architectures, including a prominent nucleus, the absence of a cell wall, and the presence of cilia/flagella. Cilia number varies amongst land plant phylogeny, from the biflagellated cells found in all bryophytes and most lycophytes, to a few dozens/hundreds in the remaining lycophytes and all monilophytes, and reaching the thousands in gymnosperms (Garbary et al., 1993; Renzaglia and Garbary, 2001).

Resembling animal spermatids, the biflagellated sperm of land plants undergo complex morphological changes, yielding an elongated coiled cell, with condensed chromatin and reduced cytosol (Renzaglia and Garbary, 2001). Interestingly, protamine orthologs, the proteins responsible for chromatin compaction in animal species, are found in the genome of some land plants, including those with biflagellated sperm

(Borg and Berger, 2015). Moreover, macroautophagy appears to be involved in cytoplasmic reduction in both mice and the moss *P. patens* (Shang et al., 2016; Sanchez-Vera et al., 2017). This suggests that cytodifferentiation mechanisms might be common to both animal and plant spermatogenesis. Yet, despite the presence of Golgi apparatuses in differentiating spermatids of land plants, these do not form acrosomes, implying distinct mechanisms for sperm penetration onto the egg cell (Paolillo, 1981; Renzaglia and Garbary, 2001).

Fully differentiated biflagellated plant sperm cells contain only four or five organelles: an elongated nucleus, an undifferentiated plastid, one or two mitochondria, and a very complex locomotory apparatus (Carothers and Duckett, 1980; Renzaglia and Garbary, 2001). The locomotory apparatus of the biflagellated sperm cells of land plants is composed of two 9+2 ciliary axonemes, nucleated from two basal bodies/centrioles and a multilayered structure (MLS) (Manton, 1957; Heitz, 1959; Renzaglia and Garbary, 2001). As plant vegetative cells are devoid of centrioles, these are assembled *de novo* during the final antheridial divisions or pollen germination (in cycads and *Ginkgo*) (see section 1.4)(Lepper, 1956). The MLS is a diagnostic feature of streptophyte sperm, being also found in some charophyte algae (Graham and McBride, 1979; Sluiman, 1983). This structure is composed of a spline of singlet microtubules, subtended by plates of proteinaceous material, named lamellar strip (LS). The MLS assembly appears to be synchronized with basal body reorientation, being thought to originate from the dense mitotic MTOC in biflagellated sperm or from reorganization of the blepharoplast in multiflagellated sperm, being usually also associated with one mitochondrion (Hoffman et al., 1994; Vaughn and Harper, 1998; Bernhard and Renzaglia, 1995; Renzaglia and Maden, 2000). Despite its exact functions and fate remaining unknown, the MLS was hypothesized to be involved in cellular/nuclear

elongation, control of ciliary motility, and even sperm entry into the egg (Turner, 1970; Bell and Duckett, 1976; Myles and Hepler, 1977; Wolniak et al., 2000). Moreover, while ciliary structure is highly conserved, the MLS displays phylogenetically relevant diversity (Paolillo, 1981; Renzaglia and Garbary, 2001).

Despite being morphologically very similar, small particularities distinguish the biflagellated sperm of each lineage (Renzaglia and Duckett, 1991; Renzaglia and Maden, 2000; Carothers and Duckett, 1980). Hornwort sperm cells are distinguished by a particular right-handed coil (Renzaglia and Duckett, 1989), while moss sperm cells are differentiated by their central plastid position, as opposed to a terminal location in the other biciliated sperm cells (Renzaglia and Duckett, 1987; Bernhard and Renzaglia, 1995). Finally, biflagellated sperm cells from lycophytes are distinguished by their longer anterior mitochondrion, nuclear positioning between both mitochondria, and broader spline (Renzaglia et al., 1999).

Multiciliated sperm contents are more variable than what previously described for biflagellated sperm cells, containing multiple plastids and mitochondria, and undergoing distinct levels of cytosol reduction. As a result, their cellular shapes are more variable, ranging from spiral to ovoid shaped cells (Myles and Hepler, 1977; Robbins and Carothers, 1978; Gifford and Larson, 1980; Renzaglia and Garbary, 2001). The locomotory apparatuses of multiflagellated sperm cells are similar to the one previously described for biflagellated sperm, with the obvious difference of flagella (and corresponding basal body) number. It also extends around the cellular body, overlapping with the coiled cylindrical nucleus of non-seed plants (Norstog, 1967; Myles and Hepler, 1977; Li et al., 1989; Renzaglia and Garbary, 2001). Strikingly, motile sperm cells of cycads and *Ginkgo* do not contain a coiled cylindrical nucleus and instead, the chromatin remains uncondensed throughout development,

resulting in an ovoid shaped cell (Norstog, 1974; Gifford and Lin, 1975). Yet, the locomotory apparatus of all multiciliated sperm cells is coiled, with several basal bodies and flagella staggered inscribed along its length (Renzaglia and Garbary, 2001; Hackenberg and Twell, 2019).

1.4 Centrioles in land plants

This section is adapted from: Nabais C, Gomes Pereira S, Bettencourt-Dias M (2018). Noncanonical Biogenesis of Centrioles and Basal Bodies. *Cold Spring Harbor Symposia on Quantitative Biology Volume 82*:123-135.

Archaeplastida (the group including plants and some algae) suffered multiple events of centriole loss, both in basal groups (in some green algae and in red algae altogether), but also in gymnosperms after the split of conifers and gnetales from cycads and ginkgophytes, and once again before angiosperm evolution (Figures 1.6A and 1.8)(Bremer et al., 1987; Finet et al., 2010). Centrioles are required for species that form motile cilia and, somehow, depend on a moist environment for fertilization. Within this vast group, *de novo* mechanisms for centriole biogenesis are the most prevalent, based either on bicentriole (Figure 1.6D) or blepharoplast (Figure 1.6F) structures, since most plants lack centrioles throughout their life cycle except in sperm. The bicentriole is present in most Marchantiophyta and Bryophyta, and in some species of Anthocerotophyta and Lycopodiophyta, but not in the basal species of Archaeplastida (Renzaglia and Garbary, 2001). It is possible that the blepharoplast from the Pteridophyta and some gymnosperms derived from the bicentriole.

Once centrioles are assembled *de novo* during land plant spermatogenesis, they associate with a multilayered structure (MLS). The centrioles then dock to the cellular membrane and template the extension of the ciliary axoneme (Renzaglia and Garbary, 2001). To this date, there is no evidence for centriole duplication in land plant cells. It appears that each centriole formed *de novo* only gives rise to one cilium (Mizukami and Gall, 1966; Norstog, 1967; Gifford and Lin, 1975; Norstog, 1986).

1.4.1 The blepharoplast-mediated pathway

In land plants with multiciliated sperm such as ferns, cycads and *Ginkgo*, centrioles are formed through blepharoplasts (Figure 1.6F). The blepharoplast arises *de novo* (Figure. 1.9A) as a spherical electron dense organelle which is initially amorphous, and during maturation it becomes intercalated by lighter cylinders embedded in an electron-opaque matrix. These cylinders mature into centrioles that later give rise to the basal bodies of multiple cilia (Figure 1.9)(Hepler, 1976; Gifford and Larson, 1980).

Blepharoplast biogenesis starts with the appearance of two hemispherical densely stained structures near the cell nucleus (Figure 1.9B). Then, cylinders organize within the electron dense matrix, with microtubules emanating from it. These structures grow and become spherical, giving rise to two blepharoplasts (Mizukami and Gall, 1966; Hepler, 1976; Hoffman and Vaughn, 1995). The two blepharoplasts separate and migrate to the spindle poles of the mitotic cell, where they may act as MTOCs (Figure 1.9C)(Hepler, 1976; Gifford and Larson, 1980; Doonan et al., 1986). Then, in the metaphase to anaphase transition of the last mitosis, the blepharoplast becomes more diffuse and loses its MT nucleating ability. The cylinders acquire a hub and spokes configuration with a 9-fold symmetry, therefore resembling

procentrioles. Each daughter cell appears to inherit one blepharoplast (Norstog, 1967; Gifford and Lin, 1975; Hepler, 1976). Sperm development proceeds as centrioles are formed (Figure 1.9D)(Hepler, 1976; Renzaglia and Maden, 2000). The blepharoplast eventually collapses, resulting in individualized centrioles. These centrioles associate with the MLS and function as basal bodies, nucleating axonemes (Figure 1.9E)(Mizukami and Gall, 1966; Doonan et al., 1986; Norstog, 1986).

Molecular characterization of blepharoplast assembly is still scarce. However, a few studies have reported the localization of centrin, acetylated, tyrosinated and β -tubulins at the blepharoplast (Doonan et al., 1986; Klink and Wolniak, 2001; Vaughn and Renzaglia, 2006). Centrin's function was studied in *Marsilea vestita*, where RNAi experiments highlighted its requirement for proper blepharoplast and centriole biogenesis (Klink and Wolniak, 2001).

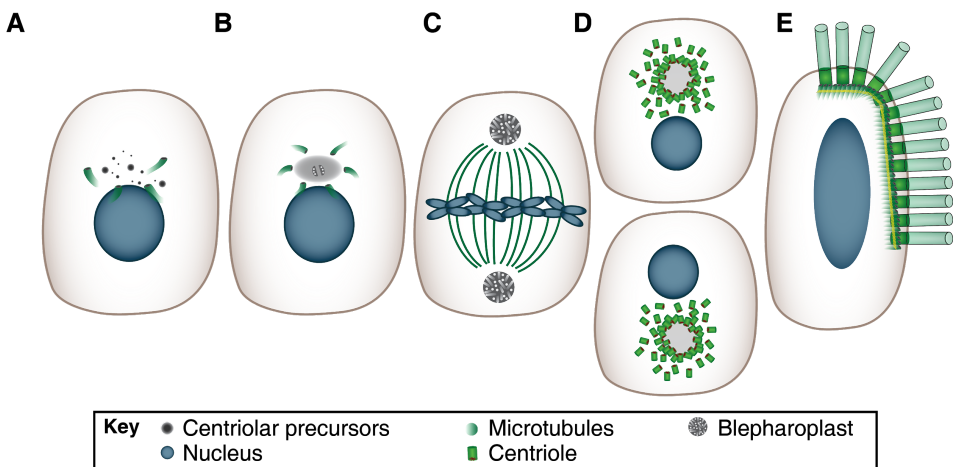


Figure 1.9: Blepharoplast-mediated centriole biogenesis. **A.** In plants with multiciliated sperm, an electron dense agglomerate of material and microtubules is first detected near the nuclear envelope of the sperm mother cell; **B.** This material develops into two darker

hemispherical lobes, intercalated by lighter cylinders; **C.** As the cell approaches mitosis, the lobes keep developing and separate. Each lobe migrates to a pole of the mitotic spindle and assembles a blepharoplast; **D.** Each spermatid inherits one blepharoplast, where many centrioles are assembled; **E.** The blepharoplast eventually collapses releasing the individual centrioles that will migrate and anchor to the multilayered structure, giving rise to the basal bodies of the several cilia. Adapted from Nabais et al., 2018.

1.4.2 The bicentriole-mediated pathway

De novo centriole biogenesis through bicentrioles is known to occur in plants with biflagellated sperm, such as bryophytes, as well as in the protist *Labyrinthula spp.* (Figure 1.6A)(Perkins, 1970). A bicentriole is described as being composed of two centrioles oriented end-to-end, aligned along the same axis and connected by a continuous cartwheel hub, while the triplet microtubules between both centrioles are discontinuous (Figure 1.6D)(Moser and Kreitner, 1970; Robbins, 1984).

Reports in land plants suggest that two bicentrioles appear simultaneously in the sperm mother cell. First, an electron dense body without any recognizable structure is detected in the outer surface of the nucleus. Microtubules emanate from this structure, suggesting that it has MTOC activity (Figure 1.10A). Next, it separates into two different lobes (probicentrioles) with a lighter stained central core surrounded by a darker matrix (Figure 1.10B)(Robbins, 1984). Before mitosis, the two probicentrioles separate, migrate towards the poles of the cell and mature into bicentrioles, assembling MT triplets (Robbins, 1984; Renzaglia and Duckett, 1987). Each bicentriole at the spindle pole contains two coaxial centrioles (Figure 1.10C)(Moser and Kreitner, 1970; Robbins, 1984).

After mitosis, each spermatid inherits one bicentriole. It is thought that the cartwheel's central hub breaks at its midpoint and the two resulting centrioles undergo planar rotation becoming almost parallel to each other, with their proximal ends facing the same direction (Figure 1.10D)(Moser and Kreitner, 1970; Kreitner and Carothers, 1976; Robbins, 1984). Centriole reorientation is accompanied by the development of the MLS, immediately below the centrioles. Finally, the centrioles associate with the MLS and mature into basal bodies for ciliogenesis (Figure 1.10E)(Moser et al., 1977; Renzaglia and Duckett, 1987).

Currently, there is no available molecular data on centriole assembly through bicentrioles, except that these structures appear to contain γ -tubulin (Shimamura et al., 2004). Furthermore, there is only one study reporting the early stages of *de novo* bicentriole assembly (Robbins, 1984). Early land plants, such as *Marchantia polymorpha*, *Physcomitrium patens* and *Selaginella moellendorffii* are all model organisms that assemble centrioles through the bicentriole-mediated pathway and therefore, could be used to better describe this pathway and understand its regulatory mechanisms.

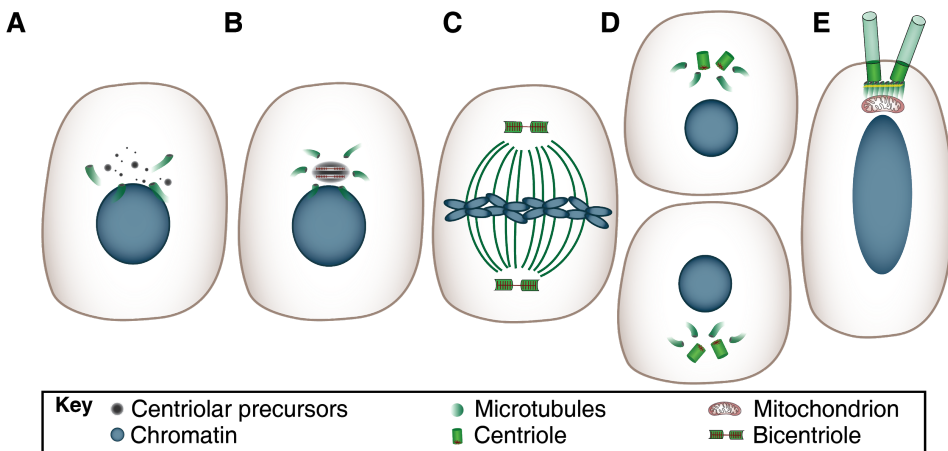


Figure 1.10: Bicentriole-mediated biogenesis in land plants. **A.** During spermatogenesis, electron dense material enriched in microtubules is found near the nuclear envelope; **B.** This material assembles into two light lobes, surrounded by a darker matrix; **C.** As mitosis begins, the two lobes separate and migrate towards the poles of the spindle and mature into bicentrioles. Bicentrioles are composed of two coaxial centrioles connected by their central hub and with discontinuous microtubule triplets; **D.** Each daughter cell (spermatid) inherits one bicentriole that breaks, separating the two centrioles; **E.** These centrioles anchor to the multilayered structure and migrate to the edge of the cell, serving as basal bodies during ciliogenesis. Adapted from Nabais et al., 2018.

1.4.3 *Physcomitrium patens* as a model organism to study *de novo* centriole biogenesis

Bryophytes, comprising hornworts, mosses and liverworts, were the first plants to colonize terrestrial environments. Amongst them, the model moss *Physcomitrium patens* (*P. patens*, previously known as *Physcomitrella patens*) was the first one to have its genome fully sequenced (Rensing et al., 2008).

P. patens haploid-dominant life cycle (Figure 1.11) starts with the germination of a haploid spore into protonema tissue, composed of two cell types: the fast apical-growing caulonema cells, and the chloroplast enriched chloronema cells (Reski and Abel, 1985). Then, meristematic buds are formed by an asymmetric cell division, initiating the development of the gametophores containing leaf-like structures and rhizoids at its base (Harrison et al., 2009; Kosetsu et al., 2017; Strotbek et al., 2013).

A shift in environmental conditions triggers sexual reproduction (Figure 1.11)(Engel, 1968; Hohe et al., 2002), with both male (antheridia)

and female (archegonia) gamete producing organs developing interspersed at the tip of the gametophore, making *P. patens* a monoecious species (Engel, 1968; Landberg et al., 2013). The first organ to be formed is the male antheridium, which localizes at the center of the shoot apex. As the first antheridium develops, more antheridia will emerge, flanking the first one. This same pattern is observed for the female archegonia, showing that *P. patens* gametogenesis proceeds asynchronously in the several gamete forming organs (Figure 1.11 inset)(Landberg et al., 2013).

Antheridia are composed of two different cell types: the outer cell layer (jacket cells) that divide to keep up with the increasing size of the organ, and the inner spermatogenous cells. By the time that the inner cells acquire a round shape, the outer cells produce a yellow pigment and the most apical cells start to swell. Afterwards, the spermatids will undergo the final cell division and will start maturation (Landberg et al., 2013). The mature sperm cells of *P. patens*, also named antherozoids, are slender and biflagellated coiled cells, being strikingly similar to the sperm of certain animals, in the way that they are elongated and flagellated cells that swim and possess no cell walls (Paolillo, 1981). These antherozoids are released after the bursting of the swollen apical cell of the antheridium. In standard growth conditions it takes 15 days from the start of the development of the antheridia by cold induction to the release of mature antherozoids (Figure 1.11 inset)(Landberg et al., 2013).

The female archegonium starts developing several days after the first antheridium. Archegonia are composed of a neck of sterile cells and a “belly” wherein the egg cell develops. When the egg cell is fully matured, the canal of the archegonium neck opens, so that fertilization can take place. Maturation of the egg cell coincides with the release of sperm cells, which will swim in order to fertilize the egg cell (Figure 1.11

inset)(Landberg et al., 2013). Upon fertilization the diploid sporophyte (apical spore capsule) starts to develop. Inside this capsule, meiosis will occur, producing about 4000-6000 haploid spores. These spores mature inside the sporophyte, and after the capsule breaks open, are released for propagation. These spores are ready to germinate, thus completing the life cycle, which under standard growing conditions, takes around 3 to 4 months (Figure 1.11)(Strotbek et al., 2013).

In addition to its haploid-dominant and relatively short life cycle, *P. patens* shows a high frequency of homologous recombination (HR), allowing efficient gene targeting and the generation of stable transgenic lines (Schaefer and Zryd, 1997). Moreover, several protocols for gene editing based on the CRISPR-Cas9 technology have been developed (Lopez-Obando et al., 2016; Mallett et al., 2019; Yi and Goshima, 2020). These characteristics, together with its ideal phylogenetic position at the base of plant evolution, allowed *P. patens* to bloom as a model for evolutionary and developmental studies (Prigge and Bezanilla, 2010; Rensing et al., 2020).

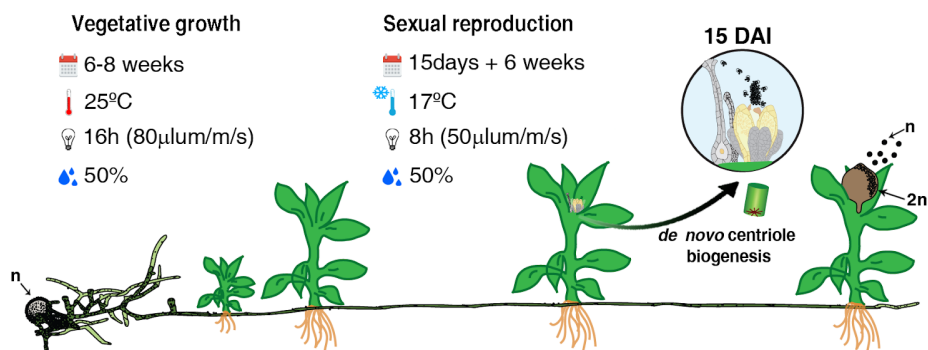


Figure 1.11: The haploid-dominant life cycle of *Physcomitrium (Physcomitrella) patens*. *P. patens* life cycle starts with the germination of a haploid spore (n) into protonemata, composed of both caulonema and chloronema cells. Eventually, after an asymmetric cell division, a

bud is formed from where a gametophore (plant body) will develop. The gametophores contain leaf-like structures, and rhizoids at their bases. After a period of 6 to 8 weeks of vegetative growth (25°C, 50% relative humidity and with 16h/8h of light/dark photoperiod), sexual reproduction is induced by changing the growth conditions (17°C, 50% relative humidity, 8h/16h light/dark). Gametangia (both male antheridia and female archegonia) develop at the top of the gametophores, while gametogenesis takes place. It is only during spermatogenesis that centrioles arise *de novo*. 15 days after induction (15 DAI) of the sexual reproduction, the first biflagellated sperm cells are released (inset). Fertilization gives rise to the embryo, which develops into the sporophyte capsule, representing the only diploid (2n) stage of the life cycle. Meiosis occurs in the cells enclosed in the sporophyte. Around 6 weeks after fertilization, the new haploid spores (n) are ready to be released, allowing the life cycle to restart. Figure adapted from Gomes Pereira et al. (*in revision*).

1.5 Framework for the thesis

Centrioles are microtubule-based structures with key functions within eukaryotic cells. They are part of the centrosome – the main MTOC in animal cells, thereby regulating the intracellular microtubule network. Moreover, centrioles are also essential for other cellular and organismal functions, such as cellular movement and signaling, extracellular signal sensing, tissue clearing and reproduction, as they anchor to the cellular membrane and enable ciliogenesis. Due to their critical functions, it is of no surprise that centrioles have been conserved throughout evolution, and that their dynamics are highly regulated.

The assembly of such a complex (structurally and molecularly) entity as the centriole continues to puzzle cell biologists. Centriole duplication appeared as an easy answer to solve the riddle: centrioles duplicate from pre-existing ones which would serve as a template, with some resemblance to the process of DNA replication. However, centrioles can also form *de novo*, in the absence of other centrioles in the cells or organism, that is, without any template. Moreover, several distinct pathways for *de novo* centriole biogenesis are known to be present across the eukaryotic tree of life since the 70s. Yet, *de novo* assembly of centrioles is still enigmatic, as research efforts have mainly focused on centriole duplication. Still, it is clear that an understanding of both assembly processes is required to fully understand centriole biogenesis, as well as to determine the minimal set of key components and events in this process.

In animals, centrioles appear to assemble *de novo* either as single entities or in deuterosomes. Additionally, molecular studies regarding *de novo* centriole biogenesis have focused almost exclusively on the deuterosome-mediated pathway. Therefore, there is still much we do not know about the overarching structural and molecular mechanisms underlying centriole biogenesis, with some pathways having been overlooked. This is the case of two particular mechanisms for *de novo* centriole biogenesis, which appear to occur almost exclusively in plants: the bicentriole and the blepharoplast-mediated pathways.

It is noteworthy that the vegetative cells of land plants have lost centrosomes, and cell division relies on acentrosomal MTOCs. Nevertheless, the bryophytes, lycophytes, monilophytes, the cycads and *Ginkgo* lineages depend on motile sperm cells to reach the egg cell, in order to achieve fertilization. In such plant species, centrioles arise *de novo* during spermatogenesis either *via* bicentrioles (in biflagellated sperm cells) or within blepharoplasts (in species with multiciliated

sperm). Therefore, spermatogenesis in such plant species offers a unique opportunity to explore naturally occurring *de novo* centriole biogenesis, in a new evolutionary context and independently of the cell cycle, contrasting to the canonical biogenesis occurring in animals.

Bryophytes, such as mosses, were the first plants to colonize terrestrial environments, a key position to understand plant evolution. Moreover, they grow in almost all terrestrial and some freshwater habitats, being critical ecological players in the particularly threatened wetlands, where they participate in water purification, nutrient retention, and in carbon retention. Still despite their ecological relevance, many features of bryophytes are still poorly understood, in particular their reproduction. In recent years, some bryophyte species have been established as model organisms in laboratories worldwide. One of such species is the moss *Physcomitrium patens* (*P. patens*).

Undoubtedly, *P. patens* spermatogenesis provides a unique system to investigate *de novo* centriole biogenesis, complementing the existing knowledge in centriole assembly and evolution; while providing valuable insights regarding plant reproduction and evolution.

The overarching aim of this thesis is to characterize *de novo* centriole biogenesis during *P. patens* spermatogenesis. Due to the lack of pre-existing protocols to study such a process, the first goal of this work (aim 1/chapter 2) was to implement the required protocols to investigate *P. patens* spermatogenesis from a cellular perspective, including both electron and super-resolution light microscopy techniques. I next proceeded to the structural characterization (aim 2/chapter 3) of *de novo* centriole assembly in *P. patens*. Combining 2D with 3D EM techniques, I have described the bicentriole-mediated pathway with unprecedented ultrastructural detail. Afterwards, guided by the structural characterization and by exploring core centriole proteins conserved

across evolution, I have added the first molecular information to centriole assembly *via* bicentrioles (aim 3/chapter 4), revealing a functional conservation across centriole biogenesis mechanisms, as well as some particularities of this system.

Finally, I discuss the relevance of our findings in the context of centriole assembly and maturation across the tree of life (chapter 5). In particular, I focus on how the structural and molecular characterization of *de novo* centriole biogenesis *via* bicentrioles supports the view that both centriole duplication and *de novo* pathways involve similar molecular and structural milestones, despite relying on particular unique structures. I also discuss the peculiar asymmetrical maturation of *P. patens*, and how it could be regulated. To conclude, I speculate about centriole remodeling in *P. patens* and how centriole features might be linked with ciliary beating behaviour. Lastly, I examine the questions that are left open and how future work could address them.

1.6 References

Adhikari, P.B., Liu, X., Wu, X., Zhu, S., and Kasahara, R.D. (2020). Fertilization in flowering plants: an odyssey of sperm cell delivery. *Plant Mol. Biol.* *103*, 9–32.

Agircan, F.G., Schiebel, E., and Mardin, B.R. (2014). Separate to operate: control of centrosome positioning and separation. *Philos. Trans. R. Soc. B Biol. Sci.* *369*, 20130461–20130461.

Akhmanova, A., and Steinmetz, M.O. (2015). Control of microtubule organization and dynamics: Two ends in the limelight. *Nat. Rev. Mol. Cell Biol.* *16*, 711–726.

Al Jord, A., Lemaître, A.-I., Delgehyr, N., Faucourt, M., Spassky, N., and Meunier, A. (2014). Centriole amplification by mother and daughter centrioles differs in multiciliated cells. *Nature* *516*, 104–107.

Ali, I., and Yang, W.C. (2020). Why are ATP-driven microtubule minus-end directed motors critical to plants? An overview of plant multifunctional kinesins. *Funct. Plant Biol.* *47*, 524–536.

Alushin, G.M., Lander, G.C., Kellogg, E.H., Zhang, R., Baker, D., and Nogales, E. (2014). High-Resolution microtubule structures reveal the structural transitions in $\alpha\beta$ -tubulin upon GTP hydrolysis. *Cell* *157*, 1117–1129.

Alvarez-Rodrigo, I., Steinacker, T.L., Saurya, S., Conduit, P.T., Baumbach, J., Novak, Z.A., Aydogan, M.G., Wainman, A., and Raff, J.W. (2019). Evidence that a positive feedback loop drives centrosome maturation in fly embryos. *Elife* *8*.

Anderson, R.G.W. (1972). The three-dimensional structure of the basal body from the rhesus monkey oviduct. *J. Cell Biol.* *54*, 246–265.

Arquint, C., and Nigg, E.A. (2016). The PLK4-STIL-SAS-6 module at the core of centriole duplication. *Biochem. Soc. Trans.* *44*, 1253–1263.

Avidor-Reiss, T., Mazur, M., Fishman, E.L., and Sindhvani, P. (2019). The Role of Sperm Centrioles in Human Reproduction – The Known and the Unknown. *Front. Cell Dev. Biol.* *7*, 1–15.

Aydogan, M.G., Wainman, A., Saurya, S., Steinacker, T.L., Caballe, A., Novak, Z.A., Baumbach, J., Muschalik, N., and Raff, J.W. (2018). A homeostatic clock sets daughter centriole size in flies. *J. Cell Biol.* *217*, 1233–1248.

Azimzadeh, J. (2014). Exploring the evolutionary history of centrosomes. *Philos. Trans. R. Soc. Lond. B. Biol. Sci.* *369*, 20130453.

Bai, S.N. (2015). The concept of the sexual reproduction cycle and its evolutionary significance. *Front. Plant Sci.* *6*, 1–8.

Banterle, N., and Gönczy, P. (2017). Centriole biogenesis: From identifying the characters to understanding the plot. *Annu. Rev. Cell Dev. Biol.* *33*, 23–49.

Banterle, N., Nievergelt, A.P., de Buhr, S., Hatzopoulos, G.N., Brillard, C., Andany, S., Hübscher, T., Sorgenfrei, F., Schwarz, U.S., Gräter, F., et al. Surface-catalyzed SAS-6 self-assembly directs centriole formation through kinetic and structural mechanisms. *BioRxiv Preprint*. doi: 2020.09.04.283184

Baroux, C., Spillane, C., and Grossniklaus, U. (2002). Evolutionary origins of the endosperm in flowering plants. *Genome Biol.* 3, 1–5.

Bateman, R.M., and DiMichele, W.A. (1994). Heterospory: The most iterative key innovation in the evolutionary history of the plant kingdom. *Biol. Rev.* 69, 345–417.

Beisson, J., and Wright, M. (2003). Basal body/centriole assembly and continuity. *Curr. Opin. Cell Biol.* 15, 96–104.

Bell, P.R., and Duckett, J.G. (1976). Gametogenesis and fertilization in *Pteridium*. *Bot. J. Linn. Soc.* 73, 47–78.

Berger, F., and Twell, D. (2011). Germline specification and function in plants. *Annu. Rev. Plant Biol.* 62, 461–484.

Bernhard, D.L., and Renzaglia, K.S. (1995). Spermiogenesis in the Moss *Aulacomnium palustre*. *Bryologist* 98, 52–70.

Bettencourt-Dias, M., Rodrigues-Martins, A., Carpenter, L., Riparbelli, M., Lehmann, L., Gatt, M.K., Carmo, N., Balloux, F., Callaini, G., and Glover, D.M. (2005). SAK/PLK4 is required for centriole duplication and flagella development. *Curr. Biol.* 15, 2199–2207.

Biswal, D.P., and Panigrahi, K.C.S. (2021). Light- and hormone-mediated development in non-flowering plants: An overview. *Planta* 253, 1–24.

Blachon, S., Cai, X., Roberts, K.A., Yang, K., Polyanovsky, A., Church, A., and Avidor-Reiss, T. (2009). A proximal centriole-like structure is present in drosophila spermatids and can serve as a model to study centriole duplication. *Genetics* 182, 133–144.

Blachon, S., Khire, A., and Avidor-Reiss, T. (2014). The origin of the second centriole in the zygote of *Drosophila melanogaster*. *Genetics* 197, 199–205.

Blackwell, R., Sweezy-Schindler, O., Edelmaier, C., Gergely, Z.R., Flynn, P.J., Montes, S., Crapo, A., Doostan, A., McIntosh, J.R., Glaser, M.A., et al. (2017). Contributions of Microtubule Dynamic Instability and Rotational Diffusion to Kinetochores Capture. *Biophys. J.* 112, 552–563.

Bodakuntla, S., Jijumon, A.S., Villablanca, C., Gonzalez-Billault, C., and Janke, C. (2019). Microtubule-Associated Proteins: Structuring the Cytoskeleton. *Trends Cell Biol.* 29, 804–819.

Borg, M., and Berger, F. (2015). Chromatin remodelling during male gametophyte development. *Plant J.* **83**, 177–188.

Borrego-Pinto, J., Somogyi, K., Karreman, M.A., König, J., Müller-Reichert, T., Bettencourt-Dias, M., Gönczy, P., Schwab, Y., and Lénárt, P. (2016). Distinct mechanisms eliminate mother and daughter centrioles in meiosis of starfish oocytes. *J. Cell Biol.* **212**, 815–827.

Bowler, M., Kong, D., Sun, S., Nanjundappa, R., Evans, L., Farmer, V., Holland, A., Mahjoub, M.R., Sui, H., and Loncarek, J. (2019). High-resolution characterization of centriole distal appendage morphology and dynamics by correlative STORM and electron microscopy. *Nat. Commun.* **10**, 1–15.

Bremer, K., Humphries, C.J., Mishler, B.D., and Churchill, S.P. (1987). On Cladistic Relationships in Green Plants. *Taxon* **36**, 339–349.

Breslow, D.K., and Holland, A.J. (2019). Mechanism and Regulation of Centriole and Cilium Biogenesis. *Annu. Rev. Biochem.* **88**, 691–724.

Brown, R.C., and Lemmon, B.E. (1988). Preprophasic microtubule systems and development of the mitotic spindle in hornworts (Bryophyta). *Protoplasma* **143**, 11–21.

Brown, R.C., and Lemmon, B.E. (2001). The cytoskeleton and spatial control of cytokinesis in the plant life cycle. *Protoplasma* **215**, 35–49.

Brown, R.C., and Lemmon, B.E. (2007). The pleiomorphic plant MTOC: An evolutionary perspective. *J. Integr. Plant Biol.* **49**, 1142–1153.

Burk, D.H., Liu, B., Zhong, R., Morrison, W.H., and Ye, Z.H. (2001). A katanin-like protein regulates normal cell wall biosynthesis and cell elongation. *Plant Cell* **13**, 807–827.

Burki, F. (2014). The eukaryotic tree of life from a global phylogenomic perspective. *Cold Spring Harb. Perspect. Biol.* a016147.

Burute, M., and Kapitein, L.C. (2019). Cellular logistics: Unraveling the interplay between microtubule organization and intracellular transport. *Annu. Rev. Cell Dev. Biol.* **35**, 29–54.

Buschmann, H., Fabri, C.O., Hauptmann, M., Hutzler, P., Laux, T., Lloyd, C.W., and Schäffner, A.R. (2004). Helical Growth of the *Arabidopsis* Mutant *tortifolia1* Reveals a Plant-Specific Microtubule-Associated Protein. *Curr. Biol.* **14**, 1515–1521.

Buschmann, H., Chan, J., Sanchez-Pulido, L., Andrade-Navarro, M.A., Doonan, J.H., and Lloyd, C.W. (2006). Microtubule-Associated AIR9 Recognizes the Cortical Division Site at Preprophase and Cell-Plate Insertion. *Curr. Biol.* *16*, 1938–1943.

Buschmann, H., Holtmannspötter, M., Borchers, A., O'Donoghue, M.T., and Zachgo, S. (2016). Microtubule dynamics of the centrosome-like polar organizers from the basal land plant *Marchantia polymorpha*. *New Phytol.* *209*, 999–1013.

Cabral, G., Laos, T., Dumont, J., and Dammermann, A. (2019). Differential Requirements for Centrioles in Mitotic Centrosome Growth and Maintenance. *Dev. Cell* *50*, 355–366.

Callaini, G., Whitfield, W.G.F., and Riparbelli, M.G. (1997). Centriole and centrosome dynamics during the embryonic cell cycles that follow the formation of the cellular blastoderm in *Drosophila*. *Exp. Cell Res.* *234*, 183–190.

Carothers, Z.B., and Duckett, J.G. (1980). The Bryophyte Spermatozoid: A Source of New Phylogenetic Information. *Bull. Torrey Bot. Club* *107*, 281–297.

Carvalho-Santos, Z., Machado, P., Branco, P., Tavares-Cadete, F., Rodrigues-Martins, A., Pereira-Leal, J.B., and Bettencourt-Dias, M. (2010). Stepwise evolution of the centriole-assembly pathway. *J. Cell Sci.* *123*, 1414–1426.

Carvalho-Santos, Z., Azimzadeh, J., Pereira-Leal, J.B., and Bettencourt-Dias, M. (2011). Tracing the origins of centrioles, cilia, and flagella. *J. Cell Biol.* *194*, 165–175.

Carvalho-Santos, Z., Machado, P., Alvarez-Martins, I., Gouveia, S.M., Jana, S.C., Duarte, P., Amado, T., Branco, P., Freitas, M.C., Silva, S.T.N., et al. (2012). BLD10/CEP135 Is a Microtubule-Associated Protein that Controls the Formation of the Flagellum Central Microtubule Pair. *Dev. Cell* *23*, 412–424.

Cavalier-Smith, T. (2002). The phagotrophic origin of eukaryotes and phylogenetic classification on Protozoa. *Int. J. Syst. Evol. Microbiol.* *52*, 297–354.

Chakraborty, S., Jasnin, M., and Baumeister, W. (2020). Three-dimensional organization of the cytoskeleton: A cryo-electron tomography perspective. *Protein Sci.* *29*, 1302–1320.

Ching, K., and Stearns, T. (2020). Centrioles are amplified in cycling progenitors of olfactory sensory neurons. *PLoS Biol.* 18, 1–17.

Chong, W.M., Wang, W.J., Lo, C.H., Chiu, T.Y., Chang, T.J., Liu, Y.P., Tanos, B., Mazo, G., Tsou, M.F.B., Jane, W.N., et al. (2020). Super-resolution microscopy reveals coupling between mammalian centriole subdistal appendages and distal appendages. *Elife* 9, 1–21.

Cizmecioglu, O., Arnold, M., Bahtz, R., Settele, F., Ehret, L., Haselmann-Weiß, U., Antony, C., and Hoffmann, I. (2010). Cep152 acts as a scaffold for recruitment of Plk4 and CPAP to the centrosome. *J. Cell Biol.* 191, 731–739.

Comartin, D., Gupta, G.D., Fussner, E., Coyaud, É., Hasegan, M., Archinti, M., Cheung, S.W.T., Pinchev, D., Lawo, S., Raught, B., et al. (2013). CEP120 and SPICE1 cooperate with CPAP in centriole elongation. *Curr. Biol.* 23, 1360–1366.

Conduit, P.T., Feng, Z., Richens, J.H., Baumbach, J., Wainman, A., Bakshi, S.D., Dobbelaere, J., Johnson, S., Lea, S.M., and Raff, J.W. (2014). The centrosome-specific phosphorylation of Cnn by Polo/Plk1 drives Cnn scaffold assembly and centrosome maturation. *Dev. Cell* 28, 659–669.

Courtois, A., Schuh, M., Ellenberg, J., and Hiiragi, T. (2012). The transition from meiotic to mitotic spindle assembly is gradual during early mammalian development. *J. Cell Biol.* 198, 357–370.

Crane, P.R., Friis, E.M., and Pedersen, K.R. (1995). The origin and early diversification of Angiosperms. *Nature* 374, 27–33.

Crozet, N., Dahirel, M., and Chesne, P. (2000). Centrosome inheritance in sheep zygotes: Centrioles are contributed by the sperm. *Microsc. Res. Tech.* 49, 445–450.

Cunha-Ferreira, I., Bento, I., Pimenta-Marques, A., Jana, S.C., Lince-Faria, M., Duarte, P., Borrego-Pinto, J., Gilberto, S., Amado, T., Brito, D., et al. (2013). Regulation of autophosphorylation controls PLK4 self-destruction and centriole number. *Curr. Biol.* 23, 2245–2254.

Cyr, R.J., and Palevitz, B.A. (1995). Organization of cortical microtubules in plant cells. *Curr. Opin. Cell Biol.* 7, 65–71.

Dallai, R., Mercati, D., Bu, Y., Yin, Y.W., Callaini, G., and Riparbelli, M.G. (2010). The spermatogenesis and sperm structure of *Acerentomon microrhinus* (Protura, Hexapoda) with considerations on the phylogenetic position of the taxon. *Zoomorphology* 129, 61–80.

de Vries, J., Stanton, A., Archibald, J.M., and Gould, S.B. (2016). Streptophyte Terrestrialization in Light of Plastid Evolution. *Trends Plant Sci.* 21, 467–476.

Delgehyr, N., Sillibourne, J., and Bornens, M. (2005). Microtubule nucleation and anchoring at the centrosome are independent processes linked by ninein function. *J. Cell Sci.* 118, 1565–1575.

Delwiche, C.F., and Cooper, E.D. (2015). The evolutionary origin of a terrestrial flora. *Curr. Biol.* 25, R899–R910.

Delwiche, C.F., and Timme, R.E. (2011). Plants. *Curr. Biol.* 21, 417–422.

Desai, A., and Mitchison, T.J. (1997). Microtubule polymerization dynamics. *Annu. Rev. Cell Dev. Biol.* 13, 83–117.

Dhonukshe, P., and Gadella, T.W.J. (2003). Alteration of microtubule dynamic instability during preprophase band formation revealed by yellow fluorescent protein-CLIP170 microtubule plus-end labeling. *Plant Cell* 15, 597–611.

Dingle, A.D., and Fulton, C. (1966). Development of the flagellar apparatus of *Naegleria*. *J. Cell Biol.* 31, 43–54.

Dirksen, E.R. (1971). Centriole morphogenesis in developing ciliated epithelium of the mouse oviduct. *J. Cell Biol.* 51, 286–302.

Dittami, S.M., Heesch, S., Olsen, J.L., and Collén, J. (2017). Transitions between marine and freshwater environments provide new clues about the origins of multicellular plants and algae. *J. Phycol.* 53, 731–745.

Dobbelaere, J., Schmidt Cernohorska, M., Huranova, M., Slade, D., and Dammermann, A. (2020). Cep97 Is Required for Centriole Structural Integrity and Cilia Formation in *Drosophila*. *Curr. Biol.* 30, 3045–3055.

Doonan, J.H., Cove, D.J., and Lloyd, C.W. (1985). Immunofluorescence microscopy of microtubules in intact cell lineages of the moss, *Physcomitrella patens*. I. Normal and CIPC-treated tip cells. *J. Cell Sci.* 75, 131–147.

Doonan, J.H., Lloyd, C.W., and Duckett, J.G. (1986). Anti-tubulin antibodies locate the blepharoplast during spermatogenesis in the fern *Platyzoma microphyllum* R.Br.: a correlated immunofluorescence and electron-microscopic study. *J. Cell Sci.* **81**, 243–265.

During, H.J. (1979). Life strategies of Bryophytes: a preliminary review. *Lindbergia* **5**, 2–18.

Engel, P.P. (1968). The Induction of Biochemical and Morphological Mutants in the Moss *Physcomitrella patens*. *Am. J. Bot.* **55**, 438–446.

Erlandson, R.A., and De Harven, E. (1971). The ultrastructure of synchronized HeLa cells. *J. Cell Sci.* **8**, 353–397.

Facette, M.R., Rasmussen, C.G., and Van Norman, J.M. (2019). A plane choice: coordinating timing and orientation of cell division during plant development. *Curr. Opin. Plant Biol.* **47**, 47–55.

Fan, Y., Burkart, G.M., and Dixit, R. (2018). The *Arabidopsis* SPIRAL2 protein targets and stabilizes microtubule minus-ends. *Curr. Biol.* **28**, 987–994.

Farache, D., Emorine, L., Haren, L., and Merdes, A. (2018). Assembly and regulation of γ -tubulin complexes. *Open Biol.* **8**.

Finet, C., Timme, R.E., Delwiche, C.F., and Marlétaz, F. (2010). Multigene phylogeny of the green lineage reveals the origin and diversification of land plants. *Curr. Biol.* **20**, 2217–2222.

Fishman, E.L., Jo, K., Nguyen, Q.P.H., Kong, D., Royfman, R., Cekic, A.R., Khanal, S., Miller, A.L., Simerly, C., Schatten, G., et al. (2018). A novel atypical sperm centriole is functional during human fertilization. *Nat. Commun.* **9**, 2210.

Franz, A., Roque, H., Saurya, S., Dobbelaere, J., and Raff, J.W. (2013). CP110 exhibits novel regulatory activities during centriole assembly in *Drosophila*. *J. Cell Biol.* **203**, 785–799.

Friedman, W.E. (1993). The Evolutionary History of the Seed Plant Male Gametophyte. *Trends Ecol. Evol.* **8**, 15–21.

Fritz-Laylin, L.K., and Fulton, C. (2016). *Naegleria*: a classic model for *de novo* basal body assembly. *Cilia* **5**.

Fritz-Laylin, L.K., Assaf, Z.J., Chen, S., and Cande, W.Z. (2010). *Naegleria gruberi de novo* basal body assembly occurs *via* stepwise incorporation of conserved proteins. *Eukaryot. Cell* **9**, 860–865.

Fritz-Laylin, L.K., Levy, Y.Y., Levitan, E., Chen, S., Cande, W.Z., Lai, E.Y., and Fulton, C. (2016). Rapid centriole assembly in *Naegleria* reveals conserved roles for both *de novo* and mentored assembly. *Cytoskeleton* 73, 109–116.

Fu, J., Lipinszki, Z., Rangone, H., Min, M., Mykura, C., Chao-Chu, J., Schneider, S., Dzhindzhev, N.S., Gottardo, M., Riparbelli, M.G., et al. (2015). Conserved molecular interactions in centriole-to-centrosome conversion. *Nat. Cell Biol.* 18, 87–99.

Fulton, C., and Dingle, A.D. (1971). Basal bodies, but not centrioles, in *Naegleria*. *J. Cell Biol.* 51, 826–835.

Gaglio, T., Saredi, A., Bingham, J.B., Hasbani, M.J., Gill, S.R., Schroer, T.A., and Compton, D.A. (1996). Opposing motor activities are required for the organization of the mammalian mitotic spindle pole. *J. Cell Biol.* 135, 399–414.

Garbary, D.J., Renzaglia, K.S., and Duckett, J.G. (1993). The phylogeny of land plants: A cladistic analysis based on male gametogenesis. *Plant Syst. Evol.* 188, 237–269.

Garber, R.C., and Aist, J.R. (1979). The ultrastructure of mitosis in *Plasmodiophora brassicae* (Plasmodiophorales). *J. Cell Sci.* 40, 89–110.

Garcin, C., and Straube, A. (2019). Microtubules in cell migration. *Essays Biochem.* 63, 509–520.

Geimer, S., and Melkonian, M. (2004). The ultrastructure of the *Chlamydomonas reinhardtii* basal apparatus: identification of an early marker of radial asymmetry inherent in the basal body. *J. Cell Sci.* 117, 2663–2674.

Gibbons, I.R., and Grimstone, A. V. (1960). On flagellar structure in certain flagellates. *J. Biophys. Biochem. Cytol.* 7, 697–716.

Gifford, E.M., and Larson, S. (1980). Developmental Features of the Spermatogenous Cell in *Ginkgo biloba*. *Am. J. Bot.* 67, 119–124.

Gifford, E.M., and Lin, J. (1975). Light Microscope and Ultrastructural Studies of the Male Gametophyte in *Ginkgo biloba*: The Spermatogenous Cell. *Am. J. Bot.* 62, 974–981.

Gimpel, P., Lee, Y.L., Sobota, R.M., Calvi, A., Koullourou, V., Patel, R., Mamchaoui, K., Nédélec, F., Shackleton, S., Schmoranzner, J., et al. (2017). Nesprin-1 α -Dependent Microtubule Nucleation from the Nuclear Envelope via

Akap450 Is Necessary for Nuclear Positioning in Muscle Cells. *Curr. Biol.* 27, 2999-3009.e9.

Goetz, S.C., Liem, K.F., and Anderson, K. V. (2012). The spinocerebellar ataxia-associated gene tau tubulin kinase 2 controls the initiation of ciliogenesis. *Cell* 151, 847–858.

Gomes Pereira, S., Dias Louro, M.A., and Bettencourt-dias, M. (2021). Biophysical and quantitative principles of centrosome biogenesis and structure. *Annu. Rev. Cell Dev. Biol.* (in press).

Gomes Pereira, S., Sousa, A.L., Nabais, C., Paixão, T., Holmes, A.J., Schorb, M., Goshima, G., Tranfield, E.M., Becker, J.D., and Bettencourt-Dias, M. The 3D architecture and molecular foundations of *de novo* centriole assembly via bicentrioles. *BioRxiv preprint*. doi: 10.1101/2020.12.21.423647

Gönczy, P., Pichler, S., Kirkham, M., and Hyman, A.A. (1999). Cytoplasmic Dynein Is Required for Distinct Aspects of MTOC Positioning, Including Centrosome Separation, in the One Cell Stage *Caenorhabditis elegans* Embryo.

Goodenough, U., and Heitman, J. (2014). Origins of eukaryotic sexual reproduction. *Cold Spring Harb. Perspect. Biol.* 6, 1–21.

Goshima, G., Mayer, M., Zhang, N., Stuurman, N., and Vale, R.D. (2008). Augmin: A protein complex required for centrosome-independent microtubule generation within the spindle. *J. Cell Biol.* 181, 421–429.

Gottardo, M., Callaini, G., and Riparbelli, M.G. (2015). Structural characterization of procentrioles in *Drosophila* spermatids. *Cytoskeleton* 72, 576–584.

Graham, L.E., and McBride, G.E. (1979). The Occurrence and Phylogenetic Significance of a Multilayered Structure in *Coleochaete* Spermatozooids. *Am. J. Bot.* 66, 887–894.

Granger, C.L., and Cyr, R.J. (2000). Microtubule reorganization in tobacco BY-2 cells stably expressing GFP-MBD. *Planta* 210, 502–509.

Greenan, G., Keszthelyi, B., Vale, R.D., and Agard, D.A. (2018). Insights into centriole biogenesis and evolution revealed by cryoTomography of doublet and triplet centrioles. *Elife* 7, 1–18.

Gueth-Hallonet, C., Antony, C., Aghion, J., Santa-Maria, A., Lajoie-Mazenc, I., Wright, M., and Maro, B. (1993). γ -Tubulin is present in acentriolar MTOCs during early mouse development. *J. Cell Sci.* *105*, 157–166.

Guichard, P., Chrétien, D., Marco, S., and Tassin, A.-M. (2010). Procentriole assembly revealed by cryo-electron tomography. *EMBO J.* *29*, 1565–1572.

Guichard, P., Desfosses, A., Maheshwari, A., Hachet, V., Dietrich, C., Brune, A., Ishikawa, T., Sachse, C., and Gönczy, P. (2012). Cartwheel architecture of *Trichonympha* basal body. *Science.* *337*, 553.

Guichard, P., Hachet, V., Majubu, N., Neves, A., Demurtas, D., Olieric, N., Fluckiger, I., Yamada, A., Kihara, K., Nishida, Y., et al. (2013). Native architecture of the centriole proximal region reveals features underlying its 9-fold radial symmetry. *Curr. Biol.* *23*, 1620–1628.

Guichard, P., Hamel, V., Le Guennec, M., Banterle, N., Iacovache, I., Nemčíková, V., Flückiger, I., Goldie, K.N., Stahlberg, H., Lévy, D., et al. (2017). Cell-free reconstitution reveals centriole cartwheel assembly mechanisms. *Nat. Commun.* *8*, 14813.

Habedanck, R., Stierhof, Y.D., Wilkinson, C.J., and Nigg, E.A. (2005). The Polo kinase Plk4 functions in centriole duplication. *Nat. Cell Biol.* *7*, 1140–1146.

Hackenberg, D., and Twell, D. (2019). The evolution and patterning of male gametophyte development. *Curr. Top. Dev. Biol.* *131*, 257–298.

Hamant, O., Heisler, M.G., Jönsson, H., Krupinski, P., Uyttewaal, M., Bokov, P., Corson, F., Sahlin, P., Boudaoud, A., Meyerowitz, E.M., et al. (2008). Developmental patterning by mechanical signals in *Arabidopsis*. *Science.* *322*, 1650–1655.

Haren, L., Stearns, T., and Lüders, J. (2009). Plk1-dependent recruitment of γ -tubulin complexes to mitotic centrosomes involves multiple PCM components. *PLoS One* *4*.

Harrison, C.J., and Morris, J.L. (2018). The origin and early evolution of vascular plant shoots and leaves. *Philos. Trans. R. Soc. B Biol. Sci.* *373*.

Harrison, C.J., Roeder, A.H.K., Meyerowitz, E.M., and Langdale, J.A. (2009). Local Cues and Asymmetric Cell Divisions Underpin Body Plan Transitions in the Moss *Physcomitrella patens*. *Curr. Biol.* *19*, 461–471.

- Hasezawa, S., Marc, J., and Palevitz, B.A. (1991). Microtubule reorganization during the cell cycle in synchronized BY-2 tobacco suspensions. *Cell Motil. Cytoskeleton* *18*, 94–106.
- Heath, I.B. (1974a). Centrioles and Mitosis in Some Oömycetes. *Mycologia* *66*, 354–359.
- Heath, I.B. (1974b). Mitosis in the fungus *Thraustotheca Clavata*. *J. Cell Biol.* *60*, 204–220.
- Heath, I.B., and Greenwood, A.D. (1970). Centriole Replication and Nuclear Division in *Saprolegnia*. *J. Gen. Microbiol.* *62*, 139–148.
- Heitz, E. (1959). Elektronenmikroskopische Untersuchungen über zwei auffallende Strukturen an der Geißelbasis der Spermatischen von *Marchantia polymorpha*, *Preissia quadrata*, *Sphaerocarpus Donnellii*, *Pellia Fabroniana* (Hepaticae). *Zeitschrift Fur Naturforsch. Sect. B J. Chem. Sci.* *14*, 399–401.
- Hepler, P.K. (1976). The blepharoplast of *Marsilea*: its *de novo* formation and spindle association. *J. Cell Sci.* *21*, 361–390.
- Hertig, A.T., and Adams, E.C. (1967). Studies on the human oocyte and its follicle. I. Ultrastructural and histochemical observations on the primordial follicle stage. *J. Cell Biol.* *34*, 647–675.
- Hilbert, M., Noga, A., Frey, D., Hamel, V., Guichard, P., Kraatz, S.H.W., Pfreundschuh, M., Hosner, S., Flückiger, I., Jaussi, R., et al. (2016). SAS-6 engineering reveals interdependence between cartwheel and microtubules in determining centriole architecture. *Nat. Cell Biol.* *18*, 393–403.
- Hiraki, M., Nakazawa, Y., Kamiya, R., and Hirono, M. (2007). Bld10p Constitutes the Cartwheel-Spoke Tip and Stabilizes the 9-Fold Symmetry of the Centriole. *Curr. Biol.* *17*, 1778–1783.
- Ho, C.M.K., Hotta, T., Guo, F., Roberson, R.W., Lee, Y.R.J., and Liu, B. (2011). Interaction of antiparallel microtubules in the phragmoplast is mediated by the microtubule-associated protein MAP65-3 in *Arabidopsis*. *Plant Cell* *23*, 2909–2923.
- Hodges, M.E., Scheumann, N., Wickstead, B., Langdale, J.A., and Gull, K. (2010). Reconstructing the evolutionary history of the centriole from protein components. *J. Cell Sci.* *123*, 1407–1413.

Hodges, M.E., Wickstead, B., Gull, K., and Langdale, J.A. (2012). The evolution of land plant cilia. *New Phytol.* 195, 526–540.

Hoffman, J.C., and Vaughn, K.C. (1995). Using the Developing Spermatogenous Cells of *Ceratopteris* to Unlock the Mysteries of the Plant Cytoskeleton. *Int. J. Plant Sci.* 156, 346–358.

Hoffman, J.C., Vaughn, K.C., and Joshi, H.C. (1994). Structural and immunocytochemical characterization of microtubule organizing centers in Pteridophyte spermatogenous cells. *Protoplasma* 179, 46–60.

Hohe, A., Rensing, S.A., Mildner, M., Lang, D., and Reski, R. (2002). Day Length and Temperature Strongly Influence Sexual Reproduction and Expression of a Novel MADS-Box Gene in the Moss *Physcomitrella patens*. *Plant Biol.* 695–602.

Huang, N., Xia, Y., Zhang, D., Wang, S., Bao, Y., He, R., Teng, J., and Chen, J. (2017). Hierarchical assembly of centriole subdistal appendages via centrosome binding proteins CCDC120 and CCDC68. *Nat. Commun.* 8, 15057.

Huang, N., Zhang, D., Li, F., Chai, P., Wang, S., Teng, J., and Chen, J. (2018). M-Phase Phosphoprotein 9 regulates ciliogenesis by modulating CP110-CEP97 complex localization at the mother centriole. *Nat. Commun.* 9, 1–15.

Hush, J.M., Hawes, C.R., and Overall, R.L. (1990). Interphase microtubule re-orientation predicts a new cell polarity in wounded pea roots. *J. Cell Sci.* 96, 47–61.

Hyman, A.A., Chretien, D., Arnal, I., and Wade, R.H. (1995). Structural changes accompanying GTP hydrolysis in microtubules: Information from a slowly hydrolyzable analogue guanylyl-(α,β)-methylene- diphosphonate. *J. Cell Biol.* 128, 117–125.

Insinna, C., Lu, Q., Teixeira, I., Harned, A., Semler, E.M., Stauffer, J., Magidson, V., Tiwari, A., Kenworthy, A.K., Narayan, K., et al. (2019). Investigation of F-BAR domain PACSIN proteins uncovers membrane tubulation function in cilia assembly and transport. *Nat. Commun.* 10, 1–17.

Ito, D., and Bettencourt-Dias, M. (2018). Centrosome Remodelling in Evolution. *Cells* 7.

Jana, S.C. (2021). Centrosome structure and biogenesis: Variations on a theme? *Semin. Cell Dev. Biol.* *110*, 123–138.

Jana, S.C., Mendonça, S., Machado, P., Werner, S., Rocha, J., Pereira, A., Maiato, H., and Bettencourt-Dias, M. (2018). Differential regulation of transition zone and centriole proteins contributes to ciliary base diversity. *Nat. Cell Biol.* *20*, 928–941.

Janke, C., and Magiera, M.M. (2020). The tubulin code and its role in controlling microtubule properties and functions. *Nat. Rev. Mol. Cell Biol.* *21*, 307–326.

Janski, N., Masoud, K., Batzenschlager, M., Herzog, E., Evrard, J.L., Houlné, G., Bourge, M., Chabouté, M.E., and Schmit, A.C. (2012). The GCP3-interacting proteins GIP1 and GIP2 are required for γ -tubulin complex protein localization, spindle integrity, and chromosomal stability. *Plant Cell* *24*, 1171–1187.

Joukov, V., Walter, J.C., and De Nicolo, A. (2014). The Cep192-Organized Aurora A-Plk1 Cascade Is Essential for Centrosome Cycle and Bipolar Spindle Assembly. *Mol. Cell* *55*, 578–591.

Judelson, H.S., Shrivastava, J., and Manson, J. (2012). Decay of Genes Encoding the Oomycete Flagellar Proteome in the Downy Mildew *Hyaloperonospora Arabidopsidis*. *PLoS One* *7*, e47624.

Kapraun, D.F. (2007). Nuclear DNA content estimates in green algal lineages: Chlorophyta and Streptophyta. *Ann. Bot.* *99*, 677–701.

Kenrick, P. (2017). How land plant life cycles first evolved. *Science.* *358*, 1538–1539.

Kenrick, P., and Crane, P.R. (1997). The origin and early evolution of plants on land. *Nature* *389*, 33–39.

Khire, A., Vizuet, A.A., Davila, E., and Avidor-Reiss, T. (2015). Asterless Reduction during Spermiogenesis Is Regulated by Plk4 and Is Essential for Zygote Development in *Drosophila*. *Curr. Biol.* *25*, 2956–2963.

Khire, A., Jo, K.H., Kong, D., Akhshi, T., Blachon, S., Cekic, A.R., Hynek, S., Ha, A., Loncarek, J., Mennella, V., et al. (2016). Centriole Remodeling during Spermiogenesis in *Drosophila*. *Curr. Biol.* *26*, 1–7.

Khodjakov, A., Rieder, C.L., Sluder, G., Cassels, G., Sibon, O., and Wang, C.L. (2002). *De novo* formation of centrosomes in vertebrate cells arrested during S phase. *J. Cell Biol.* *158*, 1171–1181.

Kies, L., and Kremer, B.P. (1986). Typification of the Glaucocystophyta. *Taxon* *35*, 128–133.

Kim, H.-K., Kang, J.-G., Yumura, S., Walsh, C.J., Jin, W.C., and Lee, J. (2005). *De novo* formation of basal bodies in *Naegleria gruberi*: Regulation by phosphorylation. *J. Cell Biol.* *169*, 719–724.

Kitagawa, D., Vakonakis, I., Olieric, N., Hilbert, M., Keller, D., Olieric, V., Bortfeld, M., Erat, M.C., Flückiger, I., Gönczy, P., et al. (2011). Structural basis of the 9-fold symmetry of centrioles. *Cell* *144*, 364–375.

Klena, N., Le Guennec, M., Tassin, A., van den Hoek, H., Erdmann, P.S., Schaffer, M., Geimer, S., Aeschlimann, G., Kovacik, L., Sadian, Y., et al. (2020). Architecture of the centriole cartwheel-containing region revealed by cryo-electron tomography. *EMBO J.* e106246.

Klink, V.P., and Wolniak, S.M. (2001). Centrin is necessary for the formation of the motile apparatus in spermatids of *Marsilea*. *Mol. Biol. Cell* *12*, 761–776.

Koblenz, B., Schoppmeier, J., Grunow, A., and Lechtreck, K.-F. (2003). Centrin deficiency in *Chlamydomonas* causes defects in basal body replication, segregation and maturation. *J. Cell Sci.* *116*, 2635–2646.

Kondrashov, A.S. (1988). Deleterious mutations and the evolution of sexual reproduction. *Nature* *336*, 435–440.

Kong, D., Sahabandu, N., Sullenberger, C., Vásquez-Limeta, A., Luvsanjav, D., Lukasik, K., and Loncarek, J. (2020). Prolonged mitosis results in structurally aberrant and over-elongated centrioles. *J. Cell Biol.* *219*, e201910019.

Kosetsu, K., Murata, T., Yamada, M., Nishina, M., Boruc, J., Hasebe, M., Van Damme, D., and Goshima, G. (2017). Cytoplasmic MTOCs control spindle orientation for asymmetric cell division in plants. *Proc. Natl. Acad. Sci. U. S. A.* *114*, E8847–E8854.

Kratz, A.S., Bärenz, F., Richter, K.T., and Hoffmann, I. (2015). Plk4-dependent phosphorylation of STIL is required for centriole duplication. *Biol. Open* *4*, 370–377.

Kreitner, G.L., and Carothers, Z.B. (1976). Studies of Spermatogenesis in the Hepaticae V. Blepharoplast Development in *Marchantia polymorpha*. *Am. J. Bot.* 63, 545–557.

Kumagai, F., Nagata, T., Yahara, N., Moriyama, Y., Horio, T., Naoi, K., Hashimoto, T., Murata, T., and Hasezawa, S. (2003). γ -tubulin distribution during cortical microtubule reorganization at the M/G1 interface in tobacco BY-2 cells. *Eur. J. Cell Biol.* 82, 43–51.

Kumar, D., and Reiter, J. (2021). How the centriole builds its cilium: of mothers, daughters, and the acquisition of appendages. *Curr. Opin. Struct. Biol.* 66, 41–48.

Kunimoto, K., Yamazaki, Y., Nishida, T., Shinohara, K., Ishikawa, H., Hasegawa, T., Okanoue, T., Hamada, H., Tamura, A., Tsukita, S., et al. (2012). Coordinated ciliary beating requires Odf2-mediated polarization of basal bodies via basal feet. *Cell* 148, 189–200.

Landberg, K., Pederson, E.R. a, Viaene, T., Bozorg, B., Friml, J., Jönsson, H., Thelander, M., and Sundberg, E. (2013). The moss *Physcomitrella patens* reproductive organ development is highly organized, affected by the two SHI/STY genes and by the level of active auxin in the SHI/STY expression domain. *Plant Physiol.* 162, 1406–1419.

Lane, H.A., and Nigg, E.A. (1996). Antibody microinjection reveals an essential role for human polo-like kinase 1 (Plk1) in the functional maturation of mitotic centrosomes. *J. Cell Biol.* 135, 1701–1713.

Le Guennec, M., Klena, N., Gambarotto, D., Laporte, M.H., Tassin, A.M., van den Hoek, H., Erdmann, P.S., Schaffer, M., Kovacic, L., Borgers, S., et al. (2020). A helical inner scaffold provides a structural basis for centriole cohesion. *Sci. Adv.* 6.

Le Guennec, M., Klena, N., Aeschlimann, G., Hamel, V., and Guichard, P. (2021). Overview of the centriole architecture. *Curr. Opin. Struct. Biol.* 66, 58–65.

Lee, K., and Rhee, K. (2011). PLK1 phosphorylation of pericentrin initiates centrosome maturation at the onset of mitosis. *J. Cell Biol.* 195, 1093–1101.

Lee, Y.R.J., and Liu, B. (2019). Microtubule nucleation for the assembly of acentrosomal microtubule arrays in plant cells. *New Phytol.* 222, 1705–1718.

Lee, J., Kang, S., Choi, Y.S., eok, Kim, H.K., Yeo, C.Y., Lee, Y., Roth, J., and Lee, J. (2015). Identification of a cell cycle-dependent duplicating complex that assembles basal bodies *de novo* in *Naegleria*. *Protist* 166, 1–13.

Leliaert, F., Smith, D.R., Moreau, H., Herron, M.D., Verbruggen, H., Delwiche, C.F., and De Clerck, O. (2012). Phylogeny and Molecular Evolution of the Green Algae. *CRC. Crit. Rev. Plant Sci.* 31, 1–46.

Lepper, R.J. (1956). The plant centrosome and the centrosome-blepharoplast homology. *Bot. Rev.* 22, 375–417.

Levy, Y.Y., Lai, E.Y., Remillard, S.P., Heintzelman, M.B., and Fulton, C. (1996). Centrin is a conserved protein that forms diverse associations with centrioles and MTOCs in *Naegleria* and other organisms. *Cell Motil. Cytoskeleton* 33, 298–323.

Li, S., Fernandez, J.J., Marshall, W.F., and Agard, D.A. (2012). Three-dimensional structure of basal body triplet revealed by electron cryo-tomography. *EMBO J.* 31, 552–562.

Li, S., Fernandez, J.J., Marshall, W.F., and Agard, D.A. (2019). Electron cryo-tomography provides insight into procentriole architecture and assembly mechanism. *Elife* 8, 1–25.

Li, Y., Wang, F.H., and Knox, R.B. (1989). Ultrastructural analysis of the flagellar apparatus in sperm cells of *Ginkgo biloba*. *Protoplasma* 149, 57–63.

Li, Y., Guo, F., Jing, Q., Zhu, X., and Yan, X. (2020). Characterisation of centriole biogenesis during multiciliation in planarians. *Biol. Cell* 1–11.

Linck, R.W., and Stephens, R.E. (2007). Functional protofilament numbering of ciliary, flagellar, and centriolar microtubules. *Cell Motil. Cytoskeleton* 64, 489–495.

Lindeboom, J.J., Nakamura, M., Hibbel, A., Gutierrez, R., Ketelaar, T., Emons, A.M.C., Bela, M., Kirik, V., and Ehrhardt, D.W. (2013). A Mechanism for Reorientation of Cortical Microtubule Arrays Driven by Microtubule Severing. *Science.* 342, 1245533.

Linkies, A., Graeber, K., Knight, C., and Leubner-Metzger, G. (2010). The evolution of seeds. *New Phytol.* 186, 817–831.

Lintilhac, P.M., and Vesecky, T.B. (1981). Mechanical Stress and Cell Wall Orientation in Plants. II. The Application of Controlled Directional Stress to

Growing Plants; with a Discussion on the Nature of the Wound Reaction. *Am. J. Bot.* **68**, 1222–1230.

Liu, B., Marc, J., Joshi, H.C., and Palevitz, B.A. (1993). A γ -tubulin-related protein associated with the microtubule arrays of higher plants in a cell cycle-dependent manner. *J. Cell Sci.* **104**, 1217–1228.

Liu, T., Tian, J., Wang, G., Yu, Y., Wang, C., Ma, Y., Zhang, X., Xia, G., Liu, B., and Kong, Z. (2014). Augmin triggers microtubule-dependent microtubule nucleation in interphase plant cells. *Curr. Biol.* **24**, 2708–2713.

Lopez-Obando, M., Hoffmann, B., Géry, C., Guyon-Debast, A., Téoulé, E., Rameau, C., Bonhomme, S., and Nogué, F. (2016). Simple and efficient targeting of multiple genes through CRISPR-Cas9 in *Physcomitrella patens*. *Genes, Genomes, Genet.* **6**, 3647–3653.

Lu, Q., Insinna, C., Ott, C., Stauffer, J., Pintado, P.A., Rahajeng, J., Baxa, U., Walia, V., Cuenca, A., Hwang, Y.S., et al. (2015). Early steps in primary cilium assembly require EHD1/EHD3-dependent ciliary vesicle formation. *Nat. Cell Biol.* **17**, 228–240.

Magnani, E. (2018). Seed Evolution, A ‘Simpler’ Story. *Trends Plant Sci.* **23**, 654–656.

Mallett, D.R., Chang, M., Cheng, X., and Bezanilla, M. (2019). Efficient and modular CRISPR-Cas9 vector system for *Physcomitrella patens*. *Plant Direct* **3**, 1–15.

Manandhar, G., Sutovsky, P., Joshi, H.C., Stearns, T., and Schatten, G. (1998). Centrosome reduction during mouse spermiogenesis. *Dev. Biol.* **203**, 424–434.

Manandhar, G., Schatten, H., and Sutovsky, P. (2005). Centrosome Reduction During Gametogenesis and Its Significance. *Biol. Reprod.* **72**, 2–13.

Manton, I. (1957). Observations with the electron microscope on the cell structure of the antheridium and spermatozoid of *Sphagnum*. *J. Exp. Bot.* **8**, 382–400.

Matsuura, K., Lefebvre, P.A., Kamiya, R., and Hirono, M. (2004). Bld10p, a novel protein essential for basal body assembly in *Chlamydomonas*: Localization to the cartwheel, the first ninefold symmetrical structure appearing during assembly. *J. Cell Biol.* **165**, 663–671.

Mazo, G., Soplop, N., Wang, W.J., Uryu, K., and Tsou, M.F.B. (2016). Spatial Control of Primary Ciliogenesis by Subdistal Appendages Alters Sensation-Associated Properties of Cilia. *Dev. Cell* 39, 424–437.

McCourt, R.M. (1995). Green algal phylogeny. *Trends Ecol. Evol.* 10, 159–163.

McFadden, G.I. (2014). Origin and evolution of plastids and photosynthesis in eukaryotes. *Cold Spring Harb. Perspect. Biol.* 6, 1–9.

Meiring, J.C.M., Shneyer, B.I., and Akhmanova, A. (2020). Generation and regulation of microtubule network asymmetry to drive cell polarity. *Curr. Opin. Cell Biol.* 62, 86–95.

Mercey, O., Al Jord, A., Rostaing, P., Mahuzier, A., Fortoul, A., Boudjema, A.R., Faucourt, M., Spassky, N., and Meunier, A. (2019a). Dynamics of centriole amplification in centrosome-depleted brain multiciliated progenitors. *Sci. Rep.* 9.

Mercey, O., Levine, M.S., LoMastro, G.M., Rostaing, P., Brotslaw, E., Gomez, V., Kumar, A., Spassky, N., Mitchell, B.J., Meunier, A., et al. (2019b). Massive centriole production can occur in the absence of deuterosomes in multiciliated cells. *Nat. Cell Biol.* 21, 1544–1552.

Meunier, A., and Azimzadeh, J. (2016). Multiciliated cells in animals. *Cold Spring Harb. Perspect. Biol.* 8, a028233.

Miki-Noumura, T. (1977). Studies on the *de novo* formation of centrioles: aster formation in the activated eggs of sea urchin. *J. Cell Sci.* 24, 203–216.

Mineyuki, Y., Marc, J., and Palevitz, B.A. (1989). Development of the preprophase band from random cytoplasmic microtubules in guard mother cells of *Allium cepa* L. *Planta* 178, 291–296.

Mishler, B.D., Lewis, L.A., Buchheim, M.A., Renzaglia, K.S., Garbary, D.J., Delwiche, C.F., Zechman, F.W., Kantz, T.S., and Chapman, R.L. (1994). Phylogenetic Relationships of the “Green Algae” and “Bryophytes.” *Ann. Missouri Bot. Gard.* 81, 451.

Mitchison, T., and Kirschner, M. (1984). Dynamic instability of microtubule growth. *Nature* 312, 237–242.

Mizukami, I., and Gall, J. (1966). Centriole replication. II. Sperm formation in the fern, *Marsilea*, and the cycad, *Zamia*. *J. Cell Biol.* 29, 97–111.

- Moody, L.A. (2020). Three-dimensional growth: a developmental innovation that facilitated plant terrestrialization. *J. Plant Res.* *133*, 283–290.
- Moser, J.W., and Kreitner, G.L. (1970). Centrosome Structure in *Anthoceros laevis* and *Marchantia polymorpha*. *J. Cell Biol.* *44*, 454–458.
- Moser, J.W., Duckett, J.G., Carothers, Z.B., Moser, J.W., and Duckett, J.G. (1977). Ultrastructural Studies of Spermatogenesis in the *Anthocerotales*. I. The Blepharoplast and Anterior Mitochondrion in *Phaeoceros laevis*: Early Development. *Am. J. Bot.* *64*, 1097–1106.
- Moyer, T.C., and Holland, A.J. (2019). Plk4 promotes centriole duplication by phosphorylating STIL to link the procentriole cartwheel to the microtubule wall. *Elife* *8*: e46054.
- Müller, S. (2019). Plant cell division — defining and finding the sweet spot for cell plate insertion. *Curr. Opin. Cell Biol.* *60*, 9–18.
- Murata, T., Sonobe, S., Baskin, T.I., Hyodo, S., Hasezawa, S., Nagata, T., Horio, T., and Hasebe, M. (2005). Microtubule-dependent microtubule nucleation based on recruitment of gamma-tubulin in higher plants. *Nat. Cell Biol.* *7*, 961–968.
- Myles, D.G., and Hepler, P.K. (1977). Spermatogenesis in the fern *Marsilea*: microtubules, nuclear shaping, and cytomorphogenesis. *J. Cell Sci.* *23*, 57–83.
- Nabais, C., Pereira, S.G., and Bettencourt-Dias, M. (2018). Noncanonical Biogenesis of Centrioles and Basal Bodies. *Cold Spring Harb. Symp. Quant. Biol.* *82*:123-135.
- Nabais, C., Pessoa, D., de-Carvalho, J., van Zanten, T., Duarte, P., Mayor, S., Carneiro, J., Telley, I.A., and Bettencourt-Dias, M. (2021). Plk4 triggers autonomous *de novo* centriole biogenesis and maturation. *J. Cell Biol.* *220* (5): e202008090.
- Nakamura, M., Ehrhardt, D.W., and Hashimoto, T. (2010). Microtubule and katanin-dependent dynamics of microtubule nucleation complexes in the acentrosomal *Arabidopsis* cortical array. *Nat. Cell Biol.* *12*, 1064–1070.
- Nakamura, M., Lindeboom, J.J., Saltini, M., Mulder, B.M., and Ehrhardt, D.W. (2018). SPR2 protects minus ends to promote severing and reorientation of plant cortical microtubule arrays. *J. Cell Biol.* *217*, 915–927.

Nakazawa, Y., Hiraki, M., Kamiya, R., and Hirono, M. (2007). SAS-6 is a Cartwheel Protein that Establishes the 9-Fold Symmetry of the Centriole. *Curr. Biol.* *17*, 2169–2174.

Nazarov, S., Bezler, A., Hatzopoulos, G.N., Nemčiková Villímová, V., Demurtas, D., Le Guennec, M., Guichard, P., and Gönczy, P. (2020). Novel features of centriole polarity and cartwheel stacking revealed by cryo-tomography. *EMBO J.* *39*, 1–17.

Nechipurenko, I. V., Berciu, C., Sengupta, P., and Nicastro, D. (2017). Centriolar remodeling underlies basal body maturation during ciliogenesis in *Caenorhabditis elegans*. *Elife* *6*, 1–12.

Nievergelt, A.P., Banterle, N., Andany, S.H., Gönczy, P., and Fantner, G.E. (2018). High-speed photothermal off-resonance atomic force microscopy reveals assembly routes of centriolar scaffold protein SAS-6. *Nat. Nanotechnol.* *13*, 696–701.

Nigg, E.A., and Holland, A.J. (2018). Once and only once: Mechanisms of centriole duplication and their deregulation in diseases. *Nat. Rev. Mol. Cell Biol.* *19*, 297–312.

Nishiyama, T., Sakayama, H., de Vries, J., Buschmann, H., Saint-Marcoux, D., Ullrich, K.K., Haas, F.B., Vanderstraeten, L., Becker, D., Lang, D., et al. (2018). The *Chara* Genome: Secondary Complexity and Implications for Plant Terrestrialization. *Cell* *174*, 448–464.e24.

Noordstra, I., Liu, Q., Nijenhuis, W., Hua, S., Jiang, K., Baars, M., Remmelzwaal, S., Martin, M., Kapitein, L.C., and Akhmanova, A. (2016). Control of apico-basal epithelial polarity by the microtubule minus-end-binding protein CAMSAP3 and spectraplakins ACF7. *J. Cell Sci.* *129*, 4278–4288.

Norstog, K. (1967). Fine Structure of the Spermatozoid of *Zamia* with Special Reference to the Flagellar Apparatus. *Am. J. Bot.* *54*, 831–840.

Norstog, K. (1974). Fine Structure of the Spermatozoid of *Zamia*. *Am. J. Bot.* *61*, 449–456.

Norstog, K.J. (1986). The blepharoplast of *Zamia pumila* L. *Bot. Gazette* *147*, 40–46.

Ohta, M., Watanabe, K., Ashikawa, T., Nozaki, Y., Yoshida, S., Kimura, A., and Kitagawa, D. (2018). Bimodal Binding of STIL to Plk4 Controls Proper Centriole Copy Number. *Cell Rep.* 23, 3160-3169.e4.

Otegui, M.S., Mastrorade, D.N., Kang, B.H., Bednarek, S.Y., and Staehelin, L.A. (2001). Three-dimensional analysis of syncytial-type cell plates during endosperm cellularization visualized by high resolution electron tomography. *Plant Cell* 13, 2033–2051.

Palazzo, R.E., Vaisberg, E., Cole, R.W., and Rieder, C.L. (1992). Centriole Duplication in Lysates of *Spisula solidissima* Oocytes. *Science.* 256, 219–221.

Palevitz, B.A., and Tiezzi, A. (1992). Organization, Composition, and Function of the Generative Cell and Sperm Cytoskeleton. *Int. Rev. Cytol.* 140, 149–185.

Paolillo, D.J. (1981). Swimming of Land Plants Sperms. *Am. Inst. Biol. Sci.* 31, 367–373.

Paredes, A.R., Somerville, C.R., and Ehrhardt, D.W. (2006). Visualization of cellulose synthase demonstrates functional association with microtubules. *Science.* 312, 1491–1495.

Park, J.E., Meng, L., Ryu, E.K., Nagashima, K., Baxa, U., Bang, J.K., and Lee, K.S. (2020). Autophosphorylation-induced self-assembly and STIL-dependent reinforcement underlie Plk4's ring-to-dot localization conversion around a human centriole. *Cell Cycle* 19, 3419–3436.

Peel, N., Stevens, N.R., Basto, R., and Raff, J.W. (2007). Overexpressing Centriole-Replication Proteins *In Vivo* Induces Centriole Overduplication and *De Novo* Formation. *Curr. Biol.* 17, 834–843.

Pelletier, L., O'Toole, E., Schwager, A., Hyman, A.A., and Müller-Reichert, T. (2006). Centriole assembly in *Caenorhabditis elegans*. *Nature* 444, 619–623.

Perkins, F.O. (1970). Formation of Centriole and Centriole- Like Structures During Meiosis and Mitosis in *Labyrinthula sp.* (Rhizopodea, *Labyrinthulida*). An electron-microscope study. *J. Cell Sci.* 6, 629–653.

Petersen, K.B., and Burd, M. (2016). Why did heterospory evolve? *Biol. Rev.* 92: 1739-1754

Petry, S., Groen, A.C., Ishihara, K., Mitchison, T.J., and Vale, R.D. (2013). Branching microtubule nucleation in *Xenopus* egg extracts mediated by augmin and TPX2. *Cell* 152, 768–777.

Phillips, D.M. (1967). Giant centriole formation in *Sciara*. *J. Cell Biol.* 33, 73–92.

Pickett-Heaps, J. (1974). The evolution of mitosis and the eukaryotic condition. *BioSystems* 6, 37–48.

Pickett-Heaps, J.D., and Northcote, D.H. (1966). Organization of microtubules and endoplasmic reticulum during mitosis and cytokinesis in wheat meristems. *J. Cell Sci.* 1, 109–120.

Pimenta-Marques, A., Bento, I., Lopes, C.A.M., Duarte, P., Jana, S.C., and Bettencourt-Dias, M. (2016). A mechanism for the elimination of the female gamete centrosome in *Drosophila melanogaster*. *Science*. 353, aaf4866.

Prigge, M.J., and Bezanilla, M. (2010). Evolutionary crossroads in developmental biology: *Physcomitrella patens*. *Development* 137, 3535–3543.

Rasmussen, C.G., Wright, A.J., and Müller, S. (2013). The role of the cytoskeleton and associated proteins in determination of the plant cell division plane. *Plant J.* 75, 258–269.

Remy, W., Gensel, P.G., and Hass, H. (1993). The Gametophyte Generation of Some Early Devonian Land Plants. *Int. J. Plant Sci.* 154, 35–58.

Rensing, S.A. (2018). Great moments in evolution: the conquest of land by plants. *Curr. Opin. Plant Biol.* 42, 49–54.

Rensing, S. a, Lang, D., Zimmer, A.D., Terry, A., Salamov, A., Shapiro, H., Nishiyama, T., Perroud, P.-F., Lindquist, E. a, Kamisugi, Y., et al. (2008). The *Physcomitrella* genome reveals evolutionary insights into the conquest of land by plants. *Science*. 319, 64–69.

Rensing, S.A., Goffinet, B., Meyberg, R., Wu, S.Z., and Bezanilla, M. (2020). The moss *Physcomitrium* (*Physcomitrella*) *patens*: A model organism for non-seed plants. *Plant Cell* 32, 1361–1376.

Renzaglia, K.S., and Duckett, J.G. (1987). Spermatogenesis in *Blasia pusilla*: From Young Antheridium through Mature Spermatozoid. *Bryologist* 90, 419–449.

Renzaglia, K.S., and Duckett, J.G. (1989). Ultrastructural studies of spermatogenesis in Anthocerotophyta V. Nuclear metamorphosis and the posterior mitochondrion of *Notothylas orbicularis* and *Phaeoceros laevis*. *Protoplasma* 151, 137–150.

Renzaglia, K.S., and Duckett, J.G. (1991). Towards an Understanding of the Differences between the Blepharoplasts of Mosses and Liverworts, and Comparisons with Hornworts, Biflagellate Lycopods and Charophytes: a Numerical Analysis. *New Phytol.* 117, 187–208.

Renzaglia, K.S., and Garbary, D.J. (2001). Motile Gametes of Land Plants: Diversity, Development, and Evolution. *CRC. Crit. Rev. Plant Sci.* 20, 107–213.

Renzaglia, K.S., and Maden, A.R. (2000). Microtubule organizing centers and the origin of centrioles during spermatogenesis in the pteridophyte *Phylloglossum*. *Microsc. Res. Tech.* 49, 496–505.

Renzaglia, K.S., Bernhard, D.L., and Garbary, D.J. (1999). Developmental Ultrastructure of the Male Gamete of *Selaginella*. *Int. J. Plant Sci.* 160, 14–28.

Reski, R., and Abel, W.O. (1985). Induction of budding on chloronemata and caulonemata of the moss, *Physcomitrella patens*, using isopentenyladenine. *Planta* 165, 354–358.

Riparbelli, M.G., and Callaini, G. (2003). *Drosophila* parthenogenesis: A model for *de novo* centrosome assembly. *Dev. Biol.* 260, 298–313.

Riparbelli, M.G., Stouthamer, R., Dallai, R., and Callaini, G. (1998). Microtubule Organization during the Early Development of the Parthenogenetic Egg of the Hymenopteran *Muscidifurax uniraptor*. *Dev. Biol.* 195, 89–99.

Rivero, S., Cardenas, J., Bornens, M., and Rios, R.M. (2009). Microtubule nucleation at the cis-side of the golgi apparatus requires AKAP450 and GM130. *EMBO J.* 28, 1016–1028.

Robbins, R.R. (1984). Origin and behavior of bicentriolar centrosomes in the bryophyte *Riella americana*. *Protoplasma* 121, 114–119.

Robbins, R.R., and Carothers, Z.B. (1978). Spermatogenesis in *Lycopodium*: The Mature Spermatozoid. *Am. J. Bot.* 65, 433–440.

Rodrigues-Martins, A., Riparbelli, M., Callaini, G., Glover, D.M., and Bettencourt-Dias, M. (2007). Revisiting the Role of the Mother Centriole in Centriole Biogenesis. *Science.* 316, 1046–1050.

Sanchez-Vera, V., Kenchappa, C.S., Landberg, K., Bressendorff, S., Schwarzbach, S., Martin, T., Mundy, J., Petersen, M., Thelander, M., and Sundberg, E. (2017). Autophagy is required for gamete differentiation in the moss *Physcomitrella patens*. *Autophagy* 13, 1939–1951.

Schaefer, D.G., and Zrýd, J.P. (1997). Efficient gene targeting in the moss *Physcomitrella patens*. *Plant J.* 11, 1195–1206.

Schaefer, E., Belcram, K., Uyttewaal, M., Duroc, Y., Goussot, M., Legland, D., Laruelle, E., De Tauzia-Moreau, M.L., Pastuglia, M., and Bouchez, D. (2017). The preprophase band of microtubules controls the robustness of division orientation in plants. *Science*. 356, 186–189.

Schatten, G., Simerly, C., and Schatten, H. (1985). Microtubule configurations during fertilization, mitosis, and early development in the mouse and the requirement for egg microtubule-mediated motility during mammalian fertilization. *Proc. Natl. Acad. Sci. USA* 82, 4152–4156.

Schmidt, K.N., Kuhns, S., Neuner, A., Hub, B., Zentgraf, H., and Pereira, G. (2012). Cep164 mediates vesicular docking to the mother centriole during early steps of ciliogenesis. *J. Cell Biol.* 199, 1083–1101.

Schmidt, T.I., Kleylein-Sohn, J., Westendorf, J., Le Clech, M., Lavoie, S.B., Stierhof, Y.D., and Nigg, E.A. (2009). Control of Centriole Length by CPAP and CP110. *Curr. Biol.* 19, 1005–1011.

Schrevel, J., and Besse, C. (1975). Un type flagellaire fonctionnel de base 6+0. *J. Cell Biol.* 66, 492–507.

Searles, R.B. (1980). The Strategy of the Red Algal Life History. *Am. Nat.* 115, 113–120.

Shang, Y., Wang, H., Jia, P., Zhao, H., Liu, C., Liu, W., Song, Z., Xu, Z., Yang, L., Wang, Y., et al. (2016). Autophagy regulates spermatid differentiation via degradation of PDLIM1. *Autophagy* 12, 1575–1592.

Sharma, A., Aher, A., Dynes, N.J., Frey, D., Katrukha, E.A., Jaussi, R., Grigoriev, I., Croisier, M., Kammerer, R.A., Akhmanova, A., et al. (2016). Centriolar CPAP/SAS-4 Imparts Slow Processive Microtubule Growth. *Dev. Cell* 37, 362–376.

Sharma, A., Olieric, N., and Steinmetz, M.O. (2021). Centriole length control. *Curr. Opin. Struct. Biol.* 66, 89–95.

Shaw, S.L., Kamyar, R., and Ehrhardt, D.W. (2003). Sustained Microtubule Treadmilling in *Arabidopsis* Cortical Arrays. *Science*. *300*, 1715–1718.

Shimamura, M., Brown, R.C., Lemmon, B.E., Akashi, T., Mizuno, K., Nishihara, N., Tomizawa, K.I., Yoshimoto, K., Deguchi, H., Hosoya, H., et al. (2004). γ -Tubulin in Basal Land Plants: Characterization, Localization, and Implication in the Evolution of Acentriolar Microtubule Organizing Centers. *Plant Cell* *16*, 45–59.

Simerly, C., Castro, C., Hartnett, C., Lin, C.C., Sukhwani, M., Orwig, K., and Schatten, G. (2016). Post-Testicular Sperm Maturation: Centriole Pairs, Found in Upper Epididymis, are Destroyed Prior to Sperm's Release at Ejaculation. *Sci. Rep.* *6*, 31816.

Simerly, C., Manil-Ségalen, M., Castro, C., Hartnett, C., Kong, D., Verlhac, M.H., Loncarek, J., and Schatten, G. (2018). Separation and Loss of Centrioles From Primordial Germ Cells To Mature Oocytes In The Mouse. *Sci. Rep.* *8*.

Sluiman, H.J. (1983). The flagellar apparatus of the zoospore of the filamentous green alga *Coleochaete pulvinata*: Absolute configuration and phylogenetic significance. *Protoplasma* *115*, 160–175.

Smith, E., Hégarat, N., Vesely, C., Roseboom, I., Larch, C., Streicher, H., Straatman, K., Flynn, H., Skehel, M., Hirota, T., et al. (2011). Differential control of Eg5-dependent centrosome separation by Plk1 and Cdk1. *EMBO J.* *30*, 2233–2245.

Sorokin, S. (1962). Centrioles and the formation of rudimentary cilia by fibroblasts and smooth muscle cells. *J. Cell Biol.* *15*, 363–377.

Sorokin, S.P. (1968). Reconstructions of centriole formation and ciliogenesis in mammalian lungs. *J. Cell Sci.* *3*, 207–230.

Southworth, D., and Cresti, M. (1997). Comparison of flagellated and nonflagellated sperm in plants. *Am. J. Bot.* *84*, 1301–1311.

Spektor, A., Tsang, W.Y., Khoo, D., and Dynlacht, B.D. (2007). Cep97 and CP110 Suppress a Cilia Assembly Program. *Cell* *130*, 678–690.

Spinner, L., Gadeyne, A., Belcram, K., Goussot, M., Moison, M., Duroc, Y., Eeckhout, D., De Winne, N., Schaefer, E., Van De Slijke, E., et al. (2013). A protein phosphatase 2A complex spatially controls plant cell division. *Nat. Commun.* *4*, 1863.

Steib, E., Laporte, M.H., Gambarotto, D., Olieric, N., Zheng, C., Borgers, S., Olieric, V., Le Guennec, M., Koll, F., Tassin, A.-M., et al. (2020). WDR90 is a centriolar microtubule wall protein important for centriole architecture integrity. *Elife* 9, e57205.

Steinborn, K., Maulbetsch, C., Priester, B., Trautmann, S., Pacher, T., Geiges, B., Küttner, F., Lepiniec, L., Stierhof, Y.D., Schwarz, H., et al. (2002). The *Arabidopsis* PILZ group genes encode tubulin-folding cofactor orthologs required for cell division but not cell growth. *Genes Dev.* 16, 959–971.

Strnad, P., Leidel, S., Vinogradova, T., Euteneuer, U., Khodjakov, A., and Gönczy, P. (2007). Regulated HsSAS-6 Levels Ensure Formation of a Single Procentriole per Centriole during the Centrosome Duplication Cycle. *Dev. Cell* 13, 203–213.

Strotbek, C., Krinninger, S., and Frank, W. (2013). The moss *Physcomitrella patens*: methods and tools from cultivation to targeted analysis of gene function. *Int. J. Dev. Biol.* 57, 553–564.

Suh, M.R., Han, J.W., No, Y.R., and Lee, J. (2002). Transient concentration of a γ -tubulin-related protein with a pericentrin-related protein in the formation of basal bodies and flagella during the differentiation of *Naegleria gruberi*. *Cell Motil. Cytoskeleton* 52, 66–81.

Sulimenko, V., Hájková, Z., Klebanovych, A., and Dráber, P. (2017). Regulation of microtubule nucleation mediated by γ -tubulin complexes. *Protoplasma* 254, 1187–1199.

Sullenberger, C., Vasquez-Limeta, A., Kong, D., and Loncarek, J. (2020). With Age Comes Maturity: Biochemical and Structural Transformation of a Human Centriole in the Making. *Cells* 9, 1–26.

Szövényi, P., Waller, M., and Kirbis, A. (2019). Evolution of the plant body plan. *Curr. Top. Dev. Biol.* 131, 1–34.

Takeda, M., Sami, M.M., and Wang, Y.C. (2018). A homeostatic apical microtubule network shortens cells for epithelial folding *via* a basal polarity shift. *Nat. Cell Biol.* 20, 36–45.

Tamm, S., and Tamm, S.L. (1980). Origin and development of free kinetosomes in the flagellates *Deltotrichonympha* and *Koruga*. *J. Cell Sci.* 42, 189–205.

Tanenbaum, M.E., Macůrek, L., Galjart, N., and Medema, R.H. (2008). Dynein, Lis1 and CLIP-170 counteract Eg5-dependent centrosome separation during bipolar spindle assembly. *EMBO J.* 27, 3235–3245.

Tang, C.J.C., Lin, S.Y., Hsu, W. Bin, Lin, Y.N., Wu, C.T., Lin, Y.C., Chang, C.W., Wu, K.S., and Tang, T.K. (2011). The human microcephaly protein STIL interacts with CPAP and is required for procentriole formation. *EMBO J.* 30, 4790–4804.

Tanos, B.E., Yang, H.J., Soni, R., Wang, W.J., Macaluso, F.P., Asara, J.M., and Tsou, M.F.B. (2013). Centriole distal appendages promote membrane docking, leading to cilia initiation. *Genes Dev.* 27, 163–168.

Terauchi, M., Nagasato, C., and Motomura, T. (2015). Plasmodesmata of brown algae. *J. Plant Res.* 128, 7–15.

Tilney, L.G., Bryan, J., Bush, D.J., Fujiwara, K., Mooseker, M.S., Murphy, D.B., and Snyder, D.H. (1973). Microtubules: Evidence for 13 protofilaments. *J. Cell Biol.* 59, 267–275.

Toya, M., Kobayashi, S., Kawasaki, M., Shioi, G., Kaneko, M., Ishiuchi, T., Misaki, K., Meng, W., and Takeichi, M. (2016). CAMSAP3 orients the apical-to-basal polarity of microtubule arrays in epithelial cells. *Proc. Natl. Acad. Sci. U. S. A.* 113, 332–337.

Traas, J., Bellini, C., Nacry, P., Kronenberger, J., Bouchez, D., and Caboche, M. (1995). Normal differentiation patterns in plants lacking microtubular preprophase bands. *Nature* 375, 676–677.

Tram, U., and Sullivan, W. (2000). Reciprocal inheritance of centrosomes in the parthenogenetic Hymenopteran *Nasonia vitripennis*. *Curr. Biol.* 10, 1413–1419.

Turner, F.R. (1970). The effects of colchicine on spermatogenesis in *Nitella*. *J. Cell Biol.* 46, 220–234.

Ueda, K., Sakaguchi, S., Kumagai, F., Hasezawa, S., Quader, H., and Kristen, U. (2003). Development and disintegration of phragmoplasts in living cultured cells of a GFP::TUA6 transgenic *Arabidopsis thaliana* plant. *Protoplasma* 220, 111–118.

Umen, J., and Coelho, S. (2019). Algal sex determination and the evolution of anisogamy. *Annu. Rev. Microbiol.* 73, 267–291.

van Deurs, B. (1973). Axonemal 12+0 Pattern in the Flagellum of the Motile Spermatozoon of *Nymphon leptocheles*. J. Ultrastruct. Res. 42, 594–598.

Vaughn, K.C., and Harper, J.D.I. (1998). Microtubule-Organizing Centers and Nucleating Sites in Land Plants. Int. Rev. Cytol. 181, 75–149.

Vaughn, K.C., and Renzaglia, K.S. (2006). Structural and immunocytochemical characterization of the *Ginkgo biloba* L. sperm motility apparatus. Protoplasma 227, 165–173.

Vladar, E.K., and Stearns, T. (2007). Molecular characterization of centriole assembly in ciliated epithelial cells. J. Cell Biol. 178, 31–42.

Vonderfecht, T., Cookson, M.W., Giddings, T.H., Clarissa, C., and Winey, M. (2012). The two human centrin homologues have similar but distinct functions at *Tetrahymena* basal bodies. Mol. Biol. Cell 23, 4766–4777.

Vorobjev, I.A., and Chentsov, Y.S. (1982). Centrioles in the cell cycle. I. Epithelial cells. J. Cell Biol. 93, 938–949.

Vos, J.W., Dogterom, M., and Emons, A.M.C. (2004). Microtubules Become More Dynamic but Not Shorter during Preprophase Band Formation: A Possible “Search-and-Capture” Mechanism for Microtubule Translocation. Cell Motil. Cytoskeleton 57, 246–258.

Wade, R.H., Chrétien, D., and Job, D. (1990). Characterization of microtubule protofilament numbers. How does the surface lattice accommodate? J. Mol. Biol. 212, 775–786.

Walia, A., Nakamura, M., Moss, D., Kirik, V., Hashimoto, T., and Ehrhardt, D.W. (2014). GCP-WD mediates γ -TuRC recruitment and the geometry of microtubule nucleation in interphase arrays of *Arabidopsis*. Curr. Biol. 24, 2548–2555.

Walker, K.L., Müller, S., Moss, D., Ehrhardt, D.W., and Smith, L.G. (2007). *Arabidopsis* Tangled Identifies the Division Plane Throughout Mitosis and Cytokinesis. Curr. Biol. 17, 1827–1836.

Wang, C., Liu, Y., Li, S.S., and Han, G.Z. (2015). Insights into the origin and evolution of the plant hormone signaling machinery. Plant Physiol. 167, 872–886.

Wang, L., Failler, M., Fu, W., and Dynlacht, B.D. (2018). A distal centriolar protein network controls organelle maturation and asymmetry. Nat. Commun. 9.

Weisenberg, R.C., Deery, W.J., and Dickinson, P.J. (1976). Tubulin-Nucleotide Interactions during the Polymerization and Depolymerization of Microtubules. *Biochemistry* 15, 4248–4254.

Werner, S., Pimenta-Marques, A., and Bettencourt-Dias, M. (2017). Maintaining centrosomes and cilia. *J. Cell Sci.* 130, 3789–3800.

Wilson, E.B. (1925). *The Cell in Development and Heredity* (Macmillan, New York.).

Wittmann, T., Hyman, A., and Desai, A. (2001). The spindle: A dynamic assembly of microtubules and motors. *Nat. Cell Biol.* 3.

Wolniak, S.M., Klink, V.P., Hart, P.E., and Tsai, C.W. (2000). Control of development and motility in the spermatozooids of lower plants. *Gravitational Sp. Biol. Bull.* 13, 85–93.

Woodland, H.R., and Fry, A.M. (2008). Pix proteins and the evolution of centrioles. *PLoS One* 3, e3778.

Woodruff, J.B., Wueseke, O., Viscardi, V., Mahamid, J., Ochoa, S.D., Bunkenborg, J., Widlund, P.O., Pozniakovsky, A., Zanin, E., Bahmanyar, S., et al. (2015). Regulated assembly of a supramolecular centrosome scaffold in vitro. *Science*. 348, 808–812.

Woodruff, J.B., Ferreira Gomes, B., Widlund, P.O., Mahamid, J., Honigmann, A., and Hyman, A.A. (2017). The Centrosome Is a Selective Condensate that Nucleates Microtubules by Concentrating Tubulin. *Cell* 169, 1066–1077.

Worden, A.Z., Follows, M.J., Giovannoni, S.J., Wilken, S., Zimmerman, A.E., and Keeling, P.J. (2015). Rethinking the marine carbon cycle: Factoring in the multifarious lifestyles of microbes. *Science*. 347.

Wu, J., de Heus, C., Liu, Q., Bouchet, B.P., Noordstra, I., Jiang, K., Hua, S., Martin, M., Yang, C., Grigoriev, I., et al. (2016). Molecular Pathway of Microtubule Organization at the Golgi Apparatus. *Dev. Cell* 39, 44–60.

Yagi, N., Matsunaga, S., and Hashimoto, T. (2018). Insights into cortical microtubule nucleation and dynamics in *Arabidopsis* leaf cells. *J. Cell Sci.* 131, 1–7.

Yang, T.T., Chong, W.M., Wang, W.J., Mazo, G., Tanos, B., Chen, Z., Tran, T.M.N., Chen, Y. De, Weng, R.R., Huang, C.E., et al. (2018). Super-resolution

architecture of mammalian centriole distal appendages reveals distinct blade and matrix functional components. *Nat. Commun.* **9**, 1–11.

Yi, P., and Goshima, G. (2018). Microtubule nucleation and organization without centrosomes. *Curr. Opin. Plant Biol.* **46**, 1–7.

Yi, P., and Goshima, G. (2020). Transient cotransformation of CRISPR/Cas9 and oligonucleotide templates enables efficient editing of target *loci* in *Physcomitrella patens*. *Plant Biotechnol. J.* **18**, 599–601.

Yubuki, N., and Leander, B.S. (2013). Evolution of microtubule organizing centers across the tree of eukaryotes. *Plant J.* **75**, 230–244.

Zhang, Y., and He, C.Y. (2012). Centrioles in unicellular organisms: Functional diversity and specialization. *Protoplasma* **249**, 459–467.

Zhang, D., Wadsworth, P., and Hepler, P.K. (1990). Microtubule dynamics in living dividing plant cells: Confocal imaging of microinjected fluorescent brain tubulin. *Proc. Natl. Acad. Sci. U. S. A.* **87**, 8820–8824.

Zhao, H., Zhu, L., Zhu, Y., Cao, J., Li, S., Huang, Q., Xu, T., Huang, X., Yan, X., and Zhu, X. (2013). The *cep63* paralogue *deup1* enables massive *de novo* centriole biogenesis for vertebrate multiciliogenesis. *Nat. Cell Biol.* **15**, 1434–1444.

Zhao, H., Chen, Q., Fang, C., Huang, Q., Zhou, J., Yan, X., and Zhu, X. (2019). Parental centrioles are dispensable for deuterosome formation and function during basal body amplification. *EMBO Rep.* **20**, 1–12.

Zheng, X., Ramani, A., Soni, K., Gottardo, M., Zheng, S., Ming Gooi, L., Li, W., Feng, S., Mariappan, A., Wason, A., et al. (2016). Molecular basis for CPAP-tubulin interaction in controlling centriolar and ciliary length. *Nat. Commun.* **7**, 1–13.

Zheng, Y., Wong, M.L., Alberts, B., and Mitchison, T. (1995). Nucleation of microtubule assembly by a γ -tubulin-containing ring complex. *Nature* **378**, 578–583.

Chapter 2.

Advanced imaging methods for the study of *P. patens* spermatogenesis

2.1 Abstract

Bryophytes were the first plants to colonize terrestrial environments, being currently widespread across Earth's habitats. Due to their ecological relevance and phylogenetic position, bryophyte research is key to understanding plant evolution and for ecosystem preservation. Nevertheless, only relatively recently have bryophyte model species been implemented in laboratories worldwide, with many successful studies focusing on processes mainly during their vegetative growth. Contrastingly, their sexual reproduction and its underlying mechanisms remain enigmatic, particularly due to the limited techniques available to study such processes.

Here, I describe two protocols for transmission electron microscopy of *P. patens* gametangia samples. While electron microscopy provides ultrastructural information, it fails at revealing molecular details. Therefore, I have developed two distinct immunostaining protocols able to provide such molecular information, with distinct tissue and cellular resolutions. Moreover, I have also optimized a protocol for live imaging of *P. patens* released sperm cells, enabling both qualitative, as well as quantitative motility assessments. While the methods presented here have been directed at studying *P. patens* spermatogenesis, they can also be employed for the study of other cellular processes, as well as tailored for diverse bryophyte species.

2.3 Introduction

The liverwort, hornwort and moss lineages compose the Bryophyta phylogenetic division. These are non-vascular land plants thought to

have been pioneers in the colonization of terrestrial environments, a key process during the evolutionary history of life on Earth (Mishler et al., 1994; Rensing, 2018). Today, bryophyte species are found in almost all terrestrial and some freshwater ecosystems, representing a significant portion of these ecosystems' diversity and biomass, performing critical roles in water purification and nutrient retention (During and van Tooren, 1987; Glime, 2020). Despite all of their critical roles, and due to their less significant relevance as food or feed, research in bryophytes has been lacking behind, with most plant research being focused on agronomically relevant crops or the model flowering plant *Arabidopsis thaliana* (Cesarino et al., 2020).

In fact, only recently have bryophyte species, such as the moss *Physcomitrium patens* (*P. patens*) and the liverwort *Marchantia polymorpha* (*M. polymorpha*), been implemented as model systems in research laboratories worldwide. Such implementation was enabled by the sequencing of their genomes, development of genetic engineering tools (aided by their characteristic haploid-dominant life cycles), together with relatively fast and inexpensive propagation techniques (Ishizaki et al., 2016; Rensing et al., 2020). Such advantages made it possible to study the evolution of plant-specific processes and gene networks (e.g. Hashida et al., 2020; Islam et al., 2021; Pu et al., 2020; Rico-Reséndiz et al., 2020; Julca et al.), as well as of fundamental cellular mechanisms (Kosetsu et al., 2017; Wu and Bezanilla, 2018; Leong et al., 2020; Van Gisbergen et al., 2020; Cheng and Bezanilla, 2021; amongst others). Most of these studies were facilitated by the fast growth of protonema cells into a filamentous 2D network composed of branching filaments, which can be imaged and manipulated without requiring sectioning and/or dissection (Rensing et al., 2020). This is contrasting to the slower development of the 3D plant body, called gametophore.

Bryophytes reproduce *via* sexual reproduction, despite some species also being capable of asexual reproduction (e.g. *M. polymorpha* gemma, Kato et al., 2020). Sexual reproduction in bryophytes relies on the differentiation of motile biflagellated sperm cells, which takes place inside specialized organs called antheridia. Upon sperm cell discharge, the released spermatids have to swim to reach the egg cells, enclosed in the female organs named archegonia. Some bryophyte species (e.g. *P. patens*) are monoecious, containing both sperm-producing antheridia and egg-containing female archegonia within the same individual (During, 1979; During and van Tooren, 1987; Hackenberg and Twell, 2019). Yet, despite the widespread distribution and importance of bryophyte sexual reproduction, few studies have explored the mechanisms acting on such process (Landberg et al., 2013; Minamino et al., 2017; Ortiz-Ramírez et al., 2017; Sanchez-Vera et al., 2017; Hisanaga et al., 2019; Inoue et al., 2019). This is mostly due to the limited techniques and protocols available to analyze this particular event in bryophyte species. Such limitations are imposed by the complex 3D architecture of the sexual organs and their surrounding tissues. Moreover, while the 2D networks of protonema cells are fast-growing (usually a few hours/days), the 3D gametophyte usually requires a few months to reach maturity and sexually reproduce (During, 1979; Hohe et al., 2002; Landberg et al., 2013; Shimamura, 2016). For instance, *P. patens* gametophores take around 6 to 8 weeks to reach maturity, upon which sexual reproduction may be triggered, by a change in environmental conditions. Gametogenesis takes around 15 days to be completed, with multiple antheridia and archegonia developing asynchronously on the top the gametophores (Landberg et al., 2013; Rensing et al., 2020). Therefore, as opposed to the availability (both timely and anatomically) of vegetative tissues, the study of bryophytes

reproductive structures requires the development of tailored protocols (Horst and Reski, 2017).

Here, aiming at understanding the cellular mechanisms underlying *P. patens* spermatogenesis, I have developed several microscopy protocols covering a broad resolution range: from the sub-cellular ultrastructural detail (transmission electron microscopy - TEM), to protein localization at the cellular or tissue level (immunostaining), and reaching into the physiological level of sperm motility/behaviour (live imaging of sperm cells). Although the protocols here detailed were tailored for the particularities of *P. patens* spermatogenesis, they might be easily adapted for the study of other cellular processes and/or cell types (e.g. oogenesis, paraphysis), as well as to other plant species (e.g. *Marchantia polymorpha*, and *Selaginella moellendorffii*). Therefore I hope these methods represent valuable resources for bryophyte and plant reproduction research.

2.4 Plant maintenance and growth

P. patens maintenance and growth was performed according to standard procedures. As these were reported elsewhere (Strotbek et al., 2013; Ortiz-Ramírez et al., 2017), I will just briefly detail them below.

P. patens protonema was maintained by weekly sub-culturing. Sub-culture was performed after mechanical disruption (TissueRuptor; Qiagen) of protonema, followed by its inoculation into new Petri dishes containing KNOPS media (Reski and Abel, 1985) supplemented with 0.5g/l ammonium tartrate dibasic (Sigma-Aldrich). Inoculated petri dishes were grown at 25°C, 50% relative humidity and 16h light (light intensity 80µlum/m/s). For development of gametophores (3D growth), protonema

tissue was inoculated into sterile peat pellets (Jiffy-7, Jiffy Products International), and grown during 6 to 8 weeks at 25°C, 50% relative humidity and 16h light (light intensity 80 μ lum/m/s) in Phytatray II (Sigma-Aldrich) boxes. Demineralized sterile water was supplied to the bottom of each box. Sexual reproduction was triggered by transferring the plants to 17°C, 50% relative humidity and 8h light (light intensity 50 μ lum/m/s) conditions.

All protocols were established using the wild-type (WT) Gransden *Physcomitrium* (*Physcomitrella*) *patens* ecotype (Ashton and Cove, 1977). Immunofluorescence protocols were further implemented in the previously published γ -tubulin2-Citrine (Nakaoka et al., 2012) reporter line. As a proof of concept, all EM and immunofluorescence images were obtained 15 days after induction (DAI) of plant sexual reproduction. As individual antheridia are only distinguishable at 10 DAI, the major spermatogenesis stages were confirmed by TEM imaging of samples at 10 DAI, 11 DAI, 12 DAI, 13 DAI, 14 DAI and 15 DAI. Then, a correspondence between the major subcellular structures identified by TEM, with the main sperm cell features observable by confocal and 3D-SIM imaging was established. Live imaging of released sperm cells was performed 16-17 DAI.

2.5 Transmission electron microscopy of developing sperm cells in *P. patens*

Transmission electron microscopy (TEM) enables the visualization and analysis of the ultrastructural features of cells and tissues. Sample fixation is a critical step in order to preserve such structural features in their native/living state. Samples can be either chemically or physically

(cryo-immobilized) fixed (Sousa, 2017; Layton et al., 2019). Both techniques are commonly employed, offering different advantages and disadvantages (see section 2.7.4). Here, I have developed and established TEM protocols for imaging of *P. patens* gametangia relying on either chemical (glutaraldehyde) fixation (section 2.5.1) or high pressure freezing (cryo-immobilization technique) of samples (section 2.5.2).

2.5.1 Chemical fixation protocol

2.5.1.1 Material and equipment

- Microscope slides;
- Hydrophobic pen (e.g. Dako pen);
- Micropipettes and respective disposable tips;
- Chemical fume hood;
- Dissection stereo microscope (e.g. Olympus SZX7);
- Tweezers;
- Plant gametophores;
- Humid chamber (or equivalent way to avoid solution evaporation during fixation);
 - Dry heater (e.g. Cole-Parmer SBH130D) or water bath;
 - Styrofoam box with ice;
 - Toothpicks;
 - Razor blade (e.g. Feather E72002-10);
 - Small spatula (e.g. VWR 231-0239);
 - 1.5ml sample tubes (e.g. 1.5ml eppendorf tubes);
 - Small glass Pasteur pipette (e.g. BRAND 747715);
 - Orbital shaker (e.g. Rotamax 120 Orbital Shaker);
 - Embedding molds (e.g. AGG3549);
 - 60°C-70°C oven (e.g. MRC PF60-SC);
 - Ultramicrotome (e.g. Leica UC7);

- Glass knife (homemade);
- Diamond knife (e.g. Diatome DU4515);
- Slot palladium-copper grids (coated with 1% formvar in chloroform);
 - TEM microscope (e.g. Hitachi H-7650 with AMT 2kX2k digital camera).

2.5.1.2 Reagents and solutions

- 0.1M Phosphate buffer (PB), pH 7.4;
- 2% (w/v) Low melting point agarose (OmniPur) solution;
- 100% Ethanol;
- Distilled water (dH₂O);
- Ethanol dilutions: 30%, 50%, 70%, and 90%;
- Reynolds' lead citrate;
- Fixative: 6% (v/v) glutaraldehyde (Polysciences), 0.5% (v/v) tween-20 in 0.1M PB;
 - Post-fixation: 0.1% (w/v) osmium tetroxide (ScienceServices) in 0.1M PB;
 - 1% (w/v) uranyl acetate in dH₂O;
 - EMbed-812 epoxy resin: made with 45.6% (v/v) EPON I resin stock (44% (v/v) EMbed-812 and 56% (v/v) DDSA (Dodeceny Succinic Anhydride Specially Distilled)), 52.7% (v/v) EPON II resin stock (54% (v/v) EMbed-812 and 46% (v/v) NMA (Methyl-5-Norbornene-2,3-Dicarboxylic Anhydride), and 1.7% (v/v) of DMP-30 (tris-(dimethylaminomethyl) phenol);
 - 3:1, 1:1 and 1:3 ethanol:EMbed-812 epoxy solutions (prepare just before use);
 - Post-staining: 1% (w/v) uranyl acetate in 70% methanol.

2.5.1.3 Protocol

Ahead of time prepare: 0.1M PB solution; 2% (w/v) low melting point agarose; 30%, 50%, 70% and 90% ethanol dilutions; EPON I and EPON II resin stocks; Reynolds' lead citrate, and 1% uranyl acetate in 70% methanol solutions.

Due to the toxicity of the chemicals involved, steps 2 to 32 should be performed in a chemical fume hood (critical between steps 15 and 32). After the resin is fully polymerized, it is no longer toxic and the samples can be stored and manipulated in the normal laboratory environment indefinitely.

a. Sample preparation, first embedding and fixation (Figures 2.1A and B):

1. Label the microscope slide (1 per genotype), then, with the hydrophobic pen, draw small circles on it (8-12 circles per slide);

2. Prepare the "Fixative solution", and add a small drop of it to each small circle;

Tip: to reduce fixative evaporation, add the "Fixative" solution to one slide and, only after the plants are incubating, start another one.

3. Under the dissection stereo microscope, use the tweezers to dissect the top portion (apical shoot) of one *P. patens* gametophore (containing the gametangia), and add it to one of the fixative drops (arrow from Figure 2.1A to B);

4. Repeat step 3 until all fixative drops contain one apical shoot (Figure 2.1B);

Note: plant dissection must be performed carefully in order to avoid mechanical damages to the sexual structures, but also quickly to reduce sample desiccation.

Tip: make sure to remove all air bubbles from the samples, as they affect fixative penetration into the sample.

5. Transfer the sample slide to a humid chamber (or an equivalent method to reduce fixative evaporation while keeping the samples inside the chemical fume hood);

6. Incubate for 2hours at room temperature (RT);

Note: if more than one genotype is processed, repeat steps 1 to 6 individually for each one. However, be careful to fix each sample for 2hours.

7. Wash each gametophore twice with 0.1M PB for 10minutes at RT;

Tip 1: removal of the fixative and washing solution should be performed carefully, to avoid aspiration of the plant tissue.

Tip 2: shortly before the end of the washing steps, prepare the styrofoam box with ice, and melt the 2% low melting point agarose solution.

8. Melt the 2% low melting agarose solution and keep it melted (by incubating at 37°C in a dry heater, hot water bath or by an equivalent method);

9. Carefully aspirate the 0.1M PB solution from one of the gametophore-containing drops;

10. Slowly add melted 2% low melting agarose on top of the gametophore tissue (Figure 2.1B Agarose embedding);

Note: the tissue should be fully embedded by the agarose and without air bubbles.

11. Repeat steps 10 and 11 for all gametophores shoots;

12. Wait for the agarose to solidify;

Tip: This step might be accelerated by placing the microscope slides on ice for a few minutes.

13. Under a dissection stereo microscope, trim the agarose drop into smaller cubes, using a razor blade and a toothpick (Figure 2.1B Agarose embedding);

Note: trim the agarose to a minimal size, but make sure to retain the full gametophore tissue embedded in the trimmed cube.

14. With a small spatula and the aid of a toothpick, transfer the trimmed gametophyte-containing agarose cubes to a 1.5ml sample tube (Figure 2.1B Agarose embedding);

Note: all gametophores from the same genotype are collected in the same sample tube.

15. Prepare “Post-fixation” and 1% (w/v) uranyl acetate aqueous solutions;

Note: the reagents used to prepare these solutions are extremely toxic. Therefore, be extremely careful when preparing them.

16. Using a small glass Pasteur pipette, add 1ml of “Post-Fixation” solution to each sample tube, and incubate with gentle agitation for 2hours on ice (Figure 2.1B Post-fixation);

17. Wash the samples twice (for 5minutes each time) with 0.1M PB;

18. Wash the samples twice (5minutes each) with dH₂O;

19. Add 1ml of 1% (w/v) uranyl acetate aqueous solution to each sample (*En bloc staining*), and incubate with gentle agitation for 1hour at RT;

b. Sample dehydration, resin infiltration and final embedding (Figures 2.1B and D):

20. Incubate samples (with gentle agitation) in 30% ethanol dilution for 10minutes at RT (Figure 2.1B Dehydration);

21. Incubate samples (with gentle agitation) in 50% ethanol solution for 10minutes at RT;

22. Incubate the samples in 70% ethanol, with gentle agitation, overnight (12-16hours) at 4°C;

23. Incubate the samples (with gentle agitation) in 90% ethanol for 10minutes on ice;

24. Incubate the samples 3 times (for 15minutes each time), in 100% ethanol on ice and with gentle agitation;

25. Prepare the “EMbed-812 epoxy resin”, followed by the 3:1 ethanol:epoxy mixture;

26. Incubate the samples (with gentle agitation) in the 3:1 ethanol:epoxy solution for 90minutes at RT;

27. Prepare the 1:1 ethanol:epoxy mixture, add 1ml to each sample, and incubate (with gentle agitation) for 90minutes at RT;

28. Prepare the 1:3 ethanol:epoxy solution, add 1ml to each sample and incubate (with gentle horizontal agitation) for 90minutes at RT;

29. Incubate the samples (with gentle agitation) in EMbed-812 epoxy resin overnight at RT;

Tip: before proceeding to the next resin infiltration step (*i.e.* incubation with a higher resin concentration), confirm that the gametophore-containing agarose cubes sink within their current resin concentration. If not, extend the incubation time until the all agarose cubes sink.

30. Add epoxy resin to the corresponding wells of the flat embedding molds, add a unique identifier to each well (*e.g.* numbered paper label), and remove all air bubbles;

31. Remove all gametophore-containing agarose cubes from one sample, and place one gametophore within each well (Figure 2.1D);

Note: annotate the block identifiers corresponding to each sample/genotype.

Tip: it is possible to orient the gametophore according to the desirable sectioning angle. Gametophores oriented in parallel to the sectioning angle will yield longitudinal antheridia sections, while from the ones oriented perpendicularly, transversal sections are obtained (Figure 2.1D, insets).

32. Polymerize the gametophore-containing resin blocks by incubating them in an oven at 60°C-70°C for at least 24hours (Figure 2.1D);

c. Sectioning, post-staining and TEM imaging (Figures 2.1E, F and G):

33. In a ultramicrotome and with a razor blade, trim the gametophore region for sectioning, forming a small pyramid containing the region of interest;

34. Align the sample pyramid of resin block with the glass knife, and trim the sample;

Tip: regularly collect a semi-thin section and observe it under a regular light microscope. This will help to evaluate if the organs of interest are already being sectioned, and save time (as the first tissue-containing sections will contain only cells from leaf-like structures).

35. When the area of interest (*e.g.* antheridia) has been reached, carefully section the sample using a diamond knife, into ultrathin-sections (usually 70-100nm);

36. Collect the ultrathin samples into formvar coated palladium-copper slot grids (Figure 2.1E);

Note: if possible, allow the sections to dry on the grids for 12-16hours before proceeding to post-staining.

37. Post-stain the sections by incubating the grids in 1% (w/v) uranyl acetate in 70% methanol for 5minutes at RT (Figure 2.1F);

38. Wash each grid twice (1minute at RT) with dH₂O;

39. Incubate the grids with Reynolds' lead citrate solution for 5minutes at RT (Figure 2.1F);

40. Wash each grid twice (1minute at RT) with dH₂O;

Note 1: uranyl acetate reacts with light, and lead citrate reacts with carbon dioxide. Therefore, avoid exposing the samples by covering and not breathing directly onto them.

Note 2: ideally, post-staining sections should be allowed to dry overnight before imaging, to avoid staining precipitates.

41. Load the section-contains grids in a TEM microscope;

42. Image the cells/structures of interest (*e.g.* developing spermatids)

(Figure 2.1G).

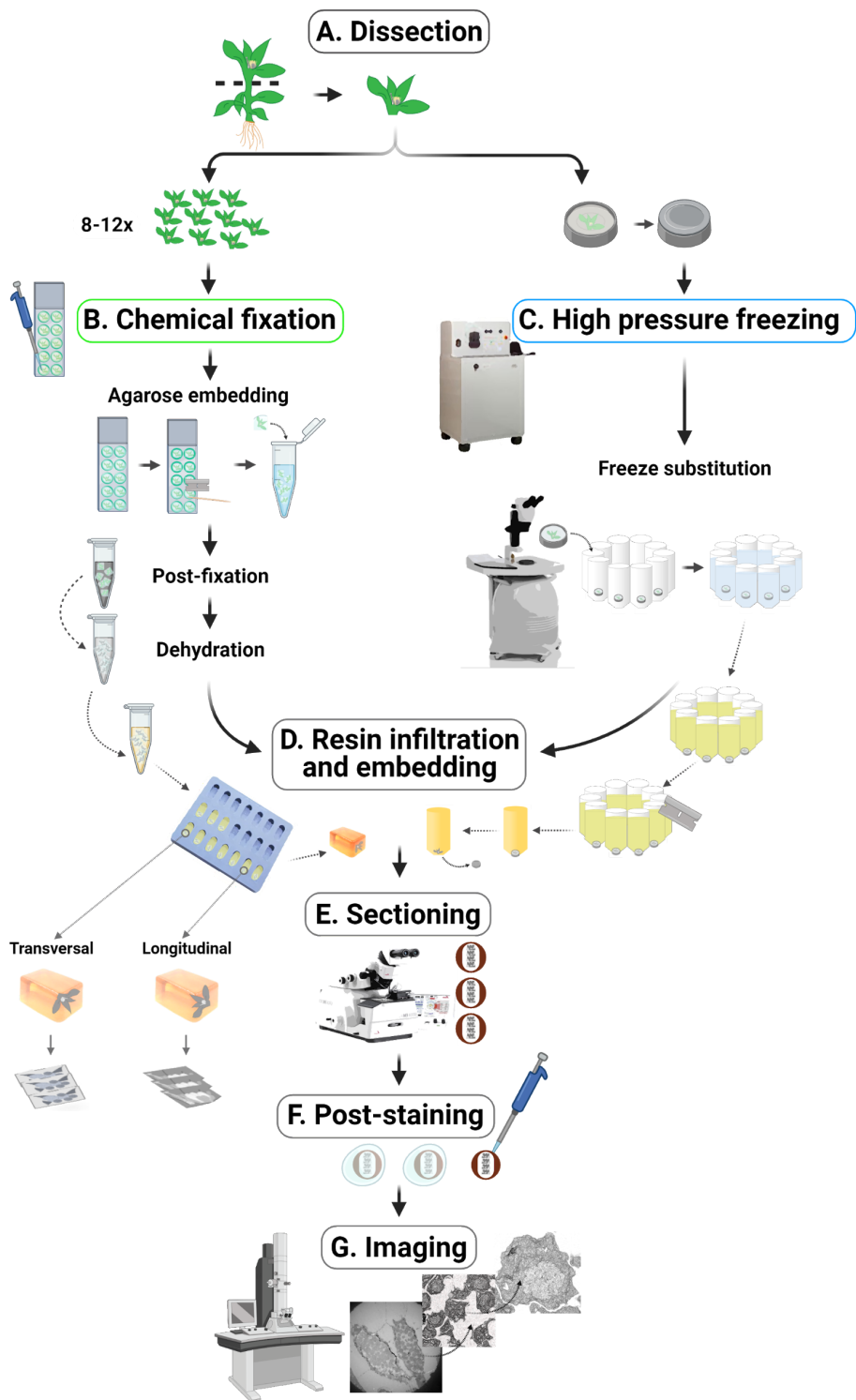


Figure 2.1: Protocols for transmission electron microscopy of *P. patens* spermatogenesis. **A.** Plant desiccation - the top region of the gametangia-containing gametophores are dissected. Then, 8-12 of them are chemically fixed (**B**) or each one is deposited in a specimen carrier containing “Cryoprotectant” solution (**C**); **B.** Chemical fixation of *P. patens* gametophores, followed by sample embedding in small agarose cubes, post-fixation and dehydration; **C.** High pressure freezing of gametangia containing carriers, which is then followed by the freeze substitution of the samples; **D.** Both chemically fixed or high pressure frozen samples are infiltrated in resin, before sample embedding and resin polymerization steps. Note that chemically fixed samples can be oriented within the embedding mold, defining the sample sectioning plane. **E.** Sectioning of the polymerized sample blocks, with samples being collected into palladium-copper slot grids; **F.** Sample sections are then post-stained before imaging; **G.** After drying, samples are ready for TEM imaging, allowing the collection of several levels of information (tissue, cellular and subcellular). Figure created with BioRender.com.

2.5.2 High pressure freezing followed by freeze substitution (HPF+FS)

2.5.2.1 Material and equipment

- Micropipettes and respective disposable tips;
- Chemical fume hood;
- Dissection stereo microscope (e.g. Olympus SZX7);
- Tweezers;
- Plant gametophores;
- Aluminium specimen carriers (e.g. Wohlwend specimen carrier Type A #241 and Type B #242);
- High Pressure Freezer (HPF) (e.g. Wohlwend High Pressure Freezer Compact 02);

- Liquid nitrogen sample storage tank (e.g. Cryo Dewar Specimen Storage Refrigerator 81750-35VHC);
 - Styrofoam box;
 - Liquid nitrogen;
 - Automated freeze substitution (AFS) processor (e.g. Leica EM AFS2);
 - Consumables for AFS (e.g. carrier for embedding inserts and embedding inserts);
 - Orbital shaker (e.g. Rotamax 120 Orbital Shaker);
 - 60°C-70°C oven (e.g. MRC PF60-SC);
 - Razor blade (e.g. Feather E72002-10);
 - Ultramicrotome (e.g. Leica UC7);
 - Glass knife (homemade);
 - Diamond knife (e.g. Diatome DU4515);
 - Slot palladium-copper grids (coated with 1% formvar in chloroform);
 - TEM microscope (e.g. Hitachi H-7650 with AMT 2kX2k digital camera).

2.5.2.2 Reagents and solutions

- Reynolds' lead citrate;
- Cryoprotectant: 10% BSA (bovine serum albumin) in 8% methanol;
 - Freeze substitution: 1% (w/v) osmium tetroxide, 0.2% (w/v) uranyl acetate in methanol, 1% (v/v) dH₂O in acetone (prepare fresh);
 - EMbed-812 epoxy resin (see 2.5.1.2; prepare fresh);
 - 5%, 10%, 25%, 50% and 75% epoxy resin solution in acetone (prepare just before use);
 - 1% (w/v) uranyl acetate in 70% methanol.

2.5.2.3 Protocol

Before starting, prepare: EPON I and EPON II resin stocks; Reynolds' lead citrate and 1% (w/v) uranyl acetate solutions.

Due to the toxicity of the chemicals involved, steps 1 to 24 should be performed in a chemical fume hood (critical during the preparation and manipulation of the "Freeze substitution" solution and between steps 14 and 24). After the resin is fully polymerized, it is no longer toxic and the samples can be stored and manipulated in the normal laboratory environment indefinitely.

a. Sample preparation and high pressure freezing (Figures 2.1A and C):

1. Prepare the "Cryoprotectant" solution;
2. Add 1 μ l of the "Cryoprotectant" solution to the bottom of a type A specimen carrier side 0.2 μ m;

Tip: pipette carefully and avoid creating air bubbles.

3. Under the dissection stereo microscope, use the tweezers to dissect the top portion (apical shoot) of one *P. patens* gametophore (containing the gametangia) (Figure 2.1A);

4. Place the dissected gametophore shoot into the carrier containing "Cryoprotectant" solution (arrow from Figure 2.1A to C);

5. Fill the carrier with more "Cryoprotectant" solution and carefully remove all air bubbles;

Note: the plant tissue should be fully embedded into "Cryoprotectant" and no air bubbles should be visible, as these air bubbles will expand during the freezing step and damage the sample.

6. Close the carrier with a type B specimen carrier flat side, and insert it into the HPF holder (arrow from Figure 2.1A to C);

7. Freeze the sample in the HPF (2000bar; -196°C) (Figure 2.1C);

Note: high pressure frozen samples can be stored for long periods of time in a liquid nitrogen storage tank.

b. Freeze substitution, resin infiltration and embedding (Figures 2.1C and D):

8. Prepare the “Freeze substitution” solution, and pre-cool the AFS chamber to -90°C;

9. Program the AFS with the following settings:

- 1 hour at -90°C;
- warm-up to -80°C (slope of 5°C/hour);
- 72 hours at -80°C;
- warm-up until 0°C (slope of 1.7°C/hour);
- 3 rounds of: 10 minutes in 100% acetone at 0°C.

10. In a styrofoam box and under liquid nitrogen, transfer the frozen samples to the pre-cooled AFS processing chamber;

11. In the AFS chamber and using tweezers, carefully open the specimen carriers and place the type A specimen carrier (containing the sample) in each of the sample embedding inserts (Figure 2.1C Freeze substitution);

Note: this is a critical step that should be performed with extreme caution, as when opening the specimen carriers the sample might be lost.

12. Add 1ml of the “Freeze substitution” solution to each of the sample embedding inserts (Figure 2.1C Freeze substitution);

13. Start the AFS program set on step 9;

14. Upon completion of the AFS program, prepare the EMbed-812 epoxy resin and its 5% dilution in 100% acetone;

15. Remove the sample embedding inserts from the AFS chamber and into a chemical fume hood;

16. Add the 5% epoxy-acetone mixture to each of the sample inserts, and incubate for (at least) 4h at RT with gentle agitation;

17. Prepare the 10% epoxy-acetone solution, add it to the inserts, and incubate for (at least) 4h at RT with gentle agitation;

18. Prepare the 25% epoxy-acetone solution, add it to the sample inserts, and incubate for (at least) 4h at RT with gentle agitation;

19. Prepare the 50% epoxy-acetone solution, add it to the sample plastic inserts, and incubate for (at least) 4h at RT with gentle agitation;

20. Prepare the 75% epoxy-acetone solution, add it to the carrier containing inserts, and incubate for (at least) 4h at RT with gentle agitation;

21. Add the 100% EMBED-812 epoxy resin solution to the sample inserts, and incubate for (at least) 4h at RT with gentle agitation;

22. Replace the EMBED-812 resin in each sample and, with a tweezer, carefully push the sample-containing carriers to the bottom of the insert (Figure 2.1C Freeze substitution);

Note: as the aluminum carrier will be removed from the polymerized block prior to sample sectioning, the open sample-containing surface should be left upright, facing the inwards of the resin block, while the aluminium surface of the carrier should face the bottom of the well.

23. Remove all air bubbles from within each of the resin-containing inserts;

24. Polymerize the resin by incubating the inserts at 60°C-70°C for at least 24hours;

c. Sectioning, post-staining and TEM imaging (Figures 2.1D - G):

25. Before proceeding to sectioning, cut the plastic inserts with a razor blade then, carefully remove the metal specimen carrier from the blocks (Figure 2.1 arrows from C to D);

26. Section, post-stain and image the samples as in section 2.5.1.3 steps 33-42 (Figures 2.1E - G).

2.6 Light microscopy approaches for *P. patens* sperm cells

Light microscopy techniques can provide molecular information related to cell/tissue organization and molecular composition (e.g. immunohistochemistry), as well as enable studies on dynamic processes in real time (live imaging), thus overcoming two major limitations of transmission electron microscopy. Immunohistochemistry techniques, such as immunofluorescence, rely on the use of antibodies and their recognition of particular proteins (antigens) (Ramos-Vara, 2005; Sanderson et al., 2019). These specific interactions enable the recognition of the antigens of interest, revealing their localization within cells and tissues. Here, I describe an immunostaining protocol for indirect immunofluorescence of *P. patens* gametangia cryosections (section 2.6.1) or individualized sperm cells (section 2.6.2). However, these protocols rely on fixed samples, with released sperm cells being lost during sample preparation (fixation and washes). Therefore, and in order to study dynamic events, namely sperm cell motility, I have optimized the previously described protocols (Horst and Reski, 2017; Ortiz-Ramírez et al., 2017) to enable qualitative and quantitative assessment of naturally released sperm cell packages (section 2.6.3).

2.6.1 Immunofluorescence of tissue cryosections

2.6.1.1 Material and equipment

- Chemical fume hood;
- Micropipettes and respective disposable tips;

- Dissection stereo microscope (e.g. Olympus SZX7);
- Tweezers;
- Plant gametophores;
- 1.5ml sample tubes (e.g. 1.5ml eppendorf tubes) - only required if samples are sectioned post-fixation (*preferential*);
- Rotary shaker (e.g. IKA Loopster digital 14033);
- Optional Cutting Temperature (OCT) compound (e.g. Sakura Tissue-Tek #4583);
- Small cryostat plastic disposable molds (e.g. Fisherbrand #22-363-553);
- Liquid nitrogen and respective container;
- Cryostat (e.g. Leica Cryostat CM 3050 S);
- Positively charged glass slides (e.g. Thermo Scientific SuperFrost Plus Adhesion slides #10149870);
- Hydrophobic pen (e.g. Dako pen);
- Humid (dark) chamber (or equivalent way to avoid solution evaporation);
- 60x24mm coverslips (e.g. Marienfeld #0101244);
- Nail polish;
- Light microscope (widefield, confocal (e.g. Leica SP5 Live), or 3D-SIM).

2.6.1.2 Reagents and solutions

- Deionized distilled water (ddH₂O) (MilliQ);
- 1x Phosphate-buffered saline (PBS): 137mM NaCl, 2.7mM KCl, 10mM Na₂HPO₄, 1.8mM KH₂PO₄ in ddH₂O, pH 7.4;
- Fixative: 4% methanol-free formaldehyde (Polysciences), 1mM MgCl₂, 50mM EGTA (ethylene glycol tetraacetic acid), 0.2% NP-40 (nonidet P-40), 1% Triton-X, 119µl/ml ddH₂O in 1x PBS (prepare in a chemical fume hood);

- Wash buffer: 0.1% NP-40, 0.5% Triton-X in 1x PBS;
- Fixative b (*alternative - Figure 2.2 dashed arrows*): 4% methanol-free formaldehyde (Polysciences), 1mM MgCl₂, 50mM EGTA, 0.1% NP-40, 0.5% Triton-X, 134µl/ml ddH₂O in 1x PBS (prepare in a chemical fume hood);

- Block buffer: 5% BSA in 1x “Wash buffer” (prepare fresh);
- Primary antibody: 1:1000 anti-acetylated- α -tubulin (Sigma-Aldrich #T7451) in “Block buffer” (prepare immediately before use);

Note: different primary antibodies can be used, however they might require optimization of optimal concentration.

- Secondary antibody: 1:500 anti-mouse-cy5 (Life Technologies A21236) in “Block buffer” (prepare immediately before use);

Note: different secondary antibodies, and/or different coupled fluorophores can be used, yet they might require optimization of optimal concentration.

- DAPI dilution: 1:1000 4',6-diamidino-2-phenylindole (DAPI) in 1x PBS (prepare immediately before use);

- Mounting medium (*e.g.* Vectashield - non hardening; or Dako Faramount Aq - hardening mounting media).

2.6.1.3 Protocol

a. Cryostat sectioning of pre-fixed gametangia samples (preferential, Figure 2.2B continuous lines):

1. Prepare the “Fixative” and “Wash buffer” solutions;
2. Add 1ml of “Fixative” solution to each 1.5ml sample tubes (1 per sample/genotype);
3. Per sample, dissect 10-12 top portions of *P. patens* gametophores (containing the gametangia), and add them to the corresponding 1.5ml sample tube, containing the “Fixative” solution (Figure 2.2A);

4. Incubate samples with rotary agitation (approximately 40rpm), overnight (12-16hours) at 4°C or 2hours at RT;

5. Wash the samples twice (for 10minutes at RT) with 1ml of “Wash buffer” with rotary agitation;

Note: fixed gametophore samples can be stored (in the dark) at 4°C for short periods of time (days/weeks).

Tip: be careful when removing the solution from the 1.5ml sample tubes, to avoid aspirating the gametophore samples. A 200µl disposable micropipette tip can be used to avoid this issue.

6. Label one small Cryostat plastic disposable mold per sample, and add optimal cutting temperature compound (OCT) to the sample chamber of the molds;

7. Transfer the fixed gametangia-containing gametophore shoots of one sample to the corresponding OCT-containing chamber mold, and carefully remove all air bubbles within the sample (Figure 2.2B Embedding in cryomolds);

Note: the gametophore shoots can be oriented within the OCT. Orienting samples in parallel (longitudinally) to the sectioning plane will yield more cells from a low number of antheridia, while transversely oriented gametangia will result in less cells from more organs within the same cryosection (Figure 2.2B inset).

8. Carefully freeze the OCT-embedded sample by placing the bottom of the disposable mold in contact with liquid nitrogen, until the OCT appears fully solidified;

9. Repeat steps 7 and 8 individually per each sample;

Note: samples frozen within OCT blocks can be stored at -20°C for short periods (some days/weeks) or -80°C for longer periods of time (months/years).

10. Set the Cryostat chamber temperature to -22°C and the object temperature to -18°C;

11. Remove the frozen OCT sample-containing block from the disposable plastic mold, and align the block with the Cryostat's blade;

12. Trim the frozen OCT block until the gametangia region is reached;

Tip: during trimming, it might be useful to regularly collect sections into a normal microscope slide and observe them under a light microscope, as this allows an evaluation of when the organs of interest are reached.

13. When the tissues/organs of interest are found, collect the cryosections into positively charged microscope slides (Figure 2.2B Cryosectioning);

Note: other coated microscope slides/coverslips (e.g. poly-L-lysine) can be used, however, *P. patens* antheridia appear to attach better to the positively charged slides than to poly-L-lysine coated ones.

14. Using a hydrophobic pen, draw a border around the slide region containing the tissue sections;

15. Air dry the sample and then, transfer it to a humid chamber;

Note: if any of the genotypes being stained contain endogenous fluorescence signals, the samples must always be kept in the dark.

16. Repeat steps 11 to 15 for each individual sample to be stained;

17. Incubate the samples 3 times (10minutes at RT) with "Wash" buffer;

18. Proceed to the immunostaining protocol (2.6.1.3.c, Figure 2.2D);

b. Cryostat sectioning non-fixed gametangia samples (alternative - Figure 2.2B dashed arrows):

1. Label one small cryostat plastic disposable mold per sample, and add optional cutting temperature compound (OCT) to the sample chamber of the molds;

2. Per sample, dissect 10-12 top portions of *P. patens* gametophores (containing the gametangia), and add place place them in

the corresponding OCT-containing chamber mold (dashed arrow from Figure 2.2A to B);

3. Carefully remove all air bubbles within the OCT;

Note: the gametophore shoots can be oriented within the OCT, as described in step 7a.

4. Carefully freeze the OCT-embedded sample by placing the bottom of the disposable mold in contact with liquid nitrogen, until the OCT appears fully solidified;

5. Repeat steps b2 to b4 individually per each sample;

Note: samples frozen within OCT blocks can be stored at -20°C for short periods (some days/weeks) or -80°C for longer periods of time (months/years).

6. Section each sample individually as in steps a10 to a13;

Note: as tissues are not yet fixed, always keep the section-containing slides within the Cryostat -22°C chamber, to avoid antigen degradation.

7. Using a hydrophobic pen, draw a border around the slide region containing the tissue sections;

8. Prepare the “Fixative b” solution;

9. Place the samples in (dark) humid chamber, and add to each of the sample-containing slides the “Fixative b” solution (Figure 2.2B Fixation);

Note: the volume of fixative solution to be added will vary according to the size of the section-containing region.

10. Incubate the samples for 1hour at 4°C;

11. Wash the samples 3 times (10minutes at RT) with “Wash” buffer;

12. Proceed to the immunostaining protocol (2.6.1.3.c, Figure 2.2D);

c. *Immunostaining* (Figure 2.2D):

Note: all of these steps should be performed in a humid chamber (reducing solution evaporation), and if any of the samples contain

endogenous fluorescent markers, these should always be kept in the dark (to avoid loss of any fluorescent signal).

1. Prepare the “Block buffer” solution;
2. Incubate the samples in “Block buffer” for 1 hour at RT;
3. Prepare the “Primary antibody” dilution, and add it to the samples;
4. Incubate the samples with the “Primary antibody” solution for 2 hours at RT, or overnight (12-16h) at 4°C;
5. Incubate the samples 3 times in “Block buffer”, for 10 minutes at RT each time;
6. Prepare the “Secondary antibody” dilution, and incubate the samples with it for 1 hour at RT;
7. Wash the sample 3 times (10 minutes at RT each time) with “Wash buffer”;
8. Prepare the DAPI 1:1000 dilution, and incubate the samples with it for 30 minutes at RT;

Note: it is possible to reduce the time for DAPI staining if incubated with a higher concentration (e.g. 1:500 DAPI for 15 minutes).

9. Incubate the samples twice (10 minutes at RT) with 1x PBS;
10. Replace the 1x PBS solution with ddH₂O, and incubate for 5 minutes at RT;
11. Remove the ddH₂O;

Tip: in order to remove the ddH₂O totally, samples can be left to air dry for a few minutes.

12. Add a few drops of mounting medium (e.g. Dako Faramount Aq) to each sample, and spread it over the section-containing region of the microscope slides;

Note: both non-hardening (e.g. Vectashield) and hardening (e.g. Dako Faramount Aq) can be used, yet they provide different advantages/disadvantages to the imaging process. One must therefore

choose the mounting solution best suited to the purpose of the experiment/imaging technique.

13. Cover the tissue-containing microscope slides with a 60x24mm coverslip;

Note: if non-hardening mounting media (e.g. Vectashield) are used, the excessive medium must be removed from the sample.

14. Seal the microscope slide-coverslip with nail polish (only if non-hardening media was used);

15. Proceed with light imaging of the stained cryosections.

Note: if a non-hardening medium is used, store the samples in the dark at 4°C at least overnight, and image the samples as soon as possible. If a hardening medium is used, allow the media to fully polymerize before imaging.

d. Imaging (Figure 2.2E):

The protocol described above is compatible with a wide range of light microscopy techniques. However, due to the tissue architecture, the sperm cells within one antheridium are very close together, making it difficult to obtain information at the single-cell level. This raises problems for some microscopy techniques, such as widefield microscope, where the signal from multiple cells will be captured simultaneously. The close proximity of several cells and signals of interest also creates problems (e.g. signal misalignments) during image reconstruction by 3D structured illumination microscopy (3D-SIM) when reconstructing multiple cells within the same image.

The steps described below are standard for confocal light microscopy, a valuable and approachable solution for imaging of cryosections of various tissues/organisms:

16. Load the sample in the microscope and, using a low magnification objective (10 or 20x) focus the sample;

17. Scan through the sample and store the positions containing regions of interest;

18. Change to a higher magnification objective (*e.g.* 63x);

Note: higher resolution objectives sometimes require particular immersion media (*e.g.* oil), make sure to add it to the sample before proceeding.

19. Select the region to image (*e.g.* organ/cells) and set the imaging parameters (*e.g.* z limits, channels and respective intensities);

Note: cytodifferentiated sperm cells contain very condensed chromatin, which might saturate the 405nm (DAPI) channel. When acquiring regions containing these cells, check for signal saturation prior to acquisition and, if needed, adjust the laser intensity accordingly.

20. Acquire the selected region;

21. Repeat steps 37 and 38 for the several marked regions/sections.

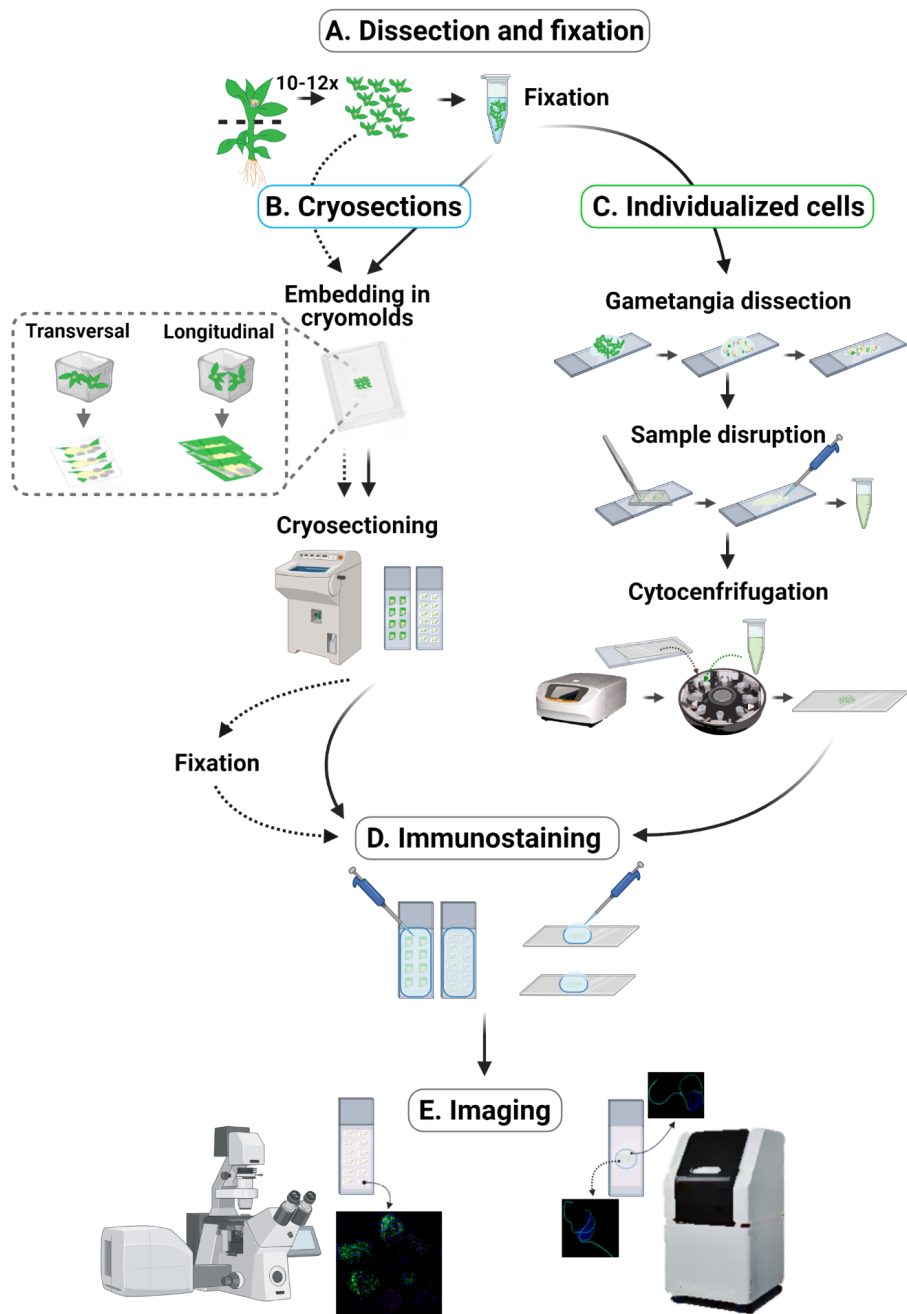


Figure 2.2: Protocols for immunofluorescence of *P. patens* developing spermatids. A. Plant desiccation and fixation - the top

portions of several gametangia-containing gametophores are dissected and fixed (with 4% formaldehyde); **B.** The fixed gametophores are then embedded into OCT containing plastic molds (cryomolds) and frozen. Note that it is possible to orient the gametophores according to the sectioning angle desirable (inset). The frozen samples are then sectioned in a cryostat and the sample sections collected into positively charged microscope slides. Alternatively (dashed arrows), non-fixed gametophores may also be embedded directly into the OCT cryomolds. In this situation, samples need to be fixed before the immunostaining; **C.** Fixed gametophore samples might also be further dissected and disrupted in order to isolate individual spermatids, which are then centrifuged onto a coverslip; **D.** Immunostaining of *P. patens* cryosections or individualized cells; **E.** After incubation of the samples in the mounting media, samples can be imaged in a wide range of light microscopes. Note that while the cryostat sections yield tissue-wide images, the isolated cells will be spread in the area where they were centrifuged into, and all tissue-context information is lost. Figure created with BioRender.com.

2.6.2 Immunofluorescence of individualized cells

2.6.2.1 Material and equipment

- Chemical fume hood;
- Micropipettes and respective disposable tips;
- Dissection stereo microscope (e.g. Olympus SZX7);
- Tweezers;
- Plant gametophores;
- 1.5ml sample tubes (e.g. 1.5ml eppendorf tubes);
- Rotary shaker (e.g. IKA Loopster digital 14033);
- Hydrophobic pen (e.g. Dako pen);
- Microscope slides;

- Small squared microscope coverslips (e.g. 22x22mm Marienfeld #0101053);
- Cytocentrifuge and respective sample adaptors (e.g. Cytopro Series 2);
- 60x24mm coverslips (e.g. Marienfeld #0101244);
- Humid (dark) chamber (or equivalent way to avoid solution evaporation);
- Nail polish;
- Light microscope (widefield, confocal, or 3D-SIM (e.g. Deltavision OMX)).

2.6.2.2 Reagents and solutions

- 1x PBS (see 2.6.1.2);
- Fixative 4% methanol-free formaldehyde (Polysciences), 1mM MgCl₂, 50mM EGTA, 0.2% NP-40, 1% Triton-X, 119µl/ml ddH₂O in 1x PBS (prepare in a chemical fume hood);
- Wash buffer (see 2.6.1.2);
- Block buffer (see 2.6.1.2; prepare fresh);
- Primary antibody (see 2.6.1.2; prepare immediately before use);
- Secondary antibody (see 2.6.1.2; prepare immediately before use);
- DAPI dilution (see 2.6.1.2; prepare immediately before use);
- Mounting medium (e.g. Vectashield - non hardening (preferential), or Dako Faramount Aq - hardening mounting media).

2.6.2.3 Protocol

a. Sample preparation (Figures 2.2A and C):

1. Prepare the “Fixative” and “Wash buffer” solutions;
2. Add 1ml of “Fixative” solution to each 1.5ml sample tubes (1 per sample/genotype);

3. Per sample, dissect 10-12 top portions of *P. patens* gametophores (containing the gametangia), and add them to the corresponding 1.5ml sample tube, containing the “Fixative” solution (Figure 2.2A);

4. Incubate samples with rotary agitation (approximately 40rpm), overnight (12-16hours) at 4°C or 2hours at RT;

5. Wash the samples twice (for 10minutes at RT) with 1ml of “Wash buffer” with rotary agitation;

Note: fixed gametophore samples can be stored (in the dark) at 4°C for short periods of time (days/weeks).

Tip: be careful when removing the solution from the 1.5ml sample tubes, to avoid aspirating the gametophore samples. A 200µl disposable micropipette tip can be used to avoid this issue.

6. Label one microscope slide and a 1.5ml sample tube per sample/genotype;

7. Draw a circle with a hydrophobic pen in each microscope sample slide;

8. Add one drop of 1x PBS to the hydrophobic circle within one slide;

9. With a tweezer, transfer the fixed gametophore shoots from the corresponding sample to the 1x PBS solution in the slide (Figure 2.2C Gametangia dissection);

10. Under a stereo microscope, carefully dissect the gametangia further, removing all the tissue debris possible (e.g. leaf-like structures, archegonia, paraphysis) and isolating the individual antheridia as much as possible (Figure 2.2C Gametangia dissection);

Tip: the first part of this dissection can be performed in another slide (or another region within the same slide), and the gametangia can be then carefully transferred to the hydrophobic circle.

11. Remove the excess 1x PBS solution, leaving only a small film around the tissues of interest (Figure 2.2C Gametangia dissection);

12. Add a small squared coverslip (e.g. 22x22mm) to the top of the 1x PBS film;

13. With the tweezers, apply pressure in the coverslip, squashing the sample between the slide and the coverslip. Stop whenever no visible organ architecture can be identified (Figure 2.2C Sample disruption);

Note: be careful not to break the coverslip and yet, apply enough force to completely destroy the organs.

Tip: perform this step while looking at the sample through the dissection stereo microscope.

14. With one tweezer, carefully dismount the coverslip from the microscope slide;

15. Add 100µl of 1x PBS solution to the hydrophobic circle region, and homogenize carefully (by slowly pipetting up-and-down) (Figure 2.2C Sample disruption);

Note: To reduce sample loss, a similar homogenization process can be performed in the coverslip, using the same 100µl of 1x PBS solution.

Tip 1: sometimes the hydrophobic circle gets damaged during tissue disruption. Therefore, perform homogenization carefully to avoid spreading the 1x PBS solution over the sample-containing region.

Tip 2: This step might also be performed while observing the sample in the stereo microscope, confirming the collection of all visible tissue debris.

16. Place the homogenized solution (containing isolated cells) in the previously labeled (step 6) 1.5ml sample collection tube (Figure 2.2C Sample disruption);

17. Repeat steps 8 to 16 for all remaining samples;

18. Label one 60x24mm coverslip per sample/genotype, assemble the coverslips and the corresponding cytocentrifuge sample adaptors in a cytocentrifuge (Figure 2.2C Cytocentrifugation);

Note: Samples can also be directly centrifuged to positively charged (or similar) microscope slides (however, this is not recommended for super resolution microscopy, as it will increase the distance between the cells and the coverslips).

Tip: some cytocentrifuges might not be appropriate for direct centrifugation into coverslips. One way around this issue is to add a normal microscope slide behind each coverslip.

19. Add 50 μ l of 1x PBS solution to each sample chambers, and centrifuge the solution into the coverslips for 1minute at 1000g;

20. Add each of the disrupted sample solutions (obtained in step 16) to the corresponding sample/coverslip chamber (Figure 2.2C Cytocentrifugation);

21. Centrifuge the cells for 7minutes at 500g (with slow acceleration/slowing speed);

Note: the standard centrifugation step of 5minutes can be used. However, this significantly reduces the number of mitotic and streamlined (mature) sperm cells detected within the final samples.

22. Carefully remove the sample adaptors and coverslips, without disturbing the sample-containing region;

23. Air dry the samples, and then transfer them to the humid (dark) chamber for staining (arrow from Figure 2.2C Cytocentrifugation to D).

b. Immunostaining (Figure 2.2D):

Note: from this step onwards, all sample manipulations should be performed carefully and samples deposited/aspirated slowly, to avoid detaching the cells from the coverslip.

Tip: although not required, it might be useful to delimit the sample-containing region of the coverslip with the hydrophobic pen. This will help contain the staining solutions, but also in the imaging step (by marking the cell-containing region).

24. Incubate the sample twice (10minutes at RT) with “Wash buffer”;

25. Prepare the “Block buffer” solution, and incubate cells with it for 1hour at RT;

26. Prepare the “Primary antibody” dilution, and add it to the samples;

27. Incubate the samples with the “Primary antibody” solution for 2hours at RT, or overnight (12-16h) at 4°C;

28. Incubate the samples 3 times (10minutes at RT each time) in “Block buffer”;

29. Prepare the “Secondary antibody” dilution, and incubate the samples with it for 1hour at RT;

30. Wash the sample 3 times (10minutes at RT each time) with “Wash buffer”;

31. Prepare the DAPI 1:1000 dilution, and incubate the samples with it for 30minutes at RT;

Note: it is possible to reduce the time for DAPI staining if incubated with a higher concentration (e.g. 1:500 DAPI for 15minutes).

32. Incubate the samples twice (10minutes at RT) with 1x PBS;

33. Replace the 1x PBS solution with ddH₂O, and incubate for 5minutes at RT;

34. Remove the ddH₂O;

Tip: in order to remove the ddH₂O totally, air dry the samples for a few minutes.

35. Add 1-2 droplets of mounting medium (e.g. Vectashield) to the middle of each sample;

Note: depending on the imaging technique to be performed, non-hardening (e.g. Vectashield) or hardening (e.g. Dako Faramount Aq) can be used.

36. Cover the coverslip with a microscope slide;

Note: if the samples were centrifuged into a microscope slide, cover them with a coverslip. If a non-hardening mounting medium is used, remove its excess from the sample.

37. If a non-hardening media was used, seal the microscope slide-coverslip with nail polish;

38. Proceed with light imaging of the isolated cells stained.

Note: if a non-hardening medium is used, store the samples in the dark at 4°C at least overnight, and image the samples as soon as possible. If a hardening medium is used, allow the media to fully polymerize before imaging.

c. Imaging (Figure 2.2E):

The samples containing individualized sperm cells can be imaged in a wide variety of microscopes. However, the main advantage of having these isolated cells is to characterize them with the best resolution possible. Therefore, the steps herein described are tailored to perform 3D-SIM using the commercial Deltavision OMX system. However, they may be adapted for other imaging systems.

Note: for 3D-SIM imaging, it is recommended that the samples are embedded in a non-hardening mounting medium, as the polymerization or hardening media will affect the sample's dimensions (particularly its thickness).

39. Add the corresponding oil to the objective, and load the sample in the microscope with the coverslip facing the objective;

40. Adjust the sample's position relative to the objective to the middle of sample-circle (delimited by the hydrophobic pen);

41. Focus the sample;

42. Acquire a spiral mosaic using a 1024x1024 field of view and the 405nm (DAPI) channel;

Note: other channels might replace, or be used in combination, with the 405nm channel. However, be careful not to bleach the signal of interest.

43. In the mosaic window identify the single isolated sperm cell;

44. Visit the corresponding cell and adjust the acquisition parameters (e.g. field of view, z limits, appropriate channels);

Note: make sure the acquisition is set for the SI (structured illumination) mode.

45. Acquire the image stacks;

46. Repeat steps 6-8 as many times as required;

47. Reconstruct the images using Applied Precision's softWorx software.

2.6.3 Live imaging of discharged sperm cells

2.6.3.1 Material, reagents and equipment

- Micropipettes and respective disposable tips;
- 60x24mm coverslips (e.g. Marienfeld #0101244);
- Dissection stereo microscope (e.g. Olympus SZX7);
- Tweezers;
- Plant gametophores (15+ DAI);
- Inverted light microscope (preferentially widefield, (e.g. Nikon HCS));
- Fluorescein diacetate (e.g. Sigma-Aldrich F7378; optional).

2.6.3.2 Solutions

- Sperm cell media (Ortiz-Ramírez et al., 2017): 0.45mM CaCl₂, 0.3mM MgSO₄, 0.02mM KNO₃, 0.081mM NaHCO₃ in ddH₂O (prepare fresh).

2.6.3.3 Protocol

This protocol enables both qualitative assessment, *i.e.* to distinguish motile from immotile sperm cells, as well as more quantitative analyses.

a. Sample preparation and live imaging (Figure 2.3A):

1. Prepare “sperm cell media” solution;

Note: for a qualitative assessment of motility, supplement the “sperm cell media” with 1µg/mL of fluorescein diacetate (FDA). This will report viable (green fluorescent) cells, allowing to distinguish dead (non fluorescent) from immotile (viable and green fluorescent) sperm cells.

2. Add 30-50µl of “sperm cell media” to a 60x24mm coverslip;

Note: samples can be prepared on microscope slides, however, as these are hydrophilic, a way to restrict the spreading of the media needs to be introduced (*e.g.* hydrophobic pen).

3. Dissect 5-10 *P. patens* gametophore shoots, and add them to the “sperm cell media” drop in the coverslip;

Note: samples can contain a variable number of gametangia clusters, yet, one needs to balance the number of sperm cell clusters released and the tissue debris left within the sample.

4. Using tweezers and under a stereo microscope, carefully dissect further the gametangia clusters from the leaf-like structures, within the “sperm cell media” drop;

Tip: tissue debris (*e.g.* leaf-like structures) can be carefully removed from the sample using tweezers.

5. Proceed to live imaging;

Note 1: as sperm cells only survive for 30-40minutes, and in order to give sufficient time for imaging, sample preparation should not take longer than 10-15minutes.

Note 2: after being discharged from the antheridia, sperm cells take 1-2minutes to start moving. Take that into consideration when imaging freshly released clusters or sperm cells.

Tip: while confocal microscopes can be used and offer better z resolution, due to the loss of out-of-focus information, it is easier to distinguish the sperm cells and their cilia/flagella by widefield microscopy.

6. Load the samples into (preferable) a widefield inverted microscope, and screen through the sample using a 20x objective, or equivalent;

7. Identify released sperm cell packages and proceed to the respective data acquisition;

b. Data acquisition for a qualitative analysis (Figure 2.3B):

Note: the “sperm cell media” solution should be supplemented with FDA prior to sample preparation. This dye will penetrate viable cells and render them fluorescent in the green (488nm) channel, while dead sperm cells will remain non fluorescent.

1. Acquire timelapse series (1-2minutes) of the whole cluster, using both 488nm (green) and brightfield channels and at a relatively low frame rate (e.g. 30 frames per second - FPS);

2. Analyze the images obtained and observe cell displacement over time. In packages composed of motile sperm cells, and due to the beating of their cilia/flagella, cells will move away from the remaining ones (Figure 2.3B motile). Clusters of immotile sperm cells will remain somewhat similar throughout time (Figure 2.3B immotile), with only diffusion or sample-wide changes being detected.

c. Data acquisition for quantitative analyses (Figure 2.3C)

1. Change to a higher magnification objective (e.g. 63x), and decrease the field of view (e.g. 512x512 pixels);

2. Set acquisition parameters for the desirable duration (e.g. 1minute) of a single-frame brightfield acquisition, with the highest time resolution possible (e.g. 200FPS);

Note: other channels can also be acquired, but they may render the imaging slower, reducing temporal resolution.

3. Focus the field of view in single sperm cell and start the acquisition (Figure 2.3C);

Note: due to the cell's movements in the 3D space, it might be required to manually adjust xyz planes throughout acquisition. However, some analyses (e.g. exact distances) may be incompatible with such adjustments. In those cases, it might be better to increase the field of view, at the expense of 2D resolution.

4. Re-focus the field of view onto a different cell and repeat acquisition (Figure 2.3C);

5. Analyze the time series obtained according to the experimental goal (Figure 2.3C).

Note: several quantifications can be obtained from the analysis resulting from such protocol, including sperm cell speed (distance/time), movement directionality (cell position over time) and ciliary/flagellar beating (cilia tracking/time).

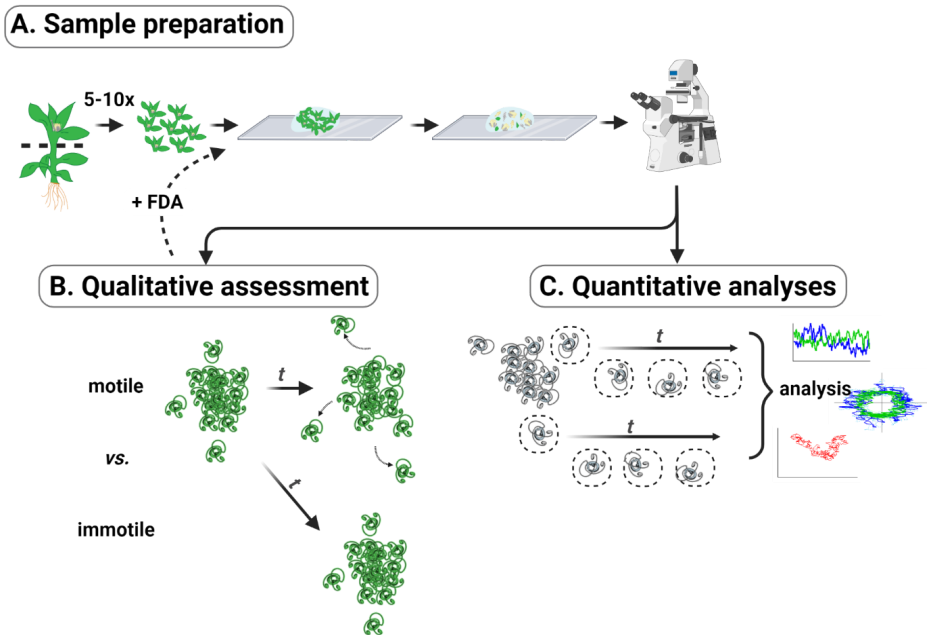


Figure 2.3: Assays for qualitative and quantitative analyses of *P. patens* sperm cell motility. **A.** Each sample contains 5 to 10 dissected gametangia clusters in the “sperm cell media” solution. Sperm cell clusters can be easily observed and imaged in a regular widefield inverted microscope; **B.** For a qualitative analysis of motility, *i.e.* to distinguish motile from imotile sperm cell packages, just record the movements from the whole sperm cell cluster for a period of time (*e.g.* 1minute) and observe the displacement (or not) of single individual cells from these released clusters. Note that, if FDA is previously added into the “sperm cell media”, viable cells can be distinguished from dead cells, as the latter will not have significant green fluorescence (this might be particularly useful to distinguish immotile from dead cells); **C.** In order to enable quantitative analyses (*e.g.* tracking of cell’s directionality and movement speed), the imaging field of view must be focused into a single sperm cell and the images recorded with the smallest time interval

possible. Note that, as cells move in three dimensions, adjustment of the xyz plane might be required. Figure created with BioRender.com.

2.7 Results and discussion

2.7.1 *P. patens* asynchronous spermatogenesis enables the analysis of several developmental stages within the same sample

P. patens sexual reproduction is triggered by a shift in environmental conditions, involving the development of both male (antheridia) and female (archegonia) sexual organs. Several antheridia and archegonia develop in bundles (named gametangia) at the tip of the gametophore apical shoot, largely enclosed by several leaf-like structures. Such particular tissue architecture can be easily recognized in both TEM (Figures 2.4A and B) and cryosectioned gametangia samples (Figures 2.4C), with several antheridia being observed within a single section. Moreover, and as previously reported by Landberg et al., 2013, I observe that *P. patens* spermatogenesis occurs asynchronously between the distinct antheridia. This is evidenced by the different cellular organization between sperm cells from distinct antheridia, while the cells within each antheridium display a similar cellular framework. Indeed, in the same section, both flagellated/ciliated (labeled by acetylated α -tubulin) cells with elongated nuclear shapes, as well as cells with round nucleus and no clear acetylated α -tubulin signal are found (Figures 2.4A-C insets).

Due to the mechanical tissue disruption required to immunostain individualized sperm cells, no tissue context/organization can be retrieved from these samples (Figure 2.4D). Nevertheless, spermatids at different stages of spermatogenesis can be detected within these samples. It is noteworthy that, due to the 7minutes cytocentrifugation

step (as opposed to the standard 5minutes), both mitotic and cells with highly elongated nuclear shapes can attach to the coverslip, resist the immunofluorescence protocol, and be imaged (Figure 2.4D insets).

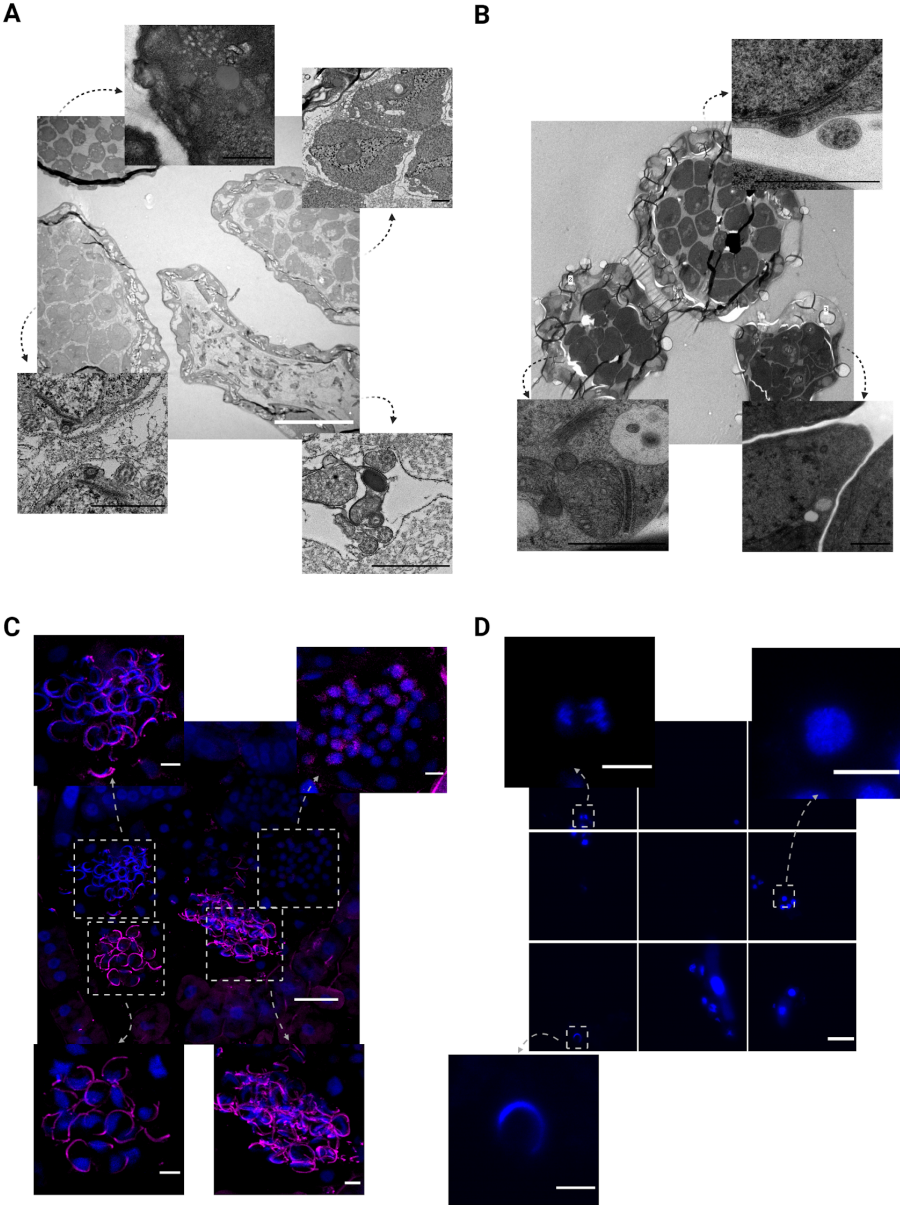


Figure 2.4: *P. patens* gametogenesis occurs asynchronously, with cells at different spermatogenesis stages being revealed by all

established protocols. **A.** Representative TEM image of a chemically fixed longitudinal sample section, containing 4 antheridia at different stages of spermatogenesis, revealed by the different subcellular structures visible within the spermatids (insets); **B.** Representative TEM image of a high pressure frozen and freeze substituted transversely oriented sample section, with 3 antheridia at distinct developmental stages, evidenced by the different subcellular structures visible within the developing sperm cells (insets); **C.** Maximum projection of a confocal image stack from an immunostained cryosection with 4 antheridia. The sperm cells contained within some of these antheridia (insets) have different nuclear (blue) and acetylated α -tubulin (magenta) signals, depicting different cellular features and developmental stages; **D.** Example of a spiral mosaic from immunostained individualized sperm cells (obtained with a Deltavision OMX microscope), revealing the presence of isolated sperm cells with distinct nuclear shapes (Blue). Scale-bars = 20 μ m (insets in A and B = 1 μ m and in C and D = 5 μ m). Figure created with BioRender.com.

Considering the different sperm cell features observed within one sample section, it becomes possible to establish a differentiation timeline. As similarly described for spermatogenesis in a variety of bryophyte species (Renzaglia and Garbary, 2001), *P. patens* sperm cells start from a round nucleus and lack clear acetylated-tubulin structures, differentiating into cells with a remarkable streamlined and condensed nucleus. Additionally, sperm cells ranging from early to mature spermatogenesis stages were found in both TEM and immunostained 15 DAI samples (Figure 2.4). Therefore, the newly established protocols here detailed (Figures 2.1 and 2.2) enable the study of multiple *P. patens* spermatogenesis stages from a single gametangia sample.

2.7.2 Spermatogenesis milestones revealed by light and electron microscopy

In order to confirm and further detail the main spermatogenesis stages, I have analyzed TEM samples obtained everyday between 10 and 15 DAI, and matched their subcellular features with those observable by immunofluorescence light (confocal and 3D-SIM) microscopy. This enabled the identification of 4 major events during the differentiation of *P. patens* sperm cells (Figures 2.5 to 2.8).

Sperm cells from antheridia between days 10 to 12 after induction (Figure 2.5) had a round nuclear shape, with many different organelles being detected within the cytoplasmic volume (e.g. endoplasmic reticulum (ER) - Figures 2.5A and B, white stars; and Golgi apparatuses - Figures 2.5B, white arrowheads). Moreover, these cells also appeared to be connected to their neighbours by cytoplasmic bridges (Figures 2.5A and B, black arrows), and no locomotory apparatus (LA) structures, known to exist in other bryophyte species (e.g. centrioles and cilia/flagella), were detected within these cells. Similarly, round nucleated cells without any clear γ -tubulin2-Citrine or acetylated α -tubulin signals were detectable by both confocal (Figure 2.5C) and 3D-SIM (Figure 2.5D) light microscopy.

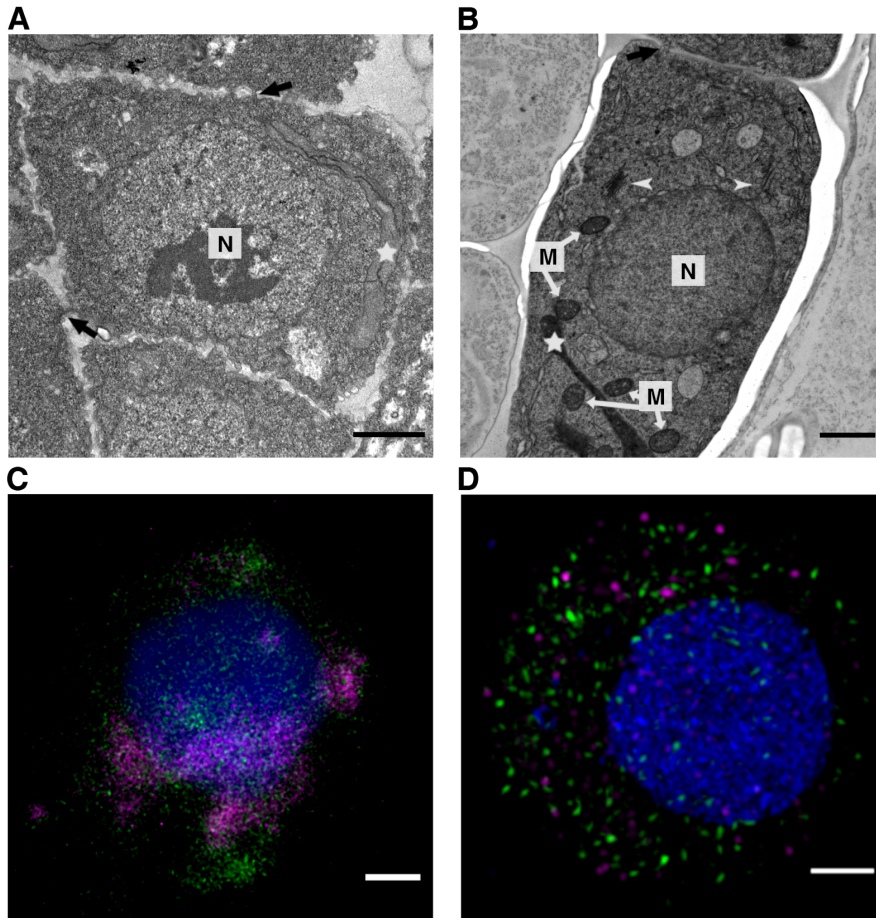


Figure 2.5: Early spermatogenesis in *P. patens*. **A.** Representative TEM image of a chemically fixed early spermatid; **B.** Early high pressure frozen and freeze substituted sperm cell; **C.** Confocal image from a cryosectioned early spermatid; **D.** 3D-SIM of an isolated early developing sperm cell. M - mitochondria; N - nucleus; black arrow - cytoplasmic bridges; white star - endoplasmic reticulum; white arrowheads - Golgi apparatus. Blue - DAPI; Green - γ -tubulin2-Citrine; Magenta - acetylated α -tubulin. Scale-bars = 1 μ m.

The locomotory apparatus of *P. patens* sperm cells appears to assemble from 13 DAI onwards (Figures 2.6A and B, LA), with two

centrioles and the plant-specific multilayered structure being frequently observed (Renzaglia and Garbary, 2001). Accordingly, immunostaining of cryosectioned and isolated spermatids revealed the concentration of both γ -tubulin2 (Figures 2.6C and D, green) and acetylated α -tubulin (Figures 2.6C and D, magenta) in a particular region near the nucleus. I believe this region might represent the assembling LA, which is also localized near the nucleus in the TEM analysis (Figures 2.6A and B, LA). At this stage, developing spermatids still contained a round nucleus and several other organelles, including multiple small mitochondria (Figures 2.6A and B, M).

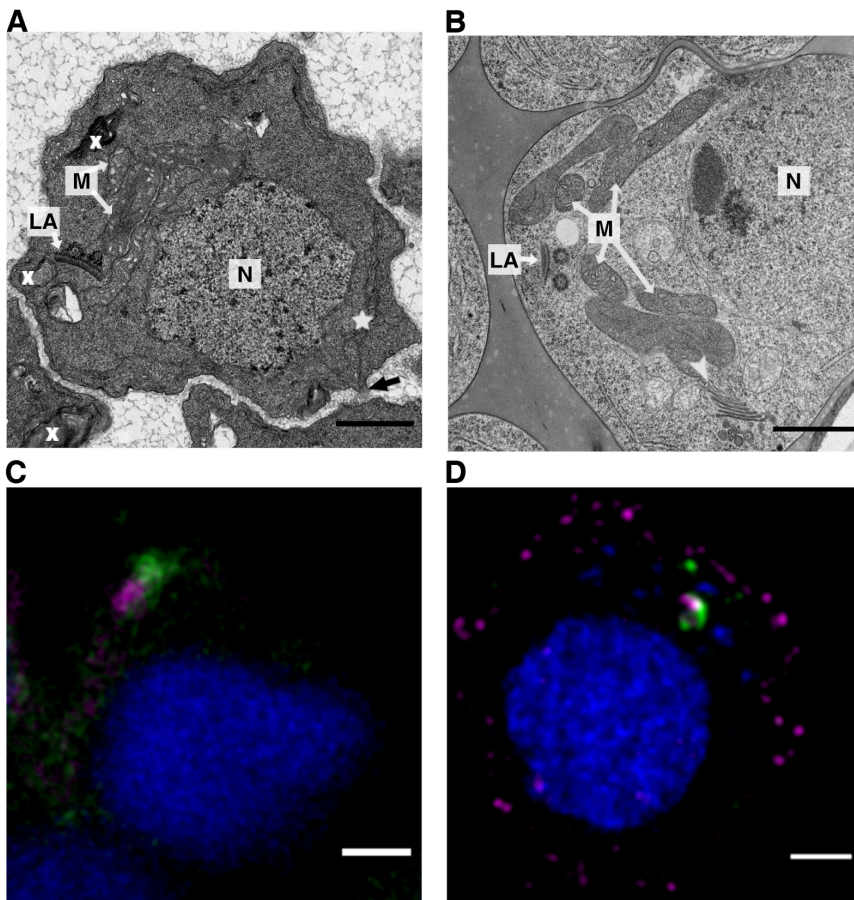


Figure 2.6: Assembly of the locomotory apparatus in *P. patens* developing sperm cells. **A.** Representative TEM image of a chemically fixed spermatid containing some locomotory apparatus (LA) structures; **B.** Developing sperm cell processed following the HPF+FS protocol, with some visible LA structures; **C.** Confocal image from a cryosectioned spermatid, with a clear region containing both γ -tubulin2-Citrine (green) and acetylated α -tubulin (magenta); **D.** 3D-SIM of an isolated early developing sperm cell, displaying a partial colocalization of both γ -tubulin2-Citrine (green) and acetylated α -tubulin (magenta) signals. LA - locomotory apparatus; M - mitochondria; N - nucleus; black arrow - cytoplasmic bridges; white star - endoplasmic reticulum; white cross - collapsed membranes. Blue - DAPI; Green - γ -tubulin2-Citrine; Magenta - acetylated α -tubulin. Scale-bars = 1 μ m.

In samples from 14 DAI onwards, cilia/flagella structures were easily found (Figures 2.7A and B, black diamonds; C and D, magenta). The nucleus of these sperm cells was no longer round, but elongated (Figures 2.7A and B, N; C and D, blue), and several cytoplasmic vesicles were apparent on some TEM images (Figure 2.7A, V). Interestingly, cytoplasmic bridges appeared to still connect these 14 DAI sperm cells amongst themselves (Figure 2.7B, black arrows). Furthermore, the immunofluorescence experiments revealed the presence of γ -tubulin2-Citrine in a region anterior to the two acetylated α -tubulin elongated filaments (Figures 2-7C and D). As eukaryotic cilia/flagella are known to be composed of stable acetylated microtubules, I believe that each of these acetylated α -tubulin filament represents one cilia/flagella.

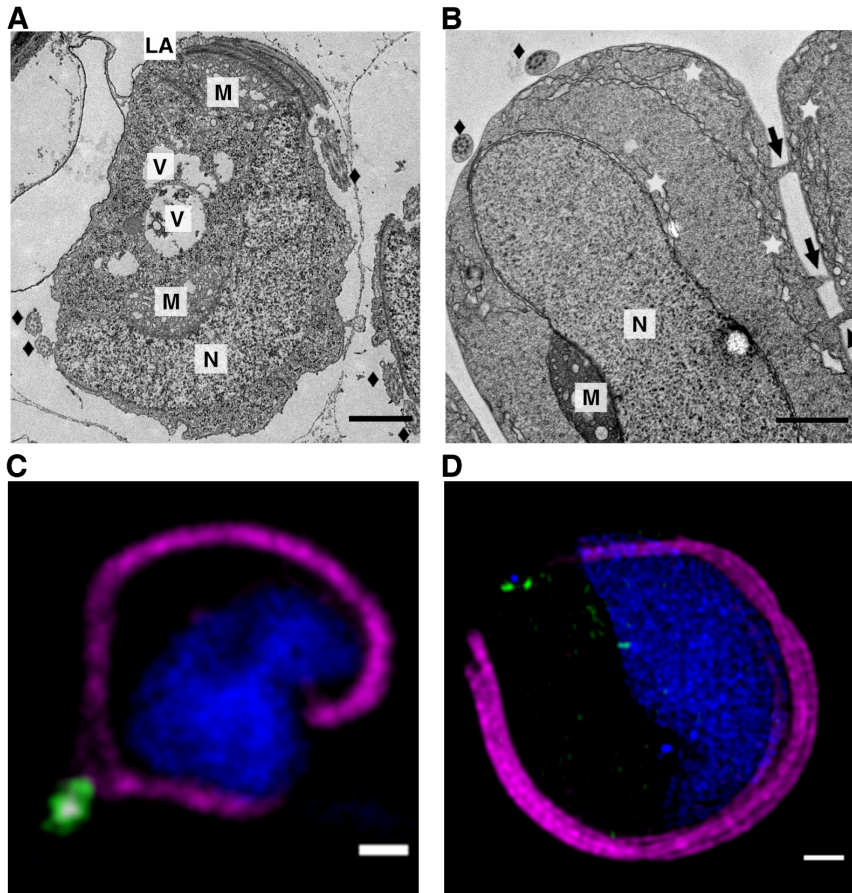


Figure 2.7: *P. patens* spermatogenesis involves nuclear elongation and ciliogenesis. **A.** TEM of a chemically fixed flagellated spermatid; **B.** TEM image of a high pressure frozen and freeze substituted sperm cell, revealing the presence of cilia/flagella, as well as clear cytoplasmic bridges; **C.** Biflagellated (acetylated α -tubulin (magenta)) spermatid from a cryosection, imaged by confocal microscopy; **D.** 3D-SIM image of an individual flagellated sperm cell. LA - locomotory apparatus; M - mitochondria; N - nucleus; V - prominent cytoplasmic vesicle; black diamond - flagella/cilia; black arrow - cytoplasmic bridges; white star - endoplasmic reticulum. Blue - DAPI; Green - γ -tubulin2-Citrine; Magenta - acetylated α -tubulin. Scale-bars = 1 μ m.

The major change observed in 15 DAI sperm cells was the presence of patches of condensed chromatin (Figures 2.8A and B, N), and cytoplasmic vesicles of significant proportions (Figures 2.8A and B, V), with electron dense material being sometimes detected within them. Furthermore, an undifferentiated plastid containing a light colored starch-like granule was also observed in these spermatids (Figure 2.8A, P). It is noteworthy that such undifferentiated plastids were also sometimes detectable within 14 DAI cells, however all 15 DAI spermatids appeared to contain such structure. The sperm cell of bryophytes is characterized by a streamlined shape composed of an elongated nucleus and reduced cytoplasmic content (Renzaglia and Garbary, 2001). Indeed, sperm cells with extensive nuclear elongation were found by light microscopy (Figures 2.8C and D, blue signal). Therefore, I believe that 15 DAI spermatids are undergoing the final events of sperm cell cytodifferentiation, including chromatin condensation and reduction of cytosol volume.

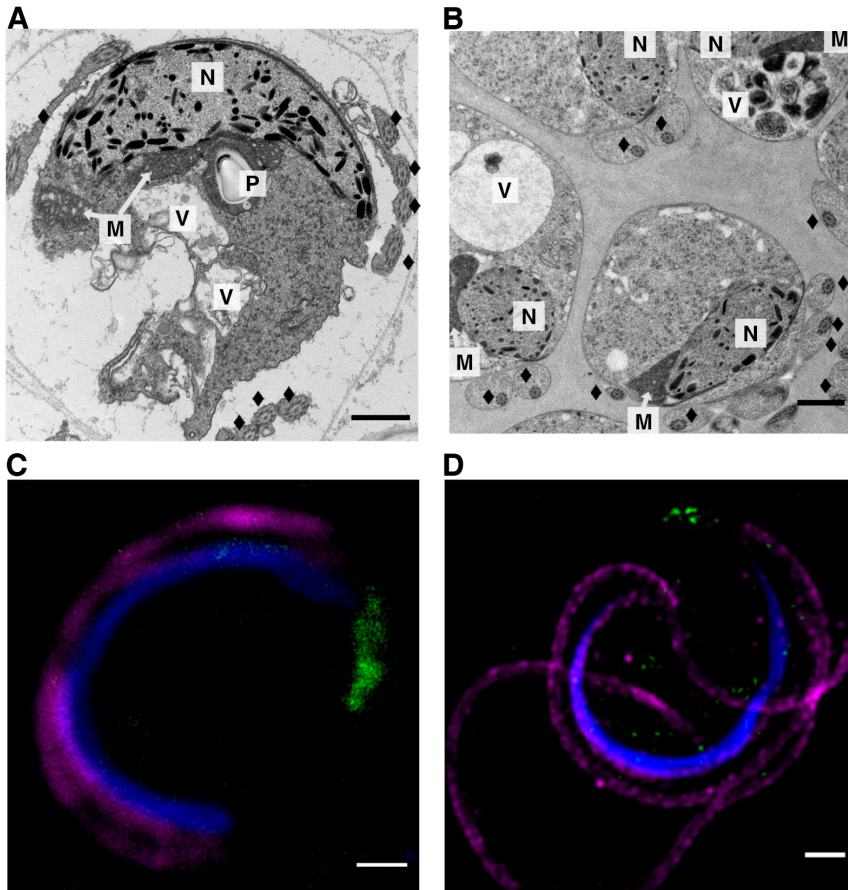


Figure 2.8: Sperm cell cytodifferentiation in *P. patens*. **A.** TEM image of a chemically fixed sperm cell undergoing the final differentiation events, evidenced by the patches of condensed (black) chromatin; **B.** TEM image of several cytodifferentiating spermatids subjected to the HPF+FS protocol, revealing the presence of pronounced cytoplasmic vesicles; **C.** Confocal image of a late developing sperm cell displaying extensive nuclear (blue) elongation and compaction; **D.** 3D-SIM image of a sperm cell in the final maturation step, containing two cilia/flagella and a characteristic streamlined nucleus (blue). M - mitochondria; N - nucleus; P - undifferentiated plastid with starch-like granules; V - prominent cytoplasmic vesicle; black diamond - flagella/cilia. Blue -

DAPI; Green - γ -tubulin2-Citrine; Magenta - acetylated α -tubulin.
Scale-bars = 1 μ m.

2.7.3 The mature spermatids of *P. patens*

Spermatogenesis culminates in the release of spermatids. In *P. patens*, all the sperm cells contained within one antheridium are discharged simultaneously, as a cluster/package of cells (Figure 2.9A). Interestingly, after being released, spermatids take around 1-2minutes to start moving. This suggests there might be a final maturation/activation event after their discharge from the antheridium.

The characteristic streamlined shape of discharged *P. patens* spermatids is mostly dictated by their prominent elongated and condensed nucleus, which occupies most of the reduced cytoplasmic volume observed in released live sperm cells (Figure 2.9B, N), as well as in TEM images of late maturing spermatids (Figure 2.9C, N). Moreover, the two cilia/flagella (Figures 2.9B and C, black diamonds) and the round plastid positioned in the middle of the cell are also distinguishable by both widefield (Figure 2.9B, P) and TEM (Figure 2.9C, P) analyses.

Once released into the surrounding aqueous environment, *P. patens* spermatids need to actively swim in order to reach the entrance of the archegonia and fertilize the egg cell therein contained (Paolillo, 1981). In order to explore the motility of *P. patens* sperm cells, I have optimized the current existing protocol for imaging of spermatid motility (Horst and Reski, 2017; Ortiz-Ramírez et al., 2017), to enable both qualitative analysis of whole sperm cell clusters, as well as more quantitative analyses (Figure 2.3). Sample preparation is similar for both assays yet, the addition of FDA to the “sperm cell media” is only recommended for qualitative analyses, as a possible effect of this dye in sperm cell motility was not yet addressed.

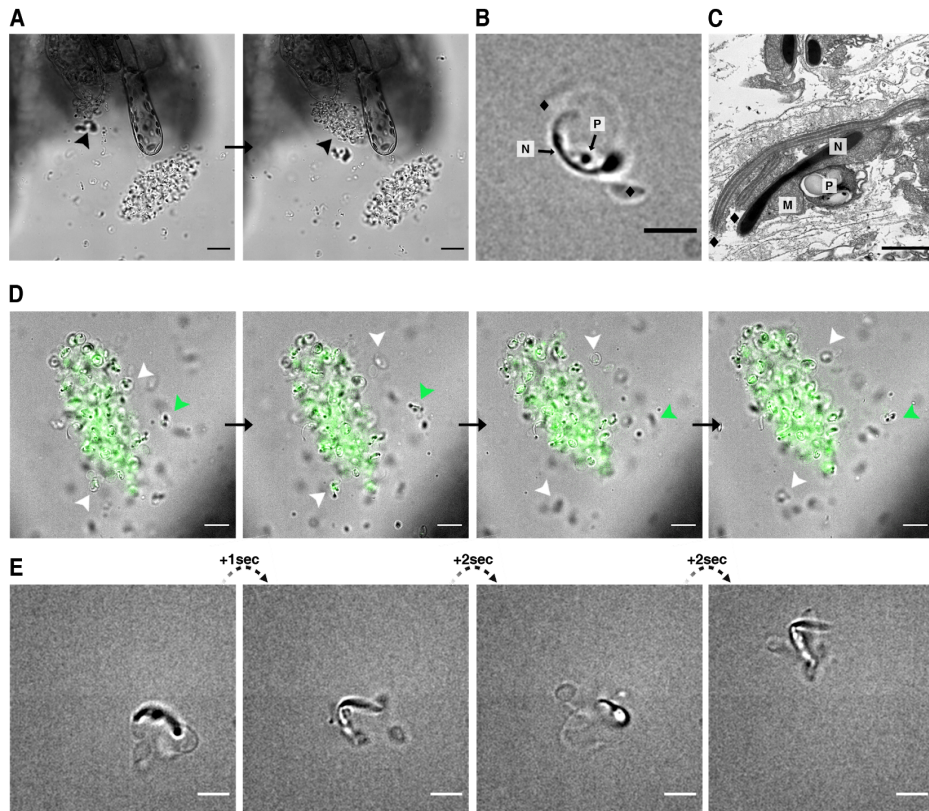


Figure 2.9: The mature spermatids of *P. patens*. **A.** Sperm cells are released from the antheridia in compact groups (clusters/packages). Scale-bar = 50 μ m; **B.** The elongated sperm cell shape, reduced cytoplasmic volume and some organelles (nucleus, plastid, flagella/cilia) can be distinguished by widefield microscopy of released spermatids. N - nucleus; P - undifferentiated plastid with starch-like granules; black diamond - flagella/cilia. Scale-bar = 5 μ m; **C.** TEM image of a fully differentiated chemically fixed sperm cell, displaying a residual cytoplasmic volume and containing few organelles: nucleus, mitochondrion, plastid and flagella/cilia. M - mitochondria; N - nucleus; P - undifferentiated plastid with starch-like granules; black diamond - flagella/cilia. Scale-bar = 1 μ m; **D.** For qualitative analysis of sperm motility, the whole sperm cell cluster can be imaged throughout time,

with individual cells revealing alterations of location (green arrow) and separation from the remaining ones (white arrows). Note that the cells are green because of the presence of FDA in the “sperm cell media”, reporting viable cells. Scale-bar = 10 μ m; **E**. In order to obtain quantitative parameters of sperm cell motility, single cell resolution might be required. For this, it is important to obtain the spatial (higher objective and smaller field of view) and temporal (more frames per second - FPS) resolutions. Scale-bar = 5 μ m.

A qualitative analysis of sperm cell motility enables the evaluation of overall movement, distinguishing motile from immotile sperm cells across different genotypes and/or conditions (e.g. temperature, pH). Such analysis relies on the imaging of whole viable sperm cell clusters throughout time (Figure 2.9D). If the spermatids composing the imaged cluster are motile, over time they will separate and move away from the main group of cells (Figure 2.9D arrowheads). However, in order to quantify particular motility parameters (e.g. speed, displacement or ciliary beating), higher cellular and temporal resolutions might be required. In order to assess such parameters, one should focus on single cells isolated from the cluster (e.g. Figure 2.9D green arrowhead), and acquire images with a higher magnification and a faster frame rate. The cellular behaviour and parameters can then be estimated from the data (Figure 2.9E). Moreover, taking into account the acquisition frame rate, it is possible to report the measured parameters in units of absolute time (e.g. seconds, minutes). This will be relevant for cross-species comparisons, which might reveal interesting aspects of plant sperm cell motility, and its relationship with cellular motility of other eukaryotic species.

2.7.4 Distinct protocols provide different, and yet complementary, insights

Due to the lack of available protocols and tools, and aiming at understanding the cellular mechanisms underlying *P. patens* spermatogenesis, I have developed several imaging protocols for fixed *P. patens* gametangia samples (Figures 2.1 and 2.2). These protocols have enabled the characterization of 4 major keysteps during *P. patens* spermatogenesis, providing critical information at different resolution scales (Figures 2.5 to 2.8).

Transmission electron microscopy protocols are not constrained by the availability of prior molecular knowledge or reagents (e.g. antibodies). However, they were the only ones to provide precious ultrastructural cellular resolution (below 100nm), and in a tissue-specific context. Still, both TEM protocols require specialized technical knowledge and equipment (Table 2.1). Nevertheless, these protocols offer distinct advantages, mainly differing in the quality of sample preservation, with particularly membrane-rich structures (e.g. Golgi apparatuses, ER) being significantly better preserved by the HPF+FS protocol (Figures 2.5B and 2.7B). Moreover, as the HPF+FS protocol relies on cryofixation of cells, it is less prone to the artifacts induced by chemical fixation (e.g. membrane collapse - Figure 2.6A white crosses).

Still, HPF+FS sample preservation comes at a cost, as the HPF+FS is a longer protocol that requires the availability of specialized equipment (high pressure freezer and automated freeze substitution processor), as well as significant amounts of liquid nitrogen. Furthermore, less samples can be frozen in each freezing session, when compared to the number of samples that can be chemically fixed. Additionally, a significant amount of these frozen samples are severely damaged by the formation of cubic ice within the cells, disrupting their structures (e.g. white cells

around the depicted cell on Figure 2.5B). These features significantly reduce the number of well-preserved cells and samples that can be analyzed within each experiment, while increasing their monetary burden (Table 2.1). Yet, their main limitation of both TEM protocols here described, is that they fail to provide the molecular details required to fully understand the biological mechanisms at play (Table 2.1).

Table 2.1: Comparison between the 4 established protocols for fixed cell imaging of *P. patens* spermatogenesis. Note that the time estimation for the TEM protocols does not take into account sectioning or imaging. Similarly, the time displayed for the immunofluorescence protocols does not consider the imaging time.

Protocols and imaging techniques	<i>Transmission electron microscopy (TEM)</i>		<i>Immunofluorescence</i>	
	Chemically fixed samples	HPF+FS samples	Cryosections + confocal microscopy	Individualized cells + 3D-SIM
Resolution	<100nm	<100nm	≈300nm	110-200nm
Structural information	Yes	Yes	No	No
Molecular information	No	No	Yes	Yes
Tissue context	Yes	Yes	Yes	No
Cells/sample	+++	++	+++	++
Samples/experiment	+++	+	++	+++
Time	3.5days +	6days +	2-3days	2-3days
Cost	++	+++	+	+
Equipment	++	+++	+	++

Therefore, in order to obtain molecular insights into *P. patens* sperm cell development, I have developed two distinct immunostaining protocols. Both of these protocols required the *a priori* molecular knowledge that cilia/flagella structures should contain acetylated α -tubulin, which allowed the distinction between flagellated and non-flagellated spermatogenesis stages. Moreover, both protocols take an approximately similar amount of time to be completed, and can be employed to determine protein localization of both antibody stained (e.g. acetylated α -tubulin) as well as endogenous (e.g. γ -tubulin2-Citrine) labeled proteins (Table 2.1).

Nonetheless, due to the technical challenges of performing 3D-SIM in cryostat sample sections, both protocols here detailed provide molecular information at different spatial resolutions (Table 2.1), with particular features being only possible to clarify by 3D-SIM. This is the case of the presence of two small γ -tubulin2 containing *foci*, which can be clearly distinguished by 3D-SIM (Figures 2.7D and 2.8D, green) but not by confocal microscopy (Figures 2.7C and 2.8C, green). However, the immunofluorescence of cryosections is critical to provide molecular information in a tissue-context (Figure 2.4C).

Overall, the protocols detailed here provide a new scope to the techniques available to study *P. patens* sexual reproduction. Despite providing distinct levels of information, both TEM and immunofluorescence protocols can be employed to obtain complementary details. For instance, the chemically fixed TEM protocol provides a more cost-effective way to analyze several samples. However, as the structures of interest might be altered during chemical fixation, a confirmation of their particular details by HPF+FS might be required. Similarly, while the resolution of 3D-SIM might be critical to reveal specific particularities regarding a localization of a target protein, the immunostaining of gametangia cryosections might be useful as a first

approach. This protocol offers an overview of the target protein's localization across several distinct spermatogenesis stages, despite being limited by the time required to section each sample. Then, the particular stages of interest might be selected, and thoroughly characterized by 3D-SIM.

Nevertheless, these 4 protocols are limited in providing details regarding the discharged spermatids, which are lost during sample fixation (unless samples are cryo-embedded prior to fixation - alternative cryosections protocol, see section 2.6.1.3). Therefore, the current methods available to study *P. patens* released sperm cells mostly rely on live imaging, which although useful for particular applications, fails to provide clear and detailed molecular or structural information.

2.8 Conclusion

Due to the particular complexity of the sexual organs and the 3D architecture of the gametangia and surrounding tissues, tailored protocols are required to explore the cellular mechanisms underpinning *P. patens* sexual reproduction. In this work, I have established 4 distinct protocols that enable imaging of *P. patens* gametangia at different cellular and molecular resolutions. I have employed those protocols for the characterization of the spermatogenesis process. Moreover, this work also describes an optimized live imaging assay that enables qualitative as well as quantitative studies of sperm cell motility.

Overall, the protocols and techniques detailed in this work allow for the exploration of *P. patens* reproduction from a cellular perspective. However, these tools are also of value for a wider research community,

as they can easily be adapted to study different processes/tissues across a range of plant species.

2.9 Author contributions and acknowledgements

2.9.1 Author contributions

All TEM protocols and experiments were established and performed by myself and Ana Laura Sousa (Electron Microscopy Facility technician at Instituto Gulbenkian de Ciência (IGC)). Ana Laura Sousa performed the sectioning of all TEM samples and I acquired the images. Development, implementation and data acquisition of light microscopy experiments was performed by myself. Jörg D. Becker (then head of the “Plant Genomics” laboratory at IGC, currently at Instituto de Tecnologia Química e Biológica António Xavier (ITQB)) and Mónica Bettencourt-Dias (head of the “Cell Cycle Regulation” laboratory at IGC) have jointly supervised this work.

2.9.2 Acknowledgements

I am grateful to Gohta Goshima (Sugashima marine biological laboratory and division of biological science of Nagoya University, Japan) for his generosity in sharing the γ -tubulin2-Citrine line; Swadhin C. Jana (from the “Cell Cycle Regulation” laboratory at IGC, currently at National Centre for Biological Sciences-TIFR Bangalore, India) for teaching me to perform an immunofluorescence assay; Carla Lopes (from the “Cell Cycle Regulation” laboratory at IGC) for instructions regarding the use of the cytocentrifuge; and Catarina Nabais (then PhD student at “Cell Cycle Regulation” and “Principles of Nuclear Dynamics” laboratories from IGC, currently at Max Planck Institute of Molecular Cell Biology and Genetics)

for useful discussions regarding light microscopy and live imaging. I thank Joana Rodrigues (Histopathology Unit technician at (IGC) for guidance in cryostat sectioning.

I would like to acknowledge the following IGC facilities: Plant facility (plant chamber maintenance), Histopathology (for cryostat training and availability), Light Microscopy (for microscope availability), Electron Microscopy (for equipment availability).

2.10 References

Ashton, N.W., and Cove, D.J. (1977). The isolation and preliminary characterisation of auxotrophic and analogue resistant mutants of the moss, *Physcomitrella patens*. *Mol. Gen. Genet.* 154, 87–95.

Cesarino, I., Dello Iorio, R., Kirschner, G.K., Ogden, M.S., Picard, K.L., Rast-Somssich, M.I., and Somssich, M. (2020). Plant science's next top models. *Ann. Bot.* 126, 1–23.

Cheng, X., and Bezanilla, M. (2021). SABRE populates ER domains essential for cell plate maturation and cell expansion influencing cell and tissue patterning. *Elife* 10, e65166.

During, H.J. (1979). Life strategies of Bryophytes: a preliminary review. *Lindbergia* 5, 2–18.

During, H.J., and van Tooren, B.F. (1987). Recent developments in bryophyte population ecology. *Trends Ecol. Evol.* 2, 89–93.

Glime, J.M. (2020). *Bryophyte Ecology*. Ebook sponsored by Michigan Technological University and the International Association of Bryologists. Available at: <https://digitalcommons.mtu.edu/bryo>.

Hackenberg, D., and Twell, D. (2019). The evolution and patterning of male gametophyte development. *Curr. Top. Dev. Biol.* 131, 257–298.

Hashida, Y., Takechi, K., Abiru, T., Yabe, N., Nagase, H., Hattori, K., Takio, S., Sato, Y., Hasebe, M., Tsukaya, H., et al. (2020). Two *ANGUSTIFOLIA* genes

regulate gametophore and sporophyte development in *Physcomitrella patens*. *Plant J.* *101*, 1318–1330.

Hisanaga, T., Yamaoka, S., Kawashima, T., Higo, A., Nakajima, K., Araki, T., Kohchi, T., and Berger, F. (2019). Building new insights in plant gametogenesis from an evolutionary perspective. *Nat. Plants* *5*, 663–669.

Hohe, A., Rensing, S.A., Mildner, M., Lang, D., and Reski, R. (2002). Day Length and Temperature Strongly Influence Sexual Reproduction and Expression of a Novel MADS-Box Gene in the Moss *Physcomitrella patens*. *Plant Biol.* 695–602.

Horst, N.A., and Reski, R. (2017). Microscopy of *Physcomitrella patens* sperm cells. *Plant Methods* *13*, 1–8.

Inoue, K., Nishihama, R., Araki, T., and Kohchi, T. (2019). Reproductive induction is a far-red high irradiance response that is mediated by phytochrome and phytochrome interacting factor in *Marchantia polymorpha*. *Plant Cell Physiol.* *60*, 1136–1145.

Ishizaki, K., Nishihama, R., Yamato, K.T., and Kohchi, T. (2016). Molecular Genetic Tools and Techniques for *Marchantia polymorpha* Research. *Plant Cell Physiol.* *57*, 262–270.

Islam, M., Inoue, T., Hiraide, M., Khatun, N., Jahan, A., Kuwata, K., Katagiri, S., Umezawa, T., Yotsui, I., Sakata, Y., et al. (2021). Activation of SnRK2 by Raf-like kinase ARK represents a primary mechanism of ABA and abiotic stress responses. *Plant Physiol.* *185*, 533–546.

Julca, I., Ferrari, C., Flores-Tornero, M., Proost, S., Lindner, A.-C., Hackenberg, D., Steinbachová, L., Michaelidis, C., Gomes Pereira, S., Shekhar Misra, C., et al. Comparative transcriptomic analysis reveals conserved transcriptional programs underpinning organogenesis and reproduction in land plants. *BioRxiv preprint*. doi: 10.1101/2020.10.29.361501

Kato, H., Yasui, Y., and Ishizaki, K. (2020). Gemma cup and gemma development in *Marchantia polymorpha*. *New Phytol.* *228*, 459–465.

Kosetsu, K., Murata, T., Yamada, M., Nishina, M., Boruc, J., Hasebe, M., Van Damme, D., and Goshima, G. (2017). Cytoplasmic MTOCs control spindle orientation for asymmetric cell division in plants. *Proc. Natl. Acad. Sci. U. S. A.* *114*, E8847–E8854.

Landberg, K., Pederson, E.R. a, Viaene, T., Bozorg, B., Friml, J., Jönsson, H., Thelander, M., and Sundberg, E. (2013). The moss *Physcomitrella patens* reproductive organ development is highly organized, affected by the two SHI/STY genes and by the level of active auxin in the SHI/STY expression domain. *Plant Physiol.* *162*, 1406–1419.

Layton, C., Bancroft, J.D., and Suvarna, K.S. (2019). 4. Fixation of Tissues. *In Bancroft's Theory and Practise of Histological Techniques*, pp. 40–63.

Leong, S.Y., Edzuka, T., Goshima, G., and Yamada, M. (2020). Kinesin-13 and Kinesin-8 function during cell growth and division in the moss *Physcomitrella patens*. *Plant Cell* *32*, 683–702.

Minamino, N., Kanazawa, T., Nishihama, R., Yamato, K.T., Ishizaki, K., Kohchi, T., Nakano, A., and Ueda, T. (2017). Dynamic reorganization of the endomembrane system during spermatogenesis in *Marchantia polymorpha*. *J. Plant Res.* *130*, 433–441.

Mishler, B.D., Lewis, L.A., Buchheim, M.A., Renzaglia, K.S., Garbary, D.J., Delwiche, C.F., Zechman, F.W., Kantz, T.S., and Chapman, R.L. (1994). Phylogenetic Relationships of the “Green Algae” and “Bryophytes.” *Ann. Missouri Bot. Gard.* *81*, 451.

Nakaoka, Y., Miki, T., Fujioka, R., Uehara, R., Tomioka, A., Obuse, C., Kubo, M., Hiwatashi, Y., and Goshima, G. (2012). An inducible RNA interference system in *Physcomitrella patens* reveals a dominant role of augmin in phragmoplast microtubule generation. *Plant Cell* *24*, 1478–1493.

Ortiz-Ramírez, C., Michard, E., Simon, A.A., Damineli, D.S.C., Hernández-Coronado, M., Becker, J.D., and Feijó, J.A. (2017). GLUTAMATE RECEPTOR-LIKE channels are essential for chemotaxis and reproduction in mosses. *Nature* *549*, 91–95.

Paolillo, D.J. (1981). Swimming of Land Plants Sperms. *Am. Inst. Biol. Sci.* *31*, 367–373.

Pu, X., Yang, L., Liu, L., Dong, X., Chen, S., Chen, Z., Liu, G., Jia, Y., Yuan, W., and Liu, L. (2020). Genome-wide analysis of the MYB transcription factor superfamily in *Physcomitrella patens*. *Int. J. Mol. Sci.* *21*, 1–18.

Ramos-Vara, J.A. (2005). Technical aspects of immunohistochemistry. *Vet. Pathol.* *42*, 405–426.

Rensing, S.A. (2018). Great moments in evolution: the conquest of land by plants. *Curr. Opin. Plant Biol.* 42, 49–54.

Rensing, S.A., Goffinet, B., Meyberg, R., Wu, S.Z., and Bezanilla, M. (2020). The moss *Physcomitrium* (*Physcomitrella*) *patens*: A model organism for non-seed plants. *Plant Cell* 32, 1361–1376.

Renzaglia, K.S., and Garbary, D.J. (2001). Motile Gametes of Land Plants: Diversity, Development, and Evolution. *CRC. Crit. Rev. Plant Sci.* 20, 107–213.

Reski, R., and Abel, W.O. (1985). Induction of budding on chloronemata and caulonemata of the moss, *Physcomitrella patens*, using isopentenyladenine. *Planta* 165, 354–358.

Rico-Reséndiz, F., Cervantes-Pérez, S.A., Espinal-Centeno, A., Dipp-Álvarez, M., Oropeza-Aburto, A., Hurtado-Bautista, E., Cruz-Hernández, A., Bowman, J.L., Ishizaki, K., Arteaga-Vázquez, M.A., et al. (2020). Transcriptional and morpho-physiological responses of *Marchantia polymorpha* upon phosphate starvation. *Int. J. Mol. Sci.* 21, 1–25.

Sanchez-Vera, V., Kenchappa, C.S., Landberg, K., Bressendorff, S., Schwarzbach, S., Martin, T., Mundy, J., Petersen, M., Thelander, M., and Sundberg, E. (2017). Autophagy is required for gamete differentiation in the moss *Physcomitrella patens*. *Autophagy* 13, 1939–1951.

Sanderson, T., Wild, G., Cull, A.M., Marston, J., and Zardin, G. (2019). 19. Immunohistochemical and immunofluorescent techniques. *In Bancroft's Theory and Practise of Histological Techniques*, pp. 337–394.

Shimamura, M. (2016). *Marchantia polymorpha*: Taxonomy, phylogeny and morphology of a model system. *Plant Cell Physiol.* 57, 230–256.

Sousa, A.L.V.C. (2017). Characterising the Formation and Functional Role of Vesicular Clustering during Influenza A Virus Infection. Faculdade de Ciências, Universidade de Lisboa.

Strotbek, C., Krinninger, S., and Frank, W. (2013). The moss *Physcomitrella patens*: methods and tools from cultivation to targeted analysis of gene function. *Int. J. Dev. Biol.* 57, 553–564.

Van Gisbergen, P., Wu, S.Z., Cheng, X., Pattavina, K.A., and Bezanilla, M. (2020). *In vivo* analysis of formin dynamics in the moss *P. patens* reveals functional class diversification. *J. Cell Sci.* 133.

Wu, S.Z., and Bezanilla, M. (2018). Actin and microtubule cross talk mediates persistent polarized growth. *J. Cell Biol.* 217, 3531–3544.

Chapter 3.

**The 3D architecture of *P. patens* centrioles:
bicentriole-mediated assembly and
asymmetrical maturation**

This section is adapted from: Gomes Pereira, S., Sousa, A.L., Nabais, C., Paixão, T., Holmes, A.J., Schorb, M., Goshima, G., Tranfield, E.M., Becker, J.D., and Bettencourt-Dias, M. The 3D architecture and molecular foundations of *de novo* centriole assembly *via* bicentrioles (*BioRxiv preprint, in revision*).

3.1 Abstract

Centrioles are structurally conserved organelles, composing both centrosomes and cilia. In animal cycling cells, centrioles often form through a highly characterized process termed canonical duplication. However, a large diversity of eukaryotes form centrioles *de novo* through uncharacterized cellular and molecular pathways. This unexplored diversity is key to understanding centriole assembly mechanisms and how they evolved to assist specific cellular functions. Here, combining 2D transmission electron microscopy and 3D electron tomography, I show that during spermatogenesis of the moss *Physcomitrium patens*, centrioles are born as a co-axially oriented centriole pair united by what appears to be a continuous cartwheel hub. Several microtubules emanate from those bicentrioles, suggesting it may act as a microtubule organizing center. Moreover, the two sister centrioles appear to be connected with inverted polarities. Thereafter, the two resulting sister centrioles mature asymmetrically, elongating independently their microtubule triplets and naked cartwheels. Afterwards, they dock to the cell membrane with similar polarities, and template the assembly of two cilia. Despite being structurally similar, these cilia appear to be capable of beating synchronously, yet most often beating asynchronously. Here, I

performed the first ultrastructural characterization of centriole biogenesis and locomotory apparatus maturation in *P. patens*. This work raises many intriguing questions regarding the establishment of centriole and cartwheel polarities, and the regulation of centriole maturation, as such ultrastructurally distinct centrioles are produced.

3.2 Introduction

Centrioles are microtubule (MT)-based structures that compose centrosomes and cilia. The centrosome is the main microtubule organizing center (MTOC) in most animal cells, regulating intracellular transport, spindle pole formation and cell migration. Centrioles, then called basal bodies, can also anchor to the cell membrane and template cilia growth, with important roles in cell signaling and motility (Joukov and De Nicolo, 2019). Centriole biogenesis needs to be tightly regulated in space, time and number, as failure in regulating this process can lead to diseases, such as cancer (Levine et al., 2017; Lopes et al., 2018; Marteil et al., 2018) and ciliopathies (Shaheen et al., 2012; Khan et al., 2014).

Centrioles are widespread across eukaryotes, being assembled by numerous pathways. The most prevalent and well-characterized of such pathways is canonical centriole duplication, a process by which one daughter centriole is assembled orthogonally to a pre-existing one (its mother) in a cell-cycle dependent manner. Accordingly, mature centrioles and the cell cycle impose a numerical, spatial and temporal regulation on centriole duplication, which has been extensively characterized (Nigg and Holland, 2018). However, centrioles can also assemble *de novo* independently of pre-existing ones, raising the question of how such a

process is regulated (Miki-Noumura, 1977; Khodjakov et al., 2002; Peel et al., 2007). This significantly less studied mechanism occurs for instance in vertebrate cells that form multiple cilia (Sorokin, 1968; Mercey et al., 2019). Moreover, it is clear from older electron microscopy studies that *de novo* centriole biogenesis is spread across eukaryotes, underlying the diversification of essential cellular functions such as stress evasion, spermatogenesis and embryo development (Nabais et al., 2018). The regulation, structures and molecules underpinning *de novo* centriole biogenesis remain enigmatic, in part due to the lack of amenable model systems and tools required to tackle this problem. This knowledge is key to shedding light on the evolutionary history and general principles governing centriole assembly.

Early land plants (such as bryophytes), ferns and some gymnosperms (*Ginkgo* and cycads) are critical ecological players, which reproduce through means of multiciliated motile sperm cells (Renzaglia and Garbary, 2001). In these plant species, sperm cells are the only centriole-containing cells in the entire organism. Therefore, during spermatogenesis either two (*e.g.* bryophytes) (Moser and Kreitner, 1970; Robbins, 1984) or many (*e.g.* *Ginkgo biloba*) (Gifford and Larson, 1980) centrioles arise *de novo*, through mechanisms that have remained poorly understood, despite their importance for the reproductive process of such species. These plant-specific pathways have been vastly overlooked, yet early electron microscopy studies have described the formation of intriguing structures during centriole assembly in plants, such as two co-axially linked centrioles at the origin of the locomotory apparatus of the biflagellated sperm cells of bryophytes (Moser and Kreitner, 1970; Robbins, 1984). Such studies raise important questions about the architecture, molecular composition and function of these puzzling structures.

In this work, I used the moss *Physcomitrium patens* (*P. patens*, previously known as *Physcomitrella patens*) to investigate naturally occurring *de novo* centriole biogenesis in early land plants. Traditionally used as a model to study plant evolution (Rensing et al., 2008; Prigge and Bezanilla, 2010), the bryophyte *P. patens* reproduces *via* motile biciliated sperm cells, which develop inside specialized male organs called antheridia (Landberg et al., 2013). In addition to its simple anatomy, the haploid-dominant life cycle and availability of genetic engineering tools make *P. patens* an attractive model for cell biology studies (Rensing et al., 2020). As a first step to explore the cell biology of centriole and cilia assembly during spermatogenesis in *P. patens* I employed 2D and 3D electron microscopy techniques. This allowed to uncover the bicentriole-mediated pathway for centriole biogenesis with unprecedented detail (and for the first time in *P. patens*), revealing unknown and surprising structural features. Unexpectedly, this pathway results in distinctive centrioles that bear long portions of MT-deprived (“naked”) cartwheels and MT triplets of different lengths. These asymmetric centrioles form cilia that appear structurally similar. However, these cilia most frequently display an asynchronous beating pattern, despite also being capable of synchronous beating. This raises intriguing questions as to the regulation and functional relevance of the centriole asymmetries discovered, as well as to their link with cilia behaviour.

3.3 Methods

3.3.1 *P. patens* strains and growth conditions

The Gransden wild-type (WT) *Physcomitrium* (*Physcomitrella*) *patens* strain (Ashton and Cove, 1977) was used in this work. Plant tissue was

regularly renewed by vegetative propagation of protonemata sub-cultured on Petri dishes containing KNOPS media (Reski and Abel, 1985) supplemented with 0.5g/L ammonium tartrate dibasic (Sigma-Aldrich) every week by mechanical disruption (TissueRuptor; Qiagen), and grown at 25°C, 50% relative humidity and 16h light/8h dark photoperiod, with a light intensity of 80µlum/m/s. Centrioles arise during spermatogenesis, with gametangia developing on the tip of the gametophores. Therefore, to allow for gametophore development, plant tissue was grown for 6-8 weeks in Phytatray II (Sigma-Aldrich) containing 4 sterile peat pellets (Jiffy-7, Jiffy Products International), in the same growth conditions as detailed previously for the vegetative propagation of protonemata. Demineralized sterile water (MilliQ) was supplied to the bottom of each box. Induction of sexual reproduction (triggering gametangia and sporophyte development) was achieved by transferring the Phytatray boxes to 17°C, 50% relative humidity and 8h light/16h dark, with 50µlum/m/s of light intensity. Experiments, unless otherwise stated, were performed 15 days after induction (DAI) of sexual reproduction.

3.3.2 Transmission electron microscopy

3.3.2.1 Chemically fixed samples

The top portion from individual gametophores was fixed for 2h at room temperature (RT) in a 6% (v/v) glutaraldehyde (Polysciences), 0.5% (v/v) tween-20, and 0.1M phosphate buffer (PB) solution. Each sample was washed twice with 0.1M PB and embedded in 2% (w/v) low melting point agarose. The resulting agarose blocks were post-fixed in 1% (v/v) osmium tetroxide, in 0.1M PB solution for 2h on ice, then washed twice with 0.1M PB and twice with distilled water. Afterwards, samples were stained for 1h at RT, with a 1% (w/v) uranyl acetate aqueous solution, and dehydrated in an ethanol series: 30% for 10 min

at RT; 50% for 10 min at RT; 70% overnight at 4°C; 90% for 10 min at 4°C; and finally three incubations in 100% ethanol for 15min at 4°C. Then, samples were infiltrated by 90min incubations with increasing concentrations of EMBED-812 epoxy resin (EMS) in ethanol (25%, 50% and 75%), before being embedded in 100% epoxy resin. Resin-enclosed samples were incubated at 60°C for 24h, polymerizing the resin blocks. Samples were sectioned using a Leica UC7 Ultramicrotome, and ultrathin (70 nm) sections were collected on palladium-copper grids coated with 1% (w/v) formvar (Agar Scientific) in chloroform. Sample sections were post-stained for 5min (at RT) with 1% (w/v) uranyl acetate and for another 5min (at RT) with Reynolds' lead citrate. Finally, sample sections were imaged using a Hitachi H-7650 (100 keV) TEM coupled to a XR41M mid mount AMT digital camera. Number of analyzed structures/cells, individual sample blocks, and independent experiments are detailed in Table 3.1.

3.3.2.2 High pressure frozen-freeze substituted samples

Plant top portions were placed in 0.2µm aluminum specimen carriers with 10% (w/v) BSA, 8% (v/v) methanol cryoprotectant solution and frozen using a High Pressure Freezer Compact 02 (Wohlwend Engineering Switzerland). Samples were freeze substituted in a Leica EM AFS2 with a solution of 2% (v/v) osmium tetroxide, 0.2% (w/v) uranyl acetate in methanol, 1% (v/v) distilled water in acetone for 1h at -90°C, followed by a warm-up with a slope of 5°C/h until -80°C. At -80°C samples were incubated for 72h and then warm-up until 0°C where three washes with acetone were done for 10min each. Samples were infiltrated in increasing concentrations (5%, 10%, 25%, 50%, 75% and 100%) of EMBED-812 epoxy resin at RT for at least 4h each. Resin was polymerized at 60°C for 24h. Ultrathin sections of 70 and 300nm were obtained for ultrastructural analysis and tomography acquisitions,

respectively. 70nm sections were collected and post-stained as described for chemical fixed samples, and imaged with a Hitachi H-7650 (100keV) transmission electron microscope coupled using a XR41M mid mount AMT digital camera. For sample size considerations, please refer to Table 3.1.

Table 3.1: WT samples analyzed by electron microscopy. Samples were grouped by protocol (chemically fixed or high pressure frozen-freeze substituted samples), analysis (2D TEM or 3D electron tomography), and developmental stage (Dev. stage, as defined in Figure 3.2). Number of samples is given by number of structures (cells) imaged, number of blocks (samples) those structures belonged to, and finally number of independent experiments performed.

Protocol and analysis	Chemical fixation	High pressure freezing followed by freeze substitution		
	2D imaging (70nm)	2D imaging (70nm)	Electron tomography (300nm)	
			Reconstructed	Segmented
Dev. stage	No. of structures, blocks, ind. experiments			
I. Concentrator	10, 6, 3	2, 2, 2	0, 0, 0	0, 0, 0
II. Bicentriole	3, 2, 2	1, 1, 1	3, 2, 1	1, 1, 1
III. Separated sister centrioles	76, 19, 5	40, 10, 4	3, 2, 1	1, 1, 1
IV. Docked centrioles and ciliogenesis	148, 18, 4	54, 7, 3	3, 2, 1	1, 1, 1
V. Final cytodifferentiation	120, 10, 3	23, 3, 2	0, 0, 0	0, 0, 0

3.3.2.3 Electron tomography and segmentation

300nm thick sections from high pressure frozen-freeze substituted samples were collected as described previously, however these were not post-stained. In these sections, dual-axis tilt series of serial sections were rapidly acquired (Schorb et al., 2019) using a Gatan OneView Camera and SerialEM Software (Mastronarde, 2005) on a Tecnai F30 (FEI) operated at 300keV. Electron tomograms were reconstructed from the dual-axis tilt series, and serial section tomograms were all stitched in z using eTomo/IMOD software (Kremer et al., 1996). Some electron tomograms were automatically reconstructed according to (Mastronarde and Held, 2017), while others were individually processed. At least three tomogram series of each stage/structure of interest were reconstructed and stitched, with one being also segmented in IMOD (Table 3.1).

3.3.3 Fast timelapse imaging of sperm cell motility, tracking and analysis

Gametangia from 5 individual WT plants were dissected onto a coverslip containing 30 μ l of sperm cell media (0.45mM CaCl₂, 0.3mM MgSO₄, 0.02mM KNO₃ and 0.081mM NaHCO₃)(Ortiz-Ramírez et al., 2017). Individualized sperm cells from released clusters were imaged on a commercial Nikon High Content Screening microscope equipped with an Andor Zyla 4.2 sCMOS camera, using a 63x 1.27NA water objective in the BF (brightfield) channel, at 200 frames per second (FPS) during 1min. Acquired image sequences were analyzed using Fiji (Schindelin et al., 2012). A total of 135 cells were imaged with 89 being classified into two categories based on observed cilia beating patterns (synchronous vs. asynchronous cilia beating). Both cilia's tip and nucleus from 5 sperm cells from each category were manually tracked using TrackMate (Tinevez et al., 2016) Fiji plugin, for 1000 frames (5sec). Cilia tip

distance was calculated by frame using Euclidean distance in relation to the nucleus.

3.4 Results

3.4.1 The bicentriole-mediated pathway for *de novo* centriole biogenesis

The centriole is known for its 9-fold symmetry, complex ultrastructure and small size (LeGuennec et al., 2021). Centriole biogenesis has been studied in different organisms using several electron microscopy (EM) techniques, as these offer a unique opportunity to study small cellular structures with a high level of detail and are not constrained by antibody availability, nor molecular conservation. Therefore, as a first approach to investigate centriole assembly in *P. patens* I employed transmission electron microscopy (TEM). As *P. patens*' spermatogenesis occurs asynchronously amongst the several antheridia from the same individual, with the first sperm cells maturing within 15 days after induction (DAI) of sexual reproduction, I performed TEM imaging of samples chemically fixed at successive DAI to define the order of events that characterize *de novo* centriole biogenesis during *P. patens*' spermatogenesis. Then, sample size was increased using 15 DAI chemically fixed samples (Figure 3.1B), and all the structures/stages involved confirmed by using high pressure frozen-freeze substituted 15 DAI samples (Figure 3.2A-E). This systematic analysis allowed me to build an overview of the *de novo* centriole assembly pathway (Figure 3.2F).

At early stages of spermatogenesis (10-12 DAI) I failed to detect any centriole-like structures within sperm cells. However, I observed near the

nucleus a cloud of electron dense unstructured material with MTs emanating from it (Figures 3.1A arrows, and 3.2A arrows). This electron dense material may act as an MTOC and precede centriole biogenesis, perhaps concentrating its precursors. Therefore I named it “concentrator” (Figure 3.2F). From 13 DAI onwards, I started to observe bicentriole-like structures (Figures 3.1B and 3.2B). These are composed of an apparently continuous cartwheel hub (Figure 3.1B star), which is surrounded by a MT wall that shows a small discontinuity between two co-axially oriented centrioles (Figures 3.1B arrowheads, 3.2B arrowheads; and 3.2F).

As spermatogenesis proceeds, two individual centrioles per sperm cell were observed (Figures 3.1C), likely resulting from splitting of the bicentriole. Below the individualized centrioles, a multilayered structure (MLS) was recognizable. The MLS is composed of a spline of parallel singlet MTs on top of electron dense protein plates called lamellar strip (LS) (Figures. 3.1D and 3.2C)(Carothers and Duckett, 1980). The complex consisting of the two centrioles and the MLS migrated towards the cell surface, after which the centrioles docked to the membrane (Figure 3.1E). Both centrioles became basal bodies, assembling axonemes (Figures 3.1E, F and G) with the characteristic 9+2 MT arrangement of motile cilia (Figures 3.1H and I; 3.2D and F).

At this point, the sperm cells' locomotory apparatus was composed of two centrioles and cilia, as well as the plant-specific MLS (Figure 3.2F). The final step of cytodifferentiation (14-15 DAI) involved chromatin condensation and nuclear elongation (Figure 3.1H and I; and 3.2E), cytosolic volume reduction, mitochondria fusion, and the presence of what appears to be an undifferentiated plastid containing starch-like material (Figures 3.2E and F). Interestingly, the lamellar strip component of the MLS disappeared in the final stage of development (Figure 3.1I), which is similar to what is found in other plant species, such as

Marchantia polymorpha and *Phaeoceros laevis* (Carothers and Duckett, 1980).

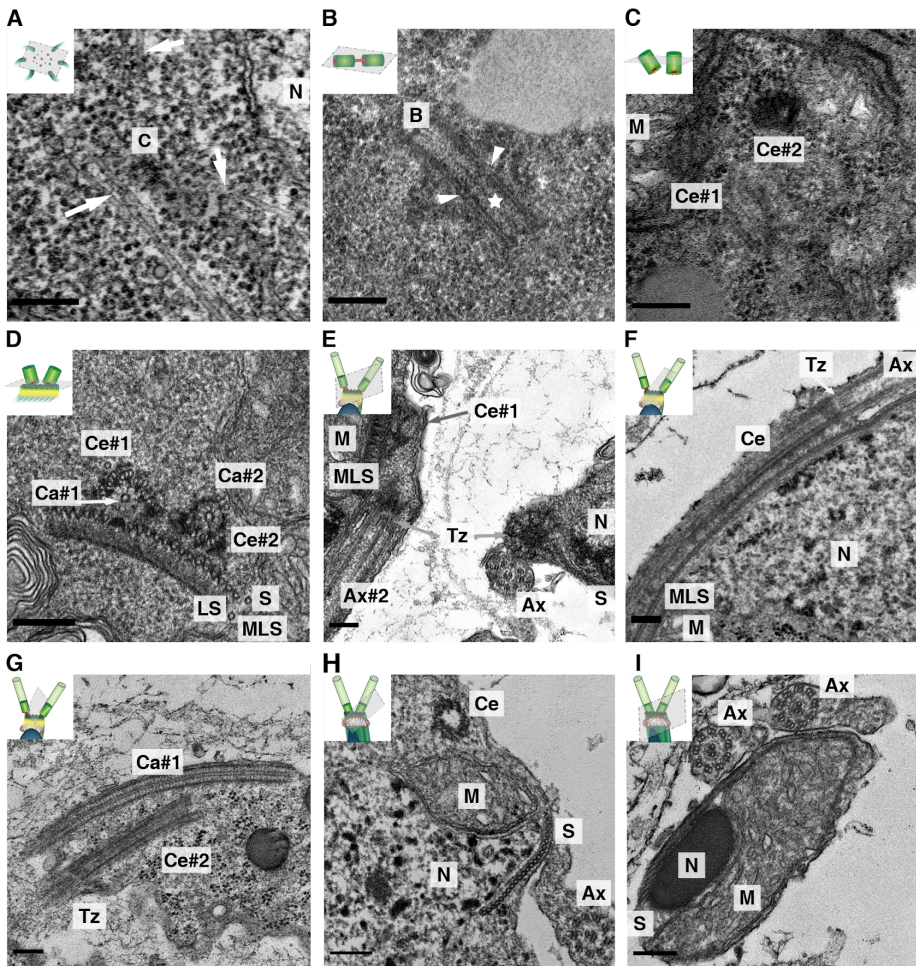


Figure 3.1: 2D TEM representative images of the bicentriole-mediated centriole assembly pathway in chemically fixed samples. A. Electron dense agglomeration of material, which I named “concentrator” with microtubules emanating from it (arrows); **B.** Bicentriole structure, with the arrowheads highlighting the discontinuity of the centriolar walls, and the star pinpointing the continuous cartwheel hub; **C.** Individualized centrioles organized side-by-side. **D.** Sister centrioles associated with the multilayered structure (MLS). Note the

incomplete centriolar walls; **E.** Centrioles docked to the cellular membrane assemble the transition zone (Tz) of the cilia; **F.** Longitudinal view of a centriole docked to the cellular membrane and templating the growth of the ciliary axoneme. **G.** Longitudinal view of both centrioles. While one centriole appears to be fully decorated by microtubules and docked to the membrane (Ce#2), only a long naked cartwheel region of the other centriole is observed (Ca#1); **H.** Example of a cell undergoing chromatin condensation. Note the absent cartwheel structure in the centriole's lumen (Ce); **I.** Sperm cell cytodifferentiation yields an elongated mitochondrion and condensed nucleus. Note the absence of the lamellar strip and the clear 9+2 axonemal organization. Scale-bars = 200nm. C – concentrator; N – nucleus; B – bicentriole; M – mitochondrion; Ce – centriole; Ce#1 and Ce#2 – centrioles numbered 1 and 2 (numbering is arbitrary); Ca#1 and Ca#2 – cartwheel from centriole #1 and #2, respectively; MLS – multilayered structure, composed of the spline (S) and lamellar strip (LS); Tz – transition zone; Ax – ciliary axoneme (Ax#1 and Ax#2 – axonemes number 1 and 2, arbitrary numbering). For sample size, please refer to Table 3.1. Figure adapted from Gomes Pereira et al. (*in revision*).

This analysis revealed several intriguing features of *P. patens* centrioles, such as frequent incomplete centriolar walls (Figures 3.1D and F; and 3.2C), long cartwheel structures with no attached MTs (Figure 3.1G) and the apparent absence of a cartwheel within the centriolar walls of cytodifferentiating cells (Figure 3.1H). Those observations are unlikely to represent artifacts from the chemical fixation (Figure 3.1), as similar observations were made from cells subjected to high pressure freezing and freeze substitution (Figure 3.2). Therefore, I believe that such features may reflect unknown steps of biogenesis

and/or maturation, that are difficult to capture and to thus fully understand with 2D TEM.

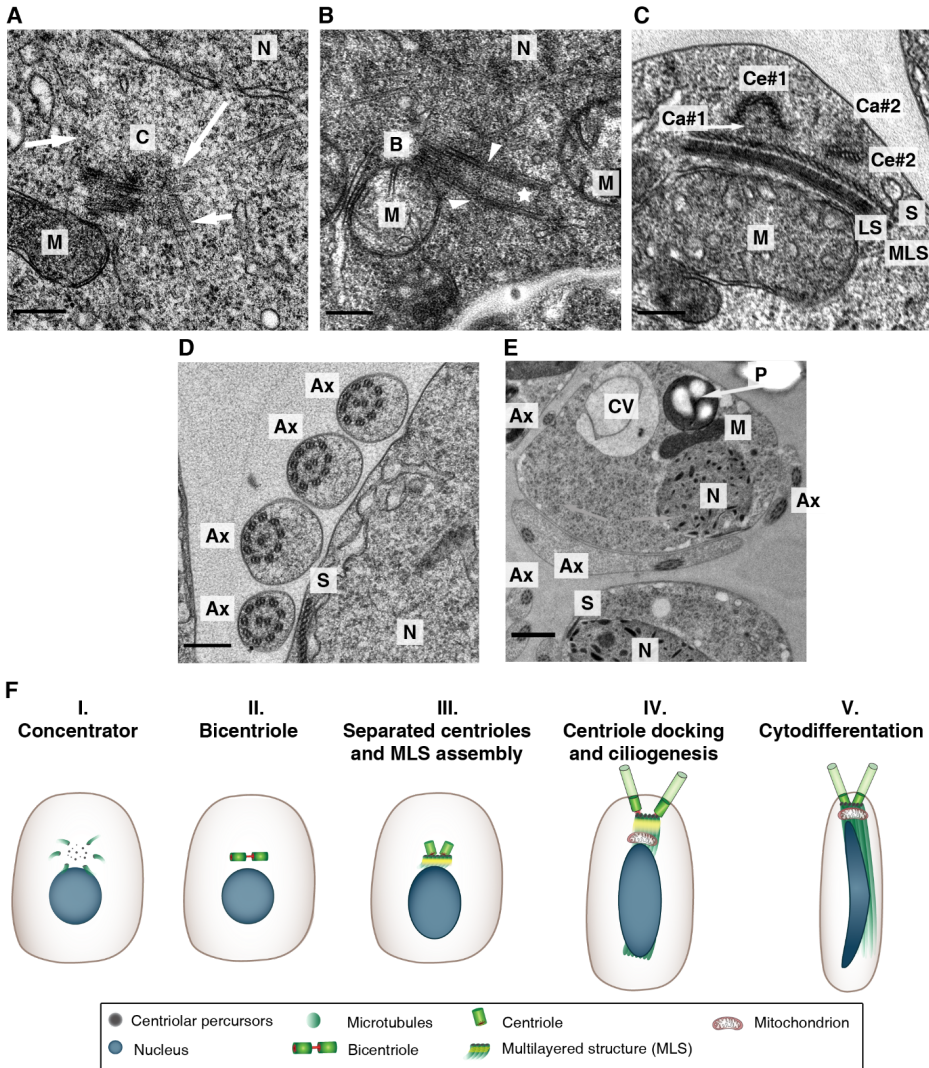


Figure 3.2: The bicentriole-mediated pathway for *de novo* centriole biogenesis in *P. patens*. **A.** Microtubule-rich (arrows) and electron dense region, representing a “concentrator”, seen in a high pressure frozen-freeze substituted (HPF+FS) sample; **B.** The bicentriole (B) by HPF+FS, composed of two discontinuous centriolar walls (arrowheads).

The star indicates the cartwheel's hub, although in this electron micrograph it is not clear its possible continuity; **C.** Centrioles, with incomplete centriolar walls, associated with the multilayered structure (MLS); **D.** 9+2 axonemal organization of *P. patens* cilia. Note that each cell should have 2 cilia, yet in this caption 4 axonemal cross-sections are observed. As the axonemes might be curved and cells are in close proximity inside the antheridium therefore, such cross-sections might derive from individual cilia or several sections through the same axoneme; **E.** Overview of a sperm cell undergoing the final stage of cytodifferentiation, characterized by cytoplasmic reduction (likely through autophagy in cytoplasmic vesicles (CV)), an undifferentiated plastid (P) with starch-like material (white regions), and undergoing chromatin condensation. Scale-bars = 200nm (A-D) and 1 μ m in E. C – concentrator; N – nucleus; M – mitochondrion; B – bicentriole; Ce#1 and Ce#2 – centrioles numbered 1 and 2 (numbering is arbitrary); Ca#1 and Ca#2 – cartwheel from centriole #1 and #2, respectively; MLS – multilayered structure, composed of the spline (S) and lamellar strip (LS); Ax – ciliary axoneme; CV – cytoplasmic vesicles; P - plastid. For sample size considerations, please see Table 3.1. **F.** Major steps in *de novo* centriole assembly *via* bicentrioles in *P. patens* sperm cells. I. Concentrator - before any centriolar-like structure being detected, only electron dense material near the nucleus and with MTOC activity is observed; II. Bicentriole - then, two sister centrioles assemble *de novo*, coaxially oriented and potentially connected by their cartwheel hub; III. Separated centrioles and MLS assembly - the sister centrioles separate, and associate with the newly assembled MLS; IV. Centriole docking and ciliogenesis - the complex of centrioles and MLS moves towards the cell membrane, allowing centrioles to dock and ciliogenesis to begin; V. Cytodifferentiation - finally, the cell undergoes the final stage of cytodifferentiation, characterized by extensive chromatin condensation

and cytosol reduction. At this point, the lamellar strip is no longer observed, and centrioles appear to lack cartwheels. Scheme adapted from Gomes Pereira et al. (*in revision*).

3.4.2 3D ultrastructural analysis of centriole assembly reveals asymmetrical centriole maturation

Given the limitations of 2D TEM, and to better characterize the organization of *P. patens* locomotory apparatus, I proceeded to perform 3D electron tomography (ET) throughout different maturation stages (Figures 3.3 to 3.6). In ET, the information collected by tilting the sample at incremental degrees is used to assemble a three-dimensional image of the target structure. 3 tomograms of each of the following stages: bicentriole (II), separated centrioles + MLS (III), and docked centrioles (IV) were obtained, and one of each was segmented. This allowed me to characterize, with an unprecedented level of detail, the structures involved in locomotory apparatus assembly and maturation. Unfortunately, due to difficulty in finding samples at this stage, no “concentrator” tomograms were obtained and, due to technical limitations, tomograms of the final stage of cytodifferentiation couldn't be reconstructed.

3.4.2.1 Centrioles assemble as a bicentriole which contains two centrioles of opposite polarities and nucleates microtubules

The bicentriole is an intriguing structure formed by *de novo* biogenesis, and for which little detail is known (Moser and Kreitner, 1970; Robbins, 1984). I was able to capture the bicentriole stage by ET. Its segmentation (3D model - Figure 3.3) confirms previous observations that this structure comprises two similar 9-fold symmetrical centrioles arranged linearly (Figure 3.3D and E) and connected by a common

cartwheel (Figure 3.3F). Furthermore, several individual MTs emanate from this bicentriole, suggesting it functions as an MTOC (Figure 3.3C).

A closer examination of the bicentriole features from the three reconstructed tomograms allowed the confirmation of an apparent continuity of the cartwheel hub between both centrioles (Figures 3.4 A-C arrows). Moreover, both sister centrioles (centrioles from the same bicentriole) have very similar lengths (262nm vs. 270nm - Figure 3.4A; 210nm vs. 212nm - Figure 3.4B; and 260nm vs. 256nm - Figure 3.4C), being composed of both doublet and triplet microtubules (Figures 3.4 D-I arrowheads), suggesting that both centrioles might still be assembling. Interestingly, these electron tomograms also revealed that connected sister centrioles appear to have opposite polarities, with microtubules from one centriole displaying a clockwise twist (Figures 3.4 D-F), while the other centriole microtubules appear to be twisted anticlockwise (Figure 3.4 G-I).

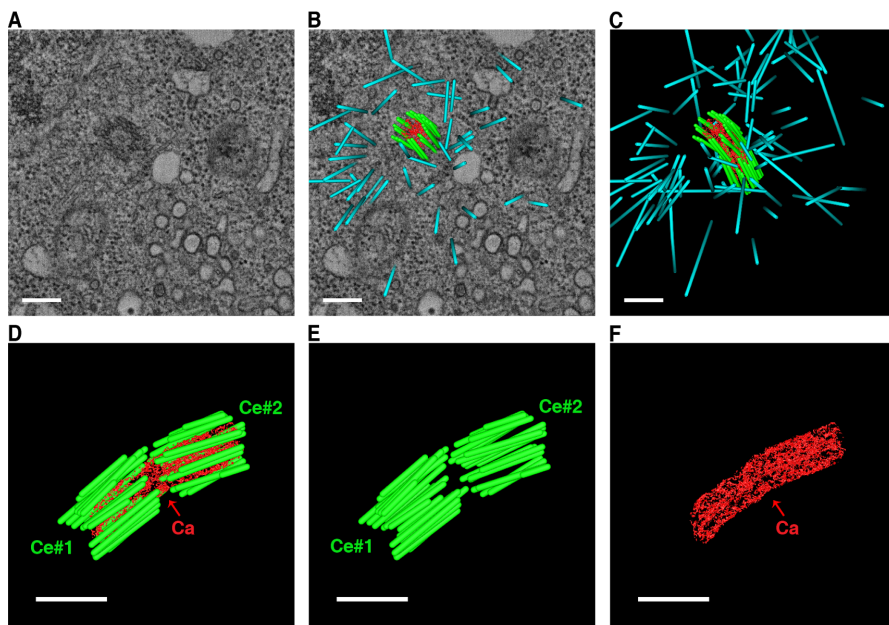


Figure 3.3: 3D model and analysis of a bicentriole. **A.** Electron tomogram snapshot; **B.** Superimposition of the tomogram with its

segmentation; **C**. 3D model of a bicentriole, with several astral microtubules (cyan) emanating from the structure; **D**. Rotated 3D model of the bicentriole, composed of two centriolar units (Ce#1 and Ce#2, green) connected by their inner continuous cartwheel (Ca, red); **E**. The walls of the two sister centrioles (Ce#1 and Ce#2) of the same bicentriole are discontinuous; **F**. Isosurface model of the continuous cartwheel (Ca) that connects both centrioles. Scale-bars = 200nm. Figure adapted from Gomes Pereira et al. (*in revision*).

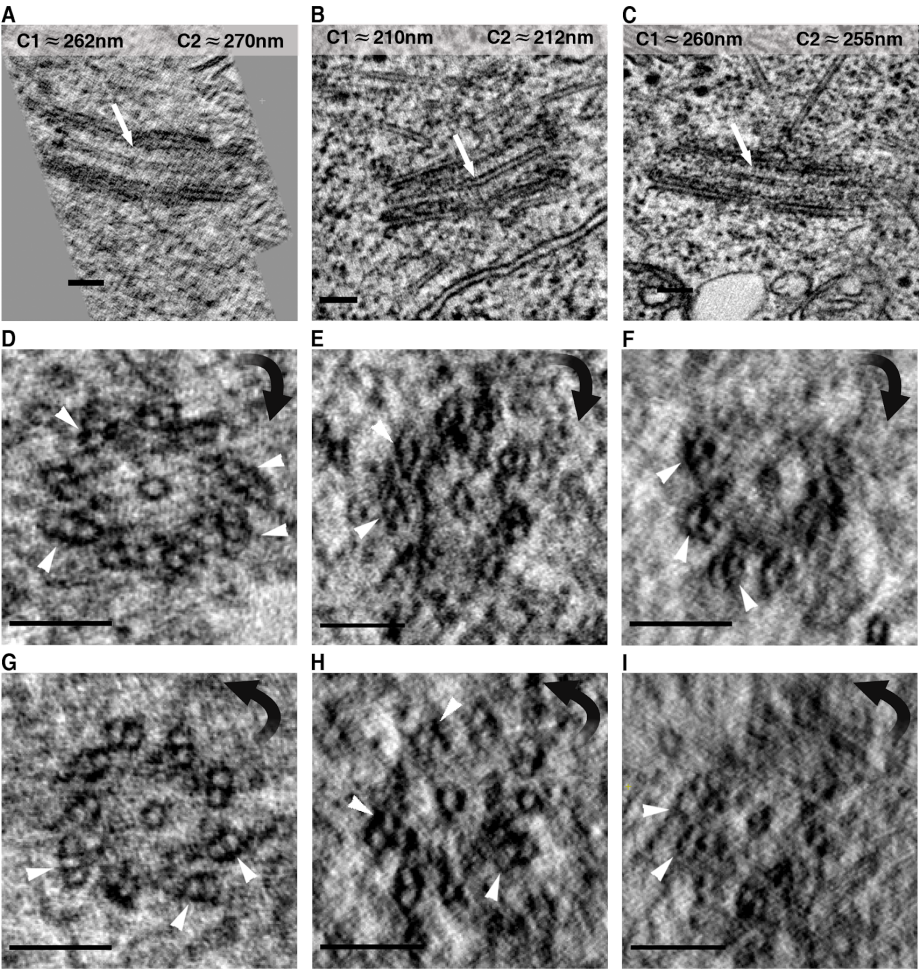


Figure 3.4: A detailed view into the bicentriole structure: two centrioles of similar lengths but opposite polarities, connected by a continuous cartwheel hub. A to C. Splicer longitudinal view of each of the three tomograms reconstituted (**A**, **B** and **C**), revealing the continuity of the cartwheel hub (arrows) and similar lengths of both centrioles within each pair (C1 and C2); **D to I.** Splicer transversal views of each centriole within the three bicentrioles reconstructed, showing that their walls have doublet and triplet microtubule blades (arrowheads depict visible microtubule triplets), and revealing centrioles within each bicentriole to have opposite polarities (clockwise - **D to F**; or anticlockwise twist - **G to I**). Note that images in each column derive from the same bicentriole tomogram, *i.e.* D and G represent the sister centrioles shown in A; Similarly, E and H belong to the bicentriole displayed in B; and C depicts the centriolar pair seen in F and I. Scale-bars = 100nm.

3.4.2.2 The two similar centrioles separate and associate with the multilayered structure

Electron tomograms of the stage after bicentriole splitting and before ciliogenesis (stage III. in Figure 3.2F), where centrioles are individualized and associated with the MLS (Figure 3.5) were also captured. In the 3D model corresponding to such stage (Figures 3.5C and D), one centriole (Ce#1) appeared to be slightly longer (approximately 750nm) than the other (Ce#2, approximately 550nm), suggesting that centrioles elongate independently. At this stage both centrioles contained nine MT triplet blades of slightly different sizes and a cartwheel structure throughout their entire length (Ca#1 and #2 respectively, Figure 3.5E). Both centrioles resided above the multilayered structure (MLS) (Figures 3.5C and D). Below the parallel microtubules of the spline (S), the striation of the lamellar strip (LS) was apparent (Figures 3.5A and F). Moreover, a

gap between adjacent MTs was seen within the spline, under one of the centrioles (Ce#2). This gap was occupied by a previously uncharacterized amorphous electron density (AeD) that localizes between the LS and the centriole (Figure 3.5F).

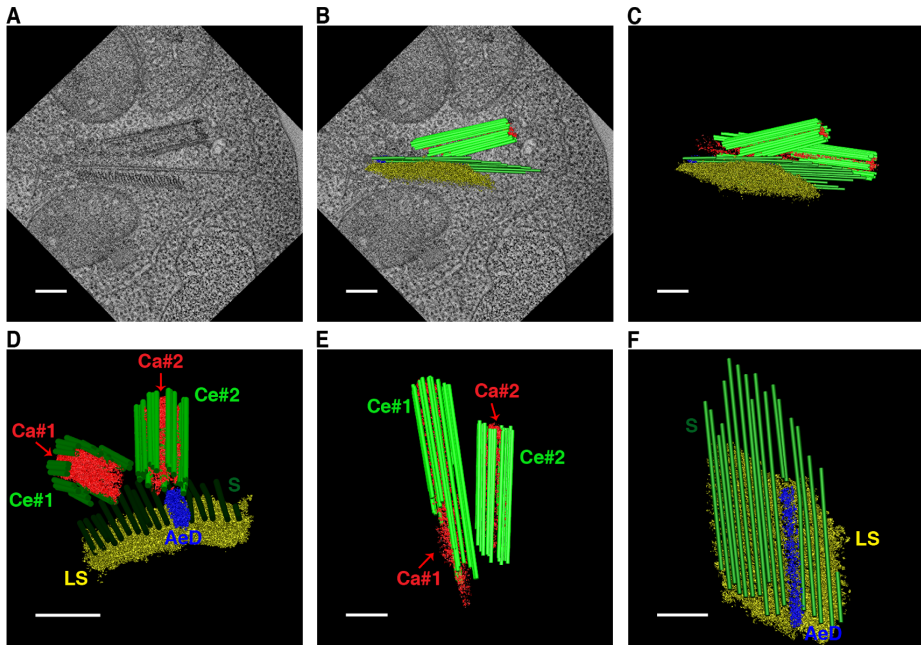


Figure 3.5: 3D architecture of individualized sister centrioles anchored to the multilayered structure. **A.** Snapshot of an electron tomogram showing a longitudinal view of one centriole anchored to the MLS. Striation is visible on the lamellar strip, below the centriole and spline; **B.** Electron tomogram and its 3D model overlapping; **C.** 3D model of centrioles associated with the MLS; **D.** Rotated view of the 3D model represented in C, highlighting the existence of an amorphous electron density (AeD, dark blue) between the LS (yellow) and one of the centrioles (Ce#2, light green); **E.** Top view of the two individualized centrioles (Ce#1 and Ce#2, light green) and their corresponding cartwheels (Ca#1 and Ca#2 respectively, red); **F.** Top view of the MLS structure. The AeD (dark blue) is located in a gap of the spline's

microtubules (S, dark green) and directly above the LS (yellow). Scale-bars = 200nm. Figure adapted from Gomes Pereira et al. (*in revision*).

3.4.2.3 Sister centrioles mature asymmetrically

Centriole maturation to basal body involves its docking to the cell's membrane and formation of a transition zone, an area at the distal part of the basal body which connects the axoneme with the membrane, while controlling the transport of molecules into this axoneme.

3D electron tomography data of this stage revealed very intriguing structural features, namely a remarkable asymmetry and a unique centriolar architecture (Figure 3.6). I observed that both cartwheels outgrew from the centriole walls without any MTs attached – from here onwards called “naked” cartwheels; with one of them extending much further (Figure 3.6D Ca#1, red). Such stable elongation of naked cartwheel regions was surprising, given that cartwheels and microtubules were suggested to cooperatively establish a proper stable centriole architecture (Hilbert et al., 2016). The shortest cartwheel (Ca#2) was decorated by a full 9-fold symmetrical centriolar wall constituted by microtubule triplets (Figures 3.6D and E, Ca#2 (cartwheel - red) and Ce#2 (centriole - light green)). A naked cartwheel was found at the proximal end of this centriole, while at its distal end, a transition zone connected the basal body to the membrane and the axoneme (Figures 3.6D and E, Tz magenta). This transition zone showed a similar structure as observed for *Chlamydomonas reinhardtii* (O'Toole et al., 2003) and *Marchantia polymorpha* (Carothers and Kreitner, 1968) encompassing the characteristic stellate fiber pattern (Figure 3.6G).

The centriole with the longest naked cartwheel (Ca#1) showed only two MT triplets throughout the depth of the tomogram obtained (around 3.3µm) (Figures 3.6C, D and E), suggesting that some MT triplets within

the same centriole, might elongate further than others. No major alterations were detected in terms of the organization of the multilayered structure in this stage of spermatogenesis in *P. patens* (Figure 3.6F). The previously described amorphous electron density (AeD) was observed in close contact with the LS and the shortest cartwheel (Figures 3.6H), while the lamellar strip showed its characteristic striations (Figures 3.6I) (Carothers and Duckett, 1980).

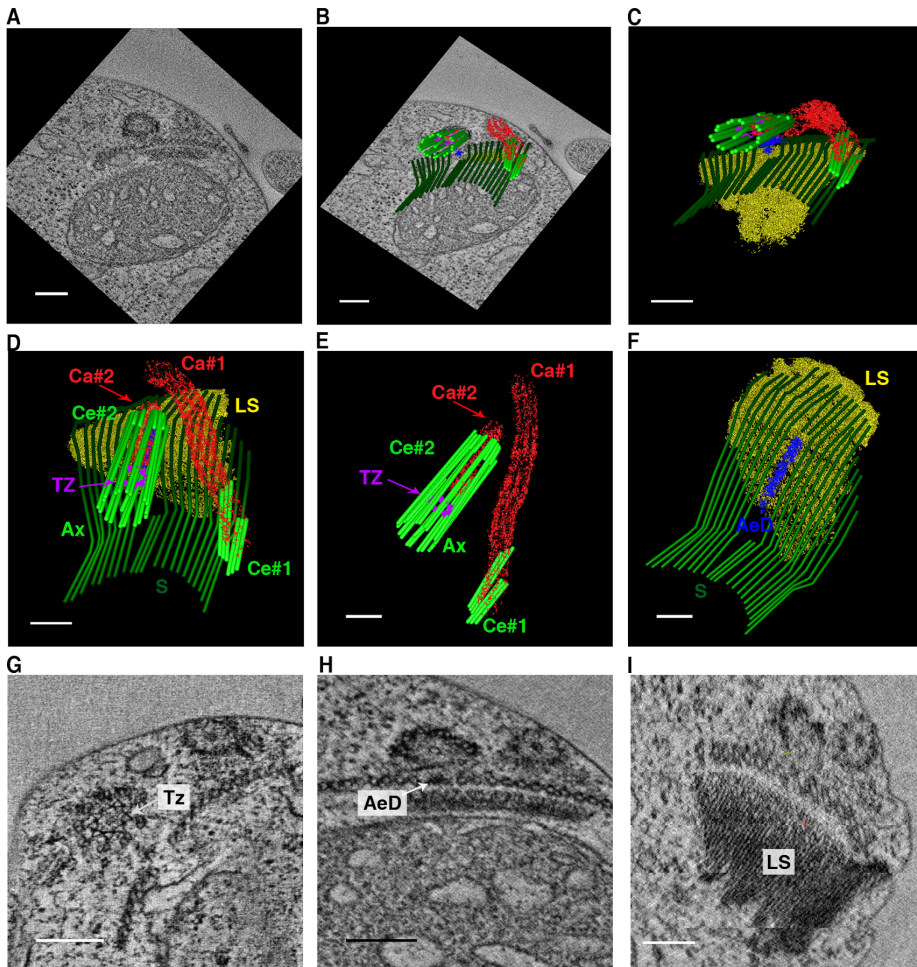


Figure 3.6: 3D analysis of centriole maturation reveals asymmetries between sister centrioles and a long “naked” cartwheel. A. Snapshot of the electron tomogram modeled; **B.** Correspondence

between the tomogram snapshot and its segmentation; **C.** View of the 3D model; **D.** Top view of the 3D reconstruction is shown in C, revealing clear asymmetries between the two sister centrioles (Ce#1 and Ce#2, light green); **E.** The two individual centrioles, revealing clear asymmetries between them. Note that a big portion of one cartwheel (Ca#1) is seen deprived of centriolar microtubules – here called “naked” cartwheel. Furthermore, while one centriolar wall is 9-fold symmetrical (Ce#2), only 2 of the 9 centriolar triplets are observed in the other centriole (Ce#1); **F.** Top view of the MLS, similar to what has been observed in Figure 3.5F; **G.** Tomogram snapshot highlighting the structure of *P. patens*' transition zone (Tz); **H.** Tomogram view highlighting the AeD connecting one centriole (Ce#2) to the LS; **I.** Splicer view of the tomogram, highlighting the striation of the lamellar strip (LS). Ce #1 and #2 (light green) – wall of centrioles numbered 1 and 2 (arbitrary numbering); Ca #1 and #2 (red) – cartwheel of centrioles number #1 or #2, respectively; LS (yellow) – lamellar strip of the MLS; S (dark green) – spline of the MLS; AeD (blue) – amorphous electron density; TZ (magenta) – transition zone (templated from Ce#2); Ax – ciliary axoneme (templated from Ce#2). Scale-bars = 200nm. Figure modified from Gomes Pereira et al. (*in revision*).

Together, these electron tomography observations showed that centrioles assembled from the same bicentriole (sister centrioles) are initially identical, despite being connected with opposite polarities. However, upon splitting and maturation they elongate asymmetrically, docking to the membrane with similar orientation/polarity. The centriole asymmetries revealed indicate that cartwheel, and possibly centriole length are, at least temporarily, distinct between the two sister centrioles. Furthermore, different MT triplets seem to have different lengths along the same mature centriole, in concordance with previous observations in

the bryophyte *Marchantia polymorpha* (Carothers and Kreitner, 1968). This surprising asymmetry raises important questions as to how distinct features are generated from seemingly similar entities, in particular, what molecular processes regulate the elongation of the naked cartwheel and/or specific MT triplets, and whether there is a functional consequence of such differences.

3.4.3 *P. patens* cilia display two distinct behaviours: synchronous and asynchronous beating

I then asked what could be the physiological significance for the unexpected centriole asymmetry seen between the two *P. patens* sister centrioles (Figure 3.6). In *Marchantia polymorpha*, sperm cells were suggested to have different beating patterns, with the posterior cilium beating in a 3D-lasso pattern while the anterior one displayed only planar beating (Miyamura et al., 2002). I hypothesized that a similar mechanism could be present in *P. patens*, in which the centriole structural asymmetry would render the centrioles differentially resistant to mechanical stresses and/or docked at distinct positions/angles on the cell membrane. Both these non-mutually exclusive scenarios could constrain ciliary motility, making the two cilia functionally distinct, and enable distinct beating patterns.

In order to understand if *P. patens*' cilia could beat differently, I imaged isolated sperm cells at a high frame rate (200FPS) and manually tracked cilia tip displacement (relative to the nucleus). The data obtained shows that in 83% (74/89) of the imaged cells, only one cilium appeared to be actively moving (Figure 3.7A green line), while the inactive one appeared to passively follow the cell's rotation (Figure 3.7A blue line). By averaging cilia beating patterns from 5 cells it was possible to distinguish the beating cilia, with frequent changes its nuclear distance (Figure 3.7B

green line) from those cilia that appeared to be inactive (Figure 3.7B blue line).

The remaining 17% of the analyzed sperm cells (15/89) appeared to have both cilia actively beating, with no clear differences being detected between their beating patterns (Figure 3.8). These observations indicate that while both cilia are able to beat, most often cells show asynchronous beating, with only one cilium appearing to be active.

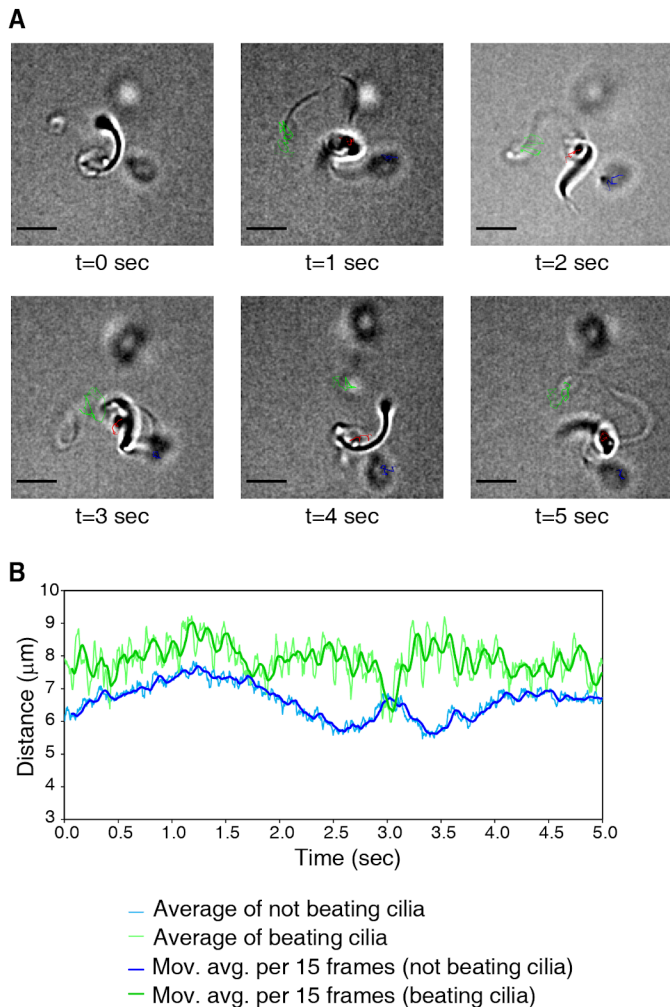


Figure 3.7.: The majority of cells display asynchronous ciliary beating. A. Snapshots of a sperm cell tracked over time, showing

asynchronous ciliary beating: one cilium appears to be actively beating (green), while the other (blue) moves only passively (following nuclear movement, red). Scale-bars = 5 μ m; **B**. Ciliary-tip distance across time, showing a distinct pattern between both cilia. Thin lines represent average displacement for the beating cilium (green) or inactive cilium (blue) while thicker and lines represent their respective running averages across 15 frames. Pooled data from 5 cells. Figure adapted from Gomes Pereira et al. (*in revision*).

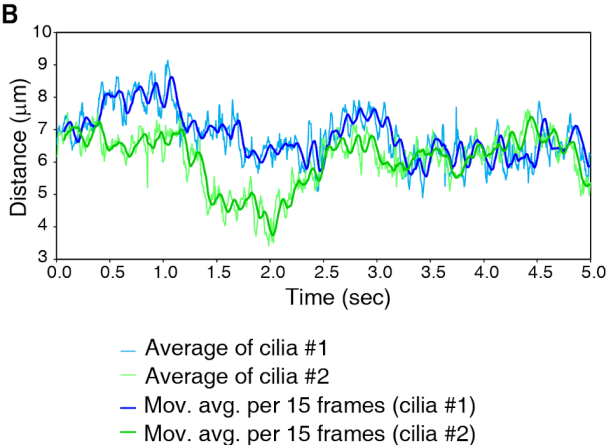
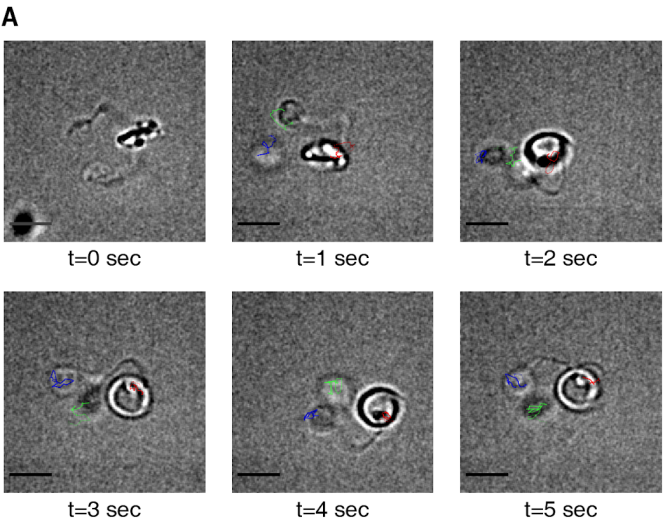


Figure 3.8: Both cilia are able to beat, and appear to do so synchronously. **A.** Example of a sperm cell tracked over time (cilia tracked in green and blue, nucleus in red). Scale-bars = 5 μ m; **B.** Ciliary-tip distance over 5 seconds, showing a similar pattern for both (green and blue) cilia. Thin lines represent average displacement for one cilium (green) or the other (blue) while thicker lines represent their respective running averages over 15 frames. Cilia colors were attributed randomly. Pooled data from 5 cells. Figure modified from Gomes Pereira et al. (*in revision*).

3.5 Discussion

While centriole duplication has been extensively described in the literature, not many studies have dwelt into *de novo* centriole biogenesis and within these, particular focus has been given to the deuterosome pathway (Mercey et al., 2019a; b; Zhao et al., 2019). In fact, only two previous studies have focused on describing the bicentriole-mediated pathway in bryophytes (Moser and Kreitner, 1970; Robbins, 1984).

With this work, I have characterized *de novo* centriole biogenesis in the model moss *Physcomitrium patens* for the first time. 2D TEM analyses (Figures 3.1 and 3.2) allowed me to reconstruct the main events occurring during both *de novo* centriole assembly and locomotory apparatus maturation, while 3D electron tomography data revealed surprising features of such process.

As seen in the other bryophyte species where centriole assembly has been characterized (Moser and Kreitner, 1970; Robbins, 1984), *P. patens* centrioles assemble *via* a bicentriole structure. No centriole-like structures or possible structure intermediates could be recognized

consistently in samples collected before 13 DAI (when the first bicentriole structures are detected). Only amorphous electron dense material seems to concentrate in a region near the nuclear envelope, from where several microtubules appear to emanate (Figures 3.1A and 3.2A). The bicentrioles seen throughout this study also localize near the nucleus, and electron tomography data has revealed several microtubules to radiate from the bicentriole region (Figures 3.3 and 3.4). Therefore, I believe this “concentrator” could represent the first step towards bicentriole assembly, in resemblance to what has been suggested to occur in other *de novo* centriole assembly pathways, where concentration of centriolar precursors *via* microtubules is thought to trigger centriole assembly (Nabais et al., 2018; Mercey et al., 2019b; Nabais et al., 2021).

The bicentriole is the first centriole-like structure recognizable, being composed of two co-axially oriented 9-fold symmetrical centrioles, which I named sister centrioles, and that appear to be connected by a common cartwheel (Figures 3.1B, 3.2B). Such structure was previously described in other plant species that possess biciliated sperm (Moser and Kreitner, 1970; Robbins, 1984; Renzaglia et al., 1999) but also in the protist *Labyrinthula* spp. (Perkins, 1970). Yet, the unprecedented 3D analysis revealed that the two sister centrioles are arranged with opposite polarities (Figure 3.4). Moreover, both centrioles appear to have similar length and to still contain some microtubule doublet blades, as opposed to the 9 microtubule triplets of mature centrioles (Figure 3.4). Therefore, I believe sister centrioles assemble at a similar time, in accordance with what has been described in the only report on early events of bicentriole assembly by Robbins (1984). Such observation raises interesting questions regarding the establishment of centriole polarity and the role of the cartwheel in this process. For instance, is the cartwheel responsible for the different sister centriole polarities? If so, how does the seemingly

continuous cartwheel establish a different polarity to each side? And, does it grow on both sides? Or could it be that the cartwheel is not fully continuous, but indeed each sister centriole has its own cartwheel, and these are just too close to be individualized, even by electron tomography? Alternatively, it is also possible that whether continuous or not, the cartwheel has no major role in the establishment of *P. patens* centriole polarity. However, in order to address many of these questions and to properly assess cartwheel continuity and polarity, higher resolution structural techniques such as cryo-electron tomography are needed.

After sister centrioles assemble within a bicentriole, they must separate. Unfortunately, the particular moment of bicentriole splitting was never observed during this work, possibly because this might occur relatively fast. Therefore, in order to catch this unique event, samples would need to be fixed quickly and in a precise (and unknown) moment in time. Nevertheless, I have observed the already separated individualized centrioles (Figure 3.1C), which are then associated with the multilayered structure (Figures 3.1D, 3.2C and 3.5). The MLS is a plant-specific structure, being composed of a spline of parallel singlet microtubules which reside below the centrioles, with the electron dense striated lamellar structure beneath. While the MLS functions remain unclear, its structure appears to be particularly conserved (Renzaglia and Garbary, 2001). Yet, the structural analysis here described did reveal the existence of an amorphous electron dense region (Figure 3.3 AeD), located in a gap of the spline that appears to connect the LS to one of the centrioles. Interestingly, above the MLS the two sister centrioles reside almost parallel to one another, and appear to be similarly oriented (polarity-wise), implying a rotation/rearrangement process after bicentriole splitting.

After their association to the MLS, centrioles start to migrate towards the tip of the cell, and eventually dock to the cell membrane, maturing into basal bodies of, what appear to be, two structurally similar cilia (Figures 3.1 and 3.2). Surprisingly, I have revealed that centriole maturation yields distinct centriole architectures, resulting in microtubule-“naked” cartwheels of variable lengths (Figure 3.6). Moreover, only two microtubule triplets were observable in the segmented tomogram, suggesting that triplet MTs within the same mature centriole may have distinct lengths (Figure 3.6). Such observation corroborates the incomplete centriole walls frequently seen in our 2D TEM analyses (Figures 3.1D and 3.2C). Unfortunately, the reconstruction of tomograms from cytodifferentiated cells has failed, which would have been critical to understand if the observed centriole asymmetries represent transient or final states of centriole elongation. Still, the remarkable centriole asymmetries unravelled in this ultrastructural characterization of *P. patens*' locomotory apparatus raise many questions regarding the regulation of such features, and also their physiological relevance.

In order to explore a possible physiological relevance for the centriole asymmetries revealed here (Figure 3.6), and supported by observations from ciliary beating of sperm cells of the bryophyte *Marchantia polymorpha* (Miyamura et al., 2002), I hypothesized that the two cilia from *P. patens* sperm cells could also beat differently. Indeed, I observed two distinct ciliary behaviours, the most common beating pattern being asynchronous, with only one cilium actively beating (Figure 3.7). However, both cilia were also able to beat synchronously, which I believe might lead to the helical motion described by Ortiz-Ramírez et al. (2017) (Figure 3.8). *Chlamydomonas* cells grown in the dark can alternate their swimming behavior between periods of synchronous and asynchronous ciliary beating, leading to cells moving in a nearly straight trajectory or its

reorientation, respectively (Polin et al., 2009). I envision that *P. patens*' cilia might be capable of alternating their beating behaviour, potentially guided by external cues (such as signals from the egg), supporting sperm cell guidance. However, this data is highly limited, with only a low number of cells analyzed and for a short period of time. Moreover, due to technical and sample limitations, it is possible that the cells released from randomly oriented antheridia may be too far from the egg, or its signal too diluted, to activate proper steering and motility. Finally, my structural work was not focused at analyzing ciliary structures deeply, so one cannot exclude the existence of subtle differences between both cilia, which may have escaped such analyses.

With this work, I pioneered the structural characterization of the locomotory apparatus of *P. patens* sperm cells, confirming the existence of common features with the locomotory apparatus and centriole assembly processes described in closely related species. Yet, a detailed 3D structural analysis allowed me to expose, with unprecedented detail, new structural features of bicentrioles, such as the opposite polarity of its centrioles, and its apparent MTOC capacity; as well as to reveal the surprising asymmetrical maturation of sister centrioles. In the future, it will be important to also characterize both the ciliary structure, exploring possible asymmetries between both cilia; as well as the locomotory apparatus of a fully mature sperm cell, as to determine if centriole asymmetries remain after final cytodifferentiation. Moreover, studies should also aim at clarifying the possible link, if any, between centriole asymmetry and ciliary beating.

3.6 Author contributions and acknowledgements

3.6.1 Author contributions

All plants were grown by myself. Electron microscopy experiments were optimized and performed by myself and Ana Laura Sousa (Electron Microscopy Facility (EMF) technician at Instituto Gulbenkian de Ciência (IGC)). Ana Laura Sousa sectioned the EM samples for all experiments, and assisted me with some of the imaging. Ciliary beating experiments were optimized and performed by myself, with the help of Catarina Nabais (then PhD student at “Cell Cycle Regulation” and “Principles of Nuclear Dynamics” laboratories from IGC, currently at Max Planck Institute of Molecular Cell Biology and Genetics). Martin Schorb (Electron Microscopy Core Facility (EMCF) technician in the European Molecular Biology Laboratory (EMBL)) assisted in acquisition and automated reconstruction of the electron tomography data. Alex J. Holmes (then summer school student at IGC, now at Institute for Medical Research, The Keith Peters Building, University of Cambridge) and I, segmented the electron tomograms. Erin M. Tranfield (head of the EMF at IGC) aided in acquisition of the electron tomography data. Finally, this work was supervised by Jörg D. Becker (then head of the “Plant Genomics” laboratory at IGC, currently at Instituto de Tecnologia Química e Biológica António Xavier (ITQB)) and Mónica Bettencourt-Dias (head of the “Cell Cycle Regulation” laboratory at IGC).

3.6.2 Acknowledgements

I thank the Electron Microscopy Core Facility (EMBL, Heidelberg) for supporting electron tomography data acquisition, and Pedro Machado (King's College London, UK) for support with tomogram segmentation. I would like to acknowledge the IGC's Electron Microscopy Facility (EM

protocol optimization, sample preparation and equipment availability), and Plant Facility for maintenance of the plant's growth chambers).

3.7 References

Ashton, N.W., and Cove, D.J. (1977). The isolation and preliminary characterisation of auxotrophic and analogue resistant mutants of the moss, *Physcomitrella patens*. *Mol. Gen. Genet.* *154*, 87–95.

Carothers, Z.B., and Duckett, J.G. (1980). The Bryophyte Spermatozoid : A Source of New Phylogenetic Information. *Bull. Torrey Bot. Club* *107*, 281–297.

Carothers, Z.B., and Kreitner, G.L. (1968). Studies of Spermatogenesis in the Hepaticae. II. Blepharoplast structure in the spermatid of *Marchantia*. *J. Cell Biol.* *36*, 603–616.

Gifford, E.M., and Larson, S. (1980). Developmental Features of the Spermatogenous Cell in *Ginkgo biloba*. *Am. J. Bot.* *67*, 119–124.

Gomes Pereira, S., Sousa, A.L., Nabais, C., Paixão, T., Holmes, A.J., Schorb, M., Goshima, G., Tranfield, E.M., Becker, J.D., and Bettencourt-Dias, M. The 3D architecture and molecular foundations of *de novo* centriole assembly via bicentrioles. *BioRxiv Preprint*. doi: 10.1101/2020.12.21.423647

Hilbert, M., Noga, A., Frey, D., Hamel, V., Guichard, P., Kraatz, S.H.W., Pfreundschuh, M., Hosner, S., Flückiger, I., Jaussi, R., et al. (2016). SAS-6 engineering reveals interdependence between cartwheel and microtubules in determining centriole architecture. *Nat. Cell Biol.* *18*, 393–403.

Joukov, V., and De Nicolo, A. (2019). The Centrosome and the Primary Cilium: The Yin and Yang of a Hybrid Organelle. *Cells* *8*, 2–46.

Khan, M.A., Rupp, V.M., Orpinell, M., Hussain, M.S., Altmüller, J., Steinmetz, M.O., Enzinger, C., Thiele, H., Höhne, W., Nürnberg, G., et al. (2014). A missense mutation in the PISA domain of HsSAS-6 causes autosomal recessive primary microcephaly in a large consanguineous pakistani family. *Hum. Mol. Genet.* *23*, 5940–5949.

Khodjakov, A., Rieder, C.L., Sluder, G., Cassels, G., Sibon, O., and Wang, C.L. (2002). *De novo* formation of centrosomes in vertebrate cells arrested during S phase. *J. Cell Biol.* *158*, 1171–1181.

Kremer, J.R., Mastronarde, D.N., and McIntosh, J.R. (1996). Computer Visualization of Three-Dimensional Image Data Using IMOD. *J. Struct. Biol.* *116*, 71–76.

Landberg, K., Pederson, E.R. a, Viaene, T., Bozorg, B., Friml, J., Jönsson, H., Thelander, M., and Sundberg, E. (2013). The moss *Physcomitrella patens* reproductive organ development is highly organized, affected by the two SHI/STY genes and by the level of active auxin in the SHI/STY expression domain. *Plant Physiol.* *162*, 1406–1419.

Le Guennec, M., Klena, N., Aeschlimann, G., Hamel, V., and Guichard, P. (2021). Overview of the centriole architecture. *Curr. Opin. Struct. Biol.* *66*, 58–65.

Levine, M.S., Bakker, B., Boeckx, B., Moyett, J., Lu, J., Vitre, B., Spierings, D.C., Lansdorp, P.M., Cleveland, D.W., Lambrechts, D., et al. (2017). Centrosome Amplification Is Sufficient to Promote Spontaneous Tumorigenesis in Mammals. *Dev. Cell* *40*, 313–322.

Lopes, C.A.M., Mesquita, M., Cunha, A.I., Cardoso, J., Carapeta, S., Laranjeira, C., Pinto, A.E., Pereira-Leal, J.B., Dias-Pereira, A., Bettencourt-Dias, M., et al. (2018). Centrosome amplification arises before neoplasia and increases upon p53 loss in tumorigenesis. *J. Cell Biol.* *217*, 2353–2363.

Martel, G., Guerrero, A., Vieira, A.F., De Almeida, B.P., Machado, P., Mendonça, S., Mesquita, M., Villarreal, B., Fonseca, I., Francia, M.E., et al. (2018). Over-elongation of centrioles in cancer promotes centriole amplification and chromosome missegregation. *Nat. Commun.* *9*.

Mastronarde, D.N. (2005). Automated electron microscope tomography using robust prediction of specimen movements. *J. Struct. Biol.* *152*, 36–51.

Mastronarde, D.N., and Held, S.R. (2017). Automated tilt series alignment and tomographic reconstruction in IMOD. *J. Struct. Biol.* *197*, 102–113.

Mercey, O., Al Jord, A., Rostaing, P., Mahuzier, A., Fortoul, A., Boudjema, A.R., Faucourt, M., Spassky, N., and Meunier, A. (2019a). Dynamics of centriole amplification in centrosome-depleted brain multiciliated progenitors. *Sci. Rep.* *9*.

Mercey, O., Levine, M.S., LoMastro, G.M., Rostaing, P., Brotslaw, E., Gomez, V., Kumar, A., Spassky, N., Mitchell, B.J., Meunier, A., et al. (2019b). Massive centriole production can occur in the absence of deuterosomes in multiciliated cells. *Nat. Cell Biol.* *21*, 1544–1552.

Miki-Noumura, T. (1977). Studies on the *de novo* formation of centrioles: aster formation in the activated eggs of sea urchin. *J. Cell Sci.* *24*, 203–216.

Miyamura, S., Matsunaga, S., and Hori, T. (2002). High-speed video microscopical analysis of the flagellar movement of *Marchantia polymorpha* sperm. *Bryol. Res.* *8*, 79–83.

Moser, J.W., and Kreitner, G.L. (1970). Centrosome Structure in *Anthoceros laevis* and *Marchantia polymorpha*. *J. Cell Biol.* *44*, 454–458.

Nabais, C., Pereira, S.G., and Bettencourt-Dias, M. (2018). Noncanonical Biogenesis of Centrioles and Basal Bodies. *Cold Spring Harb. Symp. Quant. Biol.* *82*:123-135.

Nabais, C., Pessoa, D., de-Carvalho, J., van Zanten, T., Duarte, P., Mayor, S., Carneiro, J., Telley, I.A., and Bettencourt-Dias, M. (2021). PIK4 triggers autonomous *de novo* centriole biogenesis and maturation. *J. Cell Biol.* *220* (5): e202008090.

Nigg, E.A., and Holland, A.J. (2018). Once and only once: Mechanisms of centriole duplication and their deregulation in diseases. *Nat. Rev. Mol. Cell Biol.* *19*, 297–312.

O'Toole, E.T., Giddings, T.H., McIntosh, J.R., and Dutcher, S.K. (2003). Three-dimensional Organization of Basal Bodies from Wild-Type and δ -Tubulin Deletion Strains of *Chlamydomonas reinhardtii*. *Mol. Biol. Cell* *14*, 2999–3012.

Ortiz-Ramírez, C., Michard, E., Simon, A.A., Damineli, D.S.C., Hernández-Coronado, M., Becker, J.D., and Feijó, J.A. (2017). GLUTAMATE RECEPTOR-LIKE channels are essential for chemotaxis and reproduction in mosses. *Nature* *549*, 91–95.

Peel, N., Stevens, N.R., Basto, R., and Raff, J.W. (2007). Overexpressing Centriole-Replication Proteins *In Vivo* Induces Centriole Overduplication and *De Novo* Formation. *Curr. Biol.* *17*, 834–843.

Perkins, F.O. (1970). Formation of Centriole and Centriole- Like Structures During Meiosis and Mitosis in *Labyrinthula sp.* (Rhizopodea, Labyrinthulida). An electron-microscope study. *J. Cell Sci.* 6, 629–653.

Polin, M., Tuval, I., Drescher, K., Gollub, J.P., and Goldstein, R.E. (2009). *Chlamydomonas* swims with two “gears” in a eukaryotic version of run-and-tumble locomotion. *Science.* 325, 487–490.

Prigge, M.J., and Bezanilla, M. (2010). Evolutionary crossroads in developmental biology: *Physcomitrella patens*. *Development* 137, 3535–3543.

Rensing, S. a, Lang, D., Zimmer, A.D., Terry, A., Salamov, A., Shapiro, H., Nishiyama, T., Perroud, P.-F., Lindquist, E. a, Kamisugi, Y., et al. (2008). The *Physcomitrella* genome reveals evolutionary insights into the conquest of land by plants. *Science.* 319, 64–69.

Rensing, S.A., Goffinet, B., Meyberg, R., Wu, S.Z., and Bezanilla, M. (2020). The moss *Physcomitrium (Physcomitrella) patens*: A model organism for non-seed plants. *Plant Cell* 32, 1361–1376.

Renzaglia, K.S., and Garbary, D.J. (2001). Motile Gametes of Land Plants: Diversity, Development, and Evolution. *CRC. Crit. Rev. Plant Sci.* 20, 107–213.

Renzaglia, K.S., Bernhard, D.L., and Garbary, D.J. (1999). Developmental Ultrastructure of the Male Gamete of *Selaginella*. *Int. J. Plant Sci.* 160, 14–28.

Reski, R., and Abel, W.O. (1985). Induction of budding on chloronemata and caulonemata of the moss, *Physcomitrella patens*, using isopentenyladenine. *Planta* 165, 354–358.

Robbins, R.R. (1984). Origin and behavior of bicentriolar centrosomes in the bryophyte *Riella americana*. *Protoplasma* 121, 114–119.

Schindelin, J., Arganda-Carreras, I., Frise, E., Kaynig, V., Longair, M., Pietzsch, T., Preibisch, S., Rueden, C., Saalfeld, S., Schmid, B., et al. (2012). Fiji: An open-source platform for biological-image analysis. *Nat. Methods* 9, 676–682.

Schorb, M., Haberbosch, I., Hagen, W.J.H., Schwab, Y., and Mastrorarde, D.N. (2019). Software tools for automated transmission electron microscopy. *Nat. Methods* 16, 471–477.

Shaheen, R., Faqeih, E., Shamseldin, H.E., Noche, R.R., Sunker, A., Alshammari, M.J., Al-Sheddi, T., Adly, N., Al-Dosari, M.S., Megason, S.G., et al.

(2012). POC1A truncation mutation causes a ciliopathy in humans characterized by primordial dwarfism. *Am. J. Hum. Genet.* *91*, 330–336.

Sorokin, S.P. (1968). Reconstructions of centriole formation and ciliogenesis in mammalian lungs. *J. Cell Sci.* *3*, 207–230.

Tinevez, J.Y., Perry, N., Schindelin, J., Hoopes, G.M., Reynolds, G.D., Laplantine, E., Bednarek, S.Y., Shorte, S.L., and Eliceiri, K.W. (2016). TrackMate: An open and extensible platform for single-particle tracking. *Methods* *115*, 80–90.

Zhao, H., Chen, Q., Fang, C., Huang, Q., Zhou, J., Yan, X., and Zhu, X. (2019). Parental centrioles are dispensable for deuterosome formation and function during basal body amplification. *EMBO Rep.* *20*, 1–12.

Chapter 4.

**An evolutionary conserved module for
centriole assembly and diversification**

This section is adapted from: Gomes Pereira, S., Sousa, A.L., Nabais, C., Paixão, T., Holmes, A.J., Schorb, M., Goshima, G., Tranfield, E.M., Becker, J.D., and Bettencourt-Dias, M. The 3D architecture and molecular foundations of *de novo* centriole assembly *via* bicentrioles (*BioRxiv preprint, in revision*).

4.1 Abstract

Centrioles are microtubule-based organelles conserved throughout eukaryotic evolution, being essential to assemble both centrosomes and cilia. Centrioles might duplicate from pre-existing ones or assemble *de novo*. Despite *de novo* centriole biogenesis being widespread across eukaryotes, most of its molecular players and regulators remain largely unknown. Particularly, molecular data regarding the almost plant-exclusive bientriole and blepharoplast pathways remains very scarce, as these pathways have been mostly overlooked so far. Still, such knowledge is critical to fully understand centriole assembly, its regulation and evolution.

The recently established model plant species with motile sperm provide excellent opportunities to explore the uncharted diversity in centriole biogenesis and evolution. Pre-existing and newly developed tools, together with the structural characterization of centriole assembly in *Physcomitrium patens*, have finally enabled the molecular study of centriole biogenesis *via* bicentrioles. Here, I have explored the functional conservation of players known as essential for centriole assembly across different species and pathways, showing that such components appear to be preferentially expressed during *P. patens* spermatogenesis. Moreover, the data obtained supports the evolutionary conservation of

cartwheel and centriole wall assembly/stability mechanisms, relying on critical structural components such as SAS6, Cep135/Bld10 and POC1. Still, not all conserved core components appear to have kept their key role in centriole biogenesis, as others such as CPAP/SAS4, appear to play less critical functions in *P. patens* centrioles.

Therefore, this work reinforces the idea that centriole biogenesis in most eukaryotes relies on a conserved molecular module, whose diversification might have supported the generation of new pathways and species-specific structures.

4.2 Introduction

Centrioles are key to organizing both centrosomes and cilia, thereby regulating intracellular transport, spindle pole formation, cellular migration, motility and signalling (Joukov and De Nicolo, 2019). As a result of their critical functions, centrioles are tightly regulated in number, space and throughout time. Centriole biogenesis is no exception. Indeed, problems in centriole biogenesis are known to promote diseases, such as cancer (Levine et al., 2017; Lopes et al., 2018; Marteil et al., 2018) and ciliopathies (Shaheen et al., 2012; Khan et al., 2014).

Regardless of centrioles being able to assemble in the absence of pre-existing ones, *i.e. de novo*, most of the knowledge regarding centriole biogenesis draws from centriole duplication studies. Centriole duplication is a cell-cycle coupled process whereby a new daughter centriole assembles associated with its pre-existing mother, usually in an orthogonal configuration. Hence, the spatiotemporal and numerical regulation of centriole duplication is imposed by both the cell-cycle and the mother centriole (Nigg and Holland, 2018). Still, it remains unclear

how such regulation is achieved when centrioles assemble *de novo* (Nabais et al., 2018).

De novo centriole biogenesis may be achieved through many different pathways. Even though most of their structural characterization was performed in the late 60s/early 70s (Dirksen, 1961; Miki-Noumura, 1977; Moser and Kreitner, 1970; Hepler, 1976), only recently it became possible to investigate the molecular mechanisms at play. Still, the vast majority of studies have focused on the deuterosome-mediated centriole biogenesis that occurs during vertebrate multiciliogenesis (e.g. Vldar and Stearns, 2007; Hoh et al., 2012; Klos Dehring et al., 2013; Zhao et al., 2013; Arbi et al., 2017; Mori et al., 2017; Nanjundappa et al., 2019), or on the assembly of single centrioles, either naturally or artificially triggered, in animal cells (e.g. Suh et al., 2002; La Terra et al., 2005; Peel et al., 2007; Kuriyama, 2009; Fritz-Laylin et al., 2010; Lee et al., 2015; Nabais et al., 2021). Consequently, in part due to the lack of amenable model systems and tools required to tackle this problem, the plant-specific pathways remain vastly overlooked. Nevertheless, such knowledge is key to shedding light on the evolutionary history and general principles governing centriole assembly.

Plant cells lack centrioles. Hence, these organelles are only assembled *de novo* during spermatogenesis in species which differentiate motile sperm cells, such as bryophytes, ferns, and *Ginkgo* (Renzaglia and Garbary, 2001). In these plant species, sperm cells can either be biflagellated (e.g. bryophytes), assembling two centrioles *de novo* through the bicentriole-mediated pathway (Moser and Kreitner, 1970; Robbins, 1984); or multiflagellated (e.g. *Ginkgo biloba*), assembling variable numbers of centrioles within electron dense structures named blepharoplasts (Gifford and Larson, 1980). The recently established model plant species with motile sperm, such as the moss *Physcomitrium patens* (*P. patens*), provide excellent opportunities

to explore the uncharted diversity in centriole biogenesis and evolution, particularly given *P. patens*' relatively short and haploid-dominant life cycle, available genetic engineering tools, and newly established protocols for advanced imaging (Chapter 2). Moreover, given the particular features of *P. patens* locomotory apparatus, I asked whether the same molecular players were involved in bicentriole assembly, and in the asymmetrical centriole maturation previously revealed (see Chapter 3).

Here, armed with modern molecular, light and electron microscopy tools, I investigated the functional conservation of several known core centriole components, during spermatogenesis in *P. patens*. The data shows that the conserved cartwheel components SAS6 and Cep135/Bld10 are critical for cartwheel assembly and stability in *P. patens*, a function which has been conserved throughout evolution. Similarly, *P. patens* POC1 appears to be essential for assembly/stability of a proper centriolar wall. However, not all conserved proteins retained their critical role in centriole biogenesis. Indeed CPAP/SAS4, known to be essential for centriole assembly and length regulation in animals, appears to be dispensable for biogenesis in *P. patens*. Nevertheless, evidence also indicates that the centriolar wall components POC1 and CPAP/SAS4 might cooperate in order to support proper and stable assembly of *P. patens* centrioles. Overall, this work suggests that an evolutionary conserved centriole assembly module is required for the biogenesis of diverse centriole structures, underlying critical cellular and organismal functions such as motility and fertility.

4.3 Methods

4.3.1 Ortholog identification, similarity and expression analysis

To explore the similarity of the previously identified core centriolar proteins (SAS6, Cep135/Bld10, POC1 and CPAP/SAS4) (Carvalho-Santos et al., 2010; Hodges et al., 2010) between *P. patens* and other model organism species (*Chlamydomonas reinhardtii*, *Drosophila melanogaster* and *Homo sapiens*) I started by confirming these sequences to represent best bidirectional hits with protein BLAST (Basic Local Alignment Search Tool) using an expected threshold of 0.1, a word size of 3 amino acids, BLOSUM62 similarity matrix with a penalty for gap existence of 11 and gap extension of 1. I then aligned the bidirectional best hit sequences to one another using protein BLAST, and retrieved the identity percentage and query coverage values. Note that *P. patens* sequences were used as queries. In the cases where the identified sequences were not reciprocally the best hits and/or no significant hit was identified, the protein sequences identified as orthologues in previous studies (Carvalho-Santos et al., 2010; and Hodges et al., 2010) were considered.

The search for conserved functional domains and features (coiled-coil and disordered regions) was performed using HMMer 2.41.1 (Potter et al., 2018). The similarity percentage was retrieved from the HMMer hits identified between *P. patens* queries and the selected species.

Gene expression values across *P. patens* life cycle were obtained from the publicly available EVOREPRO database (www.evorepro.plant.tools (Julca et al.)). Note that two POC1 coding genes are found in *P. patens* genome and transcriptome: Pp3c16_11590V3.1 and Pp3c16_11580V3.1. However, Pp3c16_11580V3.1 is shorter and contained within the Pp3c16_11590V3.1 annotated coding region. Therefore, in this work, I

have named these two genes “POC1_long” (Pp3c16_11590V3.1) and “POC1_short” (Pp3c16_11580V3.1).

4.3.2 *P. patens* transgenic strain generation

4.3.2.1 Vector construction and preparation

Gene sequences for the conserved centriolar proteins (Carvalho-Santos et al., 2010; Hodges et al., 2010) SAS6 (Pp3c23_8210v3.1), Bld10 (Pp3c9_9030v3.1), POC1’s longest coding sequence (Pp3c16_11590V3.1) and SAS4 (Pp3c14_14590V3.1) were obtained from Phytozome (<https://phytozome.jgi.doe.gov/pz/portal.html>). Genetic engineering was employed based on homologous recombination (HR) with CRISPR/Cas9 technology being used in specific cases to create targeted double-strand breaks. In both knock-in (fluorescent protein tagging) and knock-out (K.O.) strategies (gene deletion), one of the homology arms was the 600bp-1kb sequence downstream of the stop codon. In the knock-in (protein fusion) vectors, the other homology arm was the 600bp-1kb sequence before the stop codon, which was immediately followed by a linker and mCherry or Citrine fluorescent protein coding sequences. The other homology arm in the knock-out constructs was the 600bp-1kb upstream sequence to the start codon. In both cases, an antibiotic resistance cassette was introduced between the two homology arms. After molecular cloning of the respective vectors, these were confirmed by endonuclease restriction digestion and Sanger sequencing (GATC) of the engineered regions. The correct HR constructs were linearized, ethanol precipitated and eluted in molecular grade water. The gRNAs for the CRISPR/Cas9 strategy were synthesized as single-stranded oligos (Integrated DNA Technologies), annealed to become double-stranded and then inserted in the same plasmid containing the Cas9 sequence. After sequence confirmation by Sanger sequencing (GATC), these vectors were ethanol

precipitated and eluted in molecular grade water. For further details on plasmid engineering, please refer to Table S4.1.

4.3.2.2 Transformation

5-day old protonema tissue was digested in a 2% Driselase solution (Sigma-Aldrich) in 0.5M D-Mannitol for 2h at RT. Protoplasts were collected by 2 rounds of centrifugation (5min at 250g) and filtration (EASYstrainer 40µm, Greiner Bio-One International), followed by a last centrifugation and re-suspension into 3M media (15mM MgCl₂; 0.1% MES (w/v) and 0.5M D-Mannitol). 2 million *P. patens* protoplasts (counted in a hemocytometer) were transformed with a total of 30µg of DNA (when several plasmids were used, their amount was equally distributed to a total of 30µg) by careful addition of 300µl 40% PEG-4000 (polyethylene glycol, Serva) in 3M media, followed by incubation at 45°C for 5min. After the heat shock, the transformants were incubated at RT for 15min before careful addition of 10mL of 3M media followed by homogenization. Finally, the transformants were centrifuged (5min at 250g) and re-suspended into 3mL of REG media (KNOPS media, 5% Glucose and 3% D-Mannitol). The protoplasts were then transferred to 3.5cm petri dishes (Sarstedt), incubated in the dark overnight (25°C) and regenerated for 10 days at normal growth conditions (25°C, 50% relative humidity, and 16h light/8h dark photoperiod, with a light intensity of 80µlum/m/s).

4.3.2.3 Selection and genotyping

Selection of transformants was achieved by 2-3 rounds of 10-day growth in selective media, followed by 10-days in non-selective media. Selective media was KNOPS media (Reski and Abel, 1985) supplemented with the respective antibiotics: 25µg/mL G418 (Sigma-Aldrich), 30µg/mL Hygromycin B (Alfa Aesar) or 100µg/mL

Zeocin (Invitrogen). DNA from surviving plant colonies was extracted by phenol-chloroform and PCR reactions were performed to test for proper genetic integration. Whenever possible, experiments were performed using two independent lines from the same genotype. For further details on transformation and genotyping see Tables S4.1 and S4.2, and Supplementary Figures S4.1-4.5.

4.3.3 *P. patens* strains and growth conditions

The Gransden wild-type (WT) *Physcomitrium* (*Physcomitrella*) *patens* strain (Ashton and Cove, 1977) was used as genetic background for single reporter lines (SAS6-mCherry and POC1-Citrine). All other plant genotypes were derived from these single reporter lines or γ -tubulin2-Citrine (Pp3c22_2850V3.1; Nakaoka et al., 2012). A list of genotypes used in this work is presented in Tables S4.2 and S4.3.

Plant material was routinely maintained by vegetative propagation of protonema sub-cultured every 7 days after mechanical disruption (TissueRuptor; Qiagen) on Petri dishes containing KNOPS media (Reski and Abel, 1985) supplemented with 0.5g/L ammonium tartrate dibasic (Sigma-Aldrich) and grown at 25°C, 50% relative humidity and 16h light/8h dark photoperiod (light intensity 80 μ lum/m/s). As centrioles only assemble during spermatogenesis, these require gametangia development. For that, plants were grown for 6-8 weeks at 25°C, with 50% relative humidity and 16h light/8h dark photoperiod (light intensity 80 μ lum/m/s) in Phytatray II (Sigma-Aldrich) containing 4 sterile peat pellets (Jiffy-7, Jiffy Products International). Water was supplied to the bottom of each box. Sexual reproduction (leading to gametangia and sporophyte development) was induced by transferring the Phytatray boxes to 17°C, 50% relative humidity and 8h light/16h darkness photoperiod (light intensity 50 μ lum/m/s). Except fertility assessments, all

other experiments were performed 15 days after induction (DAI) of sexual reproduction.

4.3.4 Immunofluorescence, 3D-SIM imaging and signal length analysis

4.3.4.1 Immunofluorescence and 3D-SIM

Apical shoots of 10-15 plants were fixed overnight at 4°C with 4% formaldehyde (Polysciences), 1mM MgCl₂, 50mM EGTA, 0.2% NP-40 and 1% Triton-X in 1x phosphate buffer saline (PBS). Fixed samples were washed twice with 1x PBS. Next, gametangia were carefully dissected under a stereo microscope onto a microscope slide and then crushed between the slide and a coverslip. Crushed samples were re-suspended into 100µl of 1x PBS by washing the coverslip and slide with this solution. The solution containing the individualized cells was then centrifuged (Cytopro cytocentrifuge) for 7min at 500g onto a coverslip.

The samples' coverslips were then immunostained. First, nonspecific antibody binding was blocked by incubating the samples at RT for 1h with a blocking solution (5% BSA, 0.1% NP-40 and 0.5% Triton-X in 1x PBS). Immediately afterwards, samples were incubated for 2h at RT with the primary anti-acetylated- α -tubulin antibody (1:1000, Sigma-Aldrich #T7451) in blocking solution, washed three times (10min each) with the blocking solution and incubated for 1h at RT with secondary anti-mouse-cy5 (1:500, Life Technologies A21236) in blocking solution. Next, coverslips were washed with 1x PBS, 0.1% NP-40 and 0.5% Triton-X for 10min. DAPI (or 4',6-diamidino-2-phenylindole, 1:500, Sigma-Aldrich) was added to this washing solution for a second 20min wash and a last 10min wash (without DAPI) followed. Finally, samples were washed with distilled water for 5min and mounted on slides using

vectashield (Vector Laboratories). All samples were blinded before imaging.

3D-SIM (structured illumination microscopy) imaging was performed on an GE HealthCare Deltavision OMX system, equipped with 2 PCO Edge 5.5 sCMOS cameras, using a 60x 1.42NA Oil immersion objective. Images were reconstructed with Applied Precision's softWorx software considering a Weiss filter of 0.05. For experimental sample sizes please refer to Table S4.3.

4.3.4.2 Signals length quantification and distribution

In order to measure SAS6 and POC1 signals, 3D-SIM images from SAS6-mCherry (75 stages III. and IV. cells) and SAS6-mCherry; POC1-Citrine (100 cells from stages III. to V.) sperm cells were selected. In these images, the individual channels were split and an auto-Huang threshold applied. Afterwards, automatic regions of interest (ROIs) were defined and manually curated to remove regions with overlapping signals from both cartwheels and/or MLS signals. Finally, the longest axis from those ROIs was considered as its length. Signal length distributions per cell were plotted using GraphPad Prism version 5.00.

In order to test if two distinct length populations of centrioles exist, a Gaussian mixture model with an increasing number of Gaussian distributions was fitted to the data, disregarding the origin of each value. The model with the lowest Bayesian information criterion (BIC) was selected as the most parsimonious number of Gaussians. This model was then used to predict the class ("long" or "short") of each pair of centrioles in each cell. The number of cells that were classified as having one "long" and one "short" centriole was recorded. Analyses were performed using python's sklearn package version 0.21.3.

4.3.5 Transmission electron microscopy of chemically fixed samples

Top parts of individual plants were fixed for 2h at RT in a 6% (v/v) glutaraldehyde (Polysciences) and 0.5% (v/v) tween-20 in 0.1M phosphate buffer (PB) solution. Samples were then washed twice with 0.1M PB and individually embedded in 2% (w/v) low melting point agarose. The agarose blocks were post-fixed in 1% (v/v) osmium tetroxide in 0.1M PB for 2h on ice. Samples were then washed twice with 0.1M PB and twice with distilled water, followed by *en bloc* staining with a 1% (w/v) uranyl acetate aqueous solution for 1h at RT. Samples were dehydrated through an ethanol series (30%, 50% for 10 min each; 70% overnight at 4°C; 90% for 10 min at 4°C and 3 times 100% for 15min at 4°C) and infiltrated with increasing concentrations of EMbed-812 epoxy resin (EMS) of 25%, 50%, 75% in ethanol for 90min each. Finally, samples were embedded in 100% epoxy resin which was polymerized at 60°C for 24 h. Ultrathin (70 nm) sections were obtained using a Leica UC7 Ultramicrotome, and collected on palladium-copper grids coated with 1% (w/v) formvar (Agar Scientific) in chloroform. Sections were post-stained with 1% (w/v) uranyl acetate and Reynolds' lead citrate for 5min each and imaged on a Hitachi H-7650 (100 keV) with a XR41M mid mount AMT digital camera or a FEI Tecnai G2 Spirit BioTWIN (120keV) using an Olympus-SIS Veleta CCD camera transmission electron microscopes. All samples were blinded before imaging. For sample size considerations, please see Table S4.3.

4.3.6 Correlative light and electron microscopy (CLEM)

Pre-embedding CLEM was performed as described by Sousa et al., 2021. Briefly, the top part of SAS6-mCherry individual plants were fixed for 2h at RT using a solution of 2% (v/v) formaldehyde (EMS), 0.2% (v/v) glutaraldehyde, 0.5% (v/v) tween-20 in 0.1M phosphate buffer (PB).

Then samples were washed three times with PB and incubated with 0.15% (w/v) glycine in distilled water for 10min at RT. Samples were washed three times with distilled water and infiltrated in 30% (w/v) sucrose for cryo-protection ON at 4°C on a rotary shaker. The embedding was made with optimal cutting temperature (OCT) compound (Sakura) before freezing in liquid nitrogen. Then, samples were sectioned using the cryostat (Leica CM 3050 S)(object temperature -18°C and chamber temperature -22°C). 10µm thick sections were picked-up in coverslips coated with 2% (v/v) 3-aminopropyltriethoxysilane (Sigma-Aldrich) in acetone and stained with DAPI (Sigma-Aldrich) 1:1000 in PBS for 5min at RT. After washing the sections with PBS three times, the coverslips were mounted with PBS and imaged. The imaging was done using the objectives 20x 0.70NA dry and 63x 1.4NA oil in a confocal microscope (Leica SP5 Live) with DAPI and mCherry signals being excited using 405nm and 561nm lasers respectively. Sections that had signal and were structurally preserved were dismantled from the slide, washed 10 times with PB and post-fixed using a solution of 1% (w/v) potassium ferrocyanide, 1% (v/v) osmium tetroxide in 0.1M PB for 30min at 4°C. Sections were washed twice in 0.1M PB and twice in distilled water before dehydration in an ethanol series of 30%, 50%, 70%, 90% and 100% for 10min each and embedding in 100% EMbed-812 epoxy resin, which was polymerized at 60°C for 24h. Sections were picked-up and post-stained as described for the chemical fixed samples. The low magnification TEM and confocal images were aligned considering DAPI/nucleus shape. Cells with clear SAS6-mCherry signals were selected and serial TEM images were obtained. The confocal images were then superimposed on the serial TEM pictures and the best alignment between DAPI signal and nuclear shape was selected. 2 Independent CLEM experiments were performed.

4.3.7 Sperm cell motility assessment

Gametangia from 10-12 individual plants were dissected onto a coverslip containing 50 μ l of sperm cell media (0.45mM CaCl₂, 0.3mM MgSO₄, 0.02mM KNO₃ and 0.081mM NaHCO₃)(Ortiz-Ramírez et al., 2017) supplemented with 1 μ g/mL of the viability dye fluorescein diacetate (Sigma-Aldrich F7378). Released and viable (checked with the GFP filterset) sperm cells' clusters were imaged on a commercial Nikon High Content Screening microscope equipped with an Andor Zyla 4.2 sCMOS camera, using a 20x 0.75NA dry objective in the BF channel (at 33frames per second) during 1min. Acquired movie sequences were analyzed using Fiji (Schindelin et al., 2012) to assess if sperm cells were motile or not. Clusters from at least 3 independent experiments were analyzed per genotype (see Table S4.3).

4.3.8 Fertility rate analysis and statistics

Assessment of fertility rate was performed as described by Ortiz-Ramírez et al., 2017. Fertility rate is the percentage of gametophores containing sporophytes, considering at least 100 randomly collected gametophores per sample, 6 weeks after induction of sexual reproduction. All rates were measured in randomized blinded samples. Statistical differences were evaluated by one-way ANOVA followed by Tukey's *post-hoc*. For sample size considerations, please see Table S4.3.

4.4 Results

4.4.1 Conserved core centriole proteins are preferentially expressed during *P. patens* gametogenesis

A set of core centriolar components including SAS6, Cep135/Bld10, POC1 and CPAP/SAS4, amongst a few others, have been identified as evolutionary conserved across ciliated species, including *P. patens* (Carvalho-Santos et al., 2010; Hodges et al., 2010). Centriolar and centrosomal components are normally enriched in several coiled-coil and disordered regions (Nido et al., 2012). Similarly, these features also appear to be present in *P. patens* protein sequences (Figure 4.1A). Moreover, the characteristic domains of SAS6 (SAS6_N) and POC1 (WD40 repeats) are also present in their respective *P. patens* orthologs (Figure 4.1A), while the conserved Tcp10_C domain of CPAP/SAS4 was not detected in PpSAS4 (Figure 4.1A). Cep135/Bld10 lacks any particular feature and appears to be less similar amongst all the species analyzed (Figure 4.1A). Nevertheless, the medium to high similarity levels observed between *P. patens* and *C. reinhardtii* sequences (43-74%; Figures 4.1A) suggest that these key components in centriole assembly might have conserved their functions across evolution, playing similar roles during centriole biogenesis in *P. patens*.

A. Protein similarity



B. Gene expression

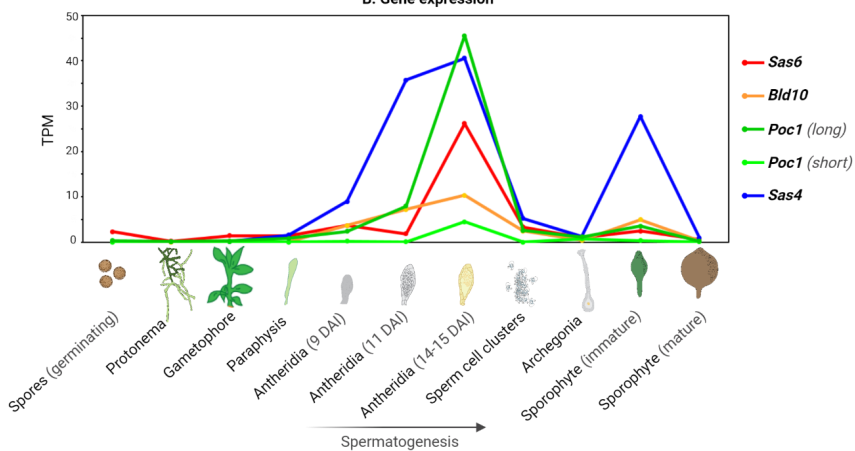


Figure 4.1: The core centriolar proteins and their expression in *P. patens*. **A.** Annotation and similarity levels of the core centriolar components SAS6, Cep135/Bld10, POC1 and CPAP/SAS4 across the following model species: *Physcomitrium patens* (*P. patens*) - moss; *Chlamydomonas reinhardtii* (*C. reinhardtii*) - green algae; *Drosophila melanogaster* (*D. melanogaster*) - fruit fly; and *Homo sapiens* (*H. sapiens*) - human. One asterisk indicates that the sequences were not bidirectional best hits, while two asterisks represent the lack of significant hits in the BLAST® search. In both these cases, the alignments were performed with the sequences previously identified by Carvalho-Santos et al., 2010; and Hodges et al., 2010 (see section 4.3.1). The conserved SAS6 protein is characterized by the presence of a SAS6_N (Centriolar protein SAS6 N-terminal; red) domain in its N-terminus, and less structured C-terminal regions. In humans, SAS6 also contains an Sas6_CC (Sas6/XLF/XRCC4 coiled-coil; orange) domain; Cep135/Bld10 orthologs contain multiple coiled-coil regions (grey loops) throughout their lengths, lacking any particular domain/feature in any of the species analyzed; POC1 is composed of several WD40 (WD or beta-transducin; light green) repeats. In *P. patens*, *C. reinhardtii* and *D. melanogaster* it also contains a ANAPC4_WD40 (Anaphase-promoting complex subunit 4 - WD40 domain; dark green), and in *C. reinhardtii* an eIF2A factor (Eukaryotic translation initiation factor; magenta); CPAP/SAS4 proteins are very rich in disordered regions (light orange shade), containing an Tpc10_C (T-complex protein 10 C-terminus; blue) domain in their C-terminal regions, which is undetected in *P. patens* SAS4; **B.** Expression of the core centriolar component genes *Sas6* (Pp3c23_8210v3.1; red line), *Bld10* (Pp3c9_9030v3.1; orange line), *Poc1* (long) (Pp3c16_11590V3.1; dark green line), *Poc1* (short) (Pp3c16_11580V3.1; light green line) and *Sas4* (Pp3c14_14590V3; blue line). Data collected from

www.evorepro.plant.tools (Julca et al.). Figure created with BioRender.com.

In order for centrioles to assemble, its components must be transcribed and translated. Using a gene expression atlas publicly available in the EVOREPRO database (www.evorepro.plant.tools (Julca et al.)), I inspected the expression patterns of the genes coding for the conserved core centriolar components SAS6 (*PpSas6*), Cep135/Bld10 (*PpBld10*), POC1 (*PpPoc1* “long” and “short”) and CPAP/SAS4 (*PpSas4*). Interestingly, I have determined such genes to be preferentially expressed during spermatogenesis (Figure 4.1B). Nevertheless, some expression is also detected in the immature sporophyte stage, wherein meiosis occurs. This is particularly evident for *PpSas4* (Figure 4.1B). As centrioles only assemble during spermatogenesis, this data further supports a possible role for such proteins in *P. patens de novo* centriole biogenesis.

4.4.2 Localization of SAS6 and POC1 reveal differences between sister centrioles

Aiming at understanding centriole assembly and the possible roles of the conserved centriolar proteins, I explored the localization of two of such components throughout spermatogenesis in *P. patens*. I focused on the major core component of the cartwheel – SAS6 (Nakazawa et al., 2007; Gopalakrishnan et al., 2010; Guichard et al., 2017), as well as POC1, which is known to be involved in centriole length regulation (Keller et al., 2009). In order to study the localization of these proteins, I generated transgenic reporter plant lines, knocking-in fluorescent proteins as tags through homologous recombination guided by CRISPR (see section 2.3.2, Supplementary Table S4.2 and Figure S4.1 for more details). Given the small size of the structures and difficulty in resolving

them by conventional light microscopy, I characterized the localization of SAS6-mCherry and POC1-Citrine by 3D-Structured Illumination Microscopy (3D-SIM) of isolated developing sperm cells from these transgenic lines (Figures 4.2 and 4.3).

4.4.2.1 SAS6 and POC1 localization reflect the bicentriole-mediated pathway for centriole biogenesis

In young sperm cells both proteins, SAS6 and POC1, co-localize in two parallel bars near the characteristic round nucleus. These structures also appear to contain a weak acetylated tubulin signal (Figure 4.2A), and might possibly represent bicentrioles. Since I detected two structures, each containing two “dots” of the centriolar components SAS6 and POC1 (Figure 4.2B), it is likely that two bicentrioles assemble in the sperm mother cell. Furthermore, these bicentrioles localize in the spindle poles during mitosis (Figure 4.2C). Potentially, such positioning at the poles ensures that each daughter cell inherits only one bicentriole and forms only two cilia.

As spermatogenesis proceeds, a broad and faint tubulin acetylation signal appears along one side of the elongating nucleus (Figure 4.3A arrowhead), which may represent the spline, as this structure is composed of microtubules. Moreover, a clear tubulin acetylation signal can also be observed on both ciliary axonemes (Figure 4.3B). SAS6-mCherry and POC1-Citrine signals also elongate, however such elongation appears to occur asymmetrically between the two originally identical bars, yielding distinct signal lengths of SAS6 and POC1 (Figure 4.3).

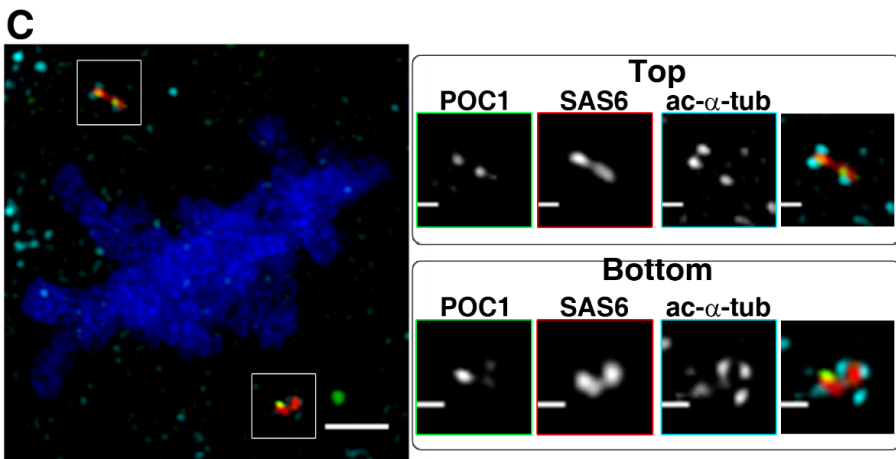
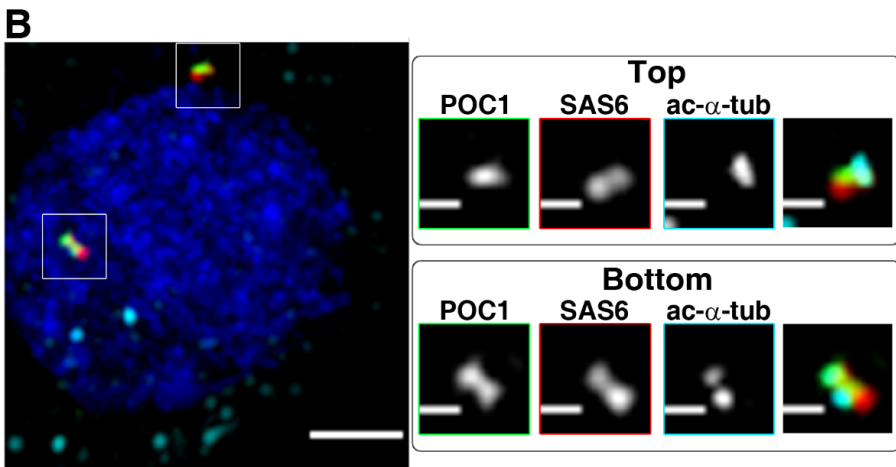
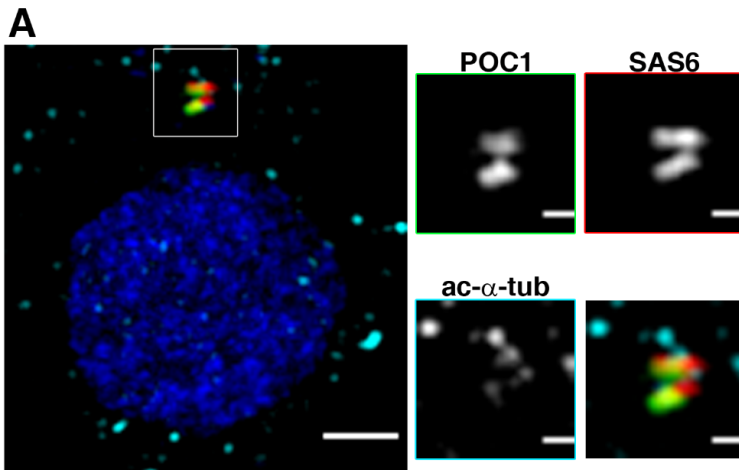


Figure 4.2: Representative 3D-SIM images of POC1-Citrine;SAS6-mCherry individualized sperm cells at early spermatogenesis. A. Differentiating sperm cell containing two small parallel bars composed of both SAS6 and POC1; **B.** Sperm cell with two bars containing SAS6 and POC1; **C.** Mitotic sperm cell with two regions containing SAS6 and POC1, one at each pole of the spindle. Blue – DAPI; Cyan - acetylated- α -tubulin; Green – POC1-Citrine; Red – SAS6-mCherry. Scale-bars = 1 μ m or 250nm (insets). For sample size please refer to Table S4.3. Adapted from Gomes Pereira et al. (*in revision*).

It is noteworthy that only a thinner portion of the POC1 bar elongates (Figure 4.3A inset arrow), contrary to what I observed for the SAS6 signal. As POC1 in *Chlamydomonas* was suggested to localize to the A-C linker and inner scaffold of the centriole wall (Li et al., 2019; Le Guennec et al., 2020), this partial elongation of POC1 signal suggests an incomplete elongation of the centriolar wall. Interestingly, POC1 signal also doesn't fully decorate the whole extension of SAS6-mCherry, which results in regions where only SAS6 signal is observed (Figures 4.3A and B). This suggested that centriole and cartwheel lengths might differ, with cartwheels being significantly longer. Additionally, in some cells (24%, 24/98) a third SAS6-containing elongated signal is observed, which lacks POC1 at its tip and does not nucleate a cilium (Figure 4.3B). Finally, while POC1 signal remained during final cell maturation, which was characterized by an elongated streamlined nucleus, SAS6 signal disappeared (Figure 4.3C).

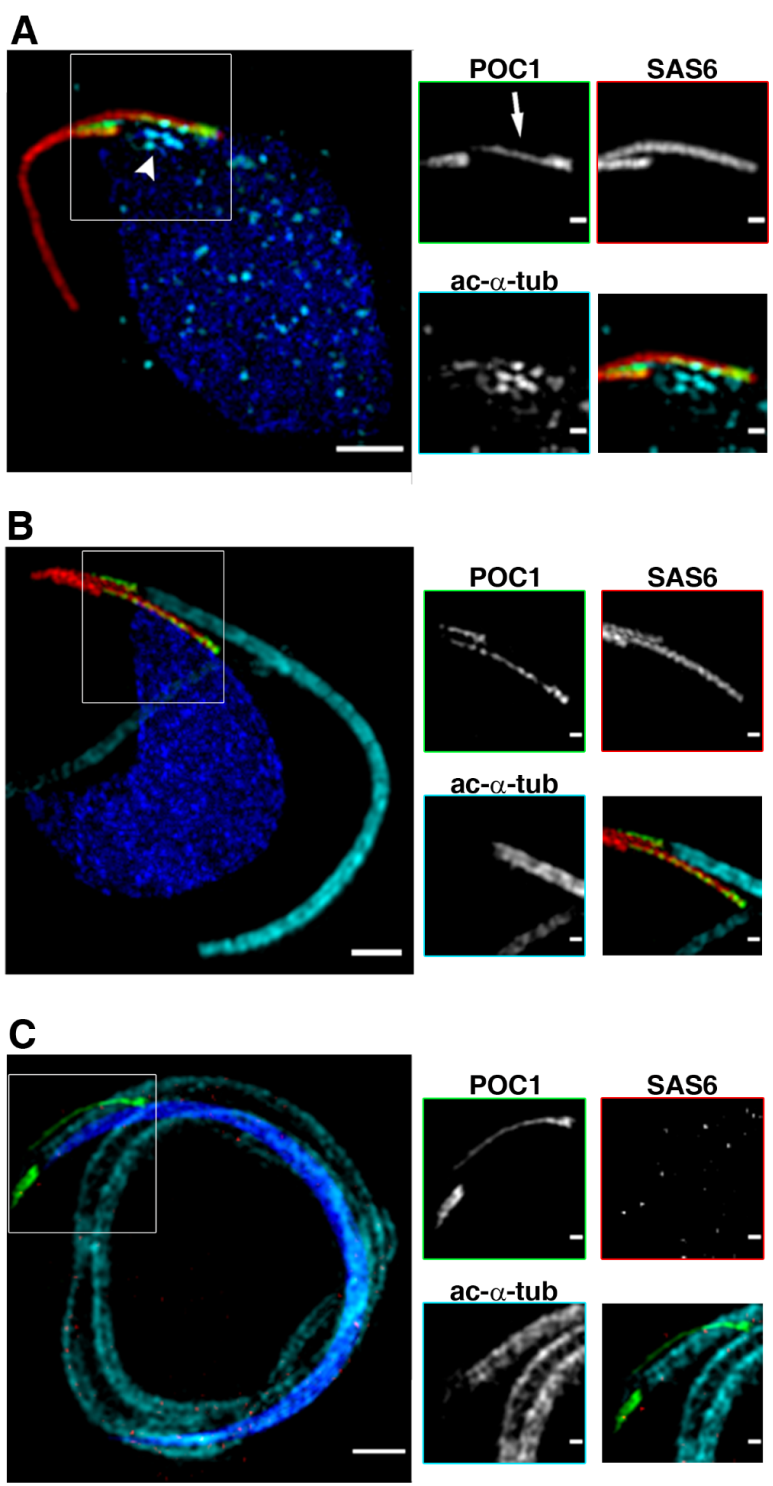


Figure 4.3 Representative 3D-SIM images of individualized sperm cells at different developmental stages from POC1-Citrine;SAS6-mCherry plants. Developmental stages were differentiated based on the shape of the nucleus and presence of cilia. **A.** Nuclear elongation without cilia. Note the acetylated- α -tubulin signal in the spline (arrowhead) and the elongation of a thinner portion of one POC1 signal (inset arrow); **B.** Nuclear elongation with cilia (stained by acetylated- α -tubulin); **C.** Condensed and thin nuclear shape. Blue – DAPI; Cyan - acetylated- α -tubulin; Green – POC1-Citrine; Red – SAS6-mCherry. Scale-bars = 1 μ m or 250nm (insets). For sample size please refer to Table S4.3. Adapted from Gomes Pereira et al. (*in revision*).

4.4.2.2 Two distinct SAS6 and POC1 length populations

To further clarify the consistency of the observed asymmetry, I measured the length of SAS6 and POC1 fluorescence signals. Analysis of the signal length distribution suggested the existence of two different length classes, with the shorter signals per cell separating from the longest ones. This is seen for both SAS6 (Figure 4.4A) and for POC1 (Figure 4.4B), being clearer in the latter. In order to test if indeed two distinct SAS6/POC1 length populations existed, Gaussian mixture models with an increasing number of Gaussian distributions were fitted to the total set of signal lengths obtained, not considering the pairwise data per cell. Indeed, 2 Gaussian distributions appeared to best fit both SAS6 and POC1 length distributions (Figures 4.4C and D, respectively), confirming the existence of two distinct populations both for SAS6 (“short”: average of $1.83 \pm 0.72 \mu\text{m}$ and “long”: $3.31 \pm 0.68 \mu\text{m}$ - Figure 4.4E) and POC1 (“short”: average length of $0.87 \pm 0.20 \mu\text{m}$ and “long”: average length of $2.28 \pm 0.49 \mu\text{m}$ - Figure 4.4F).

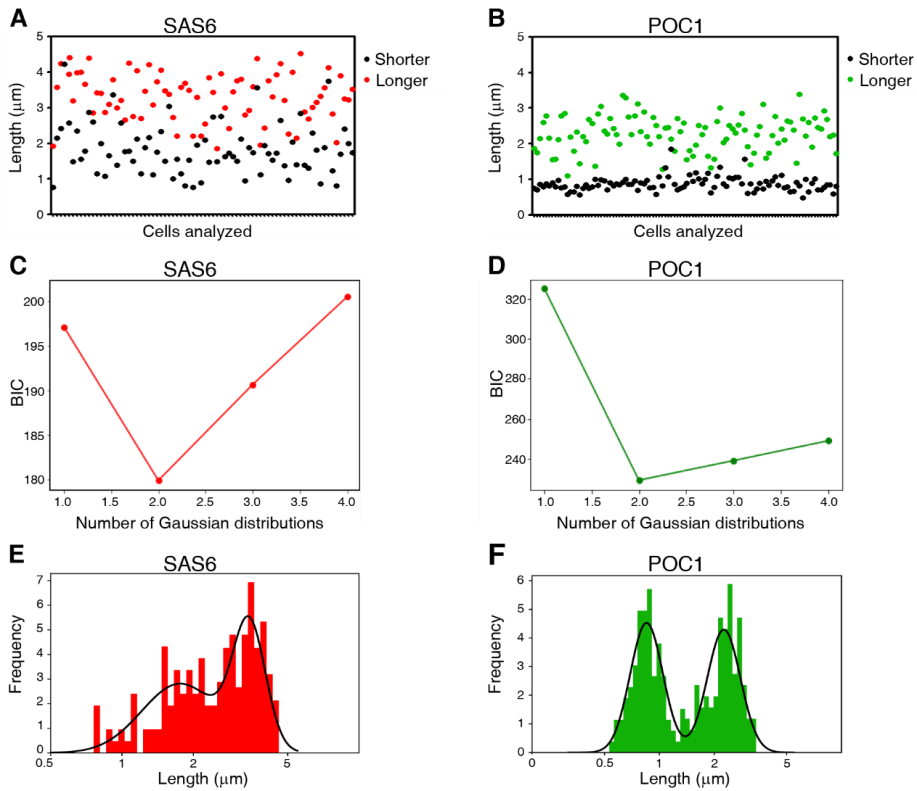


Figure 4.4: Analysis of the length of SAS6-mCherry and POC1-Citrine signals reveals the existence of two distinct cartwheel and centriole populations. **A** and **B**. Pairwise length of each SAS6-mCherry (**A**) and POC1-Citrine (**B**) signals per cell analyzed. The black dots represent the shorter signals in each of the cells, while the red dots represent the longest ones; **C** and **D**. Bayesian information criterion (BIC) of the fitting of Gaussian mixture models with a variable number of Gaussian distributions to SAS6-mCherry (**C**) and POC1-Citrine (**D**) signal length distributions. Note that in both cases, 2 is the number of Gaussian curves that result in the lowest BIC, therefore the most parsimonious number of populations; **E**. SAS6-mCherry length distribution (red) and corresponding Gaussian fitting for both curves (black line). Measurements from 75 cells; **F**. POC1-Citrine length

distribution (green) and respective Gaussian fitting of the two distributions (black line). Measurements from 100 cells. Adapted from Gomes Pereira et al. (*in revision*).

While the existence of two different SAS6 and POC1 signal populations is an interesting finding, it does not prove the existence of asymmetrical centrioles within the same cell. It could rather represent different elongation steps, *i.e.* some cells could have both short/long signals in one population because they are both less/more elongated. To confirm that the two distinct populations represented different centrioles within the same cell, the pairwise lengths per cell were taken in consideration, and using the Gaussian mixture model previously fitted to the data, each one of the cell's signal was attributed to its respective length population. Importantly, the classification of pairwise lengths per cell into these populations has revealed that 71% (54/76) of cells contained one "long" and one "short" SAS6-mCherry signal, while this occurred in 94% (94/100) of cells containing POC1-Citrine. These results strongly support the existence of two centrioles with different lengths in each cell, as well as that there is part of the centriole which is both SAS6 positive and POC1 negative, with SAS6 length populations being longer than those of POC1.

4.4.2.3 PpSAS6 localizes to both cartwheels as well as to the MLS

Surprisingly, our 3D-SIM imaging of protein localization throughout spermatogenesis revealed the presence of three SAS6-mCherry filaments per cell, while POC1 and cilia were only seen protruding from two of those (Figure 4.3B). SAS6 is a major cartwheel component, yet there are only two cartwheels in *P. patens*. This, together with the observation that SAS6-mCherry signal (Figure 4.3C), cartwheels and the LS, all seem to disappear upon sperm cell cytodifferentiation, led us to

hypothesize that SAS6 could localize to the MLS besides the cartwheels. To test this hypothesis, correlative light and electron microscopy (CLEM) using SAS6-mCherry plants (Figure 4.5) was performed.

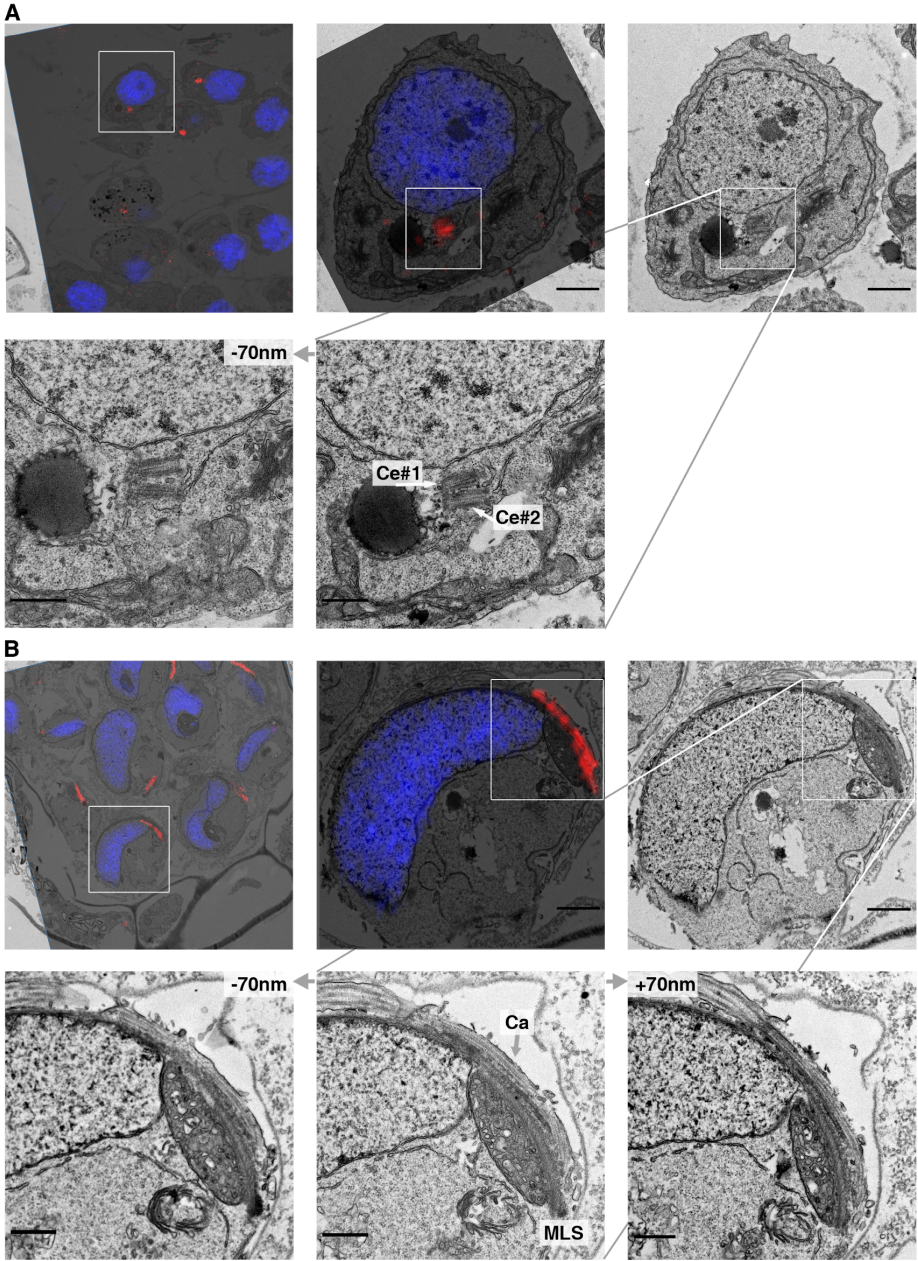


Figure 4.5: CLEM of SAS6-mCherry (red signal) sperm cells

confirming its localization to the cartwheel and MLS. A. At early developing sperm cells (round nucleus), SAS6 localizes to both parallel centrioles; **B.** As spermatogenesis proceeds, SAS6 localizes to both the elongated naked cartwheel regions, as well as to the plant-specific MLS (adapted from Gomes Pereira et al., *in revision*). Alignment of TEM and confocal microscopy images (selected cell highlighted), was performed based on nuclear shape (stained with DAPI - blue). By analysis of the serial EM sections obtained, and their alignment with the confocal images, the identification of the SAS6-containing structures was performed. Ca – cartwheel; Ce#1 and Ce#2 - centrioles arbitrarily numbered 1 or 2, respectively; MLS – multilayered structure Scale-bars = 1 μ m (TEM images of the selected cell), 500nm (higher magnification TEM images).

Indeed, our CLEM data of early spermatids allowed us to confirm the localization of SAS6 to both centrioles (Figure 4.5A). However, only the data from a later developing spermatid (with cilia already assembled), allowed us to confirm SAS6 localization to the elongated (and naked) cartwheel regions (Figure 4.5B). Moreover, as hypothesized, SAS6 also appeared to localize to the MLS (Figure 4.5B). This unique localization of PpSAS6 to both elongated cartwheels and to the plant-specific MLS, suggests putative new roles for SAS6 in land plants.

Collectively, these results support the presence of the conserved cartwheel (SAS6) and centriolar (POC1) components in *P. patens* centrioles, suggesting the assembly of two bicentrioles (Figures 4.2A-C), and revealing an asymmetrical maturation of both centrioles (Figures 4.3 and 4.4). SAS6 and POC1 are centriolar components involved in cartwheel assembly (Nakazawa et al., 2007; Gopalakrishnan et al., 2010; Guichard et al., 2017) and centriole elongation (Keller et al.,

2009), respectively. Therefore, I speculated whether these proteins could have maintained the same core function while tailoring it to the specificities encountered in *P. patens*.

4.4.3 Core centriolar proteins appear to have conserved their functions throughout evolution

To investigate the functions of the core conserved centriolar proteins identified in *P. patens* centriole assembly and maturation, I employed a reverse genetics approach, generating deletion mutant plant lines. As γ -tubulin is a known component of both the centrosome (Stearns et al., 1991) and plant acentrosomal MTOCs (Shimamura et al., 2004), I used the γ -tubulin2-Citrine (Nakaoka et al., 2012) *P. patens* strain as genetic background to generate null mutants of the conserved centriole cartwheel component SAS6. Unexpectedly, although no ultrastructural defects were observable in this genetic background (Figures 4.6A and B), I found that γ -tubulin2 does not localize to the base of the cilia, where centrioles/basal bodies are (Figure 4.6C). Furthermore, when SAS6-mCherry was introduced into this strain, despite also not showing any visible ultrastructural defect (Figures 4.6D and E), γ -tubulin2 foci were still not found to localize with the centrioles. Instead, the γ -tubulin2-signal was detected in a non-overlapping manner below the SAS6 signal (Figure 4.6F). Therefore, I conclude that in *P. patens* sperm cells γ -tubulin2 does not localize to its centrioles. Nevertheless, as no ultrastructural alterations were visible, and the SAS6-mCherry signal would be informative, the generated γ -tubulin2-Citrine;SAS6-mCherry plant was used as genetic background for the deletion of the remaining conserved proteins (Bld10, POC1 and SAS4).

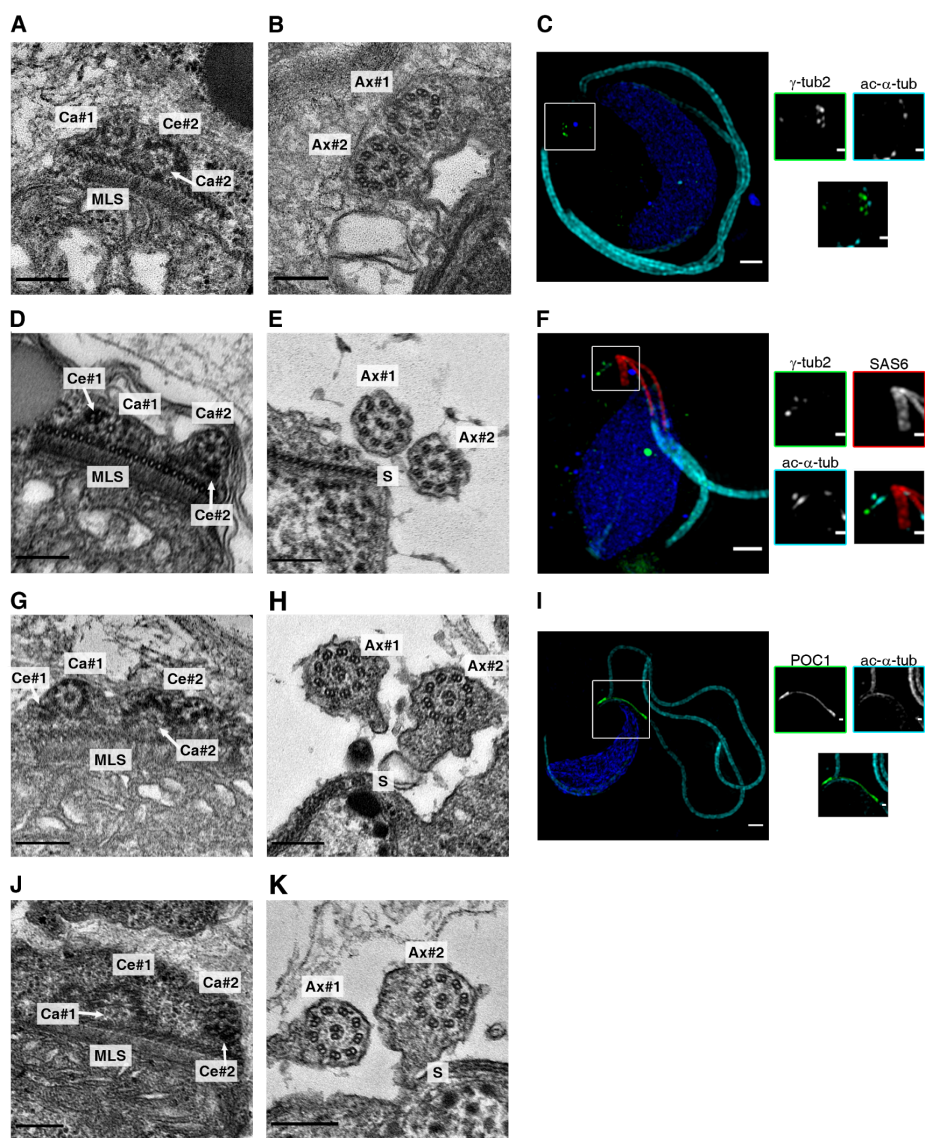


Figure 4.6: Cellular analysis of the genetic backgrounds used for the deletion of the conserved centriolar components. A to C. γ -tubulin2-Citrine genotype, with both centrioles associated with MLS (A) and templating the assembly of normal cilia (B); C. 3D-SIM showing a clear ciliary staining, and the concentration of γ -tubulin2-Citrine in a particular region of the cell (highlighted); D to F.

γ -tubulin2-Citrine;SAS6-mCherry sperm cells; **D**. Centrioles associated with the MLS; **E**. 9+2 ciliary organization; **F**. 3D-SIM showing the characteristic ciliary staining and elongated SAS6-mCherry signal not overlapping with the γ -tubulin2 enriched region; **G to I**. POC1-Citrine sperm cells with both centrioles associated with the MLS (**G**) and 9+2 axonemes (**H**); **I**. 3D-SIM of a developing spermatid, with clear ciliary staining and two asymmetrical centrioles reported by the POC1 signal; **J and K**. POC1-Citrine;SAS6-mCherry genotype (note that 3D-SIM data for this genotype can be found in Figures 4.2 and 4.3). Scale-bars = 200nm (TEM), 1 μ m (3D-SIM). TEM: Ca - cartwheel (#1 - number 1; Ca#2 - number 2, arbitrary defined); Ce - centriole (#1 - number 1; #2 - number 2, according the cartwheels numbering); MLS - multilayered structure; S - spline; Ax - axoneme (#1 - number 1; #2 - number 2, numbering is arbitrary). 3D-SIM: Blue - DAPI; Cyan - acetylated- α -tubulin; Green - γ -tubulin2-Citrine (C and F) or POC1-Citrine (I); Red - SAS6-mCherry. For considerations on sample size refer to Table S4.3. Adapted from Gomes Pereira et al. (*in revision*).

In order to further confirm the phenotypes observed, and to explore how PpSAS6, PpBld10 and PpSAS4 deletions affect the localization of POC1, I used POC1-Citrine and POC1-Citrine;SAS6-mCherry genetic background plants for the deletion of *PpSas6* (POC1-Citrine), *PpBld10* and *PpSas4* (POC1-Citrine;SAS6-mCherry). Neither of these control background genotypes displayed any ultrastructural defect (Figures 4.6 G, H, J and K), with a normal ciliary staining being visible by 3D-SIM (Figures 4.3 and 4.6I).

4.4.3.1 Despite localizing to the MLS, PpSAS6 is only required for cartwheel assembly

In order to address PpSAS6 functions, I analyzed spermatogenesis in SAS6 K.O. ($\Delta sas6$) plants by both TEM and 3D-SIM (Figure 4.7). No cartwheel structures were observed, although electron dense material still concentrated above the spline, where the cartwheel is seen in wild-type cells (Figure 4.7A star). Despite SAS6 being localized to the MLS (Figure 4.5), no obvious defects were visible in this structure in γ -tubulin2-Citrine; $\Delta sas6$ plants (Figure 4.7A). Interestingly, despite the lack of cartwheels, abnormal microtubule bundles were assembled in axoneme-like structures, suggesting the presence of cartwheel independent mechanisms to generate organized microtubule bundles (Figures 4.7B and C). Concordantly, individual MT doublets and triplets could be frequently found above the MLS in $\Delta sas6$ sperm cells, in both γ -tubulin2-Citrine; $\Delta sas6$ as well as POC1-Citrine; $\Delta sas6$ (Figures 4.7A and D). Similar aberrant ciliary structures were observed when SAS6 was depleted in the background of POC1-Citrine (POC1-Citrine; $\Delta sas6$ - Figures 4.7E to G). Moreover, POC1 localization was affected by SAS6 deletion, with several small and discontinuous *foci* being visible in multiple (66%, Figure 4.7F) or one (34%, Figure 4.7G) regions of the cell. Therefore, SAS6 is essential for the formation of cartwheels in *P. patens*, however it plays no significant role in the assembly of the plant specific MLS (Figures 4.7A and D).

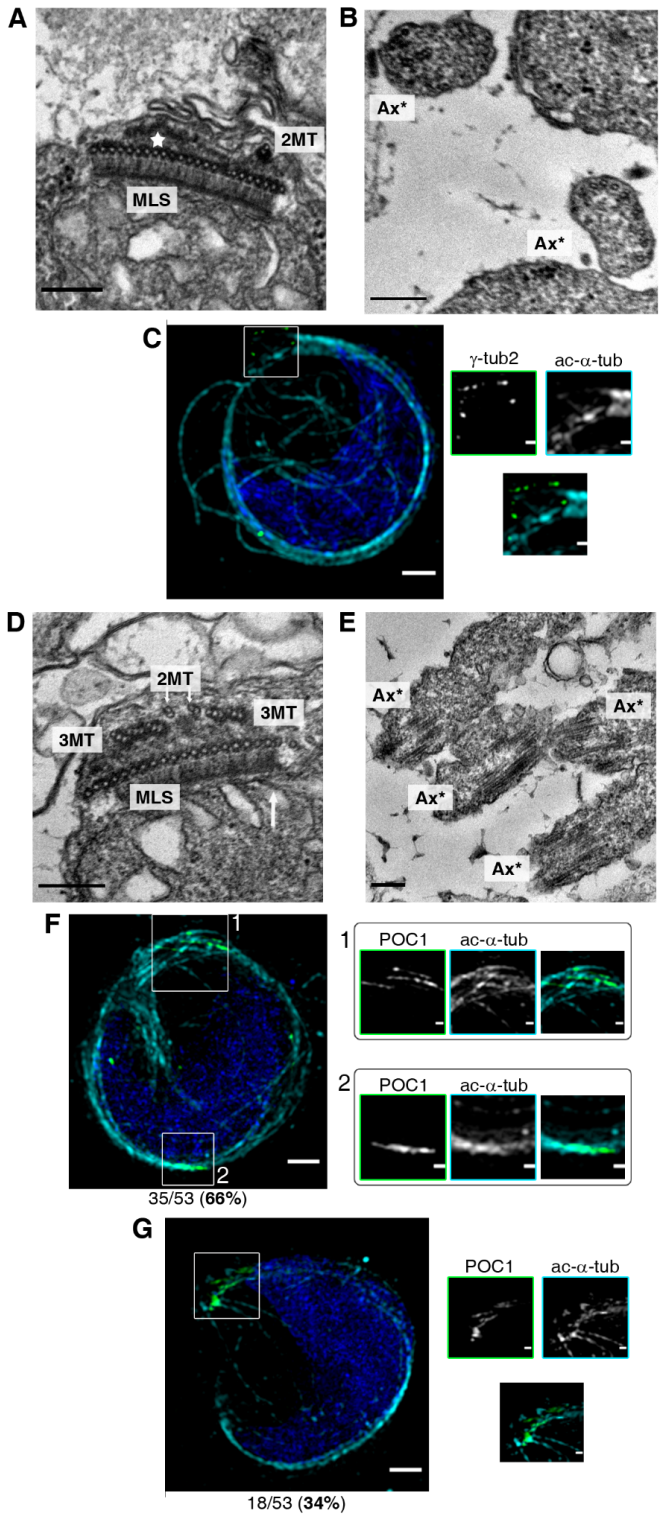


Figure 4.7: SAS6 is essential for cartwheel assembly in *P. patens*. A to C. γ -tubulin2-Citrine; $\Delta sas6$ sperm cells show the absence of any recognizable cartwheel structure, despite presence of a normal MLS (**A**). Disorganized cilia-like structures are seen by both TEM (**B**) and 3D-SIM (**C**); **D to G.** POC1-Citrine; $\Delta sas6$ plants also lack cartwheels (**D**), containing abnormal axonemal-like structures (**E**). Despite localizing to multiple (**F**) or only one (**G**) region of the cell, POC1-Citrine signal is always misorganized and discontinuous. EM: MLS - multilayered structure; white star - accumulation of electron dense disorganized material; 2MT - doublet microtubule; 3MT - microtubule triplet; Ax* - abnormal axoneme organization. Scale-bars = 200nm. 3D-SIM: Blue - DAPI; Cyan - acetylated- α -tubulin; Green - γ -tubulin2-Citrine (C) or POC1-Citrine (F and G). Scale-bars = 1 μ m (whole cell) and 250nm (insets). For considerations on sample size refer to Table S4.3. Adapted from Gomes Pereira et al. (*in revision*).

4.4.3.2 PpBld10 is required for cartwheel elongation

In several species, Cep135/Bld10 is a known component of the cartwheel spokes required for cartwheel stability (Matsuura et al., 2004; Hiraki et al., 2007; Jerka-Dziadosz et al., 2010; Guichard et al., 2017). Given the conserved role of *P. patens* SAS6 in the formation of the long cartwheels, I asked how this structure is stabilized and the possible role of PpBld10 in this process. Our analysis of Bld10 K.O. ($\Delta bld10$) cells revealed the presence of cartwheel rings in only 23% of the analyzed MLS-containing sections. Interestingly no MTs were seen attached to these cartwheel stacks (Figure 4.8A), while singlets or doublet MTs, but never triplets were observed in the cytoplasm of these $\Delta bld10$ sperm cells. Despite the absence of any cartwheel-like structures (Figure 4.8B), normal MLS with abnormal electron dense material concentrated above the spline were frequently observed (77%). Nevertheless, all cilia-like

structures observed were composed of only disorganized singlet microtubules (Figure 4.8C).

Given the previously observed SAS6 localization at the MLS, I asked whether Bld10 is important to stabilize this SAS6 pool. Indeed, SAS6 signal elongation was compromised in $\Delta bld10$, with most sperm cells (58%) displaying several small discontinuous SAS6-mCherry *foci* (Figure 4.8D), as opposed to the long and continuous SAS6 filaments observed in control cells (Figure 4.6F). Yet, in the remaining cells analyzed (42%), no SAS6 signal could be detected (Figure 4.8D).

However, when *PpBld10* was deleted in POC1-Citrine;SAS6-mCherry plants, cartwheel structures were never observed (Figure 4.8F). Similarly to γ -tubulin2-Citrine;SAS6-mCherry; $\Delta bld10$, POC1-Citrine;SAS6-mCherry; $\Delta bld10$ also displayed abnormal electron dense material above the MLS (Figure 4.8F) and disorganized singlet microtubules in their axonemal-like structures (Figure 4.8G). Yet, in this genotype, triplet microtubules were observed in 6% (5/84) of MLS-containing sections (Figure 4.8F). Interestingly, despite cartwheel structures not having been observed, a fragmented SAS6-mCherry signal was observed in 78% of the sperm cells images. Moreover, fragmented POC1 signals were visible in close proximity to this fragmented SAS6 signal (Figure 4.8H), while only a dispersed and discontinuous POC1 signal was found in cells where no SAS6 signal was detected (Figure 4.8I).

Overall, these results support a conserved role for *PpBld10* in SAS6/cartwheel stability. Moreover, given the phenotypes observed, *P. patens* Bld10 may also be involved in cartwheel-microtubule attachment and in microtubule triplet formation/stability.

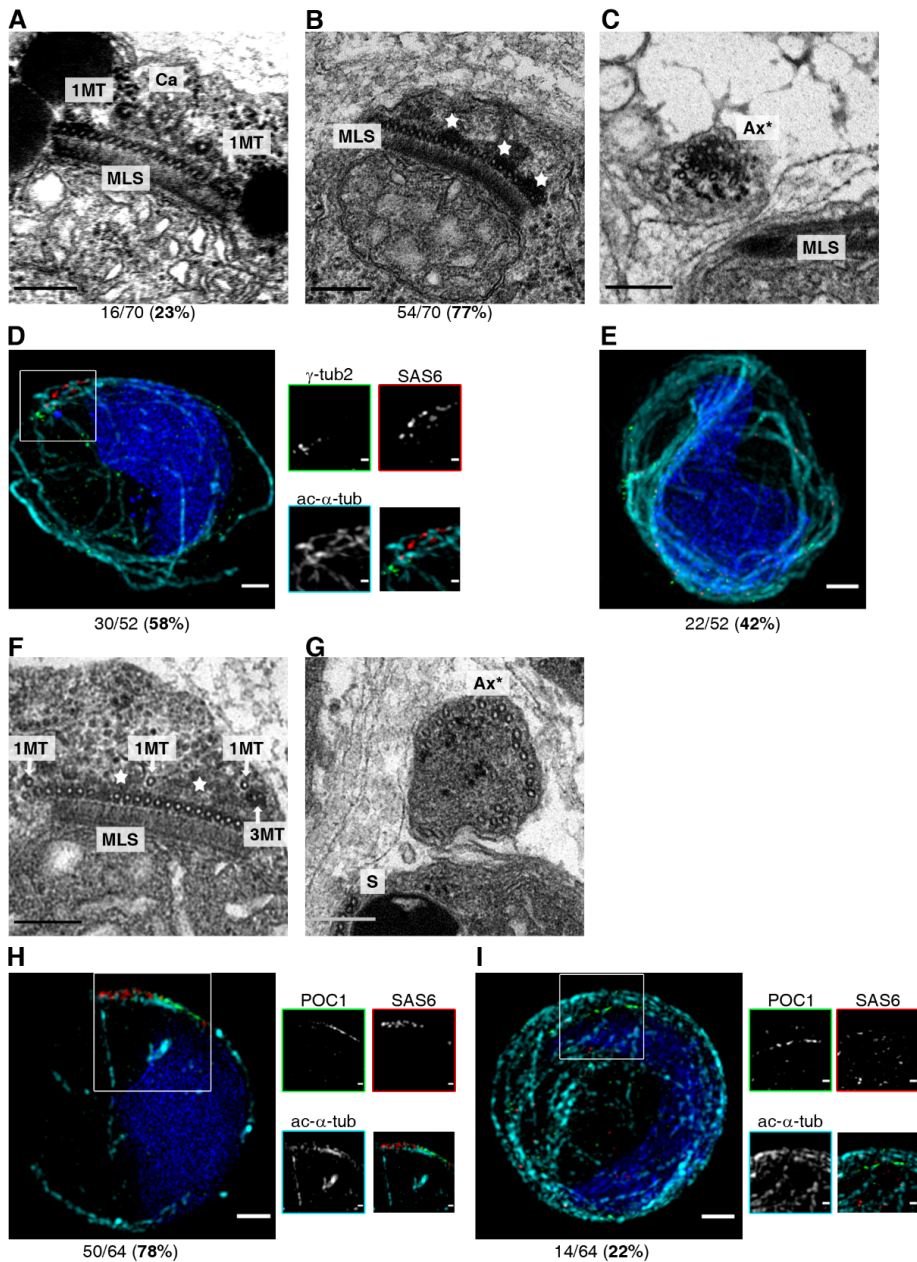


Figure 4.8: Bld10 is essential for cartwheel elongation/stability in *P. patens*. A to E. γ -tubulin2-Citrine; SAS6-mCherry; $\Delta bld10$ TEM revealing that no microtubules are bound to the few sections where cartwheel

rings are detectable (23% MLS-containing sections)(**A**). However, more often (77%) no cartwheel rings are observable above the MLS (**B**), with electron dense material concentrated in this region (white stars). Moreover, MT-containing protrusions are rarely found and severely disorganized (**C**); **D and E**. 3D-SIM analysis showing that, while some cells (58%, **D**) have compromised SAS6-mCherry signal elongation, others (42%, **E**) completely lack such signal. In both cases, disorganized microtubule filaments are observed and no SAS6 signal is observed in the MLS; **F and G**. TEM images of POC1-Citrine;SAS6-mCherry; $\Delta bld10$ sperm cells, wherein cartwheel structures were not observed and all MLS-containing sections displayed concentration of electron dense amorphous material above the spline (stars), with microtubule singlets, doublets and triplets (in 5 out of 84 sections) being visible (**F**). Cilia-like structures were composed of only microtubule singlets and contained no structural organization (**G**); **H and I**. 3D-SIM images of POC1-Citrine;SAS6-mCherry; $\Delta bld10$ sperm cells, showing the presence of discontinuous SAS6 signal (78% cells, **H**) or its absence (22%, **I**). In both cases, POC1 signal is also fragmented. EM: Ca - cartwheel ring; MLS - multilayered structure; star - accumulation of electron dense disorganized material; 1MT - singlet microtubule; 3MT - microtubule triplet; S - spline; Ax* - abnormal axoneme organization. Scale-bars = 200nm. 3D-SIM: Blue - DAPI; Cyan - acetylated- α -tubulin; Green - γ -tubulin2-Citrine (**D** and **E**) or POC1-Citrine (**H** and **I**); Red - SAS6-mCherry. Scale-bars = 1 μ m (whole cell) and 250nm (insets). For considerations on sample size refer to Table S4.3. Adapted from Gomes Pereira et al. (*in revision*).

4.4.3.3 PpPOC1 is involved in centriole wall assembly

Given the distinct size of the two sister centrioles and the possibly different length of MT triplets around the same centriolar wall, I asked if

P. patens' POC1 could be involved in the regulation of centriole MT triplet length. In contrast to the severe $\Delta sas6$ and $\Delta bld10$ phenotypes, POC1 K.O. ($\Delta poc1$) sperm cells assembled normal SAS6-containing cartwheels, capable of elongation (Figures 4.9A and C). However, no more than 3 MT triplets were ever found simultaneously attached to a cartwheel ring (Figure 4.9A). Moreover, the MTs attached to the cartwheels were always located close to the spline, suggesting this structure may have a stabilizing effect on these microtubules. Consequently, ciliary axoneme symmetry was incomplete (Figure 4.9B). Therefore, this data supports a critical role for *P. patens* POC1 in the assembly/stability of a 9-fold symmetrical centriolar wall.

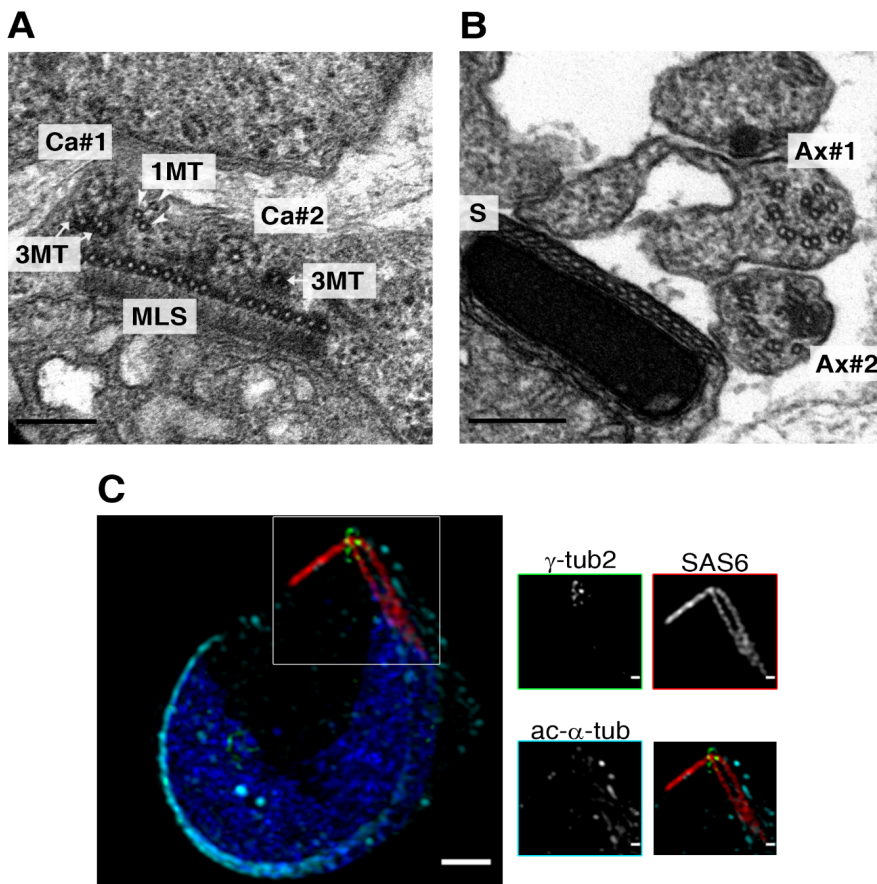


Figure 4.9: Deletion of PpPOC1 leads to incomplete centriolar walls and axonemal symmetry, without affecting cartwheel assembly or elongation. A and B. TEM images of γ -tubulin2-Citrine; SAS6-mCherry; Δ poc1 sperm cells, showing the existence of cartwheel rings with some triplet MT attached (**A**). Accordingly, axonemal symmetry is also incomplete (**B**). 1MT - microtubule singlet; 3MT - microtubule triplet. Ca#1 and #2 - cartwheels of different centrioles (arbitrary numbering); MLS - multilayered structure; Ax* - incomplete axoneme; S - spline. Scale-bars = 200nm; **C.** 3D-SIM of γ -tubulin2-Citrine; SAS6-mCherry; Δ poc1 sperm cell displaying a normal elongated SAS6 signal but abnormal acetylated tubulin organization. Blue – DAPI; Cyan – acetylated- α -tubulin; Green - γ -tubulin2-Citrine; Red - SAS6-mCherry. Scale-bars = 1 μ m or 250nm in insets. For considerations on sample size refer to Table S4.3. Adapted from Gomes Pereira et al. (*in revision*).

4.4.3.4 CPAP/SAS4 is not essential for proper centriole assembly in *P. patens*

CPAP/SAS4 is a known conserved core centriolar component, known to play key roles in centriole wall assembly and length regulation (Leidel and Gönczy, 2003; Basto et al., 2006; Kleylein-Sohn et al., 2007; Kohlmaier et al., 2009; Schmidt et al., 2009; Tang et al., 2009). Therefore, it could be possible that SAS4 played similar critical roles during *P. patens* centriole assembly and/or in the asymmetrical centriolar elongation observed. However, analysis of SAS4 K.O. (Δ sas4) plants, generated in the background of γ -tubulin2-Citrine;SAS6-mCherry, revealed that PpSAS4 is not required for centriole assembly. In fact, structurally normal centrioles were assembled in the absence of PpSAS4 (Figure 4.10A), and the only ultrastructural abnormality observed was the presence of 3 cartwheel structures in 15% of the MLS-containing

sections (Figure 4.10B). This suggests a possible role for SAS4 in determining cartwheel and/or centriole numbers in *P. patens*. Nevertheless, all ciliary axonemes observed displayed the proper 9+2 microtubule organization (Figure 4.10C), with only two cilia appearing to be nucleated in each cell (Figure 4.10D).

Intriguingly, analysis of spermatogenesis in POC1-Citrine;SAS6-mCherry; $\Delta sas4$ (Figures 4.10E to H) provided different observations from the ones for γ -tubulin2-Citrine;SAS6-mCherry; $\Delta sas4$ (Figures 4.10A to D). Indeed, no clear ciliary staining was observable in POC1-Citrine;SAS6-mCherry; $\Delta sas4$ developing sperm cells, and despite POC1-Citrine being detected at the tips of the elongated SAS6-mCherry signals, it appeared as small discontinuous fragmented *foci* (Figure 4.10E). This suggests that centriolar walls might not be properly assembled when *PpSas4* is removed from POC1-Citrine;SAS6-mCherry plants. Such observations were confirmed by TEM, revealing the absence of complete 9-fold centriolar walls in POC1-Citrine;SAS6-mCherry; $\Delta sas4$ plants, with only the microtubules closer to the spline appearing bound to the cartwheels (Figures 4.10F and G). Moreover, more than 2 cartwheel structures were recognizable in 19% (14/73) of the MLS-containing sections, yet microtubules appeared to only attach to two of such cartwheels (Figure 4.10G). However, contrary to the structurally normal cilia seen in γ -tubulin2-Citrine;SAS6-mCherry; $\Delta sas4$ (Figure 4.10C), the cilia-like structures observed in POC1-Citrine;SAS6-mCherry; $\Delta sas4$ plants were severely aberrant, being composed of misorganized microtubule singlets (Figure 4.10H), thereby explaining the aberrant acetylated- α -tubulin pattern observed by 3D-SIM (Figure 4.10E).

In conclusion, the observation of extranumerary cartwheel structures in both $\Delta sas4$ genotypes evaluated (Figures 4.10B and G) supports a

role for SAS4 in cartwheel/centriole number determination in *P. patens*. However, although SAS4 by itself does not appear to be critical for proper centriole and cilia assembly (Figures 4.10A to D), its exact functions for the assembly, elongation and/or stability of the centriolar wall, and its possible interplay with POC1/POC1-Citrine (Figures 4.10E to H), remain unclear.

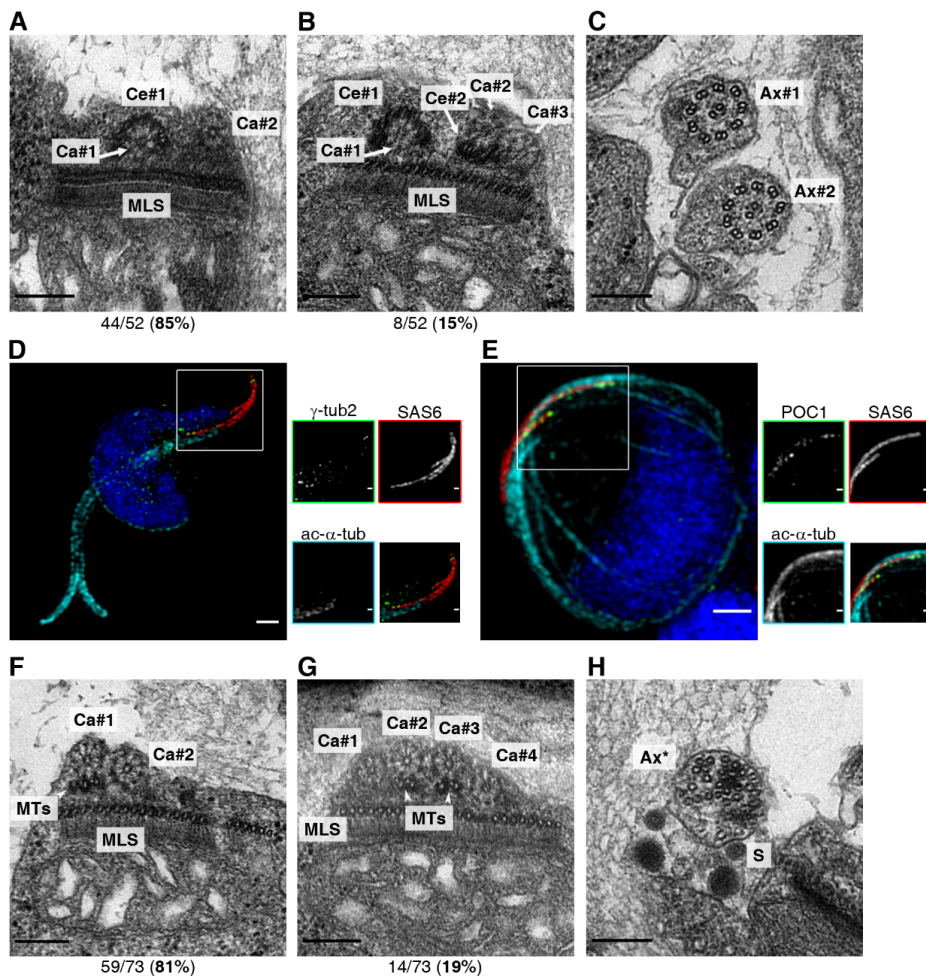


Figure 4.10: Spermatogenesis in $\Delta sas4$ plants. A to C. TEM of γ -tubulin2-Citrine;SAS6-mCherry; $\Delta sas4$ sperm cells, revealing the assembly of normal centriole structures (A), despite the existence of

extranumerary cartwheels in 15% of the MLS-containing sections (**B**). These plants assemble structurally normal 9+2 axonemes (**C**); **D**. 3D-SIM of a γ -tubulin2-Citrine;SAS6-mCherry; Δ sas4 spermatid displaying the normal SAS6-mCherry elongated signal and the existence of only 2 cilia per cell; **E**. 3D-SIM of a POC1-Citrine;SAS6-mCherry; Δ sas4 sperm cell revealing that, despite the normal elongated SAS6-mCherry signal and POC1-citrine localization, such POC1 signal is discontinuous. Moreover, no clear ciliary staining is observable and instead, irregular disorganized acetylated microtubule filaments are seen; **F to H**. TEM images of POC1-Citrine;SAS6-mCherry; Δ sas4 plants exhibiting incomplete centriolar walls (**F**), extranumerary cartwheel structures (**G**) and aberrant axonemal-like microtubule bundles (**H**). EM: Ca#1-Ca#4 - cartwheel structures numbered 1 to 4 (arbitrary numbering); Ce#1 and Ce#2 - centriolar walls of centrioles numbered 1 and 2, following cartwheels numbering; MLS - multilayered structure; Ax#1 and Ax#2 - ciliary axonemes 1 and 2 (randomly numbered); Ax* - abnormal axoneme organization; MTs - microtubules attached to the cartwheel rings. Note that these are always the centriolar microtubules closer to the spline; S - spline. Scale-bars = 200nm. 3D-SIM: Blue - DAPI; Cyan - acetylated- α -tubulin; Green - γ -tubulin2-Citrine (D) or POC1-Citrine (E); Red - SAS6-mCherry. Scale-bars = 1 μ m (whole cell) and 250nm (insets). For considerations on sample size refer to Table S4.3.

4.4.3.5 Proper centriole and cilia structures are essential for sperm motility and fertility

In agreement with the ciliary defects observed in the K.O. genotypes evaluated in this study (Δ sas6 - Figure 4.7, Δ bld10 - Figure 4.8, Δ poc1 - Figure 4.9, and POC1-Citrine;SAS6-mCherry; Δ sas4 - Figures 4.10E to H), sperm cell motility and consequently plant fertility were severely

affected in the absence of precise centriolar and ciliary structures (Figure 4.11). In fact, all K.O. genotypes were shown to have immotile sperm cells (Figure 4.11 red cells), with the exception of the seemingly normal γ -tubulin2-Citrine;SAS6-mCherry; $\Delta sas4$, wherein sperm cells appeared to have an abnormal motility (Figure 4.11 yellow cell), in accordance with their normal centriole and cilia structure (Figures 4.10A to D). In contrast, all the genotypes used as genetic backgrounds had clearly motile sperm cells (Figure 4.11 green cells).

As a consequence of sperm cell immotility (or aberrant motility), all deletion lines showed a substantial reduction in fertility when compared to their genetic background (Figure 4.11 continuous lines). Amongst these genetic backgrounds, a significant yet slight reduction in fertility was detected between the single γ -tubulin2-Citrine reporter and its combination with SAS6-mCherry (γ -tubulin2-Citrine;SAS6-mCherry), while no significant difference was found between POC1-Citrine and POC1-Citrine;SAS6-mCherry plants. Interestingly, significant differences in fertility rates appear to exist between γ -tubulin2-Citrine and POC1-Citrine, as well as between γ -tubulin2-Citrine;SAS6-mCherry and POC1-Citrine;SAS6-mCherry, revealing a potential effect of POC1-Citrine protein fusion in plant fertility, despite the absence of clear structural defects (Figure 4.6). Moreover, POC1-Citrine, POC1-Citrine;SAS6-mCherry and γ -tubulin2-Citrine;SAS6-mCherry; $\Delta sas4$ plants showed similar fertility rates (Figure 4.11 grey dashed lines). Finally, it is noteworthy that no significant differences between any $\Delta sas6$ or $\Delta bld10$ genotypes were detected, despite different genetic backgrounds. However, such a significant difference exists between $\Delta sas4$ genotypes (Figure 4.11), again supporting the different phenotypes previously described (Figure 4.10).

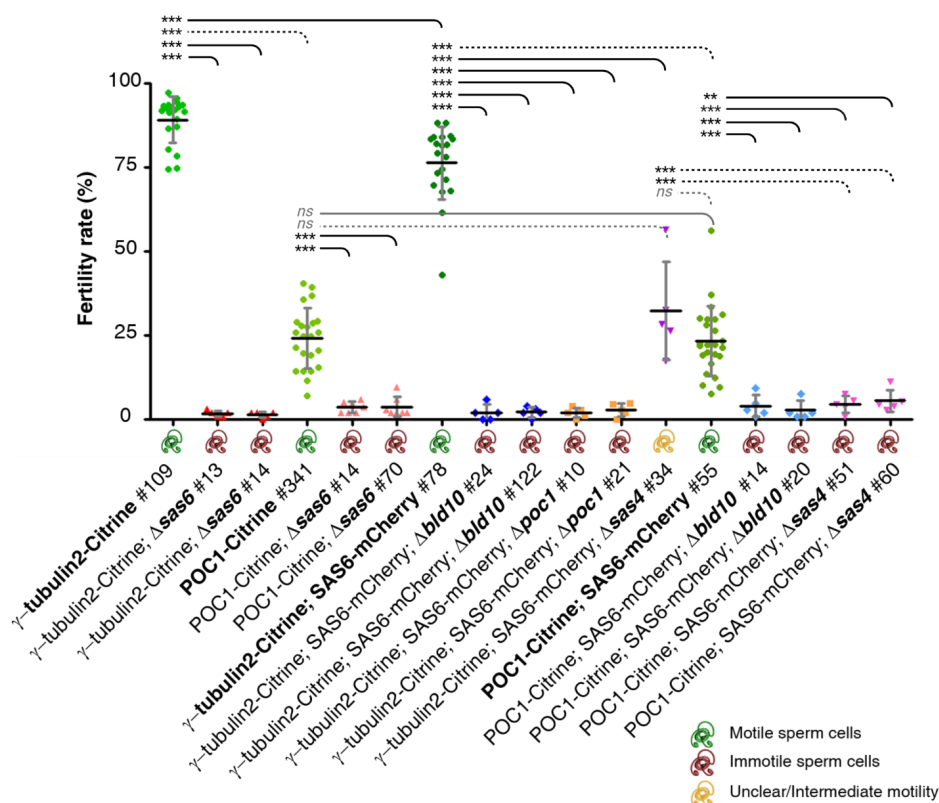


Figure 4.11: Plant fertility and sperm cell motility. Sperm cell icons shown between the fertility rate observations and the genotype identification indicate the presence of motile sperm cells (green), immotile sperm cells (red), or abnormal sperm cell motility (yellow). Each symbol in the graph represents an independent observation. Horizontal bars indicate the average and vertical bars the standard deviation of each genotype. Statistical significance between fertility rates was assessed by one-way ANOVA followed by Tukey's multiple comparison test. Pairwise comparisons between genotypes and their corresponding genetic background are represented by continuous lines, while other relevant comparisons amongst plants that are not genetically related are depicted by dashed lines. Black lines represent statistically significant differences (***) indicates p -value < 0.001; ** indicates p -value < 0.01),

and grey lines indicate that no statistically significant difference is detected (also indicated by *ns*). For considerations on sample size refer to Table S4.3.

4.5 Discussion

Centrioles play critical functions within eukaryotic cells and organisms. However, despite centrioles assembling by several pathways, only centriole duplication has been thoroughly studied. In fact, significant molecular data is only available for *de novo* centriole biogenesis *via* the deuterosome-mediated pathway (e.g. Vladar and Stearns, 2007; Zhao et al., 2013; Al Jord et al., 2014; Mori et al., 2017; Mercey et al., 2019), and although some studies have addressed *de novo* centriole assembly as single units in several systems, these relied mostly on artificial induction of centriole biogenesis (e.g. Khodjakov et al., 2002; Rodrigues-Martins et al., 2007; Wang et al., 2015; Baek et al., 2017; Nabais et al., 2021). In this work, I set out to obtain the first molecular characterization of the bicentriole-mediated centriole assembly pathway, using spermatogenesis in the moss *P. patens* as a model system for naturally occurring *de novo* centriole assembly.

Previous works had identified a set of centriolar components conserved across the vast majority of ciliated species. Moreover, these components had been shown to play critical roles in centriole assembly in many organisms, being considered key for centriole biogenesis (Carvalho-Santos et al., 2010; Hodges et al., 2010). I have explored their molecular similarity in *P. patens*, as well as reported such genes to be preferentially expressed during spermatogenesis (Figure 4.1), therefore supporting their potential role in centriole assembly in plants. Moreover,

the co-localization of PpSAS6 and PpPOC1 appeared to accompany the major steps of the previously characterized bicentriole pathway, allowing us to reveal the biogenesis of two bicentrioles and further supporting an asymmetrical maturation of the two sister centrioles (Figures 4.2, 4.3, and 4.4). Then, functional characterization of the core conserved centriole proteins SAS6, Bld10, POC1 and SAS4 revealed an impairment in cartwheel formation and stability ($\Delta sas6$ and $\Delta bld10$ - Figures 4.7 and 4.8) and microtubule wall assembly and/or stability ($\Delta poc1$ and possibly $\Delta sas4$ - Figures 4.9 and 4.10), while leaving structures such as the MLS intact. Overall the data supports the idea that SAS6, Bld10 and POC1 are part of an evolutionary conserved module required for centriole biogenesis, while SAS4 does not appear to play such a critical role in *P. patens*. Interestingly, the additive effect of SAS4 deletion together with POC1-Citrine fusion, suggests a possible undescribed cooperation between these two components.

4.5.1 Transcriptional regulation of *de novo* centriole biogenesis in *P. patens*

Regulation of centriole biogenesis is not fully understood. Contrasting with centriole duplication, which is coupled to the cell cycle, *de novo* centriole biogenesis appears to be under developmental control, with centrioles assembling only in particular cell types or developmental stages (Nabais et al., 2018). In fact, *de novo* centriole biogenesis appears to be regulated transcriptionally or post-transcriptionally, although both mechanisms might not be mutually exclusive.

Centriole biogenesis *via* deuterosomes appears to rely on the activation of a particular transcriptional program, involving several specific transcriptional factors that eventually lead to upregulation of key centriolar components and deuterosome formation (Hoh et al., 2012;

Arbi et al., 2017; Lewis and Stracker, 2021). Conversely, animal eggs are transcriptionally silent, and the initial stages of development are ensured by proteins previously deposited in the eggs (Edgar and Schubiger, 1986; Langley et al., 2014). Therefore, during insect parthenogenesis, centriole biogenesis must be triggered post-transcriptionally, and all the required centriolar precursors, or at least their transcripts, have to be loaded into the egg prior to its posture. Although the exact triggers for *de novo* centriole biogenesis remain unknown, several artificial systems have successfully recreated this process (Dirksen, 1961; Miki-Noumura, 1977; Rodrigues-Martins et al., 2007; Nabais et al., 2021).

Plant centrioles are only assembled during spermatogenesis, but molecular evidence regarding the regulation of such process remains scarce. In the water fern *Marsilea vestita*, centrioles arise *de novo* within blepharoplasts. A temporal shift between centrin transcription and translation was reported (Hart and Wolniak, 1998), revealing a post-transcriptional regulation of *de novo* centriole biogenesis in this system. However, fern reproduction depends on the release of free-living dried microspores, with spermatogenesis taking place after their hydration. This is substantially different from spermatogenesis in bryophytes, wherein two sister centrioles assemble in a bicentriole arrangement, inside antheridia still attached to the plant body.

Indeed, genes coding for conserved centriolar components are preferentially expressed throughout *P. patens* spermatogenesis (Figure 4.1B). Moreover, the expression of such genes appears to occur concomitantly to their translation, as both SAS6-mCherry and POC1-Citrine signals are observed in several stages throughout spermatogenesis (Figures 4.2 and 4.3). Nevertheless, both transcriptional and post-transcriptional regulation might co-exist. Indeed, although both *PpSas6* and *PpPoc1* transcript levels appear to be reduced simultaneously in mature sperm cells, POC1-Citrine signal

remains in these cells while SAS6-mCherry disappears (Figure 4.3C). This might be explained by a low temporal resolution of the available transcriptomic data, or different protein stabilities. However, it also opens the possibility for an active mechanism regulating SAS6 levels/degradation, similarly to the proteasomal degradation that takes place during mitosis in cycling mammalian cells (Strnad et al., 2007).

4.5.2 New findings on the bicentriole-mediated *de novo* centriole assembly, revealed by co-localization of SAS6 and POC1

In order to explore their potential role in *de novo* centriole biogenesis, transgenic lines reporting PpSAS6 and PpPOC1 localization were generated. Both proteins first appeared as small bars near the nucleus, yet these bars appeared to be composed by two distinct “lobes” that became more clear as they migrated towards opposite poles of the mitotic spindle (Figure 4.2). At mitosis, two SAS6 and POC1 co-localizing dots were clearly visible at each pole of the spindle (Figure 4.2C). This suggests that, as previously reported in *Riella americana* (Robbins, 1984), two distinct bicentrioles might assemble in *P. patens* sperm mother cell, and their localization at the spindle poles might ensure that each spermatid inherits one bicentriole (*i.e.* two sister centrioles). However, to be completely sure that this cell would represent the sperm mother cell, live imaging and lineage tracing of the bicentriole assembly and segregation would be required. As currently there are no available protocols for long-term live imaging or lineage tracing of *P. patens* spermatogenesis, such experiments are not yet feasible.

Later in spermatogenesis, as the nucleus started to elongate, both SAS6 and POC1 signals also elongated. Nevertheless, such elongation does not appear to be coupled, with SAS6-mCherry signals being always longer and not fully decorated by POC1-Citrine. Indeed, POC1-Citrine signal appears to be restricted to the distal portion of

SAS6-mCherry, from where cilia are nucleated (Figures 4.3A and B). The length of both SAS6 and POC1 filaments also differed within the same cell, yielding two distinct cartwheel/centrioles (Figures 4.3 and 4.4). Additionally, POC1-Citrine signal elongation appears to occur only in a portion of its width (Figure 4.3A inset arrow). As SAS6 localizes to both elongated and naked cartwheels (Figure 4.5), POC1-Citrine is likely to be reporting the centriolar microtubules. Overall, all of these features support the asymmetries revealed by the structural characterization of centriole biogenesis and maturation in *P. patens* (see Chapter 3), and further suggest that cartwheel and centriolar lengths might be differentially regulated.

4.5.3 A conserved cartwheel assembly module

SAS6 is known as the major component of the cartwheel rings, which are further organized and stabilized by the attachment of Cep135/Bld10 to its spokes. Together, SAS6 and Cep135/Bld10 are critical to ensure the assembly and stability of the centriolar scaffold - the cartwheel (Matsuura et al., 2004; Nakazawa et al., 2007; Jerka-Dziadosz et al., 2010; Guichard et al., 2017). In this work, I have shown both proteins to be conserved in *P. patens* (Figures 4.1A), and preferentially expressed during its spermatogenesis (Figure 4.1B). Moreover, CLEM analysis confirmed the localization of PpSAS6 to the particularly long cartwheels, as well as to the plant-specific MLS (Figure 4.5).

Functional characterization of PpSAS6 and PpBld10 revealed that both proteins are indeed required for assembly of a proper cartwheel in *P. patens*. With cartwheel rings being completely absent from $\Delta sas6$ sperm cells (Figure 4.7), and only sometimes visible in $\Delta bld10$ TEM images (Figure 4.8). Moreover, $\Delta bld10$ sperm cells displayed a fragmented SAS6-mCherry signal, further confirming defects in cartwheel elongation and/or stability (Figure 4.8). Interestingly, despite

SAS6 localization to the MLS, this structure appeared unaffected by both SAS6 or Bld10 depletion (Figures 4.7 and 4.8, respectively). Bld10 might also have an effect in SAS6 stability/concentration, as in several cells no SAS6-mCherry signal could be detected (Figures 4.8E and I), and even in those where such signal could be seen, no SAS6 MLS-pool was identifiable (Figures 4.8D and H). Bld10 is thought to compose the cartwheel spokes (Hiraki et al., 2007; Hirono, 2014; Guichard et al., 2017), and a direct interaction with SAS6 has been reported in human cells (Lin et al., 2013). Therefore, it is possible that a direct interaction between these proteins might also occur in *P. patens*. Such interaction could stabilize not only the cartwheel, but also affect SAS6 dynamics, namely making it more stable, protecting it from degradation and/or affecting its production rate. Finally, while microtubule triplets were frequently seen in $\Delta sas6$ sperm cells (Figure 4.7D), these were only detected in 3% (5 out of a total of 154) MLS-containing $\Delta bld10$ sections (Figure 4.8F), indicating a possible role for PpBld10 in microtubule triplet assembly or stability, as reported in *Tetrahymena thermophila* (Bayless et al., 2012).

In conclusion, the results here presented support the existence of a common cartwheel assembly module, relying on SAS6 for the assembly of individual cartwheel rings and Cep135/Bld10 for cartwheel stability, enabling ring stacking (elongation).

4.5.4 Conservation and particularities of *P. patens* centriolar walls

The conserved proteins POC1 and CPAP/SAS4 are both known to be involved in regulation of centriole length (Keller et al., 2009; Kohlmaier et al., 2009; Schmidt et al., 2009; Tang et al., 2009). POC1 was further suggested to localize to the inner scaffold and A-C linker, being involved in centriole assembly and stability (Pearson et al., 2009; Venoux et al.,

2012; Meehl et al., 2016; Li et al., 2019; Le Guennec et al., 2020). Indeed, *P. patens* POC1-Citrine localization is compatible with its localization to the centriolar walls (Figures 4.2 and 4.3), although no CLEM confirmation was performed. Deletion of PpPOC1 reveals this protein to have a critical function in the assembly of a 9-fold symmetrical centriolar wall, with only the microtubules closer to the spline being attached to the cartwheel spokes (Figure 4.9A). Cartwheel structure, elongation and stability do not appear to be affected by the absence of PpPOC1 (Figures 4.9A and C), confirming a role for this protein downstream of cartwheel assembly and elongation. As a consequence of an incomplete centriole symmetry, axonemal structures with incomplete symmetries were seen (Figure 4.9B), leading to immotile sperm cells and plant sterility (Figure 4.11).

Clarification of PpSAS4 functions proved to be more challenging than those of PpSAS6, PpBld10 and PpPOC1, with $\Delta sas4$ plants showing different phenotypes depending on their genetic background. Conversely, and despite its critical role in centriole biogenesis in several organisms (Leidel and Gönczy, 2003; Basto et al., 2006; Kleylein-Sohn et al., 2007), PpSAS4 depletion does not appear to compromise centriole or cilia structures (Figures 4.10A to D). Yet, even though cartwheels appear to assemble and elongate normally (Figure 4.10), extranumerary cartwheel rings were simultaneously observed in 17.6% (22/125) of all MLS-containing sections (Figures 4.10B and G). Therefore, PpSAS4 does not appear to be a critical player for centriole assembly in *P. patens*, however it might play a more subtle role in regulating cartwheel/centriole numbers. Concordantly, sperm cell motility appears to be only mildly affected by PpSas4 deletion, still leading to a significant fertility reduction in γ -tubulin2-Citrine;SAS6-mCherry; $\Delta sas4$ plants (Figure 4.11).

Nevertheless, when $\Delta sas4$ was generated in the background of POC1-Citrine;SAS6-mCherry plants (Figures 4.10E to H), no proper centrioles were assembled. Moreover, severely aberrant axonemal-like microtubule bundles were visible (Figures 4.10E and H), and sperm cell motility and fertility were severely compromised (Figure 4.11). Curiously, despite no structural defects being observable in POC1-Citrine or POC1-Citrine;SAS6-mCherry plants (Figures 4.6G to K), these plants displayed a similar fertility rate to that of γ -tubulin2-Citrine;SAS6-mCherry; $\Delta sas4$, although their sperm cell motility remained unaffected (Figure 4.11). These results indicate that SAS4 deletion might be partially compensated by POC1, but not by POC1-Citrine.

Two annotated gene sequences appear to encode POC1 proteins (Pp3c16_11590V3.1 and Pp3c16_11580V3.1) in *P. patens*. However, these localize to the same *loci*, with the shorter sequence (Pp3c16_11580V3.1) being fully embedded within the annotated region of the longer one (Pp3c16_11590V3.1). It is therefore likely that these two sequences, despite being annotated as two distinct genes, rather represent two alternative transcript isoforms. In this work, due to the highest level of similarity and expression, only the longest protein sequence was targeted. However, because the mutations performed were deletions of the full protein coding sequences, the deletion of Poc1's longer sequence also led to the removal of the shorter one. This means that $\Delta poc1$ plants actually represent the full null mutants for both potential POC1 isoforms. On the other hand, POC1-Citrine fusion will just affect the longer isoform. Therefore, if the fusion with the Citrine protein renders the protein malfunctional, the unaffected shorter POC1 isoform might rescue such defect, thus proving a possible explanation to the lack of structural defects of POC1-Citrine and POC1-Citrine;SAS6-mCherry plants (Figures 4.6H to K). However, the

longer POC1 protein might perform other particular functions, such that rescue by the shorter POC1 might not be total, potentially leading to the reduced fertility rates of these genotypes (Figure 4.11). In this scenario, it would be possible that only the longest POC1 isoform could compensate for $\Delta sas4$, enabling the assembly of proper centriole structures (Figures 4.10A to D). As this longer POC1 protein would be not fully functional in the POC1-Citrine genotypes, SAS4 would become critical to ensure the proper assembly of the centriolar wall (Figures 4.10E to H).

Despite such idea providing an interesting explanation for distinct $\Delta sas4$ phenotypes observed in γ -tubulin2-Citrine;SAS6-mCherry; $\Delta sas4$ and POC1-Citrine;SAS6-mCherry; $\Delta sas4$ plants, further experiments would be required to confirm an interplay between these two proteins. Unfortunately, due to the strong phenotype of $\Delta poc1$, a double deletion ($\Delta poc1;\Delta sas4$) by itself would unlikely be very informative. Moreover, due to lack of antibodies and functional SAS4 reporter plants, the localization of PpSAS4 cannot be easily addressed. Therefore, the best possible course of action would be to rescue $\Delta poc1$ with the transcript sequences of each individual POC1 isoform, followed by similar rescue experiments in $\Delta poc1;\Delta sas4$ double deletion plants. This would allow to explore the function, and possible cooperation, of each individual POC1 isoform with SAS4. However, it is worth mentioning that a direct interaction between POC1 and CPAP/SAS4 has not been identified in the interactome of human centrioles (Firat-Karalar et al., 2014), nor is it reported in the STRING database (Szklarczyk et al., 2019), suggesting that if conserved, such cooperation might not require/result from a direct protein-protein interaction and/or it might be particular for *de novo* assembly of centrioles.

In conclusion, this work provided the first molecular characterization of *P. patens* centriole assembly and maturation, revealing a high degree

of conservation in cartwheel (SAS6 and Cep135/Bld10) and centriolar wall (POC1) assembly and elongation/stability mechanisms. Additionally, given the high degree of functional conservation observed for PpSAS6, PpBld10 and PpPOC1, it is also tempting to speculate about a potential interplay between POC1A/B and CPAP/SAS4 in other species.

4.6 Author contributions and acknowledgements

4.6.1 Author contributions

Conceptualization, implementation and all experiments were performed by myself. Tiago Paixão (head of the Quantitative Biology & Digital Science facility at Instituto Gulbenkian de Ciência (IGC)) performed the Gaussian model mixture fitting and length classification analyses of SAS6 and POC1 length distributions. TEM and CLEM experiments and analyses were performed together with Ana Laura Sousa (Electron Microscopy Facility technician at IGC). Gohta Goshima (Sugashima marine biological laboratory and division of biological science of Nagoya University, Japan) has shared the POC1-Citrine plasmid and preliminary data on SAS6 K.O. plants. Jörg D. Becker (then head of the “Plant Genomics” laboratory at IGC, currently at Instituto de Tecnologia Química e Biológica António Xavier (ITQB)) and Mónica Bettencourt-Dias (head of the “Cell Cycle Regulation” laboratory at IGC) have jointly supervised the work.

4.6.2 Acknowledgements

I am grateful to Elena Kozgunova (Nagoya University, Japan. Currently at University of Freiburg, Germany) for sharing of plants and reagents. I thank Swadhin C. Jana (from the “Cell Cycle Regulation”

laboratory at IGC, currently at National Centre for Biological Sciences-TIFR Bangalore, India) for teaching me to perform an immunofluorescence assay, Paulo Duarte (from the “Cell Cycle Regulation” laboratory at IGC) for his support with molecular biology and plant maintenance, and Ricardo Leite (head of the Genomics facility at IGC) for helpful discussions regarding the ortholog identification and similarity analysis.

I would like to acknowledge the following IGC facilities: Plant facility (plant chamber maintenance), Light Microscopy (for equipment availability), Quantitative Biology & Digital Science (data analysis and helpful discussions), Electron Microscopy (TEM and CLEM protocols implementation and sample preparation), and Histopathology (for equipment availability).

4.7 References

Al Jord, A., Lemaître, A.-I., Delgehyr, N., Faucourt, M., Spassky, N., and Meunier, A. (2014). Centriole amplification by mother and daughter centrioles differs in multiciliated cells. *Nature* 516, 104–107.

Arbi, M., Pefani, D.-E., Taraviras, S., and Lygerou, Z. (2017). Controlling centriole numbers: Geminin family members as master regulators of centriole amplification and multiciliogenesis. *Chromosoma*.

Ashton, N.W., and Cove, D.J. (1977). The isolation and preliminary characterisation of auxotrophic and analogue resistant mutants of the moss, *Physcomitrella patens*. *Mol. Gen. Genet.* 154, 87–95.

Baek, I.K., Jang, Y.K., Lee, T.H., and Lee, J.H. (2017). Kinetic analysis of *de novo* centriole assembly in heat-shocked mammalian cells. *Cytoskeleton* 74, 18–28.

Basto, R., Lau, J., Vinogradova, T., Gardiol, A., Woods, C.G., Khodjakov, A., and Raff, J.W. (2006). Flies without Centrioles. *Cell* 125, 1375–1386.

Bayless, B.A., Giddings, T.H., Winey, M., and Pearson, C.G. (2012). Bld10/Cep135 stabilizes basal bodies to resist cilia-generated forces. *Mol. Biol. Cell* 23, 4820–4832.

Carvalho-Santos, Z., Machado, P., Branco, P., Tavares-Cadete, F., Rodrigues-Martins, A., Pereira-Leal, J.B., and Bettencourt-Dias, M. (2010). Stepwise evolution of the centriole-assembly pathway. *J. Cell Sci.* 123, 1414–1426.

Dirksen, E.R. (1961). The presence of centrioles in artificially activated sea urchin eggs. *J. Cell Biol.* 11, 244–247.

Edgar, B.A., and Schubiger, G. (1986). Parameters controlling transcriptional activation during early *Drosophila* development. *Cell* 44, 871–877.

Firat-Karalar, E.N., Sante, J., Elliott, S., and Stearns, T. (2014). Proteomic analysis of mammalian sperm cells identifies new components of the centrosome. *J. Cell Sci.* 127, 4128–4133.

Fritz-Laylin, L.K., Assaf, Z.J., Chen, S., and Cande, W.Z. (2010). *Naegleria gruberi de novo* basal body assembly occurs via stepwise incorporation of conserved proteins. *Eukaryot. Cell* 9, 860–865.

Gifford, E.M., and Larson, S. (1980). Developmental Features of the Spermatogenous Cell in *Ginkgo biloba*. *Am. J. Bot.* 67, 119–124.

Gomes Pereira, S., Sousa, A.L., Nabais, C., Paixão, T., Holmes, A.J., Schorb, M., Goshima, G., Tranfield, E.M., Becker, J.D., and Bettencourt-Dias, M. The 3D architecture and molecular foundations of *de novo* centriole assembly via bicentrioles. *BioRxiv preprint. doi: 10.1101/2020.12.21.423647*

Gopalakrishnan, J., Guichard, P., Smith, A.H., Schwarz, H., Agard, D.A., Marco, S., and Avidor-Reiss, T. (2010). Self-assembling SAS-6 multimer is a core centriole building block. *J. Biol. Chem.* 285, 8759–8770.

Guichard, P., Hamel, V., Le Guennec, M., Banterle, N., Iacovache, I., Nemčíková, V., Flückiger, I., Goldie, K.N., Stahlberg, H., Lévy, D., et al. (2017). Cell-free reconstitution reveals centriole cartwheel assembly mechanisms. *Nat. Commun.* 8, 14813.

Hart, P.E., and Wolniak, S.M. (1998). Spermiogenesis in *Marsilea vestita*: A temporal correlation between centrin expression and blepharoplast differentiation. *Cell Motil. Cytoskeleton* 41, 39–48.

Hepler, P.K. (1976). The blepharoplast of *Marsilea*: its *de novo* formation and spindle association. *J. Cell Sci.* 21, 361–390.

Hiraki, M., Nakazawa, Y., Kamiya, R., and Hirono, M. (2007). Bld10p Constitutes the Cartwheel-Spoke Tip and Stabilizes the 9-Fold Symmetry of the Centriole. *Curr. Biol.* 17, 1778–1783.

Hirono, M. (2014). Cartwheel assembly. *Philos. Trans. R. Soc. B Biol. Sci.* 369, 20130458.

Hodges, M.E., Scheumann, N., Wickstead, B., Langdale, J.A., and Gull, K. (2010). Reconstructing the evolutionary history of the centriole from protein components. *J. Cell Sci.* 123, 1407–1413.

Hoh, R.A., Stowe, T.R., Turk, E., and Stearns, T. (2012). Transcriptional Program of Ciliated Epithelial Cells Reveals New Cilium and Centrosome Components and Links to Human Disease. *PLoS One* 7, e52166.

Jerka-Dziadosz, M., Gogendeau, D., Klotz, C., Cohen, J., Beisson, J., and Koll, F. (2010). Basal body duplication in paramecium: The key role of Bld10 in assembly and stability of the Cartwheel. *Cytoskeleton* 67, 161–171.

Joukov, V., and De Nicolo, A. (2019). The Centrosome and the Primary Cilium: The Yin and Yang of a Hybrid Organelle. *Cells* 8, 2–46.

Julca, I., Ferrari, C., Flores-Tornero, M., Proost, S., Lindner, A.-C., Hackenberg, D., Steinbachová, L., Michaelidis, C., Gomes Pereira, S., Shekhar Misra, C., et al. Comparative transcriptomic analysis reveals conserved transcriptional programs underpinning organogenesis and reproduction in land plants. *BioRxiv preprint*. doi: 10.1101/2020.10.29.361501

Keller, L.C., Geimer, S., Romijn, E., John Yates, I., Zamora, I., and Marshall, W.F. (2009). Molecular Architecture of the Centriole Proteome: The Conserved WD40 Domain Protein POC1 Is Required for Centriole Duplication and Length Control. *Mol. Biol. Cell* 20, 1150–1166.

Khan, M.A., Rupp, V.M., Orpinell, M., Hussain, M.S., Altmüller, J., Steinmetz, M.O., Enzinger, C., Thiele, H., Höhne, W., Nürnberg, G., et al. (2014). A missense mutation in the PISA domain of HsSAS-6 causes autosomal

recessive primary microcephaly in a large consanguineous pakistani family. *Hum. Mol. Genet.* **23**, 5940–5949.

Khodjakov, A., Rieder, C.L., Sluder, G., Cassels, G., Sibon, O., and Wang, C.L. (2002). *De novo* formation of centrosomes in vertebrate cells arrested during S phase. *J. Cell Biol.* **158**, 1171–1181.

Kleylein-Sohn, J., Westendorf, J., Le Clech, M., Habedanck, R., Stierhof, Y.D., and Nigg, E.A. (2007). Plk4-Induced Centriole Biogenesis in Human Cells. *Dev. Cell* **13**, 190–202.

Klos Dehring, D.A., Vladoar, E.K., Werner, M.E., Mitchell, J.W., Hwang, P., and Mitchell, B.J. (2013). Deuterosome Mediated Centriole Biogenesis. *Dev. Cell* **27**, 103–112.

Kohlmaier, G., Lončarek, J., Meng, X., McEwen, B.F., Mogensen, M.M., Spektor, A., Dynlacht, B.D., Khodjakov, A., and Gönczy, P. (2009). Overly Long Centrioles and Defective Cell Division upon Excess of the SAS-4-Related Protein CPAP. *Curr. Biol.* **19**, 1012–1018.

Kuriyama, R. (2009). Centriole assembly in CHO cells expressing Plk4/SAS6/SAS4 is similar to centriogenesis in ciliated epithelial cells. *Cell Motil. Cytoskeleton* **66**, 588–596.

La Terra, S., English, C.N., Hergert, P., McEwen, B.F., Sluder, G., and Khodjakov, A. (2005). The *de novo* centriole assembly pathway in HeLa cells: Cell cycle progression and centriole assembly/maturation. *J. Cell Biol.* **168**, 713–722.

Langley, A.R., Smith, J.C., Stemple, D.L., and Harvey, S.A. (2014). New insights into the maternal to zygotic transition. *Development* **141**, 3834–3841.

Le Guennec, M., Klena, N., Gambarotto, D., Laporte, M.H., Tassin, A.M., van den Hoek, H., Erdmann, P.S., Schaffer, M., Kovacic, L., Borgers, S., et al. (2020). A helical inner scaffold provides a structural basis for centriole cohesion. *Sci. Adv.* **6**.

Lee, J., Kang, S., Choi, Y.S., eok, Kim, H.K., Yeo, C.Y., Lee, Y., Roth, J., and Lee, J. (2015). Identification of a cell cycle-dependent duplicating complex that assembles basal bodies *de novo* in *Naegleria*. *Protist* **166**, 1–13.

Leidel, S., and Gönczy, P. (2003). SAS-4 is essential for centrosome duplication in *C. elegans* and is recruited to daughter centrioles once per cell cycle. *Dev. Cell* 4, 431–439.

Levine, M.S., Bakker, B., Boeckx, B., Moyett, J., Lu, J., Vitre, B., Spierings, D.C., Lansdorp, P.M., Cleveland, D.W., Lambrechts, D., et al. (2017). Centrosome Amplification Is Sufficient to Promote Spontaneous Tumorigenesis in Mammals. *Dev. Cell* 40, 313–322.

Lewis, M., and Stracker, T.H. (2021). Transcriptional regulation of multiciliated cell differentiation. *Semin. Cell Dev. Biol.* 110, 51–60.

Li, S., Fernandez, J.J., Marshall, W.F., and Agard, D.A. (2019). Electron cryo-tomography provides insight into procentriole architecture and assembly mechanism. *Elife* 8, e43434.

Lin, Y.C., Chang, C.W., Hsu, W. Bin, Tang, C.J.C., Lin, Y.N., Chou, E.J., Wu, C.T., and Tang, T.K. (2013). Human microcephaly protein CEP135 binds to hSAS-6 and CPAP, and is required for centriole assembly. *EMBO J.* 32, 1141–1154.

Lopes, C.A.M., Mesquita, M., Cunha, A.I., Cardoso, J., Carapeta, S., Laranjeira, C., Pinto, A.E., Pereira-Leal, J.B., Dias-Pereira, A., Bettencourt-Dias, M., et al. (2018). Centrosome amplification arises before neoplasia and increases upon p53 loss in tumorigenesis. *J. Cell Biol.* 217, 2353–2363.

Martel, G., Guerrero, A., Vieira, A.F., De Almeida, B.P., Machado, P., Mendonça, S., Mesquita, M., Villarreal, B., Fonseca, I., Francia, M.E., et al. (2018). Over-elongation of centrioles in cancer promotes centriole amplification and chromosome missegregation. *Nat. Commun.* 9.

Matsuura, K., Lefebvre, P.A., Kamiya, R., and Hirono, M. (2004). Bld10p, a novel protein essential for basal body assembly in *Chlamydomonas*: Localization to the cartwheel, the first ninefold symmetrical structure appearing during assembly. *J. Cell Biol.* 165, 663–671.

Meehl, J.B., Bayless, B.A., Giddings, T.H., Pearson, C.G., and Winey, M. (2016). *Tetrahymena* Poc1 ensures proper intertriplet microtubule linkages to maintain basal body integrity. *Mol. Biol. Cell* 27, 2394–2403.

Mercey, O., Al Jord, A., Rostaing, P., Mahuzier, A., Fortoul, A., Boudjema, A.R., Faucourt, M., Spassky, N., and Meunier, A. (2019). Dynamics of centriole amplification in centrosome-depleted brain multiciliated progenitors. *Sci. Rep.* 9.

Miki-Noumura, T. (1977). Studies on the *de novo* formation of centrioles: aster formation in the activated eggs of sea urchin. *J. Cell Sci.* 24, 203–216.

Mori, M., Hazan, R., Danielian, P.S., Mahoney, J.E., Li, H., Lu, J., Miller, E.S., Zhu, X., Lees, J.A., and Cardoso, W. V. (2017). Cytoplasmic E2f4 forms organizing centres for initiation of centriole amplification during multiciliogenesis. *Nat. Commun.* 8, 15857.

Moser, J.W., and Kreitner, G.L. (1970). Centrosome Structure in *Anthoceros laevis* and *Marchantia polymorpha*. *J. Cell Biol.* 44, 454–458.

Nabais, C., Pereira, S.G., and Bettencourt-Dias, M. (2018). Noncanonical Biogenesis of Centrioles and Basal Bodies. *Cold Spring Harb. Symp. Quant. Biol.* 82:123-135.

Nabais, C., Pessoa, D., de-Carvalho, J., van Zanten, T., Duarte, P., Mayor, S., Carneiro, J., Telley, I.A., and Bettencourt-Dias, M. (2021). PIK4 triggers autonomous *de novo* centriole biogenesis and maturation. *J. Cell Biol.* 22 (5): e202008090.

Nakaoka, Y., Miki, T., Fujioka, R., Uehara, R., Tomioka, A., Obuse, C., Kubo, M., Hiwatashi, Y., and Goshima, G. (2012). An inducible RNA interference system in *Physcomitrella patens* reveals a dominant role of augmin in phragmoplast microtubule generation. *Plant Cell* 24, 1478–1493.

Nakazawa, Y., Hiraki, M., Kamiya, R., and Hirono, M. (2007). SAS-6 is a Cartwheel Protein that Establishes the 9-Fold Symmetry of the Centriole. *Curr. Biol.* 17, 2169–2174.

Nanjundappa, R., Kong, D., Shim, K., Stearns, T., Brody, S.L., Loncarek, J., and Mahjoub, M.R. (2019). Regulation of cilia abundance in multiciliated cells. *Elife* 8.

Nido, G.S., Méndez, R., Pascual-García, A., Abia, D., and Bastolla, U. (2012). Protein disorder in the centrosome correlates with complexity in cell types number. *Mol. Biosyst.* 8, 353–367.

Nigg, E.A., and Holland, A.J. (2018). Once and only once: Mechanisms of centriole duplication and their deregulation in diseases. *Nat. Rev. Mol. Cell Biol.* *19*, 297–312.

Ortiz-Ramírez, C., Michard, E., Simon, A.A., Damineli, D.S.C., Hernández-Coronado, M., Becker, J.D., and Feijó, J.A. (2017). GLUTAMATE RECEPTOR-LIKE channels are essential for chemotaxis and reproduction in mosses. *Nature* *549*, 91–95.

Pearson, C.G., Osborn, D.P.S., Giddings, T.H., Beales, P.L., and Winey, M. (2009). Basal body stability and ciliogenesis requires the conserved component Poc1. *J. Cell Biol.* *187*, 905–920.

Peel, N., Stevens, N.R., Basto, R., and Raff, J.W. (2007). Overexpressing Centriole-Replication Proteins *In Vivo* Induces Centriole Overduplication and *De Novo* Formation. *Curr. Biol.* *17*, 834–843.

Potter, S.C., Luciani, A., Eddy, S.R., Park, Y., Lopez, R., and Finn, R.D. (2018). HMMER web server: 2018 update. *Nucleic Acids Res.* *46*, 200–204.

Renzaglia, K.S., and Garbary, D.J. (2001). Motile Gametes of Land Plants: Diversity, Development, and Evolution. *CRC. Crit. Rev. Plant Sci.* *20*, 107–213.

Reski, R., and Abel, W.O. (1985). Induction of budding on chloronemata and caulonemata of the moss, *Physcomitrella patens*, using isopentenyladenine. *Planta* *165*, 354–358.

Robbins, R.R. (1984). Origin and behavior of bicentriolar centrosomes in the bryophyte *Riella americana*. *Protoplasma* *121*, 114–119.

Rodrigues-Martins, A., Riparbelli, M., Callaini, G., Glover, D.M., and Bettencourt-Dias, M. (2007). Revisiting the Role of the Mother Centriole in Centriole Biogenesis. *Science*. *316*, 1046–1050.

Schindelin, J., Arganda-Carreras, I., Frise, E., Kaynig, V., Longair, M., Pietzsch, T., Preibisch, S., Rueden, C., Saalfeld, S., Schmid, B., et al. (2012). Fiji: An open-source platform for biological-image analysis. *Nat. Methods* *9*, 676–682.

Schmidt, T.I., Kleylein-Sohn, J., Westendorf, J., Le Clech, M., Lavoie, S.B., Stierhof, Y.D., and Nigg, E.A. (2009). Control of Centriole Length by CPAP and CP110. *Curr. Biol.* *19*, 1005–1011.

Shaheen, R., Faqeih, E., Shamseldin, H.E., Noche, R.R., Sunker, A., Alshammari, M.J., Al-Sheddi, T., Adly, N., Al-Dosari, M.S., Megason, S.G., et al. (2012). POC1A truncation mutation causes a ciliopathy in humans characterized by primordial dwarfism. *Am. J. Hum. Genet.* *91*, 330–336.

Shimamura, M., Brown, R.C., Lemmon, B.E., Akashi, T., Mizuno, K., Nishihara, N., Tomizawa, K.I., Yoshimoto, K., Deguchi, H., Hosoya, H., et al. (2004). γ -Tubulin in Basal Land Plants: Characterization, Localization, and Implication in the Evolution of Acentriolar Microtubule Organizing Centers. *Plant Cell* *16*, 45–59.

Sousa, A.L., Rodrigues Lóios, J., Faísca, P., and Tranfield, E.M. (2021). The Histo-CLEM Workflow for tissues of model organisms. *Methods Cell Biol.* *162*, 13–37.

Stearns, T., Evans, L., and Kirschner, M. (1991). γ -Tubulin is a highly conserved component of the centrosome. *Cell* *65*, 825–836.

Strnad, P., Leidel, S., Vinogradova, T., Euteneuer, U., Khodjakov, A., and Gönczy, P. (2007). Regulated HsSAS-6 Levels Ensure Formation of a Single Procentriole per Centriole during the Centrosome Duplication Cycle. *Dev. Cell* *13*, 203–213.

Suh, M.R., Han, J.W., No, Y.R., and Lee, J. (2002). Transient concentration of a γ -tubulin-related protein with a pericentrin-related protein in the formation of basal bodies and flagella during the differentiation of *Naegleria gruberi*. *Cell Motil. Cytoskeleton* *52*, 66–81.

Szklarczyk, D., Gable, A.L., Lyon, D., Junge, A., Wyder, S., Huerta-Cepas, J., Simonovic, M., Doncheva, N.T., Morris, J.H., Bork, P., et al. (2019). STRING v11: Protein-protein association networks with increased coverage, supporting functional discovery in genome-wide experimental datasets. *Nucleic Acids Res.* *47*, D607–D613.

Tang, C.J.C., Fu, R.H., Wu, K.S., Hsu, W. Bin, and Tang, T.K. (2009). CPAP is a cell-cycle regulated protein that controls centriole length. *Nat. Cell Biol.* *11*, 825–831.

Venoux, M., Tait, X., Hames, R.S., Straatman, K.R., Woodland, H.R., and Fry, A.M. (2012). Poc1A and Poc1B act together in human cells to ensure centriole integrity. *J. Cell Sci.* *126*, 163–175.

Vladar, E.K., and Stearns, T. (2007). Molecular characterization of centriole assembly in ciliated epithelial cells. *J. Cell Biol.* *178*, 31–42.

Wang, W.J., Acehan, D., Kao, C.H., Jane, W.N., Uryu, K., and Tsou, M.F.B. (2015). *De novo* centriole formation in human cells is error-prone and does not require SAS-6 self-assembly. *Elife* *4*, 1–13.

Zhao, H., Zhu, L., Zhu, Y., Cao, J., Li, S., Huang, Q., Xu, T., Huang, X., Yan, X., and Zhu, X. (2013). The cep63 paralogue deup1 enables massive *de novo* centriole biogenesis for vertebrate multiciliogenesis. *Nat. Cell Biol.* *15*, 1434–1444.

4.8 Supplementary information

Table S4.1: Plasmid engineering. Details on how each plasmid, required to obtain the plant genotypes used in this study, was constructed. Unless otherwise stated, all PCR amplifications were performed from WT DNA. Integration of each region in the desired orientation, and its sequence were confirmed by Sanger sequencing. Note that all sequences are presented from 5' to 3'.

Plasmid name	5' Homology arm (strategy)	Reporter protein/Resistance cassette (strategy)	3' Homology arm (strategy)
pBNRf_SAS6-mCherry_G418	SAS6_GeneEnd_GA.For: AATTACCCTGTTATCCCTAGGC GTGCAAGCTGCTCAAAGGTT C SAS6_GeneEnd_GA.Rev: CAGCAGCACCAAGCAGGGCTAG CCCTACGCGAGAAATGGCTCT TTGC (Ligated by Gibson Assembly)	Linker-mCherry-NOsterminador; 35S::G418R from the plasmid backbone (Ligated after endonuclease restriction (NheI + SpeI) in the Gibson Assembly step)	SAS6_3END_GA_For: TGCTATACGAAGTTATACTAGT CTGTGCAAGAGCATTTCGTTGT GAC SAS6_3END_GA.Rev: CCCATGGATCGATGTTAACCG CCTATTGACCTAGCACAGTC (Ligated by Gibson Assembly)
pBNR_SAS6-mCherry_HygR_3UTR_c25a	From pBNRf_SAS6-mCherry_G418 plasmid	Replaced G418R with HygR by endonuclease restriction with NheI+EcoRV from pBNRf_SAS6-mCherry_G418 plasmid	From pBNRf_SAS6-mCherry_G418 plasmid

	<p>Followed by site directed mutagenesis (SAS6_3UTR_c25a_F: AGAGCATTCGTTGTGACACACGTTAAAGTGTCAGC)</p>		
EKv194(Pp3c1 6_11590(POC1) -CITRINE)	<p>POC1_CTRN_IF_F: GAGGTCGACGGTATCGTACTT GTCGTTACTCCCAGG POC1_CTRN_IF_R: CAAGATATCAAGCTTATCCCCT GCAGTCCTTGGTC</p>	<p>Citrine_F: AAGCTTGATATCTTGGTGAGC AA Citrine_R: ATAGGGACTTTAGGAGATCTG GA</p>	<p>POC1 3'UTR CTRN IF F: TCCTAAAGTCCCTATTCGTGGC AATTGATGCGAAGC POC1 3'UTR CTRN IF R: GTTTAGTCGTCTCGTCGCCTT CACAAGCCTGCACG</p>
<p>In Fusion cloning with backbone pCTRN-NPTII2 amplified using pCTRN-Npt II-2 F (ACGAGACGACTAAACCTGGAGCC) and pCTRN-Npt II-2 R (GATACCGTCGACCTCGAGGGGGG)</p>			
pBNR_SAS6_K O_Zeo_3UTR_ c25A	<p>pSAS6_KO_GAF: AAGCTAATTACCCTGTTATCCCT GCAGCATCTTTCTGTGTTCCAGG TGC pSAS6_KO_Zeo_GAR: GTTTCGAACCCGGCTCTTTCCC TGATCAATC</p>	<p>Zeocin_pSAS6_GAF: GAGCCGGGTTTCGAACGTACG TCGCG Zeocin_3'SAS6_GAR: GAATGCTCTTGCACAGAGTTT AAACGCGTGCGCCACTAGT</p>	<p>SAS6_3END_GA_For: TGCTATACGAAGTTATACTAGT CTGTGCAAGAGCATTTCGTTGT GAC SAS6_3END_GA.Rev: CCCATGGATCGATGTTAACCG CCTATTGACCTAGCACAGTC</p>
<p>Ligated by Gibson Assembly, followed by site-directed mutagenesis (SAS6_3UTR_c25a_F: AGAGCATTCGTTGTGACACACGTTAAAGTGTCAGC)</p>			
	<p>pBld10_KO_GAF: AAGCTAATTACCCTGTTATCCCT AGGGGGGTGAGGATTATGGAG G</p>	<p>Zeocin_pBld10_GAF: TAGGTGGCCTGCAGGTTTCGA ACGTACGTCGCG</p>	<p>Bld10_3END_GA.For: TGCTATACGAAGTTATACTAGT CGGAATGGAAATTAAGAGATC GAGAG</p>

<p>pBNR_Bld10_KO_Zeo_5end_g1057t</p>	<p>pBld10_KO_Zeo_GAR: GTTTCGAACCTGCAGGCCACCT AAGCTATGCCTG</p>	<p>Zeocin_3'Bld10_GAR: ATCTCTTAATTTCCATTCCGaC GCGTGGCGCCACTAGT</p>	<p>Bld10_3END_GA.Rev: CCCATGGATCGATGTTAACCAA AGAGGTAGCACAAAGGATCAAG GTTCA</p>
<p>Ligated by Gibson Assembly, followed by site-directed mutagenesis (Bld10_KO_5end_g1057t_F: TATTATTCAGGCATAGCTTAGGTTGCCTGCAGGTTTC)</p>			
<p>pBNR_POC1_KO_Zeo</p>	<p>PstI_POC1_5UTR_F: CTGCAGCACGCAAAGCTAGA GCAAG POC1_5UTR_XhoI_R: CTCGAGTGAGGAGTCCATAAA GTGAGTTGCC Inserted after endonuclease restriction (PstI + XhoI) and TA ligation</p>	<p>35S::BleoR (from plasmid's backbone) Ligated by TA ligation after endonuclease restriction (XhoI + MluI)</p>	<p>MluI_POC1_3UTR_F: ACGCGTTCGTGGCAATTGATG CGAAG POC1_3UTR_PacI_R: TTAATTAACCATTCCGGCAGTCG TTACTG Inserted after endonuclease restriction (MluI + PacI) and TA ligation</p>
<p>pBNR_SAS4_KO_Zeo</p>	<p>pSAS4_KO_GAF: AAGCTAATTACCCTGTTATCCG TTTAAACGCTGTCTGTGTTTCG AAGCTG pSAS4_KO_Zeo_GAR: GTTTCGAACAAGCTTGCTCAAG ATGCTCCTTATTCCCC</p>	<p>Zeocin_pSAS4_GAF: TCTTGAGCAAGCTTGTTCGAA CGTACGTCCGG Zeocin_3'SAS4_GAR: CAACGCATGCACACACTAGGC TAGCTGCGTGGCGCCACTAGT (amplified from pBZRf plasmid)</p>	<p>SAS4_3END_GA.For: TGCTATACGAAGTTATACTAGT GTGTGCATGCGTTGAAGAAAA TCAG SAS4_3END_GA.Rev: CCCATGGATCGATGTTAACGTG AGGAGGCGTAGCTTGGG</p>
<p>Ligated by Gibson Assembly</p>			

pGENIOUS_Cas9_U6_ZeoR	TA ligation of U6 promoter (from U6 plasmid) to pGENIOUS_Cas9, after endonuclease restriction with AvrII and SphI; followed by TA ligation of 35S::BleoR (from pBZRf plasmid) to pGENIOUS_Cas9, after endonuclease restriction with SphI6
pGENIOUS_Cas9_U3_U6_ZeoR	TA ligation of U3 promoter (from U3 plasmid) to pGENIOUS_Cas9_U6_ZeoR, after endonuclease restriction with SpeI and AvrII
pGENIOUS_Cas9_gRNA2_gRNA1	Annealed gRNA2 (TAACGCTGACACTTTAACGTGGG) and annealed gRNA1 (TTTCTCGCGTAGGTAGCATGTGG) were ligated (TA ligation) to pGENIOUS_Cas9_U3_U6_ZeoR plasmid after its digestion with MluI and NotI
pGENIOUS_Cas9_U6_gRNA14	Annealed gRNA14 (GAGTCCGAACTAAAAATGATCGG) was ligated (TA ligation) to pGENIOUS_Cas9_U6_ZeoR plasmid after its digestion with MluI
pGENIOUS_Cas9_gRNA2_gRNA9	Annealed gRNA2 (TAACGCTGACACTTTAACGTGGG) and annealed gRNA9 (TGATCAGGGAAAGAGCCGGATGG) were ligated (TA ligation) to pGENIOUS_Cas9_U3_U6_ZeoR plasmid after its digestion with MluI and NotI
pGENIOUS_Cas9_gRNA4_gRNA3	Annealed gRNA4 (GAGTCCGAACTAAAAATGATCGG) and annealed gRNA3 (TTATTCAGGCATAGCTTAGGTGG) were ligated (TA ligation) to pGENIOUS_Cas9_U3_U6_ZeoR plasmid after its digestion with MluI and NotI
pGENIOUS_Cas9_gRNA14_gRNA13	Annealed gRNA14 (GAGTCCGAACTAAAAATGATCGG) and annealed gRNA13 (ATACGTCGTATATCTTTCCTGGG) were ligated (TA ligation) to pGENIOUS_Cas9_U3_U6_ZeoR plasmid after its digestion with MluI and NotI

Table S4.2: Plant transformations and genotyping. Detailed information on which genetic background and plasmids were used during plant transformations, selected markers and oligonucleotide sequences (5' → 3') used for genotyping.

Final genotype	Genetic background	Plasmids used (strategy)	Selection marker	Genotyping oligonucleotides (5'→3')	
				5' recombination	3' recombination
SAS6-mCherry	WT	pBNRf_SAS6-mCherry_G418 (HR)	G418	SAS6_genotypeF:GTGGTTTGGGAGTATTCAACACG	35Sfwd: GACGCACAATCCCACTATCC SAS6_genotypeR:CTAGGTTGGGGGATGTTCTTCC
γ-tubulin2-Citrine; SAS6-mCherry	γ-tubulin2-Citrine #109	pBNR_SAS6-mCherry_HygR_3UTR_c25a + pGENIOUS_Cas9_gRNA2_gRNA1 (CRISPR/Cas9)	G418 + Hygromycin B	pBNR_Seq1_Rev:CACTTGAAGCGCATGAACTC	HygR_3b_3'_F: GTACTCGCCGATAGTGGAAAC SAS6_genotypeR:CTAGGTTGGGGGATGTTCTTCC
POC1-Citrine	WT	EKv194(Pp3c16_11590(POC1)-CITRINE) + pGENIOUS_ca	G418	POC1GeneEnd_genotype_F:CGGCCACTCTCTAGAGAAGG	35Sfwd: GACGCACAATCCCACTATCC

		s9_U6_gRNA14 (CRISPR/Cas9)		mCardinal_nSTOP_R :CTTGACAGCTCG TCCATGCC	pPOC1_genotypeR:C TTTGTAGCGGGAGC TTGATTAG
POC1-Citrine; SAS6-mCherry	POC1-Citrine #341	pBNR_SAS6-m Cherry_HygR_3 UTR_c25a + pGENIOUS_Ca s9_gRNA2_gR NA1 (CRISPR/Cas9)	G418 + Hygromycin B	SAS6_genotypeF:GT GGTTTGGGAGTATT CAACACG pBNR_Seq1_Rev:CA CCTTGAAGCGCAT GAACTC	HygR_3b_3'_F: GTA CTCTCGCCGATAG TGGAAAC SAS6_genotypeR:CTA GGTTGGGGGATGTT CTTCC
γ-tubulin2-Citrine; SAS6 K.O.	γ -tubulin2-Citrine #109	pBNR_SAS6_K O_Zeo_3UTR_ c25A + pGENIOUS_Ca s9_gRNA2_gR NA9 (CRISPR/Cas9)	G418 + Zeocin	pSAS6_genotypeF:G GCTGTATACTGCCA CCTAAG 35sZeo_rev: CGTCTTGATGAGAC CTGCTG	SAS6_genotypeR:CTA GGTTGGGGGATGTT CTTCC SAS6_3end_c25aF:G TTCCCTCACACCGG TGAC
POC1-Citrine; SAS6 K.O.	POC1-Citrine #341				
γ-tubulin2-Citrine; SAS6-mCherry; Bld10 K.O.	γ -tubulin2-Citrine; SAS6-mCherry #78	pBNR_Bld10_K O_Zeo_5end_g 1057t + pGENIOUS_Ca s9_gRNA4_gR NA3 (CRISPR/Cas9)	G418 + Hygromycin B + Zeocin	pBld10_genotype:GG GAAGCTCTCTGTAG GATTG 35sZeo_rev:CGTCTT GATGAGACCTGCT G	SAS6_3end_c25aF:G TTCCCTCACACCGG TGAC Bld10_genotypeR:CA ATCTTTGTGCCAGCT TCCTGC
POC1-Citrine; SAS6-mCherry; Bld10 K.O.	POC1-Citrine; SAS6-mCherry #55				

γ-tubulin2-Citrine; SAS6-mCherry; POC1 K.O.	γ -tubulin2-Citrine; SAS6-mCherry #78	pBNR_POC1_K O_Zeo + pGENIOUS_Ca s9_gRNA14_gR NA13 (CRISPR/Cas9)	G418 + Hygromycin B + Zeocin	pPOC1_genotypeF:C TAGTGCGTAACACA TCCTGG 35sZeo_rev: CGTCTTGATGAGAC CTGCTG	SAS6_3end_c25aF:G TTCCCTCACACCGG TGAC pPOC1_genotypeR:C TTTGTAGCGGGAGC TTGATTAG
γ-tubulin2-Citrine; SAS6-mCherry; SAS4 K.O.	γ -tubulin2-Citrine; SAS6-mCherry #78	pBNR_SAS4_K O_Zeo (HR)	G418 + Hygromycin B + Zeocin	pSAS4_seq: GAACGATAATGCAA TGGCTTCG Zeo_rev: AAGTCGTCCTCCA CGAAGTC	35S_fwd: GACGCACAATCCCA CTATCC SAS4_3seq: GTGAAATGGTGCTC ATTCTGCTC
POC1-Citrine; SAS6-mCherry; SAS4 K.O.	POC1-Citrine; SAS6-mCherry #55				

Table S4.3: Experimental samples considered in each experiment per genotype. Developmental stages (stg.) assigned as follows: I.-II. fluorescent signal only visible as dots/small bars (3D-SIM); III. elongated fluorescent signal but no cilia (3D-SIM), individualized centrioles associated to the multilayered structure (MLS) but not docked to the cell membrane (TEM); IV. cilia signal detected, nucleus elongated but not condensed (3D-SIM), ciliary axonemes visible but chromatin not condensed (TEM); V. cilia staining visible and elongated, condensed nucleus (3D-SIM), ciliary axonemes visible in cells with elongated, condensed chromatin (TEM). ND - not determined.

Genotype	Line no.	TEM (stg. III.-V.)	3D-SIM (cells, experiments)				Sperm motility (clusters, experiments)	Fertility (independent counts)
			stg. I.-II.	stg. III.	stg. IV.	stg. V.		
POC1-Citrine; SAS6-mCherry	#55	52, 6, 2	29, 5	16, 4	55, 4	38, 4	3, 3	25
	#71	9, 2, 1	6, 2	8, 2	19, 2	8, 2	7, 3	5
SAS6-mCherry	#304	ND	11, 6	8, 4	23, 6	14, 5	ND	6
γ -tubulin2-Citrine	#109	53, 6, 2	40, 11	19, 9	76, 13	16, 5	7, 3	20
γ -tubulin2-Citrine; SAS6-mCherry	#78	84, 7, 3	54, 11	16, 7	94, 13	37, 4	5, 3	20
	#61	ND	15, 6	10, 3	35, 6	9, 2	4, 3	5
POC1-Citrine	#341	48, 7, 3	13, 5	11, 4	62, 6	22, 4	6, 3	23

γ-tubulin2-Citrine; SAS6 K.O.	#13	70, 11, 3	11, 5	14, 5	37, 4	13, 3	5, 3	5
	#14	29, 2, 1	15, 4	11, 4	27, 3	16, 1	6, 3	5
POC1-Citrine; SAS6 K.O.	#14	37, 8, 3	8, 4	20, 3	53, 4	24, 3	8, 3	7
	#70	24, 3, 1	5, 2	4, 2	16, 2	10, 2	7, 3	7
γ-tubulin2-Citrine; SAS6-mCherry; Bld10 K.O.	#122	104, 10, 3	17, 6	20, 6	52, 6	21, 3	4, 3	5
	#24	47, 2, 1	12, 3	17, 3	11, 2	7, 2	4, 3	5
POC1-Citrine; SAS6-mCherry; Bld10 K.O.	#14	95, 9, 3	25, 3	25, 3	64, 3	20, 3	9, 3	5
	#20	13, 2, 1	13, 1	15, 2	33, 2	13, 1	7, 3	5
γ-tubulin2-Citrine; SAS6-mCherry; POC1 K.O.	#10	100, 6, 2	18, 4	16, 4	30, 4	13, 4	5, 4	5
	#21	10, 2, 1	15, 2	26, 2	23, 1	11, 1	7, 3	5
γ-tubulin2-Citrine; SAS6-mCherry; SAS4 K.O.	#34	116, 10, 3	28, 4	47, 4	77, 4	18, 3	6, 4	5
POC1-Citrine; SAS6-mCherry; SAS4 K.O.	#60	124, 10, 3	24, 4	25, 3	52, 4	27, 3	7, 3	5
	#51	19, 2, 2	15, 2	7, 2	30, 2	13, 1	6, 3	5

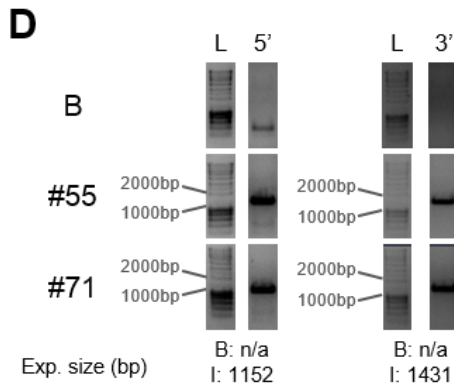
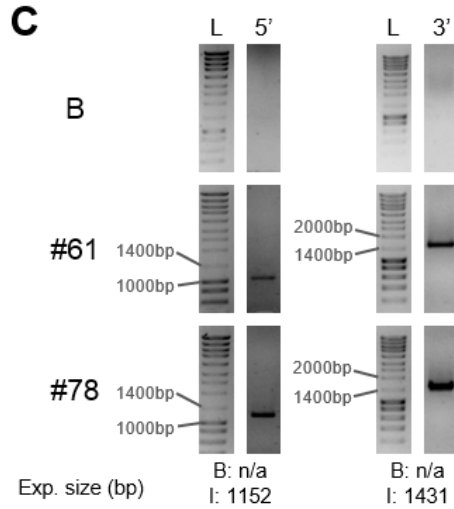
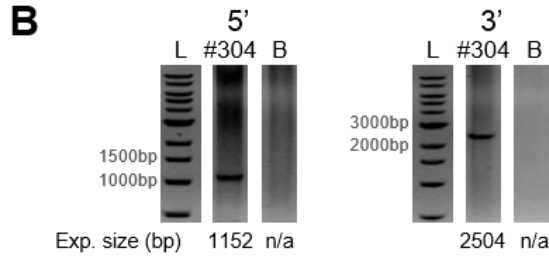
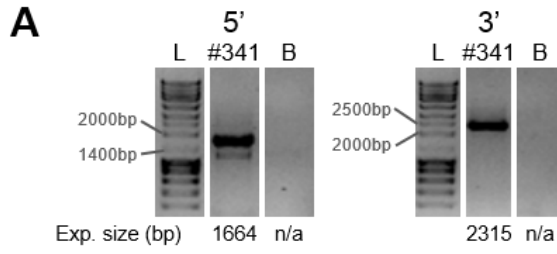


Figure S4.1: Genotyping of centriole reporter lines: A, POC1-Citrine (line #341); **B,** SAS6-mCherry (line #304); **C,** γ -tubulin2-Citrine; SAS6-mCherry (lines #61 and #78); **D,** POC1-Citrine; SAS6-mCherry (lines #55 and 71). 5' and 3' refers to PCR reactions evaluating recombinations at the 5' or the 3' ends, respectively. L - ladder; B - Genetic background; # - Positive line number. Exp. size (bp) indicates the expected size of the bands (in base pairs) obtained in either the genetic background (B) or the insertion (I) lines. n/a - non-applicable, indicating scenarios where the PCR should not yield any amplification. For details on the primer sequences used for genotyping each line, please see Table S4.2.

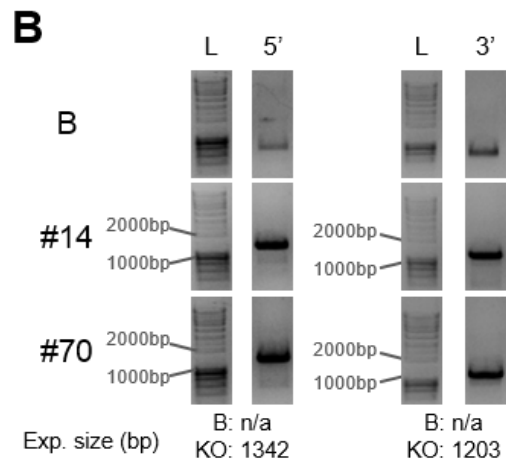
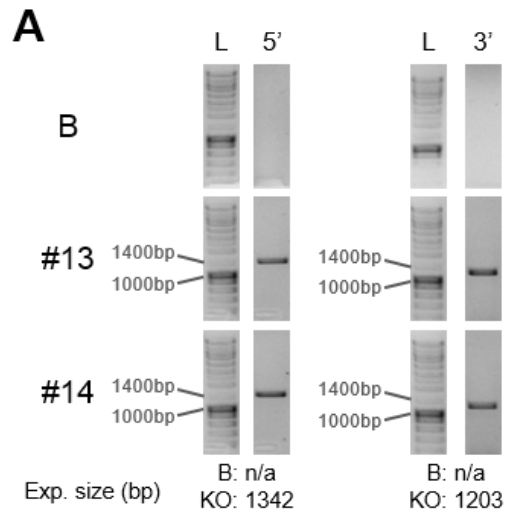


Figure S4.2: Genotyping of PpSAS6 K.O. plant lines: A, γ -tubulin2-Citrine; Δ sas6 (lines #13 and #14); **B,** POC1-Citrine; Δ sas6 (lines #14 and #70). L indicates wells with ladder, 5' and 3' refers to PCR reactions evaluating recombinations at the 5' or the 3' ends, respectively. B - Genetic background; # - Positive line number. Exp. size (bp) indicates the expected size of the bands (in base pairs) obtained in either the genetic background (B) or the insertion (I) lines. n/a - non-applicable, indicating scenarios where the PCR should not yield any

amplification. For details on the primer sequences used for genotyping each line, please see Table S4.2.

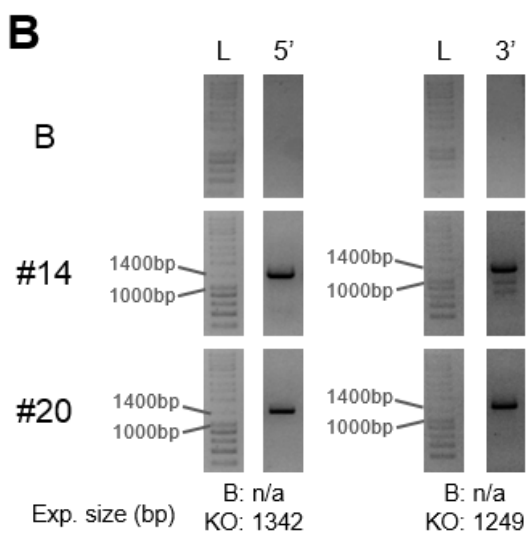
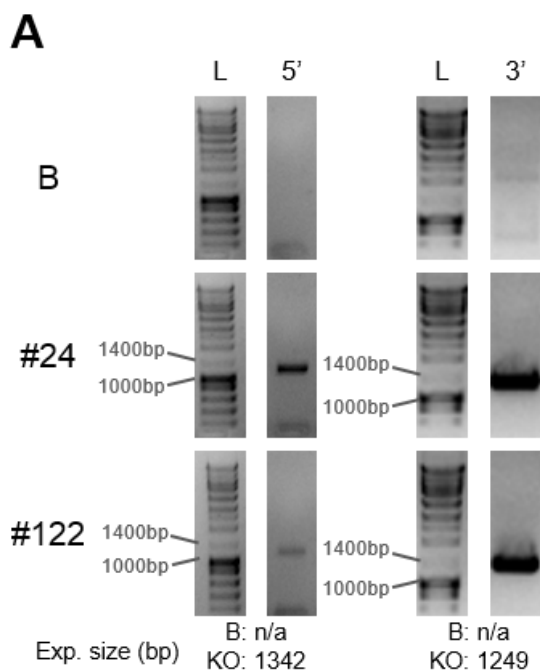


Figure S4.3: Genotyping of PpBld10 K.O. plant lines: A, γ -tubulin2-Citrine; Δ bld10 (lines #24 and #122); **B,** POC1-Citrine; Δ bld10 (lines #14 and #20). L indicates wells with ladder, 5' and 3' refers to PCR reactions evaluating recombinations at the 5' or the 3' ends, respectively. B - Genetic background; # - Positive line number. Exp. size (bp) indicates the expected size of the bands (in base pairs) obtained in either the genetic background (B) or the insertion (I) lines. n/a - non-applicable, indicating scenarios where the PCR should not yield any amplification. For details on the primer sequences used for genotyping each line, please see Table S4.2.

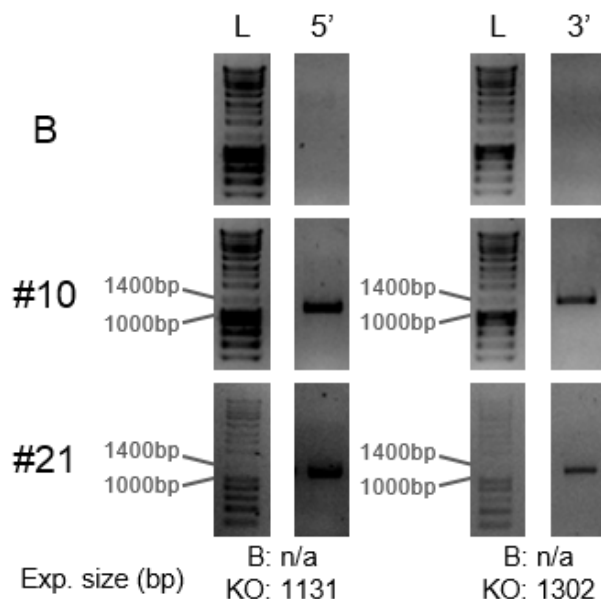


Figure S4.4: Genotyping of PpPOC1 K.O. (γ -tubulin2-Citrine; Δ poc1) plant lines #10 and #21. L indicates wells with ladder, 5' and 3' refers to PCR reactions evaluating recombinations at the 5' or the 3' ends, respectively. B - Genetic background; # - Positive line number. Exp. size (bp) indicates the expected size of the bands (in base pairs) obtained in either the genetic background (B) or the insertion (I) lines. n/a -

non-applicable, indicating scenarios where the PCR should not yield any amplification. For details on the primer sequences used for genotyping each line, please see Table S4.2.

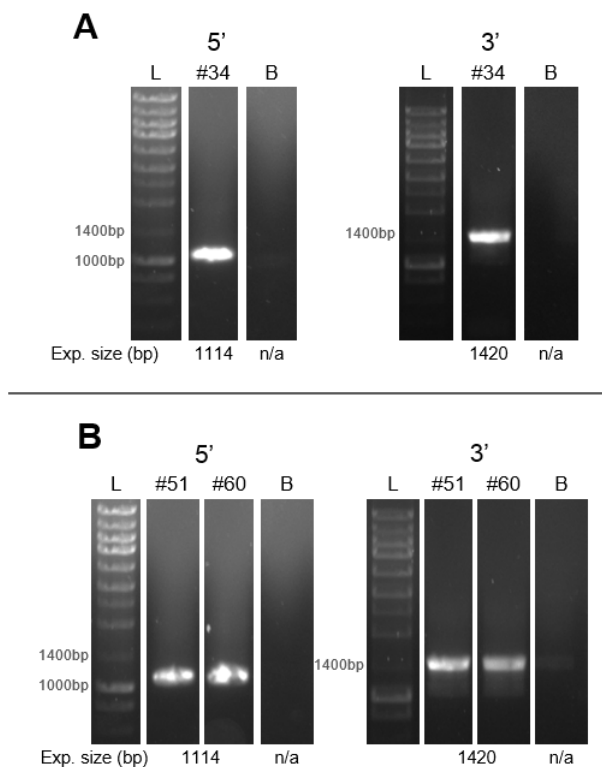


Figure S4.5: Genotyping of PpSAS4 K.O. plant lines: A, γ -tubulin2-Citrine; Δ *sas4* (line #34); **B,** POC1-Citrine; Δ *sas4* (lines #51 and #60). 5' and 3' refers to PCR reactions evaluating recombinations at the 5' or the 3' ends, respectively. L - ladder; B - Genetic background; # - Positive line number. Exp. size (bp) indicates the expected size of the bands (in base pairs) obtained in either the genetic background (B) or the insertion (I) lines. n/a - non-applicable, indicating scenarios where the PCR should not yield any amplification. For details on the primer sequences used for genotyping each line, please see Table S4.2.

Chapter 5.

General discussion

This section is adapted from: Gomes Pereira, S., Sousa, A.L., Nabais, C., Paixão, T., Holmes, A.J., Schorb, M., Goshima, G., Tranfield, E.M., Becker, J.D., and Bettencourt-Dias, M. The 3D architecture and molecular foundations of *de novo* centriole assembly *via* bicentrioles (*BioRxiv preprint, in revision*).

Centrioles are widespread in eukaryotes and can be assembled through various structural pathways. Centriole duplication has been extensively studied, however the diverse mechanisms underlying *de novo* centriole assembly have been rarely investigated. A key limitation in studying naturally occurring *de novo* centriole biogenesis is the lack of amenable model systems. The *de novo* assembly of centrioles during spermatogenesis in some land plants provides a unique opportunity to explore two almost exclusive *de novo* centriole assembly mechanisms: the bicentriole-mediated (e.g. bryophytes) and the blepharoplast-mediated (e.g. *Ginkgo biloba*) pathways.

Here, aiming at understanding the mechanisms behind centriole biogenesis *via* bicentrioles, I used the model bryophyte *Physcomitrium patens*. I took advantage of its pre-existing genetic engineering tools, and established the required imaging techniques to explore *P. patens* spermatogenesis (Chapter 2), with the cellular and subcellular resolution required to study such small structures as centrioles. These new established protocols have enabled me to characterize both structurally (Chapter 3) and molecularly (Chapter 4) the process of bicentriole-mediated *de novo* centriole assembly, as well as centriole maturation in *P. patens*.

This work delineates for the first time, a complete morphological pathway in which a bicentriole structure, composed by two centrioles

united by a common cartwheel, might arise in a MTOC, here called “concentrator”. After bicentriole splitting, the two centrioles mature asymmetrically, through elongation of the naked cartwheels and of specific microtubule triplets. These asymmetric centrioles template the assembly of two motile cilia, which often beat asynchronously. Remarkably, despite the presence of different structures in *P. patens*, I show that most of the evolutionary conserved proteins present in all branches of the eukaryotic tree of life, also have essential structural roles in bicentriole-mediated *de novo* centriole assembly.

5.1 Temporal, spatial and numerical regulation of centriole biogenesis

Centriole duplication is known to be tightly regulated in time (cycle-cycle coupling), space (daughters assemble orthogonally to their mothers), and number (one daughter per mother centriole)(Nigg and Holland, 2018). Polo-like kinase 4 (Plk4) is a master regulator of centriole biogenesis as its concentration and activity control centriole duplication in most animal cells (Bettencourt-Dias et al., 2005; Habedanck et al., 2005; Kleylein-Sohn et al., 2007). However, Plk4 orthologs have not been found outside of opisthokonts (Carvalho-Santos et al., 2010; Hodges et al., 2010). Therefore, other molecules and mechanisms are needed to regulate centriole biogenesis. Similarly to the particular transcriptional cascade upstream of deuterosome-mediated centriole assembly (Hoh et al., 2012; Arbi et al., 2017; Lewis and Stracker, 2021), I propose that the timing of centriole biogenesis in *P. patens* might be defined by the specific transcription of its centriolar components. This is supported by the fact that the known conserved

centriolar components SAS6, Cep135/Bld10, POC1 and CPAP/SAS4, appear to be preferentially expressed during *P. patens* spermatogenesis.

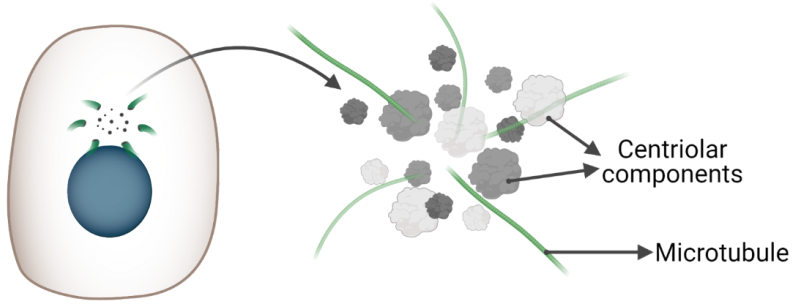
Despite their complex ultrastructure, centriole assembly appears to be a relatively fast process. Indeed, recent studies in *Naegleria gruberi* (Fritz-Laylin et al., 2016) and in *Drosophila melanogaster* (Nabais et al., 2021) suggest that centrioles might assemble within 10 to 15 minutes. Moreover, during the amoeba to flagellate transition in *Naegleria gruberi*, components are efficiently transcribed, translated and assembled into a centriole within 40 minutes (Fritz-Laylin et al., 2016). If similar temporal dynamics occur during *P. patens* centriole biogenesis, it provides a very short time interval to study this process, within the 15 days required for spermatogenesis to be completed. This might explain the low number of sperm cells detected at these particular early stages, which rendered it impossible to detail the early events (e.g. bicentriole splitting) and intermediate structures (e.g. early bicentriolar structures) during *P. patens* centriole assembly.

What could regulate the localization and number of centrioles during *de novo* biogenesis? While in centriole duplication, each mother serves as a platform for daughter centriole assembly, it is unclear how *de novo* biogenesis is spatially regulated. Recent studies highlight the existence and involvement of pericentriolar material (PCM) in *de novo* centriole assembly in animals (Mercey et al., 2019; Nabais et al., 2021). Given that many PCM components do not appear to have direct orthologs outside of the Holozoa (Hodges et al., 2010), it is possible that other molecules with similar function might exist in *P. patens*. During this work, I observed concentration of electron dense material close to the nucleus, which seemed to nucleate microtubules and to precede centriole assembly (Figure 5.1A). Furthermore, microtubules also emanated from already formed bicentrioles (Figure 5.1B). Similarly, electron dense

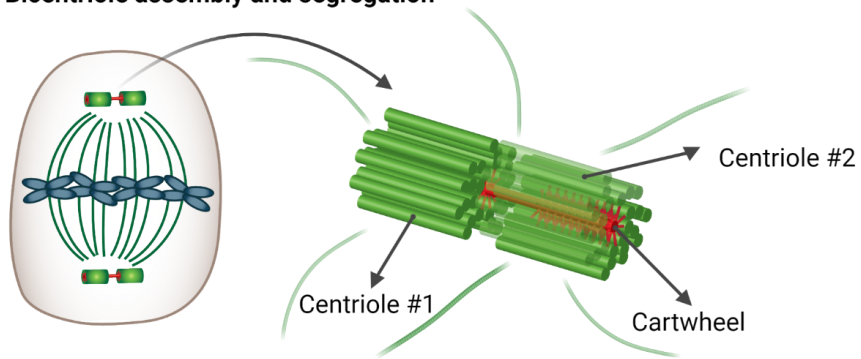
clouds which nucleate microtubules were also seen at the beginning of *de novo* centriole assembly in the bryophyte *Riella americana* (Robbins, 1984). It is tempting to speculate that microtubule trafficking towards an initially amorphous MTOC might locally concentrate centriolar precursors beyond a critical threshold required for *de novo* centriole assembly.

Finally, a variable number of centrioles assemble *de novo*, depending on the organism and pathway involved (Nabais et al., 2018). In *P. patens*, two bicentrioles appear to assemble in what could possibly be the sperm mother cell and this is also the case in *Riella americana* (Robbins, 1984) and *Marchantia polymorpha* (Moser and Kreitner, 1970), suggesting some general mechanism for number control. The localization of each bicentriole to one pole of the mitotic spindle (Figure 5.1C) is likely to ensure that each daughter cell inherits one bicentriole, or two centrioles, hence assembling only two cilia. It is possible that the linear geometry of the cartwheel (Figure 5.1B) ensures that only one centriole can assemble at each cartwheel end, while the opposite polarities of both sister centrioles (Figure 5.1B) could promote bicentriole splitting at the cartwheel's midpoint (Figure 5.1C). Such splitting could be the direct result of physical tension (due to the distinct centriole polarities), or local degradation of the continuous cartwheel at its midpoint (the only region deprived of microtubules), or alternatively, it might reflect the separation of two distinct closely positioned cartwheels. These features suggest that a structural mechanism might exist to regulate centriole copy number.

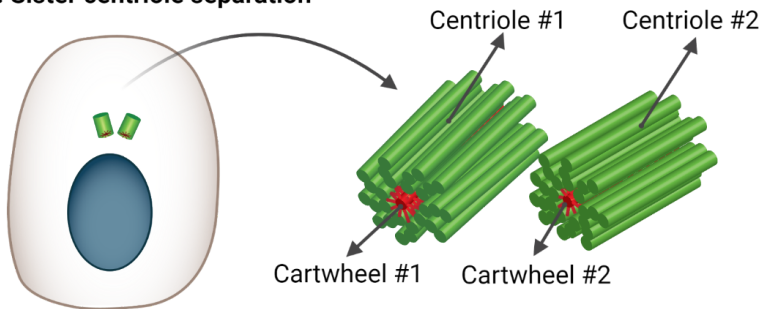
A. Concentrator



B. Bicentriole assembly and segregation



C. Sister centriole separation



Key:



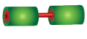

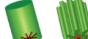

 Centriolar precursors	 Microtubules	 Bicentriole
 Nucleus / DNA	 Centriole	

Figure 5.1: *De novo* assembly of two sister centrioles during *P. patens* spermatogenesis occurs via assembly of two bicentrioles,

prior to the last mitotic division. A. Concentration of electron dense (grey) material (possibly centriolar components) is observed near the nuclear envelope in a region rich in microtubules (green), before (bi)centriole assembly; **B.** Two bicentrioles assemble in what could be the sperm mother cell. Each of them localizing at a pole of the mitotic spindle. Note the opposite polarities of both centrioles (green) and their continuous cartwheel (red); **C.** After cell division, each developing sperm cell contains two sister centrioles, originated from the splitting of the inherited bicentriole.

Although this work provides an unprecedented characterization of *de novo* centriole biogenesis *via* bicentrioles, many questions still remain. In order to fully understand the temporal dynamics of *de novo* centriole assembly in *P. patens*, and particularly due to the short time window to study this event, future studies should develop and employ live imaging of this process. The development of such live imaging protocols, combined with chemical and genetic manipulations, will likely reveal critical insights into the spatial (*e.g.* MTOC, or microtubule trafficking dependence) and numerical regulation (*e.g.* identifying limiting components) of centriole assembly.

5.2 Centriole length and asymmetries

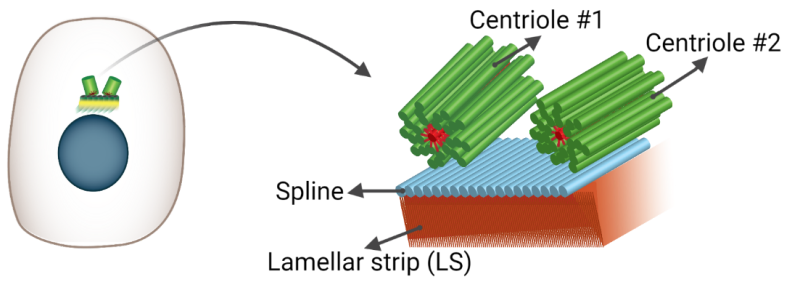
Centriole structure and size are highly regulated within each cell type in a species. However, diversity can be observed within cells/tissues from the same organism, as well as between distinct species (Gupta and Kitagawa, 2018; Jana, 2021). Such variation is present in terms of

centriole fold symmetry, size and specific adjacent features (e.g. appendages, PCM, MLS).

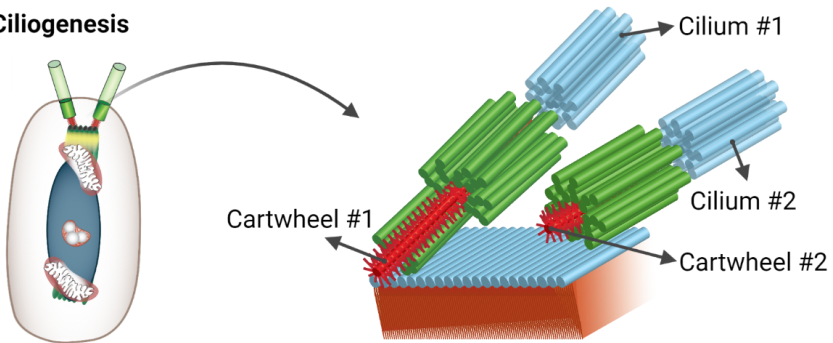
Despite reaching similar lengths upon maturation, human centriolar microtubule triplets are known to elongate individually during procentriole assembly. The A-tubule grows from its distal-end, while B and C-tubules elongate bidirectionally (Guichard et al., 2010). In contrast, cartwheels show proximal-end directional elongation (Aydogan et al., 2018) with a small (10-40nm) portion overhanging from the centriole wall (Klena et al., 2020). Nevertheless, cartwheel and centriolar microtubules appear to assemble interdependently in order to define and stabilize centriole architecture (Hilbert et al., 2016).

With this work I revealed that the two sister centrioles assembled from the same bicentriole in *P. patens* are initially very similar (Figures 5.1C and 5.2A). Yet unexpectedly, they mature asymmetrically. This asymmetry is seen both in terms of cartwheel and microtubule triplet length (Figure 5.2B), generating two distinct centriole types within the same sperm cell (Figure 5.2B). Furthermore, *P. patens* centrioles display elongated naked cartwheels overhanging from their proximal end (Figure 5.2B), in agreement with an autonomous proximal-end elongation mechanism (Aydogan et al., 2018).

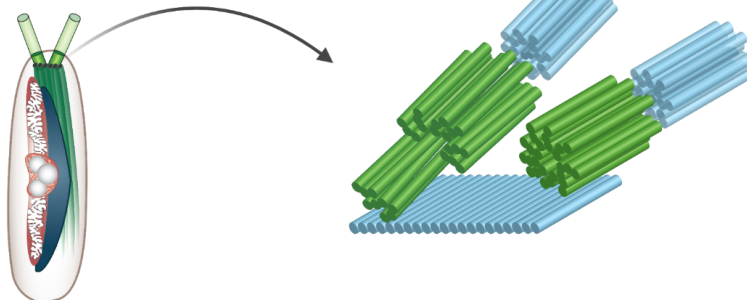
A. MLS assembly



B. Ciliogenesis



C. Cytodifferentiation



Key:

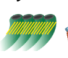
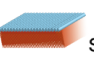

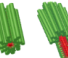

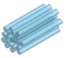



		Multilayered structure (MLS)				Centriole		Cilium
	Nucleus / DNA		Mitochondrion		Plastid			

Figure 5.2: *P. patens* sister centrioles mature asymmetrically. A. Association of the two similar sister centrioles (green) to the multilayered

structure (MLS), composed of the spline (cyan) and the lamellar strip (LS, orange); **B.** The two centrioles elongate asymmetrically, both in terms of cartwheel (red) as well as microtubule triplets (green) lengths. Note the naked cartwheel regions and the elongation of only some microtubule triplets in centriole #1. Both centrioles template seemingly similar cilia (cyan); **C.** After sperm cell cytodifferentiation, the lamellar strip and cartwheel structures appear to be absent, suggesting the existence of a remodeling process. However, the asymmetries amongst centriolar microtubule lengths, both between and within the same centriole, still remain.

The data presented throughout this work also suggests that microtubule triplets from the same mature centriole have distinct lengths (Figures 5.2B and C). This characteristic may be more widespread, as also suggested to be present in the bryophyte *Marchantia polymorpha* (Carothers and Kreitner, 1968). However, due to technical challenges, I was unable to address the directionality of such microtubule polymerization. This will possibly require long-term live imaging of spermatogenesis and/or perturbation experiments (e.g. fluorescence recovery after photobleaching - FRAP), which are not currently established for *P. patens*. Nevertheless, I envision that these particular microtubules might elongate from their proximal end, as elongation from the distal end would require the polymerizing microtubules to slide along the remaining ones. As the microtubule blades are attached by linker structures (A-C linkers and inner scaffold), such sliding would imply the absence of such linkers in *P. patens* or their temporary disassembly, while keeping centriolar stability and integrity.

Overall, these features make *P. patens* centrioles an exciting system to study cartwheel and microtubule triplet elongation, and in particular to

investigate whether distinct regulatory mechanisms operate in each centriole.

5.3 Centriole remodeling, cilia beating, and fate of the locomotory apparatus

Centriole remodeling is known to take place during spermatogenesis in several animal species, although its exact mechanisms and significance remain unknown (Manandhar et al., 2005; Avidor-Reiss et al., 2019). Similarly, *P. patens* centrioles might also be remodeled upon sperm cell cytodifferentiation, as no SAS6 signal, lamellar strip or the cartwheel structures were detected in mature spermatids (Figure 5.2C). Unfortunately, due to the extensive chromatin compaction of these cells (which rendered the nuclei too electron dense), I was unable to obtain and reconstruct electron tomograms of this particular stage. Moreover, my attempts to analyze cryo-immobilized released sperm packages by TEM were unsuccessful, as these were impossible to find in the final resin sample blocks. In the future it would be important to obtain detailed ultrastructural information of the locomotory apparatus of released spermatids, in order to confirm such remodeling.

A similar loss in SAS6 signal is observed during centriole remodeling in *Drosophila melanogaster*, although its mechanistical origin is not clear (Khire et al., 2015, 2016). SAS6 is also lost during cell division in mammalian cells. Such loss is triggered by the anaphase promoting complex that targets SAS6 for proteasomal degradation (Strnad et al., 2007). However in differentiating spermatids, centriole remodeling does not appear to co-occur with cell division. Therefore, although SAS6 degradation could still be dependent on proteasome targeting, its trigger

is likely to be specific for this unique differentiation process; or it might otherwise result from a repurposing of the cell cycle machinery, as reported during multiciliogenesis in mouse brain progenitors (Al Jord et al., 2017).

Centrosome reduction and centriole remodeling also involve loss and alterations to the pericentriolar material (PCM) that surrounds animal centrioles (Manandhar et al., 2005; Avidor-Reiss et al., 2019). The PCM is an electron dense ultrastructurally amorphous mesh of proteins (Paintrand et al., 1992; Guichard et al., 2010; Greenan et al., 2018). By contrast, the plant-specific lamellar strip (LS) is composed of organized electron dense protein layers (Figures 5.2A and B), which disappear upon sperm cell cytodifferentiation in *P. patens* (Figure 5.2C), as well as in other bryophyte species (Carothers and Duckett, 1980; Renzaglia and Garbary, 2001). Therefore, I envision that the LS could perform PCM-like functions, concentrating the required components for centriole and cilia maturation (Pimenta-Marques and Bettencourt-Dias, 2020). In agreement with this idea, centrin was shown to localize to the LS of several plant species (Vaughn et al., 1993). Here, I have shown that SAS6 also localizes to the LS, at least in *P. patens* differentiating sperm cells, however, it is not critical for its assembly. The disappearance of the LS upon locomotory apparatus maturation, could result from a depletion of its components, an active degradation mechanism, or simply the loss a critical component for its maintenance, such as observed for the PCM during oogenesis in *Drosophila melanogaster* (Pimenta-Marques et al., 2016).

Despite their particular structure and asymmetries, both sister centrioles appear to mature into basal bodies, templating the assembly of two apparently structurally similar cilia (Figures 5.2B and C) which often beat asynchronously. Still, due to several technical limitations, such

as the temporal and spatial (z) resolutions in acquiring brightfield and fluorescence images simultaneously, and a failure in fluorescently labeling the cilia, I was unable to establish a link between centriole asymmetries and ciliary (a)synchrony. Nevertheless, I believe such link might not be direct, or not exist at all. This is supported by the analysis of POC1 signal, which has revealed significant differences between sister centrioles in 94% of the cells. Therefore, if ciliary asynchrony would be a direct consequence of centriole asymmetry, then one would expect to observe such behaviour in a similar proportion of the cells. However, my analysis of ciliary behaviour has identified asynchronous beating in only 83% of the cells, with 17% displaying synchronous beating. This proportion of cells with synchronous ciliary beating contrasts with the 6% wherein centriole differences were not statistically significant. Therefore, both processes might not be directly related. Additionally, during analysis of ciliary behaviour, I was able to observe one cell (out of 135) which appeared to switch from asynchronous to synchronous beating. This suggests that cells can potentially regulate/coordinate their ciliary beating, as observed for *Chlamydomonas reinhardtii* grown in the dark (Polin et al., 2009), and many other systems (Wan, 2018).

Still, one cannot exclude that differences between cilia and their regulation might be affected by the distinct centriole structures. It could be possible that, due to their distinct sizes, centrioles could impact the trafficking rate of molecules (e.g. intraflagellar transport trains) to and from the cilia. Moreover, other asymmetries namely in the transition zone, might exist and have escaped my analyses. Therefore, future studies should optimize live imaging of ciliary beating to enable simultaneous acquisition of brightfield and fluorescence signals, or cilia labeling, with enough spatial and temporal resolution, as well as explore the existence of other structural asymmetries in the cilia, transition zone, and even in the centrioles with higher (e.g. cryoEM) resolution. Another

interesting feature to consider is a possible role for the MLS in regulating/coupling cilia beating, as in *Chlamydomonas reinhardtii* basal body connections have been shown to impact cilia synchronization (Wan and Goldstein, 2016).

Finally, a key question is what happens to these centrioles upon fertilization? While in many animal species, paternal inheritance of centrioles is critical to enable proper embryo development (e.g. Hertig and Adams, 1967; Schatten et al., 1985; Crozet et al., 2000), other species such as mice, disregard paternal centrioles and assemble these structures *de novo* during early embryogenesis (Schatten et al., 1985; Manandhar et al., 1998; Simerly et al., 2016). Plant cells divide in the absence of centriolar structures, using acentrosomal MTOCs (section 1.1.1). Therefore, four scenarios for the fate of *P. patens* locomotory apparatus can be envisioned. On one hand (scenario 1), it would be possible that this complex structure is not internalized upon gamete fusion. I consider this option highly unlikely, due to the positioning of both centrioles at the tip of the cell and the close association between the MLS and the nucleus; If, however, the locomotory apparatus is internalized into the zygote, then it could simply be passively lost throughout time (scenario 2); or actively degraded (scenario 3), as observed during spore germination in chytrid fungi (Venard et al., 2020); alternatively (scenario 4), centrioles could act as MTOCs in the first embryonic divisions, with the MLS and cilia being passively or actively degraded.

Potentially, one could distinguish scenario 1 from the remaining ones by the presence of POC1-Citrine and/or acetylated- α -tubulin bundles in early fertilized archegonia. However, distinction between the remaining scenarios would likely require live imaging and perturbation experiments (e.g. genetic engineering, laser ablation) of the fertilization and first

embryonic divisions, for which no methods are currently available in *P. patens*. Therefore, although this is a very intriguing question, I was unable to explore it, both due to technical as well as time constraints.

5.4 Evolution and diversification of centriole assembly

Several key centriolar components are known to be conserved in ciliated species (Carvalho-Santos et al., 2010; Hodges et al., 2010). By exploring their localization and function, I show that their critical structural roles in centriole assembly have been mostly conserved throughout evolution. SAS6 and Bld10 are essential for cartwheel assembly and stability respectively (Figures 5.3A and B), while Bld10 and POC1 appear to be required for assembling the 9-fold symmetrical microtubule wall (Figures 5.3B and C). Therefore, the observed phenotypes in knock-out plant lines support SAS6 as being the core component of *P. patens* cartwheel rings, Bld10 of its spokes, and POC1 as a component of the inner scaffold and/or A-C linker. Nevertheless, some specificities exist in the regulation of these components that may underlie novelties. For example, *P. patens*' SAS6 localization to the MLS and its unique elongation into naked cartwheel regions (Figures 5.3B and C).

What elements could lead to diversification of the pathways? A particular feature of *P. patens* centrioles is that they assemble in a bicentriolar configuration. Although the molecular basis for the assembly of this structure remains unknown, it is possible that a particular SAS6 conformation might enable cartwheel bidirectional elongation. Indeed, recent cryo-EM studies have unravelled species-specific differences in cartwheel architecture, and suggested that these might originate from

molecular differences in protein (namely SAS6) conformation (Klena et al., 2020; Nazarov et al., 2020). Such distinct SAS6 and/or Bld10 conformations could potentially explain the elongation of stable naked cartwheel regions (Figures 5.3B and C), as well as SAS6 localization to the LS, two additional interesting features revealed in this work.

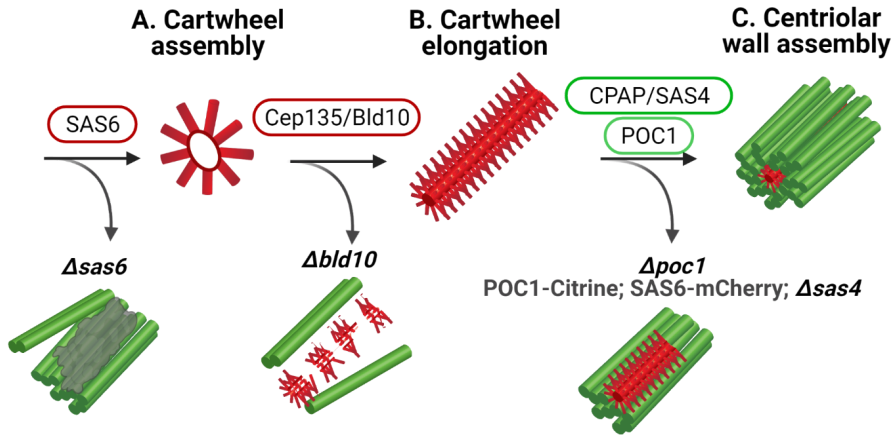


Figure 5.3: Centriole assembly in *P. patens* appears to rely on a similar molecular pathway as known in several other eukaryotic species. **A.** Cartwheel (red) assembly relies on its core component SAS6, as in the absence of this protein ($\Delta sas6$) no cartwheel rings are assembled despite the presence of microtubules (green) surrounding an electron dense (grey) region; **B.** Cep135/Bld10 is required for cartwheel's stable elongation and assembly of the centriolar wall, as when this component is lost ($\Delta bld10$) the cartwheels appear as discontinuous small fragments without any attached microtubules; **C.** POC1 is critical for assembly of 9-fold symmetrical centrioles in *P. patens*, while potentially cooperating with the less critical component SAS4. In both $\Delta poc1$ and POC1-Citrine;SAS6-mCherry; $\Delta sas4$, only some microtubule triplets attach to the cartwheel's spokes.

Another major difference between centriole biogenesis in *P. patens* appears to be the less critical role for the conserved centriolar wall component SAS4. Indeed, CPAP/SAS4 was found to be required for *de novo* assembly of centrioles upon Plk4 overexpression in *Drosophila melanogaster* unfertilized eggs (Rodrigues-Martins et al., 2007), and for centriole duplication in *C. elegans* and human cells (Leidel and Gönczy, 2003; Kleylein-Sohn et al., 2007; Kohlmaier et al., 2009; Tang et al., 2009). However, *P. patens*' SAS4 does not appear to play a critical role for centriole biogenesis *per se*. Instead, it appears to work synergistically with POC1 in the assembly and/or stabilization of the centriole wall (Figure 5.3C). Moreover, SAS4 also appears to have a subtle effect in regulating cartwheel numbers in *P. patens*. A role that may have been, at least partially conserved, as CPAP overexpression was reported to induce centriole over duplication in human cells (Kohlmaier et al., 2009; Lin et al., 2013a). Still, more studies will be required in order to clarify the exact functions of PpSAS4, its possible cooperation with POC1 in *P. patens*, as well as the conservation of such synergy in other species.

Additionally, other centriolar proteins appear to be conserved in *P. patens*, namely Cep97 and Cep120, which are known to regulate animal centriole length (Spektor et al., 2007; Comartin et al., 2013; Lin et al., 2013a; Dobbelaere et al., 2020). Moreover, Cep120 was reported to localize asymmetrically between mother and daughter centrioles in human cells, to directly cooperate with CPAP/SAS4 in regulating centriole length, and also to be required for Cep135/Bld10 localization to procentrioles (Mahjoub et al., 2010; Comartin et al., 2013; Lin et al., 2013b). Therefore, it would be very interesting to explore the localization and functions of these proteins in *P. patens*, particularly their roles in establishing and/or regulating the centriole asymmetries observed.

Finally, it is possible that specific structures, such as the MLS, might play a role in diversification of the centriolar structure. The spline was

reported to be involved in nuclear elongation in the algae *Nitella* (Turner, 1970). This work suggests that the spline may also stabilize specific microtubule triplets, as in $\Delta poc1$ and in POC1-Citrine;SAS6-mCherry; $\Delta sas4$ plants only the triplets closer to the spline appear to be able to bind the cartwheel spokes (Figure 5.3C), being also the longer ones in the asymmetrical centriole walls (Figures 5.3B and C). Consequently, I hypothesize that the MLS may perform PCM-like functions, not only in concentrating components, but also in stabilizing the structures assembled (Pimenta-Marques and Bettencourt-Dias, 2020), such as the naked cartwheels and particular microtubule triplets. Moreover, no major structural defects were observed in any of the deletion genotypes analyzed, suggesting that, despite closely associated, MLS assembly might rely on an independent mechanism from that of centriole biogenesis. In the future it will be important to manipulate the MLS, as well as to identify PCM-functional equivalents, to test whether these are critical variables in generating diverse structures, such as the ones observed here in *P. patens*.

In summary, I have described with unprecedented detail the bicentriole-mediated *de novo* centriole biogenesis pathway in the model bryophyte *Physcomitrium patens*, and how the initially identical centrioles mature into asymmetrical entities that assemble structurally similar, but often asynchronously beating cilia. My work pioneers the molecular understanding of *de novo* centriole biogenesis and maturation in land plants, supporting a scenario where centriole biogenesis and maturation is less constrained than previously thought. While I focused on a single species, other land plants have been described to show similar structural features, and many more organisms form centrioles *de novo*. Moreover, the results here presented suggest that the same molecular components can generate somewhat diverse structures, even

if associated with essential functions such as motility and fertility. Finally, this work highlights the importance of investigating fundamental processes in diverse species as more tools become available.

5.4 References

Al Jord, A., Shihavuddin, A., Servignat, R., Faucourt, M., Genovesio, A., Karaiskou, A., Sobczak-thépot, J., Spassky, N., and Meunier, A. (2017). Calibrated mitotic oscillator drives motile ciliogenesis. *Science*. 358, 803–806.

Arbi, M., Pefani, D.-E., Taraviras, S., and Lygerou, Z. (2017). Controlling centriole numbers: Geminin family members as master regulators of centriole amplification and multiciliogenesis. *Chromosoma*.

Avidor-Reiss, T., Mazur, M., Fishman, E.L., and Sindhvani, P. (2019). The Role of Sperm Centrioles in Human Reproduction – The Known and the Unknown. *Front. Cell Dev. Biol.* 7, 1–15.

Aydogan, M.G., Wainman, A., Saurya, S., Steinacker, T.L., Caballe, A., Novak, Z.A., Baumbach, J., Muschalik, N., and Raff, J.W. (2018). A homeostatic clock sets daughter centriole size in flies. *J. Cell Biol.* 217, 1233–1248.

Bettencourt-Dias, M., Rodrigues-Martins, A., Carpenter, L., Riparbelli, M., Lehmann, L., Gatt, M.K., Carmo, N., Balloux, F., Callaini, G., and Glover, D.M. (2005). SAK/PLK4 is required for centriole duplication and flagella development. *Curr. Biol.* 15, 2199–2207.

Carothers, Z.B., and Duckett, J.G. (1980). The Bryophyte Spermatozoid : A Source of New Phylogenetic Information. *Bull. Torrey Bot. Club* 107, 281–297.

Carothers, Z.B., and Kreitner, G.L. (1968). Studies of Spermatogenesis in the Hepaticae. II. Blepharoplast structure in the spermatid of *Marchantia*. *J. Cell Biol.* 36, 603–616.

Carvalho-Santos, Z., Machado, P., Branco, P., Tavares-Cadete, F., Rodrigues-Martins, A., Pereira-Leal, J.B., and Bettencourt-Dias, M. (2010).

Stepwise evolution of the centriole-assembly pathway. *J. Cell Sci.* **123**, 1414–1426.

Comartin, D., Gupta, G.D., Fussner, E., Coyaud, É., Hasegan, M., Archinti, M., Cheung, S.W.T., Pinchev, D., Lawo, S., Raught, B., et al. (2013). CEP120 and SPICE1 cooperate with CPAP in centriole elongation. *Curr. Biol.* **23**, 1360–1366.

Crozet, N., Dahirel, M., and Chesne, P. (2000). Centrosome inheritance in sheep zygotes: Centrioles are contributed by the sperm. *Microsc. Res. Tech.* **49**, 445–450.

Dobbelaere, J., Schmidt Cernohorska, M., Huranova, M., Slade, D., and Dammermann, A. (2020). Cep97 Is Required for Centriole Structural Integrity and Cilia Formation in *Drosophila*. *Curr. Biol.* **30**, 3045–3055.

Fritz-Laylin, L.K., Levy, Y.Y., Levitan, E., Chen, S., Cande, W.Z., Lai, E.Y., and Fulton, C. (2016). Rapid centriole assembly in *Naegleria* reveals conserved roles for both *de novo* and mentored assembly. *Cytoskeleton* **73**, 109–116.

Greenan, G., Keszthelyi, B., Vale, R.D., and Agard, D.A. (2018). Insights into centriole biogenesis and evolution revealed by cryoTomography of doublet and triplet centrioles. *Elife* **7**, 1–18.

Guichard, P., Chrétien, D., Marco, S., and Tassin, A.-M. (2010). Procentriole assembly revealed by cryo-electron tomography. *EMBO J.* **29**, 1565–1572.

Gupta, A., and Kitagawa, D. (2018). Ultrastructural diversity between centrioles of eukaryotes. *J. Biochem.* **164**, 1–8.

Habedanck, R., Stierhof, Y.D., Wilkinson, C.J., and Nigg, E.A. (2005). The Polo kinase Plk4 functions in centriole duplication. *Nat. Cell Biol.* **7**, 1140–1146.

Hertig, A.T., and Adams, E.C. (1967). Studies on the human oocyte and its follicle. I. Ultrastructural and histochemical observations on the primordial follicle stage. *J. Cell Biol.* **34**, 647–675.

Hilbert, M., Noga, A., Frey, D., Hamel, V., Guichard, P., Kraatz, S.H.W., Pfreundschuh, M., Hosner, S., Flückiger, I., Jaussi, R., et al. (2016). SAS-6 engineering reveals interdependence between cartwheel and microtubules in determining centriole architecture. *Nat. Cell Biol.* **18**, 393–403.

Hodges, M.E., Scheumann, N., Wickstead, B., Langdale, J.A., and Gull, K. (2010). Reconstructing the evolutionary history of the centriole from protein components. *J. Cell Sci.* *123*, 1407–1413.

Hoh, R.A., Stowe, T.R., Turk, E., and Stearns, T. (2012). Transcriptional Program of Ciliated Epithelial Cells Reveals New Cilium and Centrosome Components and Links to Human Disease. *PLoS One* *7*, e52166.

Jana, S.C. (2021). Centrosome structure and biogenesis: Variations on a theme? *Semin. Cell Dev. Biol.* *110*, 123–138.

Khire, A., Vizuet, A.A., Davila, E., and Avidor-Reiss, T. (2015). Asterless Reduction during Spermiogenesis Is Regulated by Plk4 and Is Essential for Zygote Development in *Drosophila*. *Curr. Biol.* *25*, 2956–2963.

Khire, A., Jo, K.H., Kong, D., Akhshi, T., Blachon, S., Cekic, A.R., Hynek, S., Ha, A., Loncarek, J., Mennella, V., et al. (2016). Centriole Remodeling during Spermiogenesis in *Drosophila*. *Curr. Biol.* *26*, 1–7.

Klena, N., Le Guennec, M., Tassin, A., van den Hoek, H., Erdmann, P.S., Schaffer, M., Geimer, S., Aeschlimann, G., Kovacic, L., Sadian, Y., et al. (2020). Architecture of the centriole cartwheel-containing region revealed by cryo-electron tomography. *EMBO J.* e106246.

Kleylein-Sohn, J., Westendorf, J., Le Clech, M., Habedanck, R., Stierhof, Y.D., and Nigg, E.A. (2007). Plk4-Induced Centriole Biogenesis in Human Cells. *Dev. Cell* *13*, 190–202.

Kohlmaier, G., Lončarek, J., Meng, X., McEwen, B.F., Mogensen, M.M., Spektor, A., Dynlacht, B.D., Khodjakov, A., and Gönczy, P. (2009). Overly Long Centrioles and Defective Cell Division upon Excess of the SAS-4-Related Protein CPAP. *Curr. Biol.* *19*, 1012–1018.

Leidel, S., and Gönczy, P. (2003). SAS-4 is essential for centrosome duplication in *C. elegans* and is recruited to daughter centrioles once per cell cycle. *Dev. Cell* *4*, 431–439.

Lewis, M., and Stracker, T.H. (2021). Transcriptional regulation of multiciliated cell differentiation. *Semin. Cell Dev. Biol.* *110*, 51–60.

Lin, Y.N., Wu, C.T., Lin, Y.C., Hsu, W. Bin, Tang, C.J.C., Chang, C.W., and Tang, T.K. (2013a). CEP120 interacts with CPAP and positively regulates centriole elongation. *J. Cell Biol.* *202*, 211–219.

Lin, Y.C., Chang, C.W., Hsu, W. Bin, Tang, C.J.C., Lin, Y.N., Chou, E.J., Wu, C.T., and Tang, T.K. (2013b). Human microcephaly protein CEP135 binds to hSAS-6 and CPAP, and is required for centriole assembly. *EMBO J.* 32, 1141–1154.

Mahjoub, M.R., Xie, Z., and Stearns, T. (2010). Cep120 is asymmetrically localized to the daughter centriole and is essential for centriole assembly. *J. Cell Biol.* 191, 331–346.

Manandhar, G., Sutovsky, P., Joshi, H.C., Stearns, T., and Schatten, G. (1998). Centrosome reduction during mouse spermiogenesis. *Dev. Biol.* 203, 424–434.

Manandhar, G., Schatten, H., and Sutovsky, P. (2005). Centrosome Reduction During Gametogenesis and Its Significance. *Biol. Reprod.* 72, 2–13.

Mercey, O., Levine, M.S., LoMastro, G.M., Rostaing, P., Brotslaw, E., Gomez, V., Kumar, A., Spassky, N., Mitchell, B.J., Meunier, A., et al. (2019). Massive centriole production can occur in the absence of deuterosomes in multiciliated cells. *Nat. Cell Biol.* 21, 1544–1552.

Moser, J.W., and Kreitner, G.L. (1970). Centrosome Structure in *Anthoceros laevis* and *Marchantia polymorpha*. *J. Cell Biol.* 44, 454–458.

Nabais, C., Pereira, S.G., and Bettencourt-Dias, M. (2018). Noncanonical Biogenesis of Centrioles and Basal Bodies. *Cold Spring Harb. Symp. Quant. Biol.* 82:123-135.

Nabais, C., Pessoa, D., de-Carvalho, J., van Zanten, T., Duarte, P., Mayor, S., Carneiro, J., Telley, I.A., and Bettencourt-Dias, M. (2021). Plk4 triggers autonomous *de novo* centriole biogenesis and maturation. *J. Cell Biol.* 220 (5): e202008090.

Nazarov, S., Bezler, A., Hatzopoulos, G.N., Nemčiková Villímová, V., Demurtas, D., Le Guennec, M., Guichard, P., and Gönczy, P. (2020). Novel features of centriole polarity and cartwheel stacking revealed by cryo-tomography. *EMBO J.* 39, 1–17.

Nigg, E.A., and Holland, A.J. (2018). Once and only once: Mechanisms of centriole duplication and their deregulation in diseases. *Nat. Rev. Mol. Cell Biol.* 19, 297–312.

Paintrand, M., Moudjou, M., Delacroix, H., and Bornens, M. (1992). Centrosome organization and centriole architecture: Their sensitivity to divalent cations. *J. Struct. Biol.* *108*, 107–128.

Pimenta-Marques, A., and Bettencourt-Dias, M. (2020). Pericentriolar material. *Curr. Biol.* *30*, R677–R697.

Pimenta-Marques, A., Bento, I., Lopes, C.A.M., Duarte, P., Jana, S.C., and Bettencourt-Dias, M. (2016). A mechanism for the elimination of the female gamete centrosome in *Drosophila melanogaster*. *Science*. *353*, aaf4866.

Polin, M., Tuval, I., Drescher, K., Gollub, J.P., and Goldstein, R.E. (2009). *Chlamydomonas* swims with two “gears” in a eukaryotic version of run-and-tumble locomotion. *Science*. *325*, 487–490.

Renzaglia, K.S., and Garbary, D.J. (2001). Motile Gametes of Land Plants: Diversity, Development, and Evolution. *CRC. Crit. Rev. Plant Sci.* *20*, 107–213.

Robbins, R.R. (1984). Origin and behavior of bicentriolar centrosomes in the bryophyte *Riella americana*. *Protoplasma* *121*, 114–119.

Rodrigues-Martins, A., Riparbelli, M., Callaini, G., Glover, D.M., and Bettencourt-Dias, M. (2007). Revisiting the Role of the Mother Centriole in Centriole Biogenesis. *Science*. *316*, 1046–1050.

Schatten, G., Simerly, C., and Schatten, H. (1985). Microtubule configurations during fertilization, mitosis, and early development in the mouse and the requirement for egg microtubule-mediated motility during mammalian fertilization. *Proc. Natl. Acad. Sci. USA* *82*, 4152–4156.

Simerly, C., Castro, C., Hartnett, C., Lin, C.C., Sukhwani, M., Orwig, K., and Schatten, G. (2016). Post-Testicular Sperm Maturation: Centriole Pairs, Found in Upper Epididymis, are Destroyed Prior to Sperm’s Release at Ejaculation. *Sci. Rep.* *6*, 31816.

Spektor, A., Tsang, W.Y., Khoo, D., and Dynlacht, B.D. (2007). Cep97 and CP110 Suppress a Cilia Assembly Program. *Cell* *130*, 678–690.

Strnad, P., Leidel, S., Vinogradova, T., Euteneuer, U., Khodjakov, A., and Gönczy, P. (2007). Regulated HsSAS-6 Levels Ensure Formation of a Single Procentriole per Centriole during the Centrosome Duplication Cycle. *Dev. Cell* *13*, 203–213.

Tang, C.J.C., Fu, R.H., Wu, K.S., Hsu, W. Bin, and Tang, T.K. (2009). CPAP is a cell-cycle regulated protein that controls centriole length. *Nat. Cell Biol.* 11, 825–831.

Turner, F.R. (1970). The effects of colchicine on spermatogenesis in *Nitella*. *J. Cell Biol.* 46, 220–234.

Vaughn, K.C., Sherman, T.D., and Renzaglia, K.S. (1993). A centrin homologue is a component of the multilayered structure in bryophytes and pteridophytes. *Protoplasma* 175, 58–66.

Venard, C.M., Vasudevan, K.K., and Stearns, T. (2020). Cilium axoneme internalization and degradation in chytrid fungi. *Cytoskeleton* 77, 365–378.

Wan, K.Y. (2018). Coordination of eukaryotic cilia and flagella. *Essays Biochem.* 62, 829–838.

Wan, K.Y., and Goldstein, R.E. (2016). Coordinated beating of algal flagella is mediated by basal coupling. *Proc. Natl. Acad. Sci. U. S. A.* 113, E2784–E2793.

ITQB-UNL | Av. da República, 2780-157 Oeiras, Portugal
Tel (+351) 214 469 100 | Fax (+351) 214 411 277

www.itqb.unl.pt